Development and application of ab initio electron dynamics on traditional and quantum compute architectures

Inaugural-Dissertation

to obtain the academic degree
Doctor rerum naturalium (Dr. rer. nat.)

submitted to the Department of Biology, Chemistry, Pharmacy
of Freie Universität Berlin

by
Fabian Langkabel

2023

This work was prepared under the supervision of
PD Dr. Annika Bande at the Helmholtz-Zentrum Berlin
between August 2020 and July 2023

1st Reviewer: PD Dr. Annika Bande

2nd Reviewer: Prof. Dr. Bettina G. Keller

Date of defense: 12.12.2023

Acknowledgements

A project as large as a doctoral thesis would have been almost impossible without help. Therefore, I would like to thank everyone who contributed to the success of this work.
First of all, I would like to thank Annika Bande for the chance to do this thesis in her research group and for her great support during this time. I also want to take this opportunity to thank Bettina Keller in advance for preparing the second review.
Special thanks go to the entire AG Bande for the friendly and productive atmosphere as well as professional support. This includes Sara Marando, Thorren Kirschbaum, Yannik Schütze, Xiangfei Wang, Kanishka Singh, Joana-Lysiane Schäfer, and all other current and former members. Above all, I would like to thank Pascal Krause for his outstanding cooperation and additional professional support. I would also like to thank Manuel Güterbock and Paul Anton Albrecht who trusted me with the supervision of their master theses.
I would also like to thank Garnet Chan for the kind welcome in his research group during a research stay. Thereby, my thanks also go to his whole research group especially Seunghoon Lee and Sandeep Sharma for the great atmosphere and cooperation.
Finally, I would like to thank my family, friends, and girlfriend for their extraordinary support throughout this time.

Declaration of Independence

Herewith I certify that I have prepared and written my thesis independently and that I have not used any sources and aids other than those indicated by me. This thesis has not been submitted in the same or a similar form to any other examination procedure or institution.

Date: July 7, 2023

. . . . . .

Fabian Langkabel

Contents

Zusammenfassung I

Abstract III

List of Publications V

1 Introduction 1

1.1 Simulation of the inter-Coulombic decay in quantum dots 2
1.2 Development of an electron dynamics program 4
1.3 Development of an electron dynamics algorithm for quantum computers . 5

2 Theoretical Background 8

2.1 Fundamentals of quantum mechanics 8
2.1.1 Schrödinger equation 8
2.1.2 Electronic wave function 10
2.1.3 Second quantization 12
2.2 Electronic structure theory 14
2.2.1 Hartree-Fock 14
2.2.2 Configuration interaction 19
2.2.3 Multi-configuration self-consistent field 21
2.2.4 Electronic state analysis 22
2.3 Electron dynamics 23
2.3.1 Propagator 24
2.3.2 Time-dependent configuration interaction 24
2.3.3 Time-dependent Hartree Fock 28
2.3.4 Multi-configuration Time-Dependent Hartree 28
2.4 Quantum computing 35
2.4.1 Qubits and quantum gates 35
2.4.2 Fermion-qubit mapping 38
2.4.3 Quantum algorithms 40

3 Results and Conclusion **45**
3.1 Interparticle Coulombic decay in three quantum dot arrangements 45
3.2 Development of a new program for simulation and novel analysis of electron dynamics 51
3.3 Quantum compute algorithm for electron dynamics 58
3.4 Overall conclusion 61

4 Bibliography **63**

5 Publications **70**
5.1 Three-electron dynamics of the interparticle Coulombic decay with two-dimensional continuum confinement 71
5.2 Three-Electron Dynamics of the Interparticle Coulombic Decay in Doubly Excited Clusters with One-Dimensional Continuum Confinement 81
5.3 JELLYFISH: a modular code for wave function-based electron dynamics simulations and visualizations on traditional and quantum compute architectures 105
5.4 Making optical excitations visible – An exciton wavefunction extension to the time-dependent configuration interaction method 134
5.5 Quantum-Compute Algorithm for Exact Laser-Driven Electron Dynamics in Molecules 145

Zusammenfassung

Dynamische Prozesse von Elektronen sind in der Chemie von größter Wichtigkeit. So werden lichtinduzierte Prozesse im Bereich der Photokatalyse genutzt, um durch Ladungstransfer, Bindungsbrüche oder Elektronensolvatisierung verschiedenste Produkte zu erzeugen. Auch im Bereich der Materialwissenschaften werden immer mehr solcher Prozesse bekannt und verwendet, um zum Beispiel effizientere Solarzellen zu entwerfen. Selbst die Bildung von Bindungen in Molekülen ist ein elektronendynamischer Prozess. Durch experimentelle Fortschritte ist es mittlerweile sogar möglich, durch speziellen Laserpulse bestimmte Prozesse und chemische Reaktionen gezielt auszulösen.
Um all diese Prozesse zu untersuchen, stellen computergestützte Simulationen ein unverzichtbares Werkzeug dar. Abhängig von der Größe der betrachteten Moleküle und der angestrebten Genauigkeit resultieren durch die zugrundeliegenden quantenmechanischen Eigenschaften dabei aber numerische Formeln, deren Berechnung selbst die Leistung von modernen Supercomputern bei weitem übersteigt.
In dieser Dissertation werden drei Projekte vorgestellt, die moderne Anwendungsfälle der Elektronendynamik präsentieren und aufzeigen, wie aktuelle Entwicklungen im Bereich der Computertechnologie und des Softwaredesign genutzt werden können, um effizientere und benutzerfreundlichere Programme zu entwickeln.
In dem ersten Projekt wird der inter-Coulombische-Zerfall (ICD), ein ultraschneller Energietransferprozess zwischen zwei isolierten chemischen Strukturen, untersucht. Nach Anregung einer Struktur wird die Energie auf die andere übertragen, welche dadurch ionisiert wird. Der Prozess wurde bereits in Atomen und Molekülen nachgewiesen und wird hier für Quantenpunkte untersucht, wobei Systeme mit mehr Quantenpunkten und in höheren Dimensionen fürs Kontinuum als in bisherigen Studien betrachtet werden. Ermöglicht werden diese aufwändigen Studien durch die Implementierung rechenintensiver Programmteile des genutzten Heidelberger MCTDH Programmes auf Grafikprozessoren (GPUs). Die durchgeführten Studien zeigen dabei, wie sich der ICD-Prozess mit mehreren Partnern verhält sowie welche konkurrierende Zerfallsprozesse dabei auftreten und bieten somit relevante Information für die Entwicklung von Technologien basierend auf Quantenpunkten wie Quantenpunkt-Qubits für die Verwendung in Quantencomputern.

Elektronendynamische Prozesse sind dabei nicht nur relevant in der Entwicklung neuer Quantencomputer, sondern andersherum können Quantencomputer auch die Möglichkeit bieten, Elektronendynamik mit deutlich mehr interagierenden Elektron und einem kleineren Fehler durchzuführen, als es mit traditionellen Computern je möglich wäre. In einem weiteren Projekt wurde deshalb ein Quantenalgorithmus entwickelt, der solche Simulationen und deren Auswertung in Zukunft ermöglichen könnte.
Implementiert wurde der Quantenalgorithmus in das ebenfalls im Rahmen dieser Dissertation entwickelte Dynamikprogramm *Jellyfish*. In dem Programm wird auf eine, an dem Dataflow-Programming orientierte, grafische Benutzeroberfläche gesetzt, was gleichzeitig zu einem modularen Aufbau führt. Die dabei entstehenden Module lassen sich flexibel kombinieren, womit sich *Jellyfish* für verschiedenste Anwendungen einsetzen lässt. Hierbei wurden neben Dynamikalgorithmen auch neuartige Analysemethoden entwickelt und diese an Laser-getriebenen elektronischen Anregungen in Molekülen wie Wasserstoff, Lithiumcyanid oder Guanin demonstriert. So wurden unter anderem die Generierung von elektronischen Wellenpaketen sowie resonante Übergänge zwischen elektronischen Zuständen explizit zeitabhängig betrachtet und die Bildung des Excitons in solchen Prozessen qualitativ anhand von Dichten als auch quantitativ durch sogenannte Excitondeskriptoren wie Excitongröße oder Loch- und Partikelposition beschrieben.
Zusammengefasst werden in dieser Dissertation also sowohl neuen Erkenntnissen über elektronendynamische Prozesse als auch neue Möglichkeit zur effizienteren Simulation dieser Prozesse durch GPU-Implementierungen und Quantenalgorithmen präsentiert. Das hierbei entwickelte Dynamikprogramm *Jellyfish* bietet dabei die Möglichkeit, auch in vielen Weiteren Forschungen in diesem Gebiet genutzt und erweitert zu werden, um in Zukunft zum Beispiel Simulationen mit einem Kontinuum wie in den ICD-Rechnungen zu ermöglichen.

Abstract

Electron dynamics processes are of utmost importance in chemistry. For example, light-induced processes are used in the field of photocatalysis to generate a wide variety of products by charge transfer, bond breaking, or electron solvation. Also in the field of materials science, more and more such processes are known and utilized, for example, to design more efficient solar cells. Even the formation of bonds in molecules is an electron dynamics process. Through experimental progress, it is now even possible to trigger specific processes and chemical reactions with special laser pulses.

To study all these processes, computer-aided simulations are an indispensable tool. Depending on the size of the molecules considered and the desired accuracy, however, the underlying quantum-mechanical properties result in numerical formulas whose computation far exceeds the capabilities of even modern supercomputers.

In this thesis, three projects are presented to demonstrate modern use cases of electron dynamics and show how recent developments in computer technology and software design can be used to develop more efficient and user-friendly programs.

In the first project, the inter-Coulombic decay (ICD), an ultrafast energy transfer process, between two isolated chemical structures is investigated. After the excitation of one structure, the energy is transferred to the other, which is ionized as a result. The process has already been shown experimentally in atoms and molecules and is studied here for quantum dots, focusing on systems with more quantum dots and higher dimensions for the continuum than in previous studies. These elaborate studies are made possible by implementing computationally intensive program parts of the Heidelberg MCTDH program used on graphics processing units (GPUs). The performed studies show how the ICD process behaves with multiple partners as well as which competing decay processes occur and thus provide relevant information for the development of technologies based on quantum dots such as quantum dot qubits for use in quantum computers.

Electron dynamics processes are not only relevant in the development of new quantum computers, but conversely, quantum computers can also provide the ability to perform electron dynamics with significantly more interacting electrons and a smaller error than it would ever be possible with traditional computers. In another project, therefore, a

quantum algorithm was developed that could enable such simulations and their analysis in the future.
The quantum algorithm was implemented in the dynamics program *Jellyfish*, which was also developed in the context of this dissertation. The program is based on a graphical user interface oriented on dataflow programming, which simultaneously leads to a modular structure. The resulting modules can be combined flexibly, which allows *Jellyfish* to be used for a wide variety of applications. In addition to dynamic algorithms, novel analysis methods were developed and demonstrated on laser-driven electronic excitations in molecules such as hydrogen, lithium cyanide, or guanine. Thus, the generation of electronic wave packets as well as transitions between electronic states were studied in an explicitly time-dependent manner and the formation of the exciton in such processes was described qualitatively by means of densities as well as quantitatively by so-called exciton descriptors such as exciton size or hole and particle position.
Thus, in summary, this dissertation presents both new insights into electron dynamic processes and new possibilities for more efficient simulation of these processes using GPU implementations and quantum algorithms. The developed dynamics program *Jellyfish* offers the potential to be used in many further studies in this area and to be extended to allow for example simulations with a continuum like in the ICD calculations in the future.

List of Publications

Peer-reviewed and submitted publications that are part of this thesis sorted by topic:

[1] Fabian Langkabel and Annika Bande
Three-electron dynamics of the interparticle Coulombic decay with two-dimensional continuum confinement
J. Chem. Phys. 154, 054111 (2021)
DOI: 10.1063/5.0037806

[2] Joana-Lysiane Schäfer, Fabian Langkabel and Annika Bande
Three-Electron Dynamics of the Interparticle Coulombic Decay in Doubly Excited Clusters with One-Dimensional Continuum Confinement
Molecules 27(24), 8713 (2022)
DOI: 10.3390/molecules27248713

[3] Fanian Langkabel, Pascal Krause and Annika Bande
JELLYFISH: a modular code for wave function-based electron dynamics simulations and visualizations on traditional and quantum compute architectures
Preprint version published and submitted to a peer-reviewed journal
DOI: 10.26434/chemrxiv-2023-p8384

[4] Fanian Langkabel, Paul Anton Albrecht, Annika Bande and Pascal Krause
Making optical excitations visible – An exciton wavefunction extension to the time-dependent configuration interaction method
Chem. Phys. 557, 111502 (2022)
DOI: 10.1016/j.chemphys.2022.111502

[5] Fabian Langkabel and Annika Bande
Quantum-Compute Algorithm for Exact Laser-Driven Electron Dynamics in Molecules
J. Chem. Theory Comput. 18, 7082-7092 (2022)
DOI: 10.1021/acs.jctc.2c00878

1 Introduction

Computational simulations of interacting quantum systems have become an unmatched tool for developments in chemistry, physics, pharmacy, materials science, and many other fields. They make it possible to predict the properties of molecules without having to synthesize them and thus to identify potential candidate molecules from millions of structures for certain applications, as e.g. drugs,[6,7] catalysts,[8,9] photovoltaic cells,[10,11] superconducting materials[12,13] or qubits in quantum computers.[14–16] The simulation of such quantum systems is thus an indispensable tool to address challenges humanity is facing, such as increasing resource scarcity or climate change.

In this dissertation, the focus lies on processes that are driven by the interaction of light with matter and occur in the atto- to femtosecond range. Such processes can be understood better and better with the experimental progress of the last years towards shorter time scales and better resolutions. For example, observations down to the attosecond time scale are possible using attosecond electron/ion pump-probe spectroscopy or attosecond transient absorption and reflection spectroscopy.[17] Many processes that are nowadays observed have already been described theoretically.[18–23] With the technical progress that makes it possible to observe such processes also experimentally, the interest and the possibilities of the theoretical side to improve and validate models increases as well.

The aim of this work is to further develop and apply the possibilities of such computer-aided simulations for electron dynamic processes by new techniques. This thesis is divided into three main topics. The first one deals with the inter-Coulombic decay, a light-induced decay process in quantum dots. The second topic addresses the development of a new dynamics program and the third the development of a quantum algorithm for electron dynamics processes. In the following, this chapter briefly introduces these three areas of interest. In chapter 2, the underlying theory is explained. A summary of the results is given in chapter 3. Finally, all papers that are part of this thesis are collected in chapter 5.

1.1 Simulation of the inter-Coulombic decay in quantum dots

The inter-atomic (or inter-molecular) Coulombic decay (ICD) process or short inter-Coulombic decay is one of the dynamic processes mentioned earlier, which was described theoretically before it was observed experimentally. The decay process has similarities with the so-called Auger decay, which was already discovered in the 1920s.[24] Using atoms as an example, these processes can occur after an electron has been ionized from an inner orbital of an atom. Such an ionization can be caused, for example, by X-rays. In the case of Auger decay, this usually core excited state decays when an electron in a higher orbital de-excites to an energetically lower one and another electron is ionized by the released relaxation energy (Fig. 1.1 a). However, in some cases, usually after an inner-valence excitation, the relaxation energy is lower than the second ionization energy, making the Auger decay energetically impossible. In these cases, another decay process can occur in which the relaxation in one atom ionizes another atom (Fig. 1.1 b). This process was already shown in 1997 by Cederbaum and co-workers[25] using the example of small HF and H_2O clusters and was called ICD.

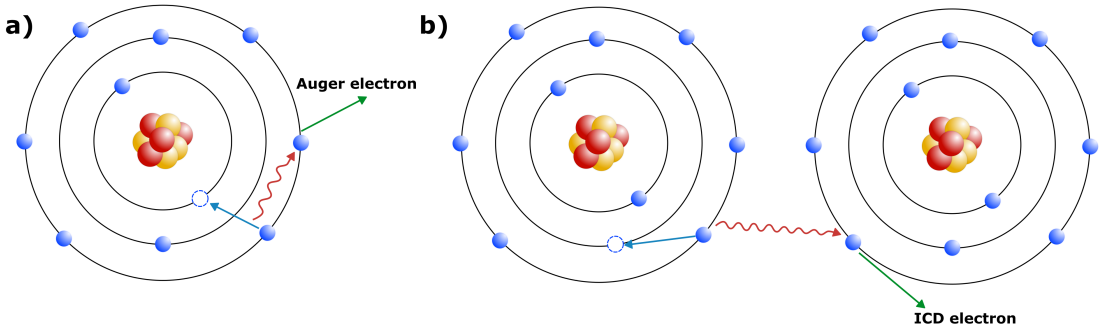

Figure 1.1: Possible decay paths of an excited state in one or two neon atoms after ionization of an inner electron. In a) the intra-atomic Auger decay and in b) the inter-atomic ICD process are shown. Both processes are illustrated in the simplified Bohr atomic model.

In 2003, Marburger and co-worker[26] provided the first experimental evidence for the ICD process and shortly thereafter Jahnke *et al.*[27] measured the ICD electron and the two ion fragments. In both of these studies, weakly bound homogeneous neon dimers were used. In the meantime, ICD has been observed in many kinds of weakly bound systems, including hydroxide ions in water,[28] water dimers,[29], and asymmetric clusters.[30,31] ICD can also occur after the collision of high-energetic ions or electrons,[32–34] after electron capture processes[35,36] or as a mechanism in DNA.[37]
With further theoretical studies, a number of interesting properties concerning the ICD

process were found. For example, a strong distance dependence for the ICD rate with R^{-6} was found due to the dipole-dipole interaction as it also occurs in the Förster resonance energy transfer.[38–40] Also, the number of decay channels, and hence the ICD rate, increases with the number of neighbors. For example, the ICD lifetime of a neon atom at a surface is thus larger than in the bulk.[41] In situations where there is another monomer C between the ionized monomer A^+ and the electron emitter monomer B, the ICD process can be much more efficient under the right energy conditions due to the virtual state $A^+C^-B^+$. This process is called superexchange ICD.[42]

ICD is not limited to atomic or molecular systems but could become important in quantum dots for nanoelectronics in the future. Quantum dots are semiconductor materials in which one or more spatial dimensions are confined to such an extent that they have individual discrete energy levels instead of the typical band structures.[43,44] Even if they consist of thousands of atoms, their behavior resembles that of single atoms due to these discrete energy levels, which is why they are also called "artificial atoms". Due to advanced synthesis possibilities, the electronic structure of quantum dots can be well-tuned through different shapes and the use of different materials. Thus, conditions can be created for the ICD decay to be used to design QD infrared photodetector.[45] Quantum dots can also be used as qubits in quantum computers,[46,47] although decay processes occurring here are usually undesirable and would change the quantum state unintentionally. Therefore, the optimization of quantum dot properties to improve as well as suppress ICD processes is a challenge for the use of quantum dots in nanoelectronics.

Although radiative and Auger decay in quantum dots has already been observed experimentally and studied in detail, this is not the case for ICD. Theoretically, however, ICD in quantum dots was already considered for the first time in 2011 by Cherkes and Moiseyev[48] and this idea was taken up by scientists from Heidelberg and subsequently continued by Bande and co-workers in Berlin.[49–53] The studies on ICD that are part of this thesis also build on this preliminary research. In most of these works, the process is simulated with explicitly time-dependent methods. Since it is impossible to consider quantum dots with thousands of atoms directly, they are approximated by inverse Gaussian potentials and the results are converted for suitable materials, mostly GaAs, using the effective mass approximation. In previous studies, the Gaussian potential was used in one dimension (z) and the motion of electrons in the other two spatial directions x and y was constrained by infinite harmonic oscillator potentials. Such a one-dimensional system corresponds most closely to so-called quantum dots in quantum wires. In addition to these one-dimensional structures, two- and three-dimensional structures can also be manufactured and are relevant. However, the simulation of these structures is significantly more complex due to

the additional dimensions of the continuum. Besides dimers, the same methods can be applied to clusters of three or more quantum dots, although again, there is a significant increase in computational time with each additional quantum dot. However, since such more elaborate calculations with more dimensions and quantum dots can give interesting insights into the interplay of multiple processes, such as different ICD processes and other decays at the same time, this work extends previous approaches in this direction. In doing so, the technical possibilities for speed-optimizing such calculations through the use of Graphic Processing Units (GPUs) will be demonstrated.

1.2 Development of an electron dynamics program

Quantum mechanical studies of atoms and molecules often consider only stationary solutions to the equation of motion of electrons in the electrostatic field of fixed atomic nuclei. The methods used to calculate these solutions are called electronic structure methods and the stationary solutions are called electronic states. Numerous different properties can be derived from the electronic states. For example, dipole moments, charge distributions, but also spectra such as UV/Vis or X-ray absorption spectra can be calculated. The application of electronic structure methods ranges over many different disciplines, from quantum materials and nanotechnology to astrophysics.

The electronic structure also provides access to many dynamic processes and their properties. However, for the cases considered here, such as the ICD process with competing decay channels, a purely stationary, i.e. time-independent, consideration is insufficient. Although methods such as complex scaling can be used to determine ICD rates,[54] many effects discussed later are not fully reflected. Also, the simulation of laser-driven electronic excitations in atoms, molecules, or quantum dots, as used to initiate the ICD process, is not accessible by time-independent methods due to the short time scales and strong electronic fields.

In order to be able to consider such explicitly time-dependent processes, time-dependent methods are needed. Since these are based on electronic structure methods, they are similarly numerous, but existing implementations are much more limited. In the field of electronic structure, there are extensive programs such as Orca,[55] Psi4,[56] PySCF,[57] to name a few, which provide a variety of different methods and applications. However, the existing electron dynamics programs are usually limited to one method and only a few applications.

Similar to the methods for the calculation of electron dynamics, the methods for the evaluation of time-dependent properties are rarely as advanced as their time-independent

counterparts. The visualization of time-independent orbitals, densities, and states has long been a standard tool and is implemented in popular programs, while time-dependent extensions of these properties have not even been developed. The one-particle transition density matrix[58–62] also falls into this category. This matrix can be used to analyze electronic transitions between static states by visualizing the exciton and quantifying exciton properties such as the hole-particle separation. In the time-dependent domain, however, these have not yet been used to observe the formation of excitons during electronic excitation in a time-dependent manner.
In the second project of this thesis, the evaluation of the one-particle transition density as well as the visualization of different densities and orbitals are transferred to the time-dependent domain and its possible application will be demonstrated. The implementation is done in the program *Jellyfish*, which is also part of this dissertation and represents a new dynamics program, especially for the time-dependent configuration interaction method. *Jellyfish* is intended to be applicable beyond this purpose and can be extended by further methods in the future.

1.3 Development of an electron dynamics algorithm for quantum computers

With the advance of computer technology, it is now possible to calculate the electronic structure and dynamic processes of a wide range of systems, from single atoms and small molecules to extended structures such as proteins or nanomaterials. However, the more particles are considered and the larger the entanglement between them, the more difficult it is to obtain accurate results. Although the exact equations leading to precise energies and properties have been known since the advent of quantum mechanics in the 1920s, they can only be solved exactly for the simplest systems. With each additional degree of freedom added to a system, the Hilbert space in which the solutions lie becomes exponentially larger. Methods for traditional computers, in which the full Hilbert space is used, suffer from the curse of dimensionality and can never be used for extended structures. While it is well known that often only a small part of the Hilbert space is physically accessible, which has led to some more efficient and nearly exact methods such as the multi-configurational self-consistent field method[63] or the density matrix renormalization group method,[64] additional approximations are still required for systems with many interacting particles, leading to significant deviations.
The fundamentally different approach of quantum computing could circumvent the problem.

Already proposed by Feynman in 1982,[65] the idea is to use one well-controllable quantum system to simulate another. In recent years in particular, progress in the realization of quantum computers has continued to accelerate, so that now, more than 30 years later, the first quantum computers can outperform traditional computers in a few special tasks.[66] There are several approaches to developing a computer based on quantum physical processes. Two important ones are adiabatic quantum computing (AQC)[67] and the boson sampling model.[68] A third and the most commonly used approach, which was also used in this thesis, is the quantum gate array model.[69] The model is based on so-called qubits, which are, physically speaking, two-state systems. The qubits carry the information in the form of a superposition of the two basis states. By combining qubits into a quantum register and the possibility of entangling them completely, the usable Hilbert space of the quantum register grows exponentially with the number of qubits. This Hilbert space can be used to map the Hilbert space of another physical system. By specific manipulations of the quantum register state, the realization of a universal, i.e. problem-independent, quantum computer is thus possible.

The structure of a quantum computer, the operating conditions and the possibilities to manipulate a state depend on the choice of qubits. Here, a number of different quantum systems are considered and explored. Besides trapped ions,[70] superconducting coils[66,71] and photons,[72,73] the already mentioned quantum dots[46,47] can also be used. The goal is not only to generate as many entangled qubits as possible but also to reduce the interaction between qubits and the environment. Through interaction with the environment and application of operations such as the measurement of a qubit, decoherence occurs and thus the loss of the quantum state, which complicates the application of longer algorithms. These effects will never be completely suppressed, which is why quantum error correction codes have been under development for some time.[74,75] Here, several error-prone physical qubits encode an error-free logical qubit. However, the current systems with about 100 qubits[76] are not yet suitable to apply such complete error correction. Accordingly, current quantum computers are error-prone and refer to the noisy intermediate-scale quantum (NISQ) era.

Parallel to the technical progress, increasingly advanced quantum algorithms are developed for a wide variety of applications. These are no longer limited to computations in quantum systems,[77–79] but also offer solutions to problems in information technology such as factorization of large numbers,[80] database searching[81] and many other areas such as computer-aided drug design,[82,83] computational materials science,[84] or artificial intelligence.[85] Some of these algorithms are designed to run on error-prone quantum computers, such as variational quantum algorithms,[86,87] while others require a nearly

error-free quantum computer. While it is still unclear for NISQ devices how large the benefit actually will be for useful applications, algorithms for error-free quantum computing can often deliver exponential speedups over their traditional counterparts.
While various quantum algorithms are already available for the computation of electronic structure,[78,79,88] both for error-prone and error-free quantum computers, relatively little attention has been paid to the area of electron dynamics. However, this area in particular is excellently suited as a field of application, since the physics of electrodynamics shows strong parallels to the functional principle of a quantum computer and the necessary substeps have already been developed for electronic structure algorithms. For example, the Jordan-Wigner transformation[89] is used to translate a fermionic wave function into a bosonic qubit wave function and algorithms such as those based on Trotter decomposition[90,91] can be used to evolve this wave function in time subsequently.
In the third project of this dissertation, an algorithm for the simulation and analysis of electron dynamics on error-free quantum computers was compiled from such smaller substeps, implemented, and tested on the example of small molecules. Among other things, propagation with non-Hermetian operators, which is a particular challenge for quantum computing, was addressed. All algorithms were implemented in the already mentioned dynamics program *Jellyfish*.

2 Theoretical Background

The following chapter presents the necessary theoretical foundations on which this thesis is based. The first section 2.1 gives a short introduction to quantum mechanics and the Schrödinger equation. Following, in section 2.2 methods used to solve the time-independent Schrödinger equation and in section 2.3 methods to solve the time-dependent Schrödinger equation are presented. The last section 2.4 contains an introduction to quantum computing and the quantum algorithms used.

2.1 Fundamentals of quantum mechanics

The basic ideas of quantum mechanics were introduced in the 1920s to explain phenomena that could not be adequately described with the existing picture of physics. The parts of quantum mechanics relevant to this work and presented in the following were taken from the books *"Modern Quantum Chemistry"*[63] and *"Introduction to Quantum Mechanics: A Time-Dependent Perspective"*[92] as well as from the article [93]. To simplify the following equations, atomic units are used. The elementary charge e, the mass of an electron m_e, the reduced Plank constant $\hbar$, and $1/4\pi\epsilon_0$ are set to 1.

2.1.1 Schrödinger equation

The central object of this work is the time-dependent Schrödinger equation (TD-SE)

$$i\hbar\frac{\partial}{\partial t}\Psi(\vec{x},t) = \hat{H}\Psi(\vec{x},t). \tag{2.1}$$

It is a partial differential equation with respect to time t. Ψ is the wave function of the system, which contains all information of the considered elementary particles at any time and for any point in space. $\hat{H}$ is the Hamiltonian operator, which describes the behavior and the interaction of the particles with each other and thus describes the energy of a system

$$\hat{H} = -\frac{\hbar^2}{2m}\nabla^2 + V. \tag{2.2}$$

Here ∇ is the Nabla operator and describes the kinetic energy of the quantum mechanical particles while $V = V(\vec{r}, t)$ represents a potential function that can depend on both coordinates and time. In most cases in the field of quantum chemistry and in a large part of this work, molecules and thus Hamiltonians of the form

$$\begin{aligned}\hat{H} = \hat{T}_e + \hat{T}_n + \hat{U}_{ee} + \hat{U}_{nn} + \hat{U}_{ne} = &- \sum_i^N \frac{\hbar^2}{2m_e} \nabla^2_{\vec{r}_i} - \sum_A^M \frac{\hbar^2}{2M_A} \nabla^2_{\vec{R}_A} \\ &+ \sum_i^N \sum_{j>i}^N \frac{e^2}{4\pi\epsilon_0 \left|\vec{r}_i - \vec{r}_j\right|} + \sum_A^M \sum_{A>B}^M \frac{Z_A Z_B e^2}{4\pi\epsilon_0 \left|\vec{R}_A - \vec{R}_B\right|} - \sum_i^N \sum_A^M \frac{Z_A e^2}{4\pi\epsilon_0 \left|\vec{R}_A - \vec{r}_i\right|}\end{aligned} \tag{2.3}$$

are considered. The first terms describe the kinetic energy of N electrons $\hat{T}_e$ with their mass m_e and the kinetic energy of M nuclei $\hat{T}_n$ with their corresponding masses M_A. ∇ is the Nabla operator for three dimensions $\{x, y, z\}$ acting on the corresponding coordinate vectors of the electrons or nuclei. Furthermore, the Hamiltonian contains the repulsive Coulomb interactions between electrons $\hat{U}_{ee}$ and between nuclei $\hat{U}_{nn}$, which scale with the inter-particle distances $\vec{r}$ and $\vec{R}$ and the charge numbers Z_A, Z_B for the nuclei and 1 for electrons, respectively. The last term $\hat{U}_{ne}$ describes the attractive Coulomb interactions between electrons and nuclei.

As seen in equation 2.3, the molecular Hamiltonian does not contain any time-dependent terms, so the potential function $V(\vec{r}, \vec{R})$ depends only on the coordinates of the electrons and nuclei. In such cases, the solution of the TD-SE can be written as the product of a time-dependent function $\Phi(t)$ and a spatial function $\psi(\vec{r}, \vec{R})$ as $\Psi(\vec{r}, \vec{R}, t) = \psi(\vec{r}, \vec{R})\Phi(t)$. If both sides of the TD-SE in equation 2.1 are now divided by $\psi(\vec{r}, \vec{R})\Phi(t)$,

$$i\hbar \frac{\dot{\Phi}(t)}{\Phi(t)} = \frac{\hat{H}\psi(\vec{x})}{\psi(\vec{x})} \tag{2.4}$$

is obtained. The variables are now separated and the left side depends on time only while the right side depends exclusively on the spatial coordinates. To solve this equation, both sides must equal the same constant, E, corresponding to the molecular system's total energy. For the left side, the differential equation

$$i\hbar\dot{\Phi}(t) = E\Phi(t) \tag{2.5}$$

is obtained, with the solution being

$$\Psi(\vec{x}, t) = \psi_E(\vec{x})\Phi_0 e^{-\frac{i}{\hbar}Et}. \tag{2.6}$$

Here, Φ_0 is a pure multiplicative factor which is absorbed in $\psi(r, R)$ and is chosen in a way that the normalization condition

$$\int_{-\infty}^{\infty} |\Psi(\vec{x}, t)|^2 \, d\vec{x} = 1 \tag{2.7}$$

is fulfilled. From the right-hand side of equation 2.4, the time-independent Schrödinger equation (TISE) is obtained as

$$\hat{H}\psi_E(\vec{x}) = E\psi_E(\vec{x}). \tag{2.8}$$

The TISE is an eigenvalue equation, where E is the eigenvalue or energy of an eigenfunction or eigenstate ψ. The solutions of the time-independent Schrödinger equation allow the prediction of all time-independent properties and observables and thus represent the central equation for large areas of theoretical chemistry.

2.1.2 Electronic wave function

Solving the full Schrödinger equation is computationally expensive if not even unfeasible for large systems. Hence attempts are made to simplify the equation by means of approximations. One such approximation is the Born-Oppenheimer approximation. Since an electron is more than 1800 times lighter than a proton, the motion of the electrons can be assumed to take place on a faster time scale than the motion of the atomic nuclei. The usually weak dynamical coupling between electron and nuclear motion is therefore neglected in the Born-Oppenheimer approximation, allowing a separation of nuclear and electronic degrees of freedom in the form of a product wave function

$$\Psi_{Total} = \Psi_{el}\Psi_{nuc}. \tag{2.9}$$

This results in a single Schrödinger equation for the motion of the electrons and one for the motion of the atomic nuclei. The electronic processes considered in this work occur on time scales where the motion of the atomic nuclei can be neglected and accordingly, only the solution of the electronic Schrödinger equation

$$\hat{H}_{el}\Psi_{el} = E_{el}\Psi_{el} \tag{2.10}$$

is relevant. Compared to the full Hamiltonian from equation 2.3, the terms for the kinetic energy of the nuclei are set to zero and their Coulomb interactions to be constant. While the kinetic energy of the atomic nuclei is always the same for a molecule and is accordingly

neglected, the Coulomb energy of the nuclei is calculated once for a nuclear configuration and added to the electronic energy to obtain the total energy. The electronic Schrödinger equation thus depends only parametrically on the nuclear coordinates.
While systems with only one electron like the hydrogen atom can be solved analytically, leading to exact solutions like the well-known hydrogen orbitals, this is no longer the case for many-electron systems. To solve the electronic Schrödinger equation for molecules, an approach for a many-electron wave function is needed. One possible approach is the so-called Hartree product in the form

$$\Psi(\vec{x}_1, \vec{x}_2, ..., \vec{x}_N) = \phi_1(\vec{x}_1)\phi_2(\vec{x}_2)...\phi_N(\vec{x}_N), \tag{2.11}$$

where ϕ denotes orbitals defined as one particle wave function. For such a product approach to work, the Hamiltonian operator would have to be separable with respect to the electrons, and therefore electrons would not interact with each other. However, electrons interact with each other and fulfill the Pauli exclusion principle, which means that single Hartree products are not suitable as electronic wave functions.
According to the Pauli exclusion principle, two electrons cannot be equal in all four quantum numbers. The first three quantum numbers, the principal quantum number n, the azimuthal quantum number l, and the magnetic quantum number m_l, describe the spatial shape of an orbital. The fourth quantum number, however, is the so-called spin quantum number and does not appear in the solution of the time-independent Schrödinger equation of the hydrogen atom. But it is part of the solution of the relativistic Dirac equation for the hydrogen atom and has to be considered for the complete description of an electron in a many-electron wave function. To do this, two spin functions $\alpha(\omega)$ and $\beta(\omega)$ are introduced. An electron is now described by a spin-orbital consisting of a spatial ($\phi(\vec{r})$) and a spin part $s(\omega)$ as

$$\chi(\vec{x}) = \phi(\vec{r})s(\omega). \tag{2.12}$$

Since the Hamiltonian does not depend on the spin of an electron, it is not sufficient to add only the spin to the wave function to satisfy the Pauli exclusion principle. However, if the wave function is required to be antisymmetric with respect to the exchange of space-spin coordinates

$$\Psi(\chi_1, ..., \chi_i, ..., \chi_j, ...\chi_N) = -\Psi(\chi_1, ..., \chi_j, ..., \chi_i, ...\chi_N), \tag{2.13}$$

then the Pauli exclusion principle is fulfilled. A wave function that fulfills this condition

is the so-called Slater determinant. It is a linear combination of Hartree products in the form

$$\Psi = \frac{1}{\sqrt{N!}} \begin{vmatrix} \chi_1(\vec{x}_1) & \chi_2(\vec{x}_1) & \cdots & \chi_N(\vec{x}_1) \\ \chi_1(\vec{x}_2) & \chi_2(\vec{x}_2) & \cdots & \chi_N(\vec{x}_2) \\ \vdots & \vdots & \ddots & \vdots \\ \chi_1(\vec{x}_N) & \chi_2(\vec{x}_N) & \cdots & \chi_N(\vec{x}_N) \end{vmatrix}. \tag{2.14}$$

Each column describes one of the N spin orbitals while each row contains the coordinates of one of the N electrons. Through this structure, each electron is related to each spin-orbital and all electrons are indistinguishable. The prefactor $\frac{1}{\sqrt{N!}}$ provides the normalization of the wave function. Since a Slater determinant can be constructed from the list of occupied orbitals $\chi_1, \chi_2, ..., \chi_N$, a notation in the form of a "ket vector" has become common: $|\chi_1, \chi_2, ..., \chi_N\rangle$.

2.1.3 Second quantization

Some of the following methods rely on the formalism of the second quantization. This is particularly the case for quantum computing algorithms. In second quantization, in addition to the observables such as the energy, (particle) fields are also quantized. Instead of assigning orbitals to electrons, occupations are now assigned to spin orbitals, meaning there is no redundant information and the description of a state becomes easier. A Slater determinant then written in terms of occupation numbers, is also called Fock state

$$|\Psi\rangle = |n_1, n_2, ..., n_k, ...\rangle, \tag{2.15}$$

where n_k is the number of electrons in the k-th spin-orbital, which are according to the Pauli exclusion principle either $n_k = 0$ or $n_k = 1$. In addition, two new operators, the electron field operators, are introduced. These allow electrons in a spin-orbital to be created or annihilated, while at the same time ensuring the antisymmetrization of the wave function.
The first operator is the creation operator for fermions $\hat{a}_p^\dagger$, which acts on a Fock state as

$$\hat{a}_p^\dagger |n_1, n_2, ..., 0_p, ...\rangle = (-1)^{\sum_{j=1}^{p-1} n_j} |n_1, n_2, ..., 1_p, ...\rangle. \tag{2.16}$$

The operator increases the occupation number of the spin-orbital χ_p, which corresponds to the creation of an electron in the orbital while maintaining the antisymmetrization of the wave function. As a result, two creation operators have an anticummutation relation

to each other

$$\hat{a}_i^\dagger \hat{a}_j^\dagger + \hat{a}_j^\dagger \hat{a}_i^\dagger = \delta_{ij} = \{\hat{a}_i^\dagger, \hat{a}_j^\dagger\}. \tag{2.17}$$

Applying a creation operator to an already occupied spin-orbital yield 0. Thus, no two electrons with the same four quantum numbers can be created and the Pauli exclusion principle is fulfilled.
The second newly introduced operator is the annihilation operator $\hat{a}_p$ which is defined as an adjoint operator to the creation operator. It annihilates an electron in the spin-orbital χ_p by its action on a Slater determinant and thus reduces the occupation number of the spin-orbital by one as

$$\hat{a}_p|n_1, n_2, ..., 1_p, ...\rangle = (-1)^{\sum_{j=1}^{p-1} n_j} |n_1, n_2, ..., 0_p, ...\rangle. \tag{2.18}$$

Like the creation operator, the annihilation operator satisfies the anticommutator relation and applying an annihilation operator to an already unoccupied orbital yields 0 again. Moreover, the second quantization satisfies the condition of *indistinguishable electrons*, since they do not even have an index to distinguish their coordinates from each other. In the second quantization also a vacuum state $|\bar{0}\rangle = |0, 0, ..., 0\rangle$ is introduced as a normalized state of the system without electrons from which any Slater determinant can be generated by applying creation operators.
It can be shown that all linear operators acting on the Fock space can be represented as a combination of such field operators. The one- and two-particle operators can be expressed as

$$\hat{O}_1 = \sum_{ij} \langle i|\hat{h}_1|j\rangle \hat{a}_i^\dagger \hat{a}_j \tag{2.19}$$

and

$$\hat{O}_2 = \frac{1}{2} \sum_{ijkl} \langle ij|\hat{h}_2|kl\rangle \hat{a}_i^\dagger \hat{a}_j^\dagger \hat{a}_l \hat{a}_k, \tag{2.20}$$

where i, j, k and l denote spin orbitals.

2.2 Electronic structure theory

The calculation of electronic states in an electrostatic field of fixed atomic nuclei – which means solving the time-independent Schrödinger equation in the framework of the Born-Oppenheimer approximation – falls into the field of electronic structure theory. A number of different approaches have already been developed for this purpose, and the used ones are discussed in the following. The theory shown here is an extract from the textbook *"Modern Quantum Chemistry"*[63] and the articles [93, 94].

2.2.1 Hartree-Fock

Using a single Slater determinant as an ansatz for the electronic wave function leads to the Hartree-Fock (HF) method. The TISE is not solved directly but instead multiplied with $\langle\Psi|$ from the left which results in

$$E = \langle\Psi|\hat{H}|\Psi\rangle. \tag{2.21}$$

The application of the Slater-Condon rules for orthonormal orbitals $\langle\chi_i|\chi_j\rangle = \delta_{ij}$, leads to an energy expression of the form:

$$E_{HF} = \sum_i \langle i|\hat{h}_1|i\rangle + \frac{1}{2}\sum_{ij}\langle ii|jj\rangle - \langle ij|ji\rangle, \tag{2.22}$$

employing the definition of the one-electron integrals

$$\langle i|\hat{h}_1|i\rangle = \int d\vec{x}_1 \chi_i^*(\vec{x}_1)\hat{h}_1(r_1)\chi_j(\vec{x}_1), \tag{2.23}$$

and two-electron integrals

$$\langle ij|kl\rangle = \int d\vec{x}_1 d\vec{x}_2 \chi_i^*(\vec{x}_1)\chi_j(\vec{x}_1)\frac{1}{r_{12}}\chi_k^*(\vec{x}_2)\chi_l(\vec{x}_2). \tag{2.24}$$

Here all one electron operators are combined to $\hat{h}_1$. It can be shown that the energy $\tilde{E}$ of a trial wave function $\tilde{\Psi}$ is always higher than the energy of the exact ground state Ψ_0 with its ground state energy E_0

$$\tilde{E} = \langle\tilde{\Psi}|\hat{H}|\tilde{\Psi}\rangle \geq E_0 = \langle\Psi_0|\hat{H}|\Psi_0\rangle. \tag{2.25}$$

To thus obtain a ground state energy and the corresponding Hartree-Fock orbitals, the variational principle is applied to minimize the energy expression from equation 2.25. To

preserve the orthonormality of the spin orbitals, Lagrange multipliers λ_{ij} are introduced (see below). The corresponding condition for the optimization is therefore

$$\delta\hat{F} \equiv \delta\left[\langle\Psi|\hat{H}|\Psi\rangle - \sum_{ij}\lambda_{ij}(\langle\chi_i|\chi_j\rangle - \delta_{ij}),\right], \tag{2.26}$$

where $\hat{F}$ is called the Fock operator. This equation gives rise to coupled integro-differential equations in the form

$$\begin{aligned}\hat{h}_1\chi_k(\vec{x}_1) + \sum_i\left[\int d\vec{x}_2|\chi_i(\vec{x}_2)|^2\frac{1}{r_{12}}\right]\chi_k(\vec{x}_1) - \sum_i\left[\int d\vec{x}_2\chi_i^*(\vec{x}_2)\chi_k(\vec{x}_2)\frac{1}{r_{12}}\right]\chi_i(\vec{x}_1)\\ = \sum_i\lambda_{ki}\chi_i(\vec{x}_1).\end{aligned} \tag{2.27}$$

They furthermore can be combined into the form

$$\left[\hat{h}_1 + \sum_i(\hat{J}_i - \hat{K}_i)\right]\chi_k = \hat{F}\chi_k = \sum_i\lambda_{ki}\chi_i, \tag{2.28}$$

by introducing the Coulomb operator $\hat{J}_i$

$$\hat{J}_i(\vec{x}_1) = \int d\vec{x}_2|\chi_i(\vec{x}_2)|^2\frac{1}{r_{12}} \tag{2.29}$$

and the action of the exchange operator $\hat{K}_i$

$$\hat{K}_i(\vec{x}_1)\chi_k(\vec{x}_1) = \left[\int d\vec{x}_2\chi_i^*(\vec{x}_2)\chi_k(\vec{x}_2)\frac{1}{r_{12}}\right]\chi_i(\vec{x}_1). \tag{2.30}$$

The Coulomb operator reflects the Coulomb interaction between the electrons. From the form of the operator it can be seen that the Coulomb interaction of the electrons is described independently by the mean Coulomb field of all other electrons and the explicit interaction between two electrons is only approximated. The exchange operator results from the antisymmetric form of the Slater determinant and, unlike the Coulomb operator, has no classical interpretation.

Equation 2.28 has several possible solutions and usually a set of Lagrange multipliers ϵ_k is chosen which satisfies the condition

$$\lambda_{ki} = \delta_{ki}\epsilon_k. \tag{2.31}$$

These Lagrange multipliers are also called orbital energies. Thus, the Hartree-Fock equation results in the eigenvalue equation

$$\hat{F}\chi_k = \epsilon_k \chi_k. \tag{2.32}$$

By using orbitals to describe a many-electron system, double counting of the interaction between electrons occurs in the Hartree-Fock formalism. With correction for this doubling, the Hartree-Fock energy based on the orbital energies ϵ_k is finally obtained as

$$E_{HF} = \sum_k \epsilon_k - \frac{1}{2}\sum_{ij} \langle ii|jj\rangle - \langle ij|ji\rangle. \tag{2.33}$$

Roothaan-Hall Equations

The solution of the Hartree-Fock equation 2.32 is carried out by an iterative procedure, which is computationally expensive since the integrals of the orbitals at each point in space have to be recalculated at each iteration step. Much more efficient is a method proposed by Roothan.[95] The idea behind the method is the expansion of the spatial orbitals in a set of static basis functions Φ

$$\chi_i(\vec{x}_1) = \sum_\mu c_{i\mu}\Phi_\mu(\vec{x}_1). \tag{2.34}$$

Furthermore, the restriction that electrons with α- and β-spin always occur in pairs and the corresponding spin orbitals share the same spatial part $\phi(\vec{x})$ in equation 2.28 is made. Accordingly, N spin orbitals can be replaced by $N/2$ spatial orbitals ϕ which yields the Fock operator as

$$\hat{F}(\vec{x}_1) = \hat{h}(\vec{x}_1) + \sum_i^{N/2} 2\hat{J}_i(\vec{x}_1) - \hat{K}_i(\vec{x}_1). \tag{2.35}$$

This approximation is commonly called restricted Hartree-Fock (RHF). While both electrons with α- and β-spin in one orbital have the same contribution with respect to the Coulomb operator, only one of the two electrons has a non-zero contribution with respect to the exchange operator K. Accordingly, the exchange operator does not obtain a factor of 2 during the transition from spin orbitals to spatial orbitals. Inserting the orbital expansion into the Hartree-Fock equation 2.32 and multiplying by $\langle\phi_\nu|$ from the left

provides

$$\sum_{\mu} c_{i\mu} \langle \phi_\nu(\vec{x}_1) | \hat{F}(\vec{x}_1) | \phi_\mu(\vec{x}_1) \rangle = \epsilon_i \sum_{\mu} c_{i\mu} S_{\nu\mu}. \tag{2.36}$$

This equation is a matrix eigenvalue problem known as the Roothan equation

$$\underline{\underline{FC}} = \underline{\underline{SC}}\epsilon. \tag{2.37}$$

Since common basis functions are not necessarily orthonormal, but this is a requirement for the spatial orbitals, the overlap matrix S appears in the equations, which ensures the necessary orthonormality of the orbitals. The orbital energies ϵ are the eigenvalues of the Fock matrix F, and C is the matrix of the corresponding eigenvectors. Since the Fock matrix depends on itself via the orbitals, the equation must be solved iteratively in a so-called self-consistent field (SCF) procedure.

Basis sets

There is a number of possible approaches with individual advantages and disadvantages for the description of orbitals through basis sets. The most obvious approach is using the solutions of the hydrogen atom which are the Slater-Type-Orbitals (STO) in the form

$$\Phi^{STO} = N r^{n-1} e^{-\mu r} Y_l^m(\delta, \Phi), \tag{2.38}$$

where N is the normalization factor, r the distance of the electron to the nucleus, $Y_l^m(\delta, \Phi)$ the exact angular functions of the hydrogen orbitals and n as well as μ further numerical parameters. Depending on the type of atom, several such STOs are used for each atom with the corresponding atomic position as the origin. Basis sets based on STOs give good results, particularly for the ground states in molecules. However, the calculation of the corresponding integrals is time-consuming. Therefore, an alternative is the description of such STOs as a linear combination of primitive Gaussian-type orbitals (GTOs) in the form

$$\Phi_l^{GTO} = Y(l) \sum_i \alpha_i e^{-\beta_i (r - r_0)^2}, \tag{2.39}$$

with $Y(l)$ a function for the angular momentum l of the basis function. The integrals of GTOs can be efficiently calculated analytically.
In general, the computation time of methods like Hartree-Fock depends directly on the

number of basis functions used. For this reason, it is attempted to obtain the most accurate results possible with the smallest possible number of basis functions. For the calculation of the ground state but also low excited states, a number of highly optimized standard basis sets based on GTOs have been developed.
For energetically higher excited states, the electron distribution is usually more complicated since a significant fraction of electron density may be found further away from atomic nuclei. In such situations, standard basis sets usually do not provide a satisfactory description anymore and additional basis functions which cover this region far from the nucleus are needed. For this purpose, single primitive Gaussian functions as they appear in GTOs can be used where the exponents β_i are developed in series as

$$\beta_i = \beta\gamma^{i-1}, \quad \alpha, \beta > 0, \gamma \neq 1 \quad i = 1, 2, ..., N. \tag{2.40}$$

Such a series of atom-centered basis functions are called even-tempered basis sets. They can be added to standard basis sets to cover a larger space evenly, but have the disadvantage that usually many basis functions are required, which makes them expensive to use.
If not only bound states are to be considered, but even continuum states, atom-centered basis functions are rather unsuitable, because they can only describe the wave function in a region just around the molecule.
To describe continuum functions nonetheless, grid-based basis sets can be used. Here, the spatial region is divided uniformly along grid points. As a result, however, the amount of resulting basis functions in grid-based methods leads to significantly longer computation times. In addition, bound states are usually insufficiently described in such grid-based methods. A solution to this problem is the combination of atom-centered and grid-based basis functions to describe both bound and continuum states.

Electron correlation

In many cases, such as the hydrogen molecule, Hartree-Fock provides ground-state energies that deviate by less than 5 % from the exact energy. However, this deviation is usually already too large to explain and predict experimental findings. The reason for this deviation is an inaccurate description of the wave function by a single Slater determinant which leads to higher energies. The difference between the exact solution of the TISE and the Hartree-Fock limit, which is the Hartree-Fock energy from a complete basis set, is called correlation energy E_{corr}

$$E_{exact} = E_{HF} + E_{corr}. \tag{2.41}$$

The term correlation energy is slightly misleading because Hartree-Fock already includes correlation effects by the exchange term. Two electrons with parallel spins can never be at the same point in space which is called Fermi correlation. However, correlations between electrons due to their Coulomb interaction (Coulomb correlation) or due to the symmetry or the total spin of the molecule are not described by Hartree-Fock.
Often, correlation effects are divided into static and dynamic correlations. Dynamic correlation refers to the correlation between the motion of electrons, which is not fully described in Hartree-Fock due to the description of one electron in an averaged Coulomb field of all other electrons. Static correlation, on the other hand, occurs when the ground state of a molecule can only be described by several energetically (nearly) degenerate Slater determinants.
Both dynamic and static correlation can be included by using several Slater determinants to describe a wave function. Since the Hartree-Fock Slater determinant and the resulting molecular orbitals are usually used to generate further Slater determinants, these methods are also referred to as post-Hartree-Fock methods.

2.2.2 Configuration interaction

The Hartree-Fock method yields as many molecular orbitals from K basis functions and thus $2K$ spin orbitals. The Hartree-Fock Slater determinant for the ground state, also called ground state configuration, consists only of the N spin orbitals with the lowest orbital energy, where N is the number of electrons. By exchanging occupied spin orbitals with unoccupied (virtual) spin orbitals, further configurations or Slater determinants can be created from the Hartree-Fock reference $|\Psi_0\rangle$

$$\hat{a}_a^\dagger \hat{a}_i |\Psi_0\rangle = |\Psi_i^a\rangle = |\chi_1 \chi_2 \cdots \chi_a \cdots \chi_N\rangle. \tag{2.42}$$

In second quantization, this exchange corresponds to applying an annihilator operator to an occupied and a creation operator to an unoccupied orbital. In the configuration interaction method, the total wave function is now described as a weighted linear combination of configurations

$$|\Psi\rangle = \left(c_0 + \sum_{ia} c_i^a \hat{a}_a^\dagger \hat{a}_i + \sum_{\substack{i<j \\ a<b}} c_{ij}^{ab} \hat{a}_a^\dagger \hat{a}_i \hat{a}_b^\dagger \hat{a}_j + ... \right) |\Psi_0\rangle. \tag{2.43}$$

If all possible configurations are included in the wave function – referred to as full configuration interaction (FCI) – the exact solutions with respect to the electronic Schrödinger equation in the used basis set is obtained. The expansion coefficients c can be determined, for example, by constructing the Hamiltonian matrix $\langle \Psi_i | \hat{H} | \Psi_j \rangle$, where Ψ_i and Ψ_j correspond to individual configurations and subsequent (partial) diagonalization of this matrix. The eigenvalues of the matrix correspond to the eigenenergies and the eigenvectors to the expansion coefficients for different states. Unlike HF, where only the ground state is determined, CI also allows the calculation of excited states. The matrix elements of the Hamiltonian matrix can be calculated by using the Slater-Condon rules. Even if FCI gives the exact solution except for the basis set error, it is unfeasible for most applications due to its exponential scaling.

In order to carry out CI computations for larger systems nevertheless, the number of configurations is systematically restricted, which is called truncated configuration interaction. When only the singly excited configuration and the ground state configuration are included, the configuration interaction singles (CIS) method is obtained. Since the matrix elements between the ground state configuration and single excited configurations are zero according to Brilloun's theorem $\langle \Psi_0 | \hat{H} | \Psi_i^a \rangle = 0$, there is no improvement of the ground state and its energy in CIS. Nevertheless, CIS is suitable for the calculation of singly excited states. If additionally doubly excited configurations are included, one speaks of configuration interaction singles doubles (CISD). In CISD and higher truncation levels, the ground states also incorporate correlation corrections.

The truncation of the CI wave function is an approximation that subsequently leads to deviations in the energy and wave function. However, the degree of deviations for CI depends on the size of the system, and the properties of size extensivity and size consistency are violated.

An ansatz for a wave function based on multiple Slater determinants, which does not suffer from these problems, is used in the Coupled-cluster (CC) method. In contrast to CI

in equation 2.43, an exponential expansion is used here

$$|\Psi\rangle = \exp(T)|\Psi_0\rangle = \exp\left(\sum_{ia} t_i^a \hat{a}_a^\dagger \hat{a}_i + \sum_{\substack{i<j \\ a<b}} t_{ij}^{ab} \hat{a}_a^\dagger \hat{a}_i \hat{a}_b^\dagger \hat{a}_j + ...\right)|\Psi_0\rangle, \tag{2.44}$$

where T is called the cluster operator. If T is now truncated to, for example, single and double excitations (CCSD), higher excitations are nevertheless described by the combination of single t_i^a and double t_{ij}^{ab} amplitudes. Coupled-cluster thus usually provides significantly better results than CI for the same number of considered configurations and similar computational effort. However, the derivation and implementation of the working equations are much more complicated than for CI.
However, both truncated CI and truncated CC, like other post-Hartree-Fock methods that build on the HF ground state as reference configuration, have one additional problem. In situations with high contributions of static correlation, such as dissociation processes, these methods fail completely. A single Slater determinant is not sufficient in such near degeneracy situations and, accordingly, the reference these methods build on is insufficient.

2.2.3 Multi-configuration self-consistent field

In order to describe static correlation, more than one configuration is necessary as a reference. For this purpose, the approaches of Hartree-Fock and CI are combined and, likewise in CI, a linear combination of Slater determinants is used as a wave function.
In addition to the expansion coefficients for the Slater determinants, the coefficients of the involved spin orbitals are simultaneously optimized with respect to the ground-state energy in a self-consistent field algorithm similar to HF. Compared to CI, this method requires significantly fewer configurations for a sufficient description of the wave function, but the optimization of basis set coefficients and CI coefficients at the same time is computationally more expensive.
For the selection of Slater determinants in the MCSCF method, different schemes are available. In the frequently used complete active space self-consistent field method (CASSCF), molecular orbitals are divided into three categories. The first category are core molecular orbitals for inner electrons, which are occupied twice. The area energetically above these orbitals is the so-called active space. In this space, a certain number of electrons is allowed to occupy all orbitals in any suitable combinations, resulting in the desired configurations. The third region are virtual molecular orbitals which remain unoccupied. The quality of the results from such a calculation is strongly dependent on

the definition of the active space.
Similar to the HF wave function in single-reference methods, the wave function of an MCSCF calculation provides the reference for a number of multi-reference methods. For example, a CI calculation can be performed based on the MCSCF wave function in a multi-reference configuration interaction (MRCI) calculation. Also, the idea to perform coupled cluster computations with an MCSCF reference is also being explored (MRCC).

Configuration state functions

Even though Slater determinants have been used in equations so far in this work for the sake of simplicity, they are usually not used in many methods in efficient implementations. Instead, configuration state functions (CSF) are used. CSFs are linear combinations of Slater determinants which are eigenfunctions of the squared angular momentum operator $\hat{s}^2$. Since the $\hat{s}^2$ operator commutes with the Hamiltonian operator, matrix elements in the Hamiltonian matrix between eigenfunctions with different eigenvalues to the $\hat{s}^2$ operator are always zero. The Hamiltonian matrix can thus be split according to different eigenvalues to the $\hat{s}^2$ operator, which can be diagonalized separately. For a CI calculation, this method is called spin-adapted CI. The same separation is also performed with respect to the angular momentum operator in the z-direction $\hat{s}_z$, which also commutes with the Hamiltonian. However, both Slater determinants and configuration state functions are eigenfunctions of the $\hat{s}_z$ operator.

2.2.4 Electronic state analysis

The ground state and excited states determined with the methods from the last chapter can be analyzed afterward to get deeper insights into the system. In particular, expectation values of further operators like the dipole moment $\vec{\mu}$

$$\hat{\mu} = -\sum_{i}^{N} \vec{r}_i + \sum_{A}^{M} Z_A \vec{R}_A \tag{2.45}$$

are of interest. Where $\vec{r}_i$ are electron coordinates, $\vec{R}_A$ are the nuclear coordinates, and Z_A are the charges of the nuclei. A number of thermodynamic properties and experiments can be predicted from such expectation values, with the ground state being of particular importance. However, to understand dynamical processes, e.g. induced by light, the transition between states becomes relevant. Fermi's golden rule derived from perturbation

theory using a continuous wave with a weak intensity as an external perturbation

$$\Gamma_{if} = \frac{2\pi}{\hbar}|\langle\psi_i|\hat{\mu}|\psi_f\rangle|^2\rho(E_f), \tag{2.46}$$

allows to determine approximate rates Γ_{if} for a transition from an initial ψ_i to a final state ψ_f. $\rho(E_f)$ is the density of states at the energy of the final state E_f. This picture is completed by further properties like the difference of the electron density of the two involved states

$$\Delta\rho_{ij}(r) = \langle\psi_i|\hat{\rho}(r)|\psi_i\rangle - \langle\psi_j|\hat{\rho}(r)|\psi_j\rangle. \tag{2.47}$$

Also, for a state-to-state transition starting from the ground state as the initial state, the so-called one-particle transition density matrix (1PTDM[58,62]) can be constructed

$$\gamma^{i0}_{\mu\nu} = \langle\psi_i|a^\dagger_\mu a_\nu|\psi_0\rangle. \tag{2.48}$$

This matrix helps to describe the resulting exciton of electron and electron hole by determining properties such as the spatial extent and distance of the particle and hole using further expectation values.

2.3 Electron dynamics

Even if, as already shown, various dynamic properties of a system can be extracted from time-independent states, in the case of pulsed laser sources or stronger field strength, explicit time-dependent considerations are necessary to obtain more realistic response properties.

The inclusion of such a laser operator turns the time-independent Hamiltonian into a time-dependent one, to which the time-independent states no longer represent eigenfunctions. However, if changes in the potential happen slowly enough, a system remains in its eigenstate according to the adiabatic theorem. Accordingly, tools such as Fermi's Golden Rule can be further used for such situations.

However, the systems considered in this thesis do not fall under the adiabatic theorem, so methods for propagating a wave function and analyzing a time-dependent wave function are needed and discussed in the following chapters.

The theory from the sections relies on the books *"Introduction to Quantum Mechanics: A Time-Dependent Perspective"*[92] and *"Multidimensional Quantum Dynamics: MCTDH Theory and Applications"*[96] as well as the articles [97–99] unless additionally stated.

2.3.1 Propagator

For time-independent Hamiltonians the Schrödinger equation (Eq. 2.1) was separated into a time-dependent and a time-independent Schrödinger equation (Eq. 2.4) by separating the variables. For time-dependent Hamiltonian operators, this cannot be done directly. Instead, by integrating the general solution

$$|\Psi(t)\rangle = \hat{U}(t, t_0)|\Psi(t_0)\rangle. \tag{2.49}$$

is obtained. Here $\hat{U}(t, t_0)$ is an operator which evolves an arbitrary wave function from time t_0 to point t in time. $\hat{U}$ is unitary and has a propagator property, and thus can be decomposed into individual propagators for smaller time steps.

$$\hat{U}(t_N, t_0) = \hat{U}(t_N, t_{N-1})\hat{U}(t_{N-1}, t_{N-2})...\hat{U}(t_1, t_0). \tag{2.50}$$

Accordingly, the operator is referred to as a propagator in the following. The evolution for a finite time can be decomposed into a product of infinitely small time steps δt with the Hamiltonian at a fixed time. Analogous to the time-dependent Schrödinger equation with time-independent Hamiltonian, the propagator for eigenstates ψ_n is now given as

$$\hat{U}(t, t_0) = e^{-iE_n\delta t} \tag{2.51}$$

and as

$$\hat{U}(t, t_0) = \sum_n e^{-i\hat{H}(t)\delta t} = \sum_n e^{-iE_n\delta t}|\phi_n\rangle\langle\phi_n| \tag{2.52}$$

for a general wave function. In practical application, an infinitely small time step δt is approximated by a finite time step Δt, where, for reasons of numerical stability, the time step must be chosen small enough for the results to converge. The propagation for a time step is thus given as

$$|\Psi(t + \Delta t)\rangle = e^{-i\hat{H}(t)\Delta t}|\Psi(t)\rangle. \tag{2.53}$$

2.3.2 Time-dependent configuration interaction

Many theories in the field of electron dynamics are based on theories for solving the TISE. This is also the case for the time-dependent configuration interaction (TD-CI) theory.

Here, the same approach for a wave function as a superposition of Slater determinants or configuration state functions is used. In contrast to time-independent CI to determine stationary states, the expansion coefficients $C_i(t)$ are time-dependent here

$$\Psi(t) = \sum_i C_i(t)\psi_i. \tag{2.54}$$

However, it is common for TD-CI to go beyond this and represent the wave function as a superposition of static CI states. The CI states ψ_i remain constant throughout the propagation and the time-dependent wave function has the same truncation as the underlying CI states.
Even if using CI states as a basis requires a preceding CI calculation, the calculation of these states often becomes necessary anyway due to their importance in the analysis of the propagations. Thus, dynamics calculations usually start from the ground state, and the population of states is used for evaluation. The population of a state is defined as the overlap between this state and the time-dependent wave function and can be easily determined in the state basis as

$$P_n(t) = |\langle\psi_n|\Psi(t)\rangle|^2 = |C_i(t)|^2. \tag{2.55}$$

Furthermore, the time-independent Hamiltonian matrix in the state basis is a diagonal matrix, which simplifies the propagation of a time step as in equation 2.53 to

$$\Psi(t + \Delta t) = \sum_i e^{-iE_i\Delta t} C_i(t)\Psi_i, \tag{2.56}$$

where the diagonal form makes the calculation of the matrix exponential trivial. Furthermore, since all off-diagonal elements of the Hamiltonian matrix in the state basis are 0, there is no change in the state population during propagation without any additional terms in the Hamiltonian. Only the (imaginary) phases of the states change depending on their energies.

Laser potential

To observe a transfer of state populations, additional terms can be added to the time-independent Hamiltonian. In this work, an external light source is included in the form of a time-dependent potential $V(\vec{r}, t) = \hat{\mu}F(t)$ to the molecular Hamiltonian. In this thesis, laser pulses are the only explicitly time-dependent operator considered. The total

Hamiltonian including an external laser pulse is given as

$$\hat{H}(\vec{r},t) = \hat{H}_{el}(\vec{r}) + \hat{\mu}F(t), \tag{2.57}$$

using the so-called semi-classical dipole approximation for the interaction with a laser. $\hat{\mu}$ represents the dipole operator already introduced in equation 2.45 and $F(t)$ an external oscillating electric field component of the form

$$F(t) = f_0 \sin(\omega(t-t_p)) \cos^2(\frac{\pi}{2\sigma}(t-t_p)), \tag{2.58}$$

where f_0 is the maximum amplitude, ω the excitation frequency and σ the pulse width. Equation 2.58 describes a pulse with a cosine squared envelope centered at t_p, therefore, the total duration of the pulse action is two times the pulse width. Other shape functions, like a Gauss envelope, for example, are possible but not used in this work. To perform a controlled state-to-state transition, the excitation frequency can be selected according to the excitation energy. Then the π-pulse condition

$$f_0 = \frac{2\pi}{\sigma\mu_{if}} \tag{2.59}$$

can be used to adjust the remaining parameters to the correct relationship. Here, μ_{if} corresponds to the transition dipole moment between the selected initial ψ_i and final ψ_f states, as in equation 2.46.

$$\mu_{if} = \langle\psi_i|\hat{\mu}|\psi_f\rangle. \tag{2.60}$$

The π-pulse condition results from the rotating wave approximation (RWA) in the limit for weak laser fields with only two states, and therefore a complete state-to-state transition often does not occur for short and intense laser pulses because of three reasons. First, short pulses have a broader spectral width, so that states that are near the target state may be addressed by the laser. Furthermore, dynamic shifts of energy levels can occur due to the coupling of permanent dipole moments with the laser field. Also, multiphoton transitions often occur in intense laser fields.

Complex absorption potential

Lasers are not only used for transitions from one bound state to another state but also to ionize systems due to strong laser fields. While it is experimentally easier to observe ionization processes than the transitions between bound states, theoreticians face greater

challenges with a description of this process. Since the electron is no longer bound, it is difficult to describe the corresponding continuum states sufficiently as shown in the overview of various basis sets in section 2.2.1. Since basis functions are spatially confined, an ionized electron is always reflected and interacts in an undesirable way with the remaining electrons or the chosen simulation area. To prevent this, complex absorption potentials (CAPs) can be used to remove electronic density under certain conditions.
CAPs are non-Hermitian operators of the form

$$\hat{V} = -i\eta W \tag{2.61}$$

with η the CAP strength and W a function depending on the type of the CAP. Two types of CAPs were used here. A spatial one where W is defined as a function in space[100,101] or an energetic one that acts on a chosen subset of CI states by assigning a lifetime to them depending on the orbital energies of the occupied spin orbitals.[21,102]

Split-Operator method

If an explicit time-dependent operator is added in addition to the molecular Hamiltonian for a dynamics calculation, the execution of a dynamics calculation usually becomes much more complex. The Hamiltonian is no longer a diagonal matrix in the state basis and changes with time, so the matrix exponential must be calculated for each time step. To minimize the computational effort, the split operator method can be used, which is shown in the following example with an additional laser operator. In the first step, the Hamiltonian operator in the matrix exponential is split into the three spatial directions of the laser field and the time-independent Hamiltonian

$$e^{i(\hat{H}_{el}+\hat{\mu}\hat{F}(t))\Delta t} \approx \left[\prod_{q\in\{x,y,z\}} e^{i\hat{\mu}_q F_q(t)\Delta t}\right] e^{i\hat{H}_{el}\Delta t}. \tag{2.62}$$

This decomposition is known as the Trotter product formula and is discussed in more detail in section 2.4.3 with respect to quantum computing. The Trotter decomposition represents an approximation for non-commutable operators, where the error for the first order scales with $O(\Delta t^2)$. After the decomposition, transformation matrices U_q are determined for the laser components, which diagonalize the dipole matrix into the corresponding spatial

directions

$$\Psi(t+\Delta t) \approx \left[\prod_{q\in\{x,y,z\}} U_q^\dagger e^{i\hat{\mu}_q F_q(t)\Delta t} U_q\right] e^{i\hat{H}_{el}\Delta t}\Psi(t). \tag{2.63}$$

Since $\hat{\mu}_q$ are diagonal matrices in the new basis, the corresponding matrix exponentials $e^{i\hat{\mu}_q F_q(t)\Delta t}$ can be efficiently determined. Because the matrix exponential of the time-independent part always remains the same, it has to be determined only once. The propagation is thus reduced to matrix multiplications which can be performed more efficiently than the calculation of matrix exponentials at every time step.

2.3.3 Time-dependent Hartree Fock

Analogous to Hartree-Fock, a single Slater determinant can be used as a time-dependent wave function. The resulting method is the time-dependent Hartree Fock method (TD-HF) with the wave function

$$\Psi = \hat{A}\chi_1(t)\chi_2(t)...\chi_N(t), \tag{2.64}$$

where $\hat{A}$ is the antisymmetrization operator. Compared to TD-CI, the TD-HF wave function is time-dependent due to the time dependence of the spin orbitals, while these remained constant in TD-CI. Various approaches based on the variational principles or perturbation theory finally provide TD-HF equations for the time evolution of the orbitals. Compared to TD-CI, the computational effort of a TD-HF propagation is significantly lower due to the use of only one Slater determinant, but TD-HF also leads to significantly less accurate results.

2.3.4 Multi-configuration Time-Dependent Hartree

In the field of time-dependent methods, the time-dependent extensions of Hartree-Fock and CI can also be combined to describe dynamic processes in systems with large static correlation. The time-dependent extension to the CASSCF method (section 2.2.3) is mainly known as the multi-configuration time-dependent Hartree Fock (MCTDHF) method. Due to limitations in the existing MCTDHF implementations, the related multi-configuration time-dependent Hartree (MCTDH) method was used in this work, which differs from MCTDHF mainly in the use of Hartree products instead of Slater determinants. The MCTDH wave function for f degrees of freedom (DOF) described by the coordinates

$q_1, ..., q_f$ has the form

$$\Psi(q_1, ..., q_f, t) = \Psi(Q_1, ..., Q_p, t) = \sum_{j_1=1}^{n_1} ... \sum_{j_p=1}^{n_p} A_{j_1...j_p}(t)\phi_{j_1}^{(1)}(Q_1, t)...\phi_{j_p}^{(p)}(Q_p, t). \quad (2.65)$$

Multiple system coordinates can be combined here to describe an artificial particle

$$Q_k = (q_a, q_b, ...), \quad (2.66)$$

which is constructed by mode combination and reduces the f DOFs to p "particles". The wave function is represented as a weighted superposition of Hartree products of so-called single-particle functions (SPF) $\phi_{j_\kappa}^{(\kappa)}(Q_\kappa, t)$, where $A_{j_1...j_p}(t)$ are the corresponding coefficients. Thus, with each particle κ, n_κ Hartree products are added to the wave function and all Hartree products are extended by one SPF.
This generalized formulation of the MCTDH wave function is based on the fact that MCTDH has already been used for a wide variety of systems from physics with a wide variety of degrees of freedom, mostly for nuclear dynamics simulations. In this thesis, a DOF is always a space dimension of a single electron. The three space dimensions and one spin coordinate could be combined by mode-combination to describe one particle (electron) κ. In this case, the SPFs would correspond to spin orbitals.
The MCTDH wave function is used in the following in a more compact form

$$\Psi(Q_1, ..., Q_p, t) = \sum_J A_J \Phi_J, \quad (2.67)$$

where a composite index $J = (j_1...j_p)$ is introduced. A_j describes the coefficient

$$A_J = A_{j_1...j_p}(t) \quad (2.68)$$

associated to J and Φ_J the associated Hartree product

$$\Phi_J = \phi_{j_1}^{(1)}(Q_1, t)...\phi_{j_p}^{(p)}(Q_p, t). \quad (2.69)$$

Setting all $n_\kappa = 1$ in the MCTDH wave function (Eq. 2.65), the wave function is reduced to a single Hartree product and corresponds to the time-dependent Hartree ansatz. Compared to the so-called standard method, where a wave function similar to the TD-FCI wave function is used with Hartree products instead of Slater determinants, $n_\kappa < N_\kappa$ is truncated in the MCTDH method.

While for the standard method and TD-CI only the expansion coefficients and for TD-H and TD-HF only orbitals are time-dependent, this applies for both in MCTDH, i.e., expansion coefficients and SPFs are time-dependent and have to be propagated in time simultaneously. Similar behavior with respect to orbitals and expansion coefficients has already been shown for HF, CI, and MCSCF for time-independent methods.
Since Hartree products are used in MCTDH, the wave function, as discussed in section 2.1.2, does not satisfy the Pauli exclusion principle due to lack of antisymmetrization and is thus unsuitable for fermions. However, this missing antisymmetrization can be restored by antisymmetrization of the A-tensor

$$A_{j_1 \dots j_k \dots j_l \dots j_p}(t) \stackrel{!}{=} -A_{j_1 \dots j_l \dots j_k \dots j_p}(t). \tag{2.70}$$

Furthermore, it is necessary to use the same set of SPFs for all Hartree products to ensure the indistinguishability of electrons.
The form of the wave function and the use of grid-based basis sets for the description of SPFs lead to the result that bound states and continuum states can be described equally, even in situations with high static correlation, with only a few SPFs. However, due to the time dependence in the A tensor and the SPFs, the method is computationally very expensive and can only be used for small electronic systems.

Equations of motion

The MCTDH equation of motion i.e. the equations describing the time evolution of a system, can be derived using a variational principle. Here the Dirac-Frankel variational principle

$$\langle \delta\Psi | \hat{H} - i\frac{\partial}{\partial t} | \Psi \rangle = 0 \tag{2.71}$$

is used. Before this variational principle can be applied, however, further restrictions have to be made concerning the SPFs. On one hand, they should be orthonormal

$$\langle \phi_j^{(\kappa)} | \phi_k^{(\kappa)} \rangle = \delta_{jk}, \tag{2.72}$$

on the other hand, the wave function should be unique, which is achieved by a Hermitian constraint operator

$$i\langle \phi_j^{(\kappa)} | \dot{\phi_k}^{(\kappa)} \rangle = \langle \phi_j^{(\kappa)} | \hat{g} | \phi_k^{(\kappa)} \rangle. \tag{2.73}$$

Without this operator, due to the flexibility of the wave function, the same time evolution could be achieved either by changing the coefficients or the SPFs. The choice of $\hat{g}$ is made in a way that the computational effort is as small as possible. By inserting the wave function into the Dirac-Frenkel variational principle, the differential equations for the time-dependent coefficients

$$i\dot{\boldsymbol{A}} = \boldsymbol{\mathcal{K}}\boldsymbol{A} \tag{2.74}$$

and differential equations for each set of SPFs

$$i\dot{\boldsymbol{\phi}}^{(\kappa)} = (1 - P^{(\kappa)})(\boldsymbol{\rho}^{(\kappa)})^{-1}\boldsymbol{\mathcal{H}}^{(\kappa)}\boldsymbol{\phi}^{(\kappa)} \tag{2.75}$$

are obtained. $\mathcal{K}$ is the Hamiltonian matrix with the elements

$$\mathcal{K}_{JL} = \langle\psi_J|\hat{H}|\psi_L\rangle. \tag{2.76}$$

Three new operators appear in the equation of motion. The first one is the projection operator $P^{(\kappa)}$ which appears as $(1 - P^{(\kappa)})$ and ensures that the SPFs represent the best possible basis for the description of the wave packet at any time. If the SPFs represent a complete basis, their time dependence is dropped and the already mentioned standard method is preserved.
For the two other operators, $\boldsymbol{\rho}^{(\kappa)}$ and $\boldsymbol{\mathcal{H}}^{(\kappa)}$, the single hole wave function

$$\Psi_a^{(\kappa)} = \sum_{j_1} ... \sum_{j_{\kappa-1}} \sum_{j_{\kappa+1}} ... \sum_{j_p} A_{j_1...j_{\kappa-1}aj_{\kappa+1}...j_p}(t)\phi_{j_1}^{(1)}...\phi_{j_{\kappa-1}}^{(\kappa-1)}\phi_{j_{\kappa+1}}^{(\kappa+1)}...\phi_{j_p}^{(p)} \tag{2.77}$$

is introduced, where the κ-th particle is removed, leaving the hole a.

$$\mathcal{H}_{ab}^{(\kappa)} = \langle\Psi_a^{(\kappa)}|\hat{H}|\Psi_b^{(\kappa)}\rangle \tag{2.78}$$

is thus a mean-field operator and correlates the motion between the different SPF sets. The last operator $\boldsymbol{\rho}^{(\kappa)}$ is the density operator as it already appeared in section 2.2.4. The matrix elements are given here as

$$\rho_{ab}^{(\kappa)} = \langle\Psi_a^{(\kappa)}|\Psi_b^{(\kappa)}\rangle. \tag{2.79}$$

Since entries close to zero are obtained in the density matrix for energetically high states,

linear dependencies of rows and columns can occur in the matrix. Because such a singular matrix cannot be inverted, as it is necessary for equation 2.75, a regularized density matrix in the form

$$\boldsymbol{\rho}_{reg}^{(\kappa)} = \boldsymbol{\rho}^{(\kappa)} + \epsilon \exp\left(\frac{-\boldsymbol{\rho}^{(\kappa)}}{\epsilon}\right) \tag{2.80}$$

is used. The general MCTDH equation of motion is obtained by adding the constraint operator $\hat{g}$ as

$$i\dot{\boldsymbol{A}} = \left(\boldsymbol{\mathcal{K}} - \sum_{\kappa} \hat{g}^{(\kappa)}\right) \boldsymbol{A} \tag{2.81}$$

for the coefficients and

$$i\dot{\boldsymbol{\phi}}^{(\kappa)} = \left[(\boldsymbol{g}^{(\kappa)})^T + (1 - P^{(\kappa)})(\boldsymbol{\rho}^{(\kappa)})^{-1}\boldsymbol{\mathcal{H}}^{(\kappa)}\right] \boldsymbol{\phi}^{(\kappa)} \tag{2.82}$$

for the SPFs. Depending on the choice of the constraint operator, different SPFs are obtained, which can be transformed into each other by a unitary transformation and therefore describe the same space. A typical constraint operator is $\hat{g}^{(\kappa)} = 0$, with which one recovers the EOMs from the equations 2.74 and 2.75. Alternatively, the one-particle terms of the corresponding Hamiltonian are often used as a constraint operator.

Discrete variable representation and Hamiltonian form

To solve the MCTDH equation of motion (Eq. 2.81 and 2.82), elements of the Hamiltonian matrix (Eq. 2.76) as well as the mean-field matrix (Eq. 2.78) have to be determined repeatedly by integration. To simplify this multidimensional integration and to make MCTDH efficient, the SPFs are expanded in a basis of so-called primitive basis functions

$$\phi_j^{(\kappa)}(Q_\kappa) = \sum_{k=1}^{N_\kappa} a_{kj}^{(\kappa)} \chi_k^{(\kappa)}(Q_\kappa). \tag{2.83}$$

The number of primitive basis functions N_κ is different from the number of SPFs n_κ in equation 2.65. The primitive basis functions are orthonormal in a discrete variable representation (DVR). The matrix representation of the position operator $\hat{q}_v$ in a basis of such DVR functions $\chi_k^{(\kappa)}$ for the coordinate q_v is a diagonal matrix

$$\langle \chi_i^{(\nu)} | q_\nu | \chi_j^{(\nu)} \rangle = q_j^{(\nu)} \delta_{ij}. \tag{2.84}$$

In this way, the corresponding eigenvalues of the position operator $\hat{q}_\nu$ represent a set of grid points in the chosen DVR basis. To determine the integrals for local potentials $V(Q_\kappa)$, which act only on one coordinate, it is now sufficient to evaluate the potentials only at the DVR points

$$\langle \chi_{i_1}^{(1)} ... \chi_{i_f}^{(f)} | V | \chi_{j_1}^{(1)} ... \chi_{j_f}^{(f)} \rangle = V(q_{j_1}^{(1)}, ..., q_{j_f}^{(f)}) \delta_{i_1 j_1} ... \delta_{i_f j_f}. \tag{2.85}$$

If several degrees of freedom d are combined into particles by mode combination and multidimensional SPFs are used, SPFs are expanded as a sum of products of primitive basis functions. For two DOFs q_1 and q_2, for example, as

$$\phi_j^{(1)}(Q_1) = \sum_{k_1=1}^{N_1} \sum_{k_2=1}^{N_2} a_{k_1 k_2 j}^{(1)} \chi_{k_1}^{(1)}(q_1) \chi_{k_2}^{(2)}(q_2). \tag{2.86}$$

Depending on the degree of freedom, different functions can be used as DVRs. For example, harmonic oscillator DVRs are suitable for vibrational motion, and exponential and sine DVRs for free motion without periodic boundary conditions.
If the Hamiltonian can be expressed in a product form as a sum of products of single-particle operators

$$\hat{H}(q_1, ..., q_f) = \sum_{r=1}^{n_s} c_r h_r^{(1)}(Q_1) ... h_r^{(p)}(Q_p), \tag{2.87}$$

the multidimensional integrals can be expressed as a sum of products of lower dimensionality d

$$\langle \phi_{j_1}^{(1)} ... \phi_{j_p}^{(p)} | \hat{H} | \phi_{k_1}^{(1)} ... \phi_{k_p}^{(p)} \rangle = \sum_{r=1}^{n_s} c_r \langle \phi_{j_1}^{(1)} | \hat{h}^{(1)} | \phi_{k_1}^{(1)} \rangle ... \langle \phi_{j_p}^{(p)} | \hat{h}^{(p)} | \phi_{k_p}^{(p)} \rangle. \tag{2.88}$$

By using DVRs, these integrals have only the dimensionality N^d where N is the number of primitive basis functions and d is the dimensionality of the corresponding particle. As shown before, these integrals can be computed efficiently. Potentials acting on more than one particle, like the Coulomb interaction, have to be approximated by a product form accordingly

$$V^{app}(Q_{i_1}^{(1)}, ..., Q_{i_p}^{(p)}) = \sum_{j_1=1}^{m_1} ... \sum_{j_p=1}^{m_p} C_{j_1,...,j_p} \nu_{j_1}^{(1)}(Q_{i_1}^{(1)}) ... \nu_{j_p}^{(p)}(Q_{i_p}^{(p)}). \tag{2.89}$$

In the MCTDH program used, the implemented POTFIT and multigrid POTFIT (MGPF) methods can be used for this purpose.

Imaginary time evolution

Since dynamics calculations are usually started from an eigenstate, most often the ground state with time-independent Hamiltonian, and other states may also be relevant for evaluations, it must also be possible to determine these in the MCTDH framework. However, unlike in the TD-CI method, in MCTDH the time-independent Schrödinger equation is not solved directly. Instead, the imaginary time evolution method is used.
The method starts with an arbitrary trial wave function, which can be represented as a linear combination of the time-independent eigenstates

$$\Psi(t_0) = \sum_n c_n(t_0)\psi_n. \tag{2.90}$$

As shown in section 2.3.2 on TD-CI, the propagation of such a wave packet can be written with the state phases explicitly as

$$\Psi(t) = \sum_n c_n(t_0)e^{-iE_n t}\psi_n. \tag{2.91}$$

If the real time t is exchanged by an imaginary time $\tau = it$, the states no longer change their phase depending on the corresponding state energies E_n but decay with a decay rate proportional to these energies. The ground state with the lowest energy decays the slowest so that the renormalized wave function in the long imaginary time limit corresponds to the ground state. If the trial wave function has no overlap with the ground state, the excited state with the lowest energy and overlap with the trial wave function is obtained. This can be used to determine higher energy states by choosing the trial wave function orthogonal to undesired states. The imaginary time evolution method is referred to as relaxation in the context of MCTDH. Furthermore, with a method called improved relaxation, several states can be calculated at once. To make this possible, the wave function must be able to represent several electronic states simultaneously and the use of a CMF (Constant Mean Field) scheme for the propagation is necessary. Here, the matrix elements $\mathcal{K}_{JL}$ and the product of the inverse density and mean-field matrices $(\boldsymbol{\rho}^{(\kappa)})^{-1}\boldsymbol{\mathcal{H}}^{(\kappa)}$ are only re-evaluated every few propagation steps as they change much slower than the MCTDH coefficients and the SPFs.
In order to perform the actual propagations in MCTDH in both real and imaginary time, a

number of other algorithms such as the Runge-Kutta method or Davidson diagonalization are needed. However, since these are more technical details, they will not be discussed in this thesis.

2.4 Quantum computing

The electron dynamics methods already mentioned always compromise accuracy and the number of interacting particles. Accurate calculations with many electrons are impossible on traditional computers due to their quantum mechanical properties. As already mentioned, one solution could be the simulation of one quantum system with the help of another in the form of quantum computing. There are different models of quantum computing which can differ drastically in the physical implementation and the algorithms. In this work, only the quantum circuit model is discussed and used. Also, this chapter does not address the realization and suitability of physical systems, but instead focuses on the development of quantum algorithms only. The basic principles and quantum algorithms presented here were largely compiled from the works [78, 79].

2.4.1 Qubits and quantum gates

The quantum circuit model has certain similarities with traditional computers. Traditional computers use logic gates like AND, OR, and NOT which act on information in the form of bits. A bit represents a binary number (usually "0" or "1"). In the quantum circuit model, quantum gates instead act on the corresponding basic unit of information, the qubit. A qubit can represent more than just two different states, instead it can represent any state in a two-dimensional Hilbert space. The basis vectors of the Hilbert space are called $|0\rangle$ and $|1\rangle$ and correspond to the so-called computational basis. A general state of a qubit can thus be written as

$$|\psi\rangle = \alpha|0\rangle + \beta|1\rangle = \begin{pmatrix} \alpha \\ \beta \end{pmatrix}, \tag{2.92}$$

where α and β can be complex $\alpha, \beta \in C$ and the state is normalized $|\alpha|^2 + |\beta|^2 = 1$. If a qubit is now measured in the computational basis, the states $|0\rangle$ or $|1\rangle$ are always obtained with the corresponding probabilities $|\alpha|^2$ and $|\beta|^2$.
If several qubits are combined into a quantum system, the state space of the system is given as the tensor product of the individual qubit state spaces. The state of an n qubit system is accordingly described as a vector in the 2^n dimensional Hilbert space spanned

by the tensor product of the n qubits. States can be distinguished between product states and entangled states. While product states can be decomposed into tensor products of pure states of fewer qubits like

$$\frac{1}{\sqrt{2}}(|00\rangle + |10\rangle) = \frac{1}{\sqrt{2}}(|0\rangle + |1\rangle) \otimes |0\rangle, \tag{2.93}$$

this is not possible for entangled states like

$$\frac{1}{\sqrt{2}}(|00\rangle + |11\rangle). \tag{2.94}$$

A pure state is a state that can be described by a single ket vector. A mixed state, on the other hand, is a statistical ensemble of pure states. While for pure states the density operator is given as $\hat{\rho} = |\Psi\rangle\langle\Psi|$, for mixed states it is defined as

$$\hat{\rho} = \sum_j p_j |\Psi_j\rangle\langle\Psi_j| \tag{2.95}$$

where p_j are the probabilities for the corresponding states Ψ_j. The use of the density matrix instead of state vectors allows, for example, to simulate noisy quantum computers where such mixed states occur. In addition, the density matrix can be used to decompose entangled states of the system AB into mixed states for the corresponding subsystems A and B. The resulting form is called a reduced density matrix.
In the following, for states consisting of n qubits as in equation 2.94, the qubit on the rightmost side of the ket vector is counted as the zeroth qubit and the qubit on the leftmost side is counted as the $(n-1)$th qubit. This ordering is different from the ordering for spin orbitals in the previous chapters but is common in quantum computing. With this ordering, binary numbers can be written directly using the computational basis such as $|5\rangle = |1\rangle|0\rangle|1\rangle = |101\rangle$. At the beginning of a quantum algorithm, the n-qubits to be used are first initialized to a well-defined state such as the state $|\bar{0}\rangle = |0\rangle^{\otimes n} = |0\rangle \otimes ... \otimes |0\rangle$. Then this state is manipulated by the quantum circuit and measured at the end to extract the desired information. A quantum circuit consists of qubit gates that act on one or more qubits. A qubit gate is always a unitary transformation and can be written as a unitary matrix acting on the basis states. Typical single qubit gates which are used in the following are the so-called Pauli gates corresponding to the Pauli matrices

$$X = \begin{pmatrix} 0 & 1 \\ 1 & 0 \end{pmatrix}, \quad Y = \begin{pmatrix} 0 & -i \\ i & 0 \end{pmatrix}, \quad Z = \begin{pmatrix} 1 & 0 \\ 0 & -1 \end{pmatrix}, \tag{2.96}$$

the single qubit rotation gates

$$R_x(\theta) = e^{-i\theta X/2}, \quad R_y(\theta) = e^{-i\theta Y/2}, \quad R_z(\theta) = e^{-i\theta Z/2} \tag{2.97}$$

as well as the Hadamard, T, and S gates

$$H = \frac{1}{\sqrt{2}} \begin{pmatrix} 1 & 1 \\ 1 & -1 \end{pmatrix}, \quad T = \begin{pmatrix} 1 & 0 \\ 0 & e^{i\pi/4} \end{pmatrix}, \quad S = \begin{pmatrix} 1 & 0 \\ 0 & i \end{pmatrix}. \tag{2.98}$$

The most relevant of the multi-qubit gates is the controlled-NOT gate (CX), which can entangle and disentangle two qubits with each other

$$CX = |0\rangle\langle 0|_C \otimes I_T + |1\rangle\langle 1|_C \otimes X_T. \tag{2.99}$$

Here, C denotes the control, and T the target qubit. The gate flips the target qubit by a Pauli-X quantum gate if the control qubit is in state $|1\rangle$. The matrix representation acting on the two-qubit basis $|i\rangle_C \otimes |j\rangle_T$ is given as

$$CX = \begin{pmatrix} 1 & 0 & 0 & 0 \\ 0 & 1 & 0 & 0 \\ 0 & 0 & 0 & 1 \\ 0 & 0 & 1 & 0 \end{pmatrix}. \tag{2.100}$$

The Hadamard gate, T gate, and CX gate represent a universal set of quantum gates, which means that any further one or multi-qubit gate can be represented as a combination of these gates. Mathematically, a quantum circuit of k quantum gates can be written as

$$|\phi\rangle = \prod_k U_k^{i_k, j_k}(\vec{\theta_k})|\bar{0}\rangle \tag{2.101}$$

where $U_k^{i_k,j_k}(\vec{\theta_k})|$ is the corresponding unitary gate acting on the qubits i_k (and j_k). $\vec{\theta_k}$ is an additional parameter, as it occurs, for example, in single qubit rotation gates. An example for a quantum circuit consisting of H, R_x and CX gates is

$$CX^{0,1} R_x^1(\pi) H^0 |00\rangle \tag{2.102}$$

and creates the state

$$\frac{1}{\sqrt{2}}(|01\rangle + |10\rangle). \tag{2.103}$$

Easier to read than the mathematical notation from equation 2.102 is the visualization of such a circuit as given in Fig. 2.1 for the same example with subsequent measurement of the qubits.

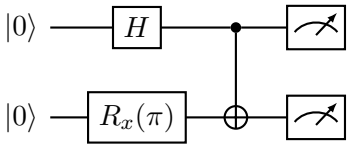

Figure 2.1: Visualization of the quantum circuit from equation 2.102 in which the state $\frac{1}{\sqrt{2}}(|01\rangle + |10\rangle)$ is generated. Additionally, both qubits are measured in the computational basis.

The expectation value of the measurement of a qubit i corresponds to the expectation value to the corresponding Pauli-Z operator $\langle\psi|Z_i|\psi\rangle$. Thus, for the determination of the expectation value, it is necessary to repeatedly prepare the state $|\psi\rangle$ and to measure the state. If the state $|0\rangle$ is measured, the measurement corresponds to the eigenvalue $+1$ and for the state $|1\rangle$ to the eigenvalue -1. The average over the measurements then corresponds to the expectation value. Expectation values for Pauli-X and Pauli-Y operators can be determined by measurement after corresponding previous single qubit rotations. The measurement of multi-qubit operators like Z_iZ_j corresponds to the product of the measurements of Z_i on qubit i and Z_j on qubit j. Since the Pauli operators and the identity matrix form a complete basis, the expectation values to any other single or multi-qubit operator can be determined using the expectation values of Pauli operators and strings of Pauli operators.

2.4.2 Fermion-qubit mapping

In order to use quantum computing for fermionic problems, it is necessary to map systems with indistinguishable fermions to distinguishable qubits. Such mappings, in the following also referred to as encodings, are possible in the first as well as in the second quantization. In this work mapping in the second quantization will be discussed exclusively. Each fermionic state in Fock space must be mapped to a qubit state in Hilbert space, and the action of the fermionic creation and annihilator operators must be reflected by qubit operators.

The first mapping of a fermionic system to a bosonic one was already introduced in 1928 with the Jordan-Wigner transformation.[89] Here a mapping between 1-dimensional spin-1/2 chains and fermions on a chain was developed. Fermionic creation and annihilation operators are encoded by spin operators. The transformation is used in different forms, among others for tensor network methods, and can also be used as a mapping for quantum computing.
In the Jordan-Wigner transformation, the occupation state of a spin-orbital f is transferred to a qubit q as state $|0\rangle$ for unoccupied spin orbitals and as state $|1\rangle$ for occupied spin orbitals, respectively

$$|f_1, f_2, ..., f_N\rangle \rightarrow |q_{N-1}, q_{N-2}, ..., q_0\rangle, f_p = q_p \in 0, 1. \tag{2.104}$$

Note again that spin orbitals and qubits are sorted in different ways. While for FCI the number of Slater determinants and the corresponding coefficients to be stored increase exponentially with the number of spin orbitals, in quantum computing only as many qubits as spin orbitals are necessary to represent the same wave function.
The creation and annihilation operators $\hat{a}_p^\dagger$ and $\hat{a}_p$ increase and decrease the occupation number of an orbital p by one and can cause a sign change (phase vector) due to the antisymmetrization principle of fermions. The translation of these operators to qubits is given in the Jordan-Wigner transformation as

$$\hat{a}_p = \hat{Q}_p \otimes Z_{p-1} \otimes ... \otimes Z_0, \hat{a}_p^\dagger = \hat{Q}_p^\dagger \otimes Z_{p-1} \otimes ... \otimes Z_0 \tag{2.105}$$

with

$$\hat{Q}_p = |0\rangle\langle 1| = \frac{1}{2}(X + iY), \hat{Q}_p^\dagger = |1\rangle\langle 0| = \frac{1}{2}(X - iY). \tag{2.106}$$

The operators $\hat{Q}_p^\dagger$ and $\hat{Q}_p$ change the occupation number of the corresponding spin-orbital, while the sequence of Z-operators corresponds to the phase vector and thus ensures the antisymmetrization of the fermionic wave function. Since creation and annihilation operators can be translated into a product of Pauli operators (Pauli strings), the full molecular Hamiltonian can also be translated into a linear combination of products of Pauli quantum gates

$$\hat{H} = \sum_{ij} \langle i|\hat{h}_1|j\rangle \hat{a}_i^\dagger \hat{a}_j + \frac{1}{2} \sum_{ijkl} \langle ij|kl\rangle \hat{a}_i^\dagger \hat{a}_j^\dagger \hat{a}_l \hat{a}_k = \sum_r h_r \hat{P}_r = \sum_r h_r \prod_s \hat{\sigma}_s^r. \tag{2.107}$$

h_r corresponds to the one- and two-electron integrals (h_{ij} and $\frac{1}{2}\langle ij|kl\rangle$) from equations 2.23 and 2.24 and P_r to the sequences of creation and annihilation operators ($\hat{a}_i^\dagger \hat{a}_j$ and $\hat{a}_i^\dagger \hat{a}_j^\dagger \hat{a}_k \hat{a}_l$). $\hat{\sigma}_s^r$ represents one of the quantum gates I, X, Y or Z acting on the s-th qubit. I corresponds to the "zeroth" Pauli matrix, whose matrix representation is the identity matrix. The application of an I quantum gate would not change a state in this case. r indexes the terms of the Hamiltonian operator.
While the occupation of a spin-orbital in the Jordan Wigner transform is encoded locally on only one qubit, the phase vector of fermionic field operators $\hat{a}_i^\dagger$ and $\hat{a}_i$ leads to nonlocal operators acting on many qubits simultaneously. This makes the JW transform simple but leads to quantum circuits with many quantum gates and long runtimes in the following quantum algorithms. Alternative encodings like the parity encoding or the Bravyi-Kitaev encoding[103] are more complicated but can reduce the number of quantum gates in many cases.

2.4.3 Quantum algorithms

Hamilton simulation

The problem to propagate an initial state under a given Hamiltonian with a quantum computer, i.e. to applying the propagator $e^{-i\hat{H}t}$ is called Hamiltonian simulation. There are several approaches to approximate the propagator by a short quantum circuit, the simplest and oldest being the Lie-Trotter-Suzuki decomposition, also called Trotter decomposition in the following.[90,91] As in the methods for traditional computers, the total propagation time is first divided into small time steps Δt. Now, for each time step, the Hamiltonian is divided into terms $\hat{h}_j$ as local as possible which are equal to the corresponding Pauli strings from equation 2.107. The propagator of a time step is now decomposed into several exponential parts according to the Lie-Trotter-Suzuki decomposition. The first-order Trotter decomposition yields

$$e^{-i\hat{H}\Delta t} = e^{-i\sum_j \hat{h}_j \Delta t} \approx \prod_j e^{-i\hat{h}_j \Delta t} + O(\Delta t^2). \tag{2.108}$$

The Trotter decomposition is only an approximation since the individual terms of the

Hamiltonian $\hat{h}_j$ do not commute with each other. The error depends on the size of the time step. Higher orders of the Trotter decomposition lead to smaller errors, but also to more exponential terms and later to more quantum gates. The general Trotter decomposition is given as

$$e^{-i\hat{H}\Delta t} = e^{-i\sum_j \hat{h}_j \Delta t} \approx \left(\prod_j e^{-i\hat{h}_j \Delta t/N} \right)^N . \tag{2.109}$$

The number j of local terms $\hat{h}_j$ scales polynomially with the number of spin orbitals due to the two-body properties of the Coulomb interaction between electrons. Each of the exponential terms is then translated into a quantum gate sequence. The number of quantum gates in the Trotter decomposition and all other product formula approaches therefore also scale polynomially $O(poly(1/\epsilon))$ depending on the encoding, the product formula, the molecule, and the accuracy ϵ. For typical molecules, a scaling of approximately $O(N^6)$ with the number of spin orbitals has been shown. TD-FCI, on the other hand, as a counterpart to Hamiltonian simulation on traditional computers, scales exponentially.
In addition to the Trotter decomposition, there are other approaches for the Hamiltonian simulation, some of which are much more efficient. These include multi-product formulas,[104,105] Taylor series expansion,[106,107] qubitization,[108,109] and several more.

Hadamard Test

Unlike propagation methods for traditional computers, quantum computing does not allow direct access to the wave function. When measuring the qubit state, the wave function would collapse and only a Slater determinant with a probability corresponding to the expansion coefficient is obtained. Reading out the complete wave function is exponentially expensive and storing all coefficients would require exponentially much memory, thus negating the main advantage of quantum computing. However, the full time-dependent wave function is rarely needed to evaluate electron dynamics calculations anyway. Although the wave function is used in traditional methods to obtain time-dependent expectation values and population, these quantities can be obtained in quantum computing by other algorithms. One possibility used in this work is the Hadamard test[110] which allows to obtain the expectation value for an arbitrary unitary operator $\hat{U}$.
For the Hadamard test an auxiliary qubit is needed, which is not used to describe the fermionic wave function. Such auxiliary qubits are called ancilla qubits. The ancilla qubit

is initialized in the $|0\rangle$ state and subsequently brought into an equal superposition of the basis states $\frac{1}{2}(|0\rangle + |1\rangle)$ by a Hadamard gate. The total qubit state is then

$$\frac{1}{2}(|0\rangle + |1\rangle) \otimes |\Psi\rangle. \tag{2.110}$$

Next, the unitary operator $\hat{U}$ is applied, controlled by the ancilla qubit, resulting in the overall state

$$\frac{1}{2}(|0\rangle \otimes |\Psi\rangle + |1\rangle \otimes \hat{U}|\Psi\rangle). \tag{2.111}$$

In the next step, a Hadamard gate is applied again, and the state

$$\frac{1}{2}(|0\rangle \otimes (I + \hat{U})|\Psi\rangle + |1\rangle \otimes (I - \hat{U})|\Psi\rangle) \tag{2.112}$$

is obtained. In the last step, the ancilla qubit is measured and the states $|0\rangle$ and $|1\rangle$ with the probabilities

$$|0\rangle : \frac{1}{4}\langle\Psi|I + \hat{U}^\dagger)(I + \hat{U})|\Psi\rangle, \quad |1\rangle : \frac{1}{4}\langle\Psi|I - \hat{U}^\dagger)(I - \hat{U})|\Psi\rangle \tag{2.113}$$

are obtained. The difference between the two probabilities corresponds to

$$\frac{1}{2}\langle\Psi|(\hat{U}^\dagger + \hat{U})|\Psi\rangle = Re\langle\Psi|\hat{U}|\Psi\rangle \tag{2.114}$$

and thus to the real part of the expectation value of $\hat{U}$.
The measurement will be repeated several times. For the case that the state $|0\rangle$ is measured the value 1 will be stored and for the case that the state $|1\rangle$ is measured the value -1 will be stored. The average of the values over many measurements then corresponds to the real part of the expectation value. To obtain the imaginary part of the expectation value of $\hat{U}$, the state

$$\frac{1}{2}(|0\rangle - i|1\rangle) \otimes |\Psi\rangle \tag{2.115}$$

has to be prepared before applying the operator $\hat{U}$. This is achieved by applying the phase gate S to the ancilla qubit after the first Hadamard gate. The Hadamard test for

measuring the real part of $\hat{U}$ is visualized as a circuit in Fig. 2.2.

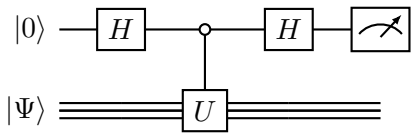

Figure 2.2: Quantum circuit of the Hadamard test to determine the real part of the expectation value to $\hat{U}$. The upper line represents an ancilla qubit which is initialized in the $|0\rangle$ state, while the other lines represent qubits that together encode the wave function $|\Psi\rangle$ whose expectation value to $\hat{U}$ is to be determined.

The number of measurements necessary to obtain an expectation value with the accuracy ϵ is $O(1/\epsilon^2)$. In the Hadamard test, the wave function is measured only indirectly and consequently modified but not completely collapsed. Instead, the state $(I \pm \hat{U})|\Psi\rangle\sqrt{(2)}$ is obtained, which can be further used for other algorithms.

Quantum Imaginary Time Evolution

While imaginary time evolution, as shown in section 2.3.4, is a good method to determine eigenstates and their eigenenergies, the same approach is not directly suitable for quantum computers. Although one can prepare states like the Hartree-Fock ground state on a quantum computer and propagate them with Hamiltonian simulation methods, the substitution of real time with imaginary time leads to a propagator which is no longer a unitary operator. Accordingly, such a propagator cannot be translated into quantum gates. Nevertheless, there are approaches to perform a similar propagation, for example, the quantum imaginary time evolution (QITE)[111] approach. The idea behind QITE is to exchange non-Hermitian operators $\hat{h}_l$ by unitary operators $\hat{A}_m$ after a Trotter decomposition. The new operator should have the same effect on the states as the old one, but preserve the norm of the wave function, which is not given for non-unitary operators

$$|\overline{\Psi}'\rangle = c^{-1/2} e^{-\hat{h}_l \Delta t}|\Psi\rangle = e^{-i\Delta t \hat{A}_m}|\Psi\rangle. \tag{2.116}$$

c is the change in the norm that would follow from applying the non-unitary propagator. The norm change can be determined on a quantum computer by measuring the expectation value of $\hat{h}_l$

$$c = 1 - 2\Delta t \langle\Psi|\hat{h}_l|\Psi\rangle + O(\Delta t^2). \tag{2.117}$$

While $\hat{h}_l$ acts only locally on a few qubits, it may be the case that $\hat{A}_m$ has to act on considerably more k qubits or even all qubits due to the correlation of the qubits. $\hat{A}_m$ is now expanded into operators acting on the k qubits. For this purpose, for example, Pauli operators can be used

$$\hat{A}_m = \sum_{i_1 \ldots i_k} a_{m,i_1 \ldots i_k} \hat{\sigma}_{i_1} \ldots \hat{\sigma}_{i_k} \equiv \sum_I a_{m,I} \hat{\sigma}_I. \tag{2.118}$$

With the definition of

$$|\Delta_0\rangle = \frac{|\overline{\Psi}'\rangle - |\Psi\rangle}{\Delta t}, \quad |\Delta\rangle = i\hat{A}_m|\Psi\rangle, \tag{2.119}$$

the target is to minimize the difference $||\Delta_0 - \Delta||$ to find the expansion coefficients $a_{m,I}$. For real coefficients, this corresponds to minimizing the quadratic equation $f(a_l)$

$$f(a_l) = f_0 + \sum_I b_I a_{m,I} + \sum_{IJ} a_{m,I} S_{IJ} a_{m,J} \tag{2.120}$$

with

$$\begin{aligned} f_0 &= \langle \Delta_0 | \Delta_0 \rangle, \\ b_I &= i\langle \Psi | \hat{\sigma}_I^\dagger | \Delta_0 \rangle - i\langle \Delta_0 | \hat{\sigma}_I | \Psi \rangle, \\ S_{IJ} &= \langle \Psi | \hat{\sigma}_I^\dagger \hat{\sigma}_J | \Psi \rangle. \end{aligned} \tag{2.121}$$

The minimum of the equation is obtained by solving the linear equation

$$(\mathbf{S} + \mathbf{S}^T)\mathbf{a}_m = -\mathbf{b}. \tag{2.122}$$

For molecular systems in particular, the problem with the QITE algorithm is that all qubits are correlated and the dimensions of S_{IJ} and b_I increase exponentially with the number of spin orbitals. Therefore, the QITE algorithm shown here scales worse than algorithms for traditional computers. However, modifications have already been developed, such as for the step-merged QITE algorithm in Gomes *et al.*,[112], which can limit the dimensions by approximations and lead to a polynomial scaling and therefore an advantage over traditional computers. Furthermore, the QITE algorithm can be used not only for imaginary time evolutions, but also for real time evolutions in open quantum systems, i.e., systems with non-Hermitian operators like the CAP operator.

3 Results and Conclusion

3.1 Interparticle Coulombic decay in three quantum dot arrangements

In the first project of this thesis and thus papers **[1, 2]**, the ICD process in model systems for three QDs was studied. Here, previous studies on this topic were built upon and extended. Quantum dots are represented as inverse Gaussians, and thus the potential of an N quantum dot system $\hat{V}_{QD}$ is represented as

$$\hat{V}_{QD}(\vec{r}) = \sum_{q} -D_q e^{-b_q(\vec{r}-\vec{r}_q)^2}, \tag{3.1}$$

where D_q is the depth, b_q the width and $\vec{r}_q$ the position of a Gaussian q. Two types of QDs are involved in the ICD process. The first type is called photon emitter (A). These are quantum dots with multiple bound one-electron levels. The second type is called photon acceptor (B) or electron emitter. As shown schematically in the introduction in section section 1.1, the ICD process is possible when one or more photon emitters are in an excited state A^*. In the process, the energy of a photon emitter is transferred to a photon acceptor via the exchange of a virtual photon. The photon acceptor is thereby ionized $B_0 \rightarrow B^+ + e^-$ while the photon emitter deexcites into an energetically lower state, here the ground state A_0. Thus, the energy condition

$$E(A^*) - E(A_0) > E(B_0) - E(B^+) \tag{3.2}$$

must be fulfilled for the ICD process. Excess energy is transferred to the ICD electron as kinetic energy. The rate of the process can be approximated according to Averbukh *et al.*[40] as

$$\Gamma_{ICD} = N \frac{3}{4\pi} \left(\frac{c}{\omega_{ph}} \right)^4 \frac{\tau_A^{-1} \sigma_B}{R^6} \tag{3.3}$$

with the assumption that the wave functions on the different quantum points do not overlap. σ_B is the absorption cross-section of the ICD electron in state B_0 at the virtual photon energy E_{ph}, τ_A^{-1} is the rate of spontaneous emission of the excited electronic state A^*, ω_{ph} is the frequency of the virtual photon and N is the number of photon acceptor quantum dots.

In this work, two different arrangements were investigated, which are shown in Fig. 3.1. In each inverse Gaussian, only one electron is bound. In the first arrangement from **[1]** (Fig. 3.1, left panel), a photon emitter with depth $D_A = 2$ a.u. and width $b_A = 0.25$ a.u. is placed between two photon acceptors with depth $D_b = 2$ a.u. and width $b_B = 1$ a.u., where this is a two-dimensional system. This results in one-electron state energies of $A_0 = -1.128$ a.u., $A^* = -0.413$ a.u. and $B_0 = -0.527$ a.u. A^* is thereby, depending on the angle, almost doubly degenerate. In the second arrangement from **[2]** (Fig. 3.1, right panel), a one-dimensional system consisting of one photon acceptor with depth $D_B = 1$ a.u. and width $b_B = 1$ a.u. between two photon emitters with depth $D_A = 1$ a.u. and width $b_A = 0.25$ a.u. is considered. Here the one-electron state energies are given as $A_0 = -0.693$ a.u., $A^* = -0.196$ a.u. and $B_0 = -0.477$ a.u.

Even if the energies for the many-electron states like $B_0 A^* B_0$ do not correspond exactly to the sums of the one-electron states, $E(B_0 A^* B_0) \neq E(B_0) + E(A^*) + E(B_0)$, because of the Coulomb interaction, the difference is relatively small due to the relatively large distances between the quantum dots. Therefore, it can already be estimated from the one-electron states, whether the energy condition for ICD (Eq. (3.2)) is fulfilled.

For both potentials considered, the MCTDH method[96] was used in the Heidelberg MCTDH program.[113] The Hamiltonian for both systems is given as

$$\hat{H} = \sum_i \left(\hat{T}_i + \hat{V}_i^{QD} + \hat{V}_i^{CAP} \right) + \sum_i \sum_{j<i} \frac{1}{r_{ij}}. \tag{3.4}$$

where $\hat{V}_i^{CAP}$ is a spatial CAP (cf. section 2.3.2).

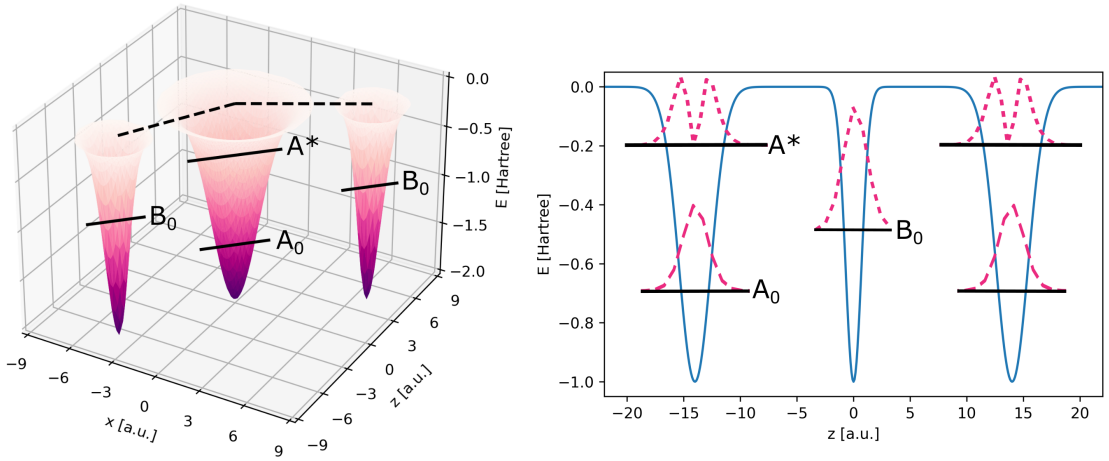

Figure 3.1: Illustration of the two quantum dot arrangements considered. (left) for a system with two external photon acceptor quantum dots and one photon emitter quantum dot in two spatial dimensions. (right) for an arrangement with one photon acceptor between two photon emitter quantum dots along one spatial dimension. Denoted by A_0 and A^* are the bound one-electron states in the photon emitters and by B_0 the bound state in the photon acceptors. In the one-dimensional case (right) the electron density of the corresponding one-electron states is shown in pink dashed lines.

Dynamics with one photon emitter and two photon acceptors

A potential quite similar to the potential with one photon emitter between two photon acceptors (Fig. 3.1, left panel) has already been investigated in previous work.[52] In one spatial dimension, it was shown both analytically and numerically that the ICD rate doubles compared to the same system with only one photon acceptor. However, due to the one-dimensional approach, effects occur that lead to strong oscillations of the ICD rate with the variation of the distance, which are not accounted for in equation Eq. (3.3). One reason for the oscillations is that the ICD electron in a one-dimensional system is limited in motion by the Coulomb potential of the remaining electrons. For ICD in two quantum dots, it could already be shown that the transition from the one-dimensional model to a two-dimensional model can drastically reduce this constraint and thus the oscillations.[51] However, this transition is accompanied by a doubling of spatial dimensions and thus DOFs, and is computationally more demanding.

To reduce the computing time, it was first evaluated to what extent the use of graphics processors (GPUs) is possible. In the standard Heidelberg MCTDH implementation employed, only the central processing units of a computer (CPUs) are used. Each processor has computational cores and each core can perform one computational operation at a time. While CPUs have a few very fast cores that can also perform complicated

calculations efficiently, GPUs are equipped with as many cores as possible that are, however, significantly slower and limited in the possible computing operations. Thus, a meaningful application of GPUs would be computations that can be divided into many simple computational operations to be executed in parallel. In such cases, a GPU can execute significantly more operations at the same time than a CPU.
For smaller test calculations, the functions that require the longest accumulated time were first determined by profiling the program. This revealed that most of the time is needed for simple matrix routines such as matrix multiplications, in which the use of GPUs is possible since the elements of the product matrix can be calculated independently from each other simultaneously. To implement the parallelization, the Fortran 77 code of the corresponding matrix routines was translated into Fortran 90 code and OpenACC was used to implement the corresponding compiler instructions. An already implemented parallelization, which performs different matrix multiplications in parallel on different CPU cores, can be used in addition to the GPU parallelization. Using the improved relaxation calculations for this project as an example, a speedup factor of 3.2 was achieved compared to the same calculations using CPU parallelization only.
The modified MCDTH version was then used to determine ICD rates in a linear configuration with two photon acceptors and one photon emitter at different distances. For this purpose, an improved block relaxation was first performed to determine the initial state $B_0 A^* B_0$ and then this state was propagated using the Hamiltonian of Eq. (3.4). Due to the 2-dimensional potential, two degenerate initial states are available, both providing the same ICD rate. The distance dependence of the ICD rate in Eq. (3.3) was removed by multiplying by R^6, revealing that the ICD rate in the three quantum dot arrangement is twice as fast as in an arrangement with only two quantum dots, i.e., with only one photon acceptor. Furthermore, in this two-dimensional case, the already mentioned distance-dependent oscillations in the rates are significantly lower than in the one-dimensional reference case considered in [52].
Unlike the one-dimensional case in previous works, angles between quantum dots other than 180° are possible in this system and have also been considered. In such cases, the two excited states in the middle quantum dot are no longer degenerate and yield different ICD rates. Nevertheless, it could be shown that with an equal superposition of both excited states as initial state almost the same ICD rate as in the linear case is obtained. All results thus indicate that in an arrangement with a central photon emitter and N photon acceptors arranged in an enclosing circle, N times the ICD rate of a corresponding two quantum dot system is obtained. This behavior has already been shown for atomic systems by Öhrwall *et al.*[41]

Dynamics with two photon emitters and one photon acceptor

In the second setup investigated in this thesis, which has a photon acceptor between two photon emitters (Fig. 3.1, right panel), the determination of ICD rates is much more complicated than in the previously studied system because more states are involved and a number of processes can occur simultaneously. It is possible that an ICD process starts from a singly-excited resonance (SE) as well as from a doubly-excited resonance (DE). A single excitation can be followed by ICD through ionization of the photon acceptor quantum dot (SE-ICD) or by energy transfer between the photon emitters (SE-ET). Using an initial state in which both photon emitters are excited, i.e. a doubly-excited resonance, even three competing ICD processes are possible. The photon acceptor can be ionized by the energy from the de-excitation of one photon emitter (DE-ICD) as well as by the energy from the simultaneous de-excitation of both photon emitters (DE-CICD). In addition, ionization of one excited photon emitter is possible by the energy of the second photon emitter (DE-exICD). To determine the influence of these individual processes on the total decay of the initial state, rates of two-electron ICD processes can be used additionally. Rates between one excited photon emitter and one photon acceptor (2e-ICD) as well as for two excited photon emitters (2e-exICD) are considered. The third empty quantum dot is either left unoccupied or removed, which can lead to different observations in each case. All these possible processes are summarized in Fig. 3.2.
Also in this work, analytical rate equations for all processes were derived using the Wigner-Weisskopf theory. For the ICD rates that refer to processes in which the central quantum dot is ionized via virtual photon transfer from one photon emitter (SE-ICD, DE-ICD, and 2e-ICD) a proportionality with R_{AB}^{-6} was derived, where SE-ICD and DE-ICD should be twice as fast as 2e-ICD. The DE-exICD and 2e-exICD processes, in which a photon emitter quantum dot is ionized, show an R_{AA}^{-6} dependence. However, since the AA distance is twice as large as the AB distance, the rates also tend to be lower. Again, it was derived that the rate in the three-electron case DE-exICD should be twice that of the two-electron case 2e-exICD. Proportionality to R_{AA}^{-6} was also determined for the energy transfer SE-ET. To determine the rate for the DE-CICD process, it is decomposed into two two-electron subprocesses, which finally yields a proportionality with R_{AB}^{-12}.[114,115] Thus, the rate for DE-CICD decreases much faster with quantum dot distance than all others.
After analytical consideration, decay rates were numerically determined for the SE, and DE resonances as well as for the two two-electron states mentioned above at different distances between the quantum dots. It was found that several properties lead to deviations from the predicted rates. For distances in the interval $R_{AB} = [14, 31]$ a.u. the distance dependence

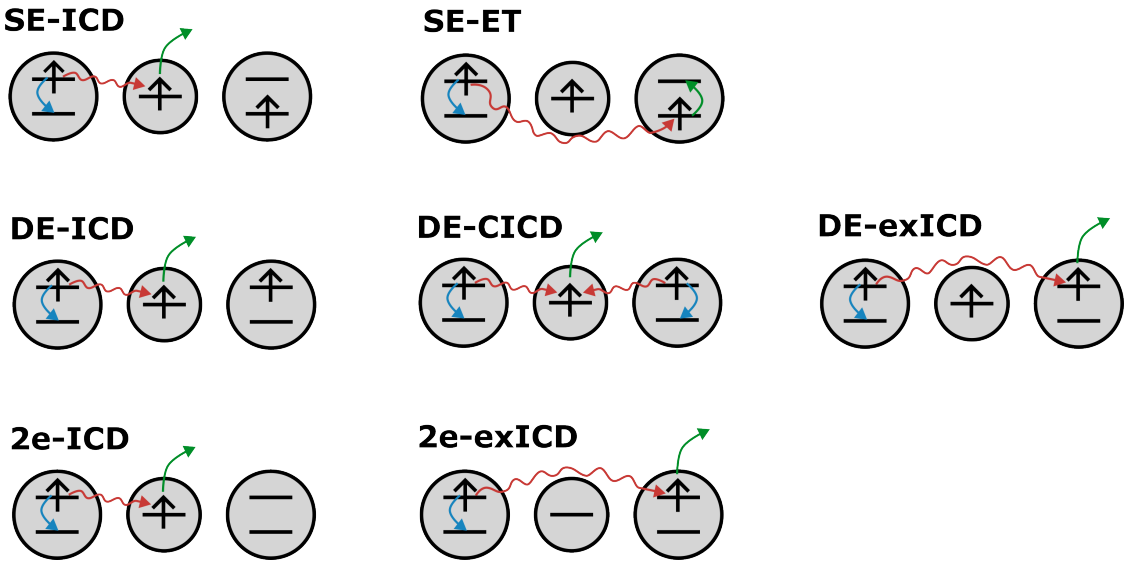

Figure 3.2: Possible electronic dynamics processes with one photon acceptor between two photon emitter quantum dots. All processes involving three electrons start with either one (SE) or both (DE) photon emitters excited. The processes are either an energy transfer (ET) or ICD process, separately referred to as exICD when one photon emitter quantum dot itself is ionized and as CICD when the energy of two photon emitters is required for ionization. Blue arrows symbolize the de-excitation of an electron, green arrows symbolize the excitation or ionization of an electron, and red arrows symbolize energy transfer via a virtual photon.

derived from the Wigner-Weisskopf theory with R_{AB}^{-6} was observed in the decay rates of both three electron resonances. As in the previous system the distance dependence is largely affected by oscillations. Outliers at larger distances can be attributed to numerical instabilities, while deviations at smaller distances were traced back to various physical effects, arising, for example, from the electron delocalization over several QDs. Moreover, it was shown for the two-electron processes 2e-ICD and 2e-exICD that an additional quantum dot, even if unoccupied, can both accelerate and slow down decay rates for various reasons, especially at small quantum dot distances.

It is particularly notable that the ICD rates in three electron calculations are not twice as large as the corresponding two electron rates but are several orders of magnitude smaller. A crucial reason for this is that in the three-electron case, the ICD electron is "trapped" between the Coulomb potentials of the remaining electrons and has to tunnel through the Coulomb barrier, which slows down the decay. An exception to this trend was found in the decay of the DE resonance at a distance of $R_{AB} \approx 25$ a.u., where a so-called shape-resonance-enhanced decay occurred. For the analysis, not only decay rates

were considered but also time-dependent populations, as they can only be determined by explicitly time-dependent methods. In the case of the dynamics of SE resonances, the distance dependence of the ET process could be observed, which became visible, especially at larger distances, and showed an R_{AB}^{-3} dependence contrary to the original prediction.

3.2 Development of a new program for simulation and novel analysis of electron dynamics

The largest project of this dissertation deals with the development of a new dynamics program for the TD-CI method. Unlike popular electronic structure methods or the MCTDH method originally developed for nuclear quantum dynamics, previous TD-CI implementations are limited in scope to the specific applications of the developers. Moreover, these programs usually cover only a small part of the workflow required for a TD-CI calculation, which makes the use of various programs for preparation and analysis calculations necessary.

To combine simulation and analysis in a single program suite with a graphical interface *Jellyfish* was developed and presented in paper **[3]**. In this process, new analysis methods for time-dependent wave functions, presented in **[4]** and discussed later in this section, were also developed and implemented. The goal was a universal and simple-to-use dynamics program.

In detail, this resulted in five requirements for *Jellyfish*. First of all, it should be possible to combine small partial calculations into individual calculations by means of a *flexible* approach in order to allow broad use of the program. These successive partial calculations should be *interactive*, step-by-step executable, in order to be able to use previous steps to adapt later ones. All of this should be as *user-friendly* and *efficient* as possible regarding computing time. In addition, the program should be easily *expandable* with new partial calculations.

In order to fulfill all these requirements, the approach of *dataflow programming* was used. Individual partial calculations are developed as self-contained modules that can be instantiated as nodes and combined to form a directed graph, also referred to as a network. The nodes in such a network can now be computed one by one with each node passing on its results to the connected nodes as input. Creating and working with such graphs does not necessarily require a graphical user interface, however, this has been developed for *Jellyfish* to simplify the process. The complete user interface with a network for a complete TD-CI calculation is shown in Fig. 3.3.

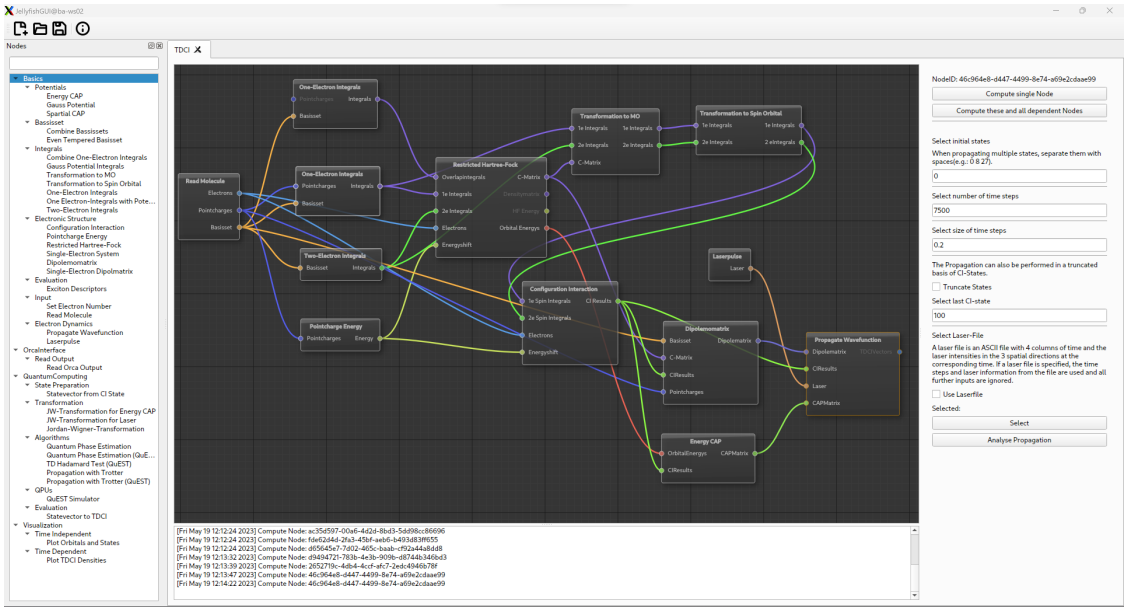

Figure 3.3: Screenshot of the *JellyfishGUI* main window. In the center is the NodeEditor where individual partial calculations in the form of nodes can be combined into a network for various applications. The modules that are available for this are listed on the left and can be added by drag and drop. After selecting a module in the NodeEditor, method-specific settings can be made on the right side. Via the menu bar in the upper area, new files can be created as well as project files be loaded and saved. The log for the project is displayed in the lower area.

The editor for modifying the network is located in the center of the user interface above the program log. After selecting a node in the network, module-dependent parameters can be set or functions executed on the right-hand side. The executable functions can range from the calculation of the node, such as the dipole moment, through supporting functions such as the optimization of a laser pulse, to the opening of own programs such as the visualization of electron densities. The left area contains a list of all available modules and allows to add them to the network. Modules are sorted into categories in the list for a better overview and are subdivided into so-called plugins ("Basics", "Orcainterface",...) in an instance above. The plugins are mainly relevant for the development of new code. These are files that can add functionalities to a program after it has been compiled. In the case of *Jellyfish*, several modules are compiled into such a plugin, and the resulting library file is then loaded by the program. Thus, for the development of new modules, it is not necessary to modify or recompile the existing code.
Plugins can thus be developed completely independently and exchanged between users. Besides *JellyfishGUI* the *Jellyfish* version with graphical user interface, *JellyfishCMD* was

developed as a command line version for use on remote systems such as HPC systems. *JellyfishCMD* uses the same plugins without additional modifications and can load and save *Jellyfish* files (.jlf) created with *JellyfishGUI* and perform the calculations in the files. Together with the program, four plugins were developed and published on GitHub at `https://github.com/FabianLangkabel/Jellyfish`. The first plugin "Basics" contains methods to perform the complete workflow of standard TD-CI calculations. For molecules, structures can be loaded, basis sets based on Gauss type orbitals (GTO) such as standard basis sets from Basis Set Exchange[116] can be read in, or even-tempered basis sets can be generated and all subsequently required integrals with respect to the molecular Hamiltonian can be calculated. Building on the integrals, a restricted Hartree-Fock calculation can be performed with further modules from the plugin. Subsequent transformation of the integrals into molecular and spin orbitals finally allows the execution of a time-independent CI calculation. For the resulting CI states, (transition) dipole moments or so-called exciton properties can be calculated by further modules. Thus, starting from a molecular structure, all preparatory steps necessary for a TD-CI calculation can be performed.
For the TD-CI calculation itself, a propagator module is available which uses the split operator method and other technical optimizations such as parallelization or the restriction of the CI space for efficient propagation. The same module can be used to extract and export properties such as state populations from the time-dependent wave function. The time-dependent Hamiltonian can be flexibly composed with different modules, with additional modules available for the CAP operators and laser potentials shown in section 2.3.2. In addition to the operators appearing in molecules, model potentials such as electron binding potentials can also be added to the Hamiltonian.
Although it is possible to perform electronic structure calculations with *Jellyfish* to enable the whole TD-CI workflow in one program, it was never the goal to compete in coverage and efficiency with established programs in that area. Instead, an interface to the electronic structure program ORCA was developed. This "ORCA Interface" plugin reads the "Molecular structure, basis set definition, MO coefficients, and CI coefficients" from an output of a CIS or linear response time-dependent density functional theory (LR-TDDFT) calculation.
The third plugin contains modules for the propagation of a wave function on quantum computers (simulators) as well as methods for the preparatory steps and subsequent analysis. Methods for simulation of electron dynamics, which are possible with this plugin, are discussed in detail in section 3.3 and paper **[5]** of this thesis.
The last plugin "Visualization" focuses on the visualization of properties of the time-independent and time-dependent CI wave functions. The goal was to transfer the analyses

of orbitals and densities, which are traditionally used on stationary wave functions, to the explicitly time-dependent domain and to extend them for this purpose. This topic will be discussed in more detail later in this section. The visualization was directly integrated into the *JellyfishGUI*. The routines for the calculation of the orbitals and densities on a three-dimensional grid were optimized to such an extent that it is possible, even for large molecules, to inspect orbitals and densities "on the fly" in a time-independent and time-dependent manner. This is made possible, among other things, by truncating the basis functions at a certain radius and precomputing all basis functions in their local area. These "local areas" can then be added up much faster on the final grid, compared to evaluating each basis function at each grid point.
The possibilities of *Jellyfish* were demonstrated with different examples. One of them shows the application of electron dynamics in inverse Gaussian model potentials, as presented in the previous section, for the modeling of quantum dots. Unlike the grid basis sets used in MCTDH, three-dimensional GTO-based basis sets were used here. The process considered in the example was a laser-driven ionization process and not an ICD process, but the Hamiltonian was composed of the same terms including a similar CAP (cf. section 2.3.2). Thus, it could be shown that *Jellyfish* already offers the technical possibilities to be used also in such model systems and not exclusively in molecular systems as in the following examples.
In the molecular examples shown, the main focus was on the newly developed possibilities for visualizing and analyzing the properties of excitons upon laser excitation. The starting point for the calculation of the exciton properties is an exciton wave function, which for time-independent considerations, is composed of the initial ground state ψ_0 and the target state ψ_f as

$$\chi_{exc}(\vec{r}_h, \vec{r}_e, t) = \int ... \int \psi_0(\vec{r}_h, \vec{r}_2, ..., \vec{r}_N) \cdot \psi_f(\vec{r}_e, \vec{r}_2, ..., \vec{r}_N) dr_2, ..., dr_N. \tag{3.5}$$

By using eigenstates as initial and final states and considering only CI singles wave functions, the exciton wave function is a single-particle wave function that can be written in the basis of spin orbitals as the one-particle transition density matrix (1PTDM) shown in Eq. (2.48). If the target state is now exchanged for the time-dependent wave function $\Psi(t)$ in a time-dependent expansion, the "1PTDM" is obtained as

$$\gamma_{\mu\nu}^{t0} = \langle \Psi(t) | \hat{a}_\mu^\dagger \hat{a}_\nu | \psi_0 \rangle. \tag{3.6}$$

In contrast to the time-independent case, however, $\Psi(t)$ is not orthogonal to the initial state, which means that the exciton wave function is no longer a one-particle wave function. To restore this picture, the non-orthogonal part was projected out $(1 - |\psi_0\rangle\langle\psi_0|)\,|\Psi(t)\rangle$. A singular value decomposition of the 1PTDM after the projection

$$\boldsymbol{\gamma}^{0t}(t) = \boldsymbol{U}(t)\boldsymbol{\Sigma}\boldsymbol{V}^T(t) \tag{3.7}$$

leads to a new set of spin orbitals with which the exciton wave function can be written as

$$\chi_{exc}(\vec{r}_h, \vec{r}_e, t) = \sum_K \sigma_K(t)\psi_K^h(\vec{r}_h, t)\psi_K^e(\vec{r}_e, t). \tag{3.8}$$

The $\psi_K^h(\vec{r}_h, t)$ and $\psi_K^e(\vec{r}_e, t)$ orbitals are called natural transition orbitals (NTOs) and are divided into hole and particle orbitals. Here, $\sigma_K(t)$ corresponds to the occupation of the corresponding orbitals. However, in the time-dependent view, the wave function was not normalized after the ground state was projected out, and therefore also NTO densities like the NTO hole density

$$\rho_h^{NTO}(\vec{r}_h, t) = \sum_K \sigma_K(t)^2\psi_K^h(\vec{r}_h, t)^2 \tag{3.9}$$

are also no longer normalized. At the beginning of a propagation in the initial state, the norm of the exciton wave function is zero, so there is no hole and particle. As the excitation progresses during laser irradiation, the norm of the exciton wave function increases and the formation of the hole and the particle can be observed. In order to not only visualize NTO holes and particles but also quantify their properties, various exciton descriptors defined among others by Dreuw and coworker[61] were transferred to the time-dependent domain.

In addition to the analysis of the 1PTDM, electron densities and the difference in electron density between the initial state and the time-dependent wave function, $\Delta\rho_{t0}(\vec{r}) = \rho(t, \vec{r}) - \rho_0(\vec{r})$, were also considered. While these densities can also provide information on hole and particle shape, they can additionally be determined for truncation levels other than TD-CIS. Furthermore, the difference densities between a time step and the previous time step were analyzed. This gradient density, $\Delta\rho_t(\vec{r}) = \rho(t, \vec{r}) - \rho(t - \Delta t, \vec{r})$, shows the "electron flow" between the time steps.

The new tools were first used to benchmark and gain new insights into already well-studied laser excitations in the hydrogen and lithium cyanide molecules.[4] For the hydrogen molecule, the excitation from the ground state to the first excited singlet state, and for lithium cyanide, an excitation to a charge-transfer state were studied. Excitations with a weak long as well as an intense short π pulse were performed for both molecules. In the case of weak pulses, the target states were almost completely populated, while in the case of short pulses, a large number of excited states were populated by the intense laser, generating electronic wave packets. For lithium cyanide, the exciton descriptors, laser field intensity, and dipole moment along the bond axis determined in this process are shown in Fig. 3.4, left for the long laser pulse and right for the short laser pulse.

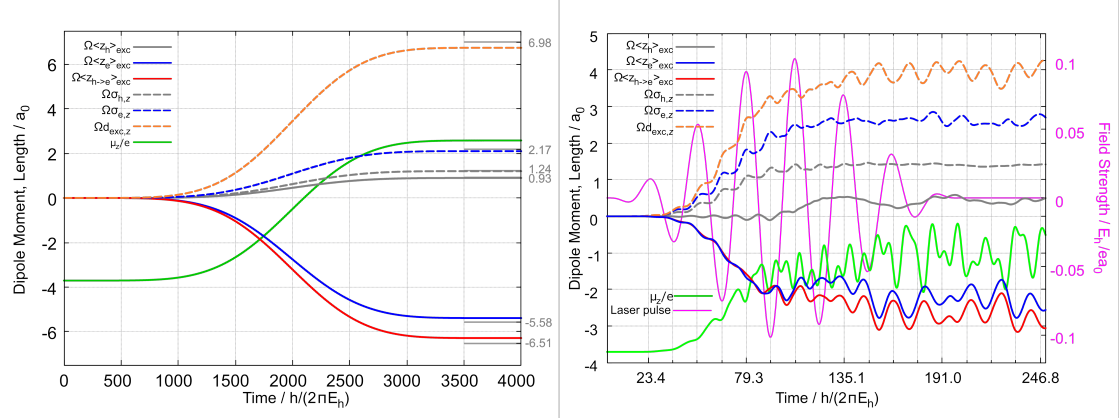

Figure 3.4: Summary of LiCN excitation dynamics with a long, weak (left) and a short, intense (right) π pulse. In both, different exciton descriptors such as the hole-particle distance $\Omega\langle z_{h\to e}\rangle_{exc}$ as well as the time-dependent dipole moment μ_z along the molecular bonds (z direction) are shown. For the long laser pulse excitation, the exciton descriptor values for a complete state-to-state transition to the target state are additionally plotted in gray on the right-hand side. For the intense laser pulse, the field strength is shown in pink. Figure adapted from **[4]**.

In the case of a long-pulse excitation, the smooth formation of an exciton by the descriptors, newly introduced in **[4]** with abbreviations, can be observed. While the hole position $\Omega\langle z_h\rangle_{exc}$ is aligned on the positive side along the z axis parallel to the C-N bond and thus on the cyanide group, the corresponding particle position $\Omega\langle z_e\rangle_{exc}$ localizes more and more on the negative side along the z axis on the lithium atom. In particular, the distance between particle and hole, $\Omega\langle z_{h\to e}\rangle_{exc}$, reflects this separation, which constitutes a charge-transfer process. The displacement of the electron can also be seen in the dipole moment change μ_z which increases from -3.7 a.u. to 2.7 a.u. From the size of hole $\Omega\sigma_{h,z}$ and particle $\Omega\sigma_{e,z}$, it can be seen that the hole is much more localized than the particle.

For the short pulses, the participation of several states leads to much more complex dynamics. Again, the hole $\Omega\langle z_h\rangle_{exc}$ and the particle position $\Omega\langle z_e\rangle_{exc}$ as well as the distance between the two $\Omega\langle z_{h\to e}\rangle_{exc}$ show that a separation of the hole and particle occurs along the molecular axis. However, the distance between the hole and the particle is shorter than in the case of the long laser pulse. The oscillations in the hole position and size are relatively small, the hole is therefore quite stationary. The electron can move much more freely in the significantly more delocalized valence orbitals, which is reflected in the larger oscillations of the position and size of the electron. It should also be noted that in cases where an electronic wave packet has been generated, these dynamics continue after the end of the laser pulse ($t = 200$ a.u.).
Similar dynamics were obtained for the excitation in the hydrogen molecule with the difference that for the selected target state, a π^* state on the H-H bond, hole, and particle are not separated and spatially overlap.
Most of these discussed properties can also be qualitatively concluded by plotting the electron and NTO densities. In this application *Jellyfish* is not limited to small molecules but also allows visualization of larger molecules such as the nucleobase guanine, which is discussed in the submitted publication **[3]** of this thesis. In this context, Fig. 3.5 shows snapshots of the difference density Δ_0, the density gradient Δ_t, and the NTO densities ρ_h^{NTO} and ρ_e^{NTO} for a nearly complete π-pulse excitation from the ground state to the first excited state. The zero crossing $t = 1000$ a.u., the minimum $t = 992$ a.u., and maximum $t = 1008$ a.u. of the central laser cycle as well as the last time step $t = 2000$ a.u. were chosen as time points for the snapshots.
Comparing the NTO densities of all time steps with each other, the hole and particle formation can be seen with the growth of the corresponding densities. Even in the central and thus most intense laser cycle, the laser is relatively weak and the changes within the periode of one cycle are small. Both hole and particle are delocalized over almost the entire molecule in this excitation and no separation is seen. The density difference also includes the shape of the particle and hole, although this is much more difficult to identify due to their overlap. As a result of resonant excitation, the density difference is displaced by the laser field, with the displacement being maximum at the zero crossings of the laser intensity as in $t = 1000$ a.u. While the deflection of the density lags behind the laser intensity in time, the density gradient reflects the change in only one time step and becomes largest when the laser intensity is also at an extreme point, as is the case for $t = 992$ a.u. and $t = 1008$ a.u.

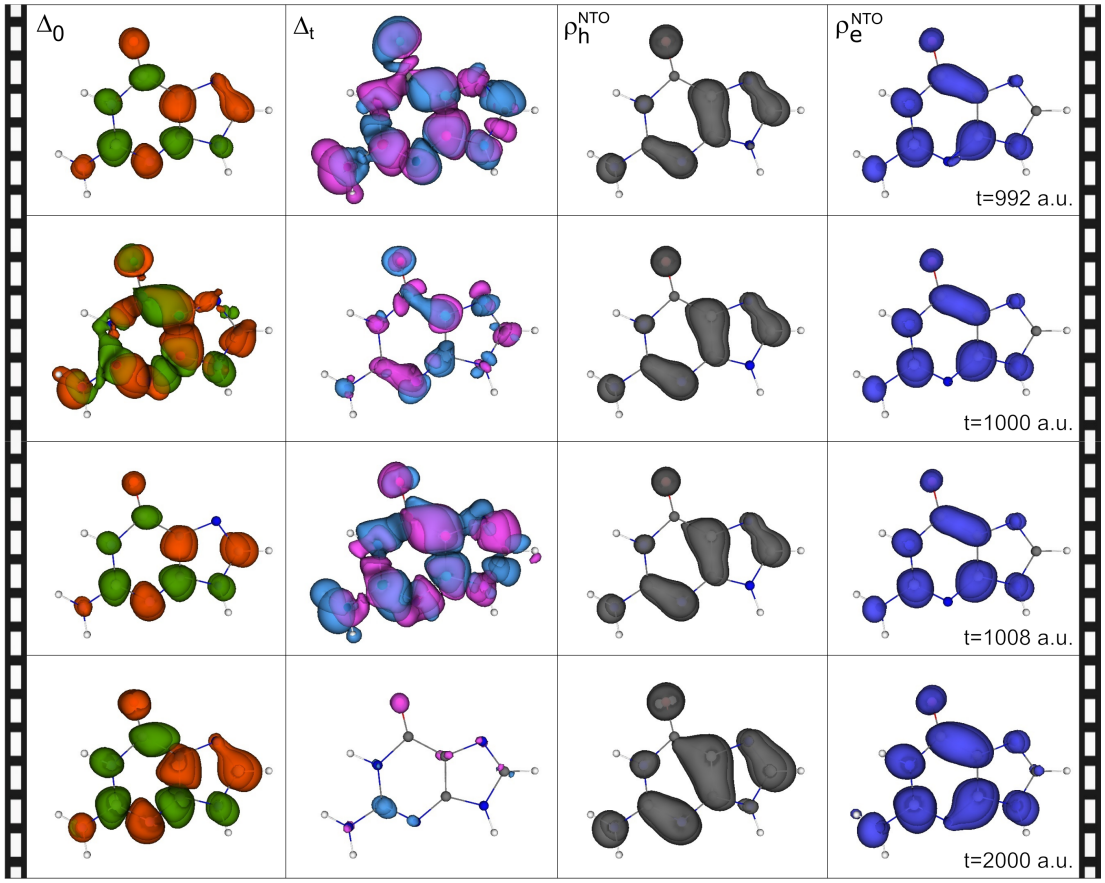

Figure 3.5: Visualization of the excitation dynamics of guanine using a resonant π-pulse. The first column shows the difference density between the time-dependent electron density and the ground state density. The second column shows the gradient density, which corresponds to the difference density with respect to the previous time step. The NTO hole densities and NTO particle density are shown in the third and fourth columns. Figure adapted from **[3]**.

3.3 Quantum compute algorithm for electron dynamics

In the third project, covered in the paper **[5]**, the goal was to develop a quantum algorithm for the electron dynamics processes shown previously, the implementation of the algorithm in a *Jellyfish* plugin, and the application of the algorithm for the computation of laser-driven dynamics in molecules. The three steps that have to be transferred from dynamics methods for traditional computers to quantum computing are the preparation of an initial state, the propagation of this state with time-dependent Hamiltonians, and the following extraction of information and properties from the wave function.

The focus of this work was mainly on the propagation and extraction of properties,

rather than the state preparation of an initial state. Therefore the ground state of a FCI calculation from "traditional" quantum chemistry was used as an initial state. Since the quantum computer was only simulated, the ground state could be directly transferred to the qubits as an initial state by using the Jordan-Wigner transformation (cf. section 2.4.2), and the use of a state preparation algorithm could be omitted. Here, each spin orbital is mapped to a qubit after transforming basis functions to molecular orbitals. For real quantum computers, for example, the QITE algorithm presented in section 2.4.3 can be used to prepare the ground state starting from the Hartree-Fock-Slater determinant.
For the Hamilton simulation used for the propagation, the Lie-Trotter-Suzuki decomposition (cf. section 2.4.3) was employed. The total propagation time was decomposed into small time steps with a time-independent Hamiltonian for each time step. Subsequently, the Hamiltonian was decomposed into its individual terms $\hat{h}_j$ using the Trotter-Suzuki decomposition, and the resulting propagators $e^{-i\hat{h}_j\Delta t}$ were translated into quantum gates. While this translation of Hermitian propagator terms is possible directly with the Trotter decomposition and thus propagations with molecular Hamiltonians and laser fields can be performed, this is not the case for non-Hermitian operators. In such cases, the propagator terms do not represent unitary transformations. The problem occurs, for example, when a CAP operator (cf. section 2.3.2) is used to simulate ionization processes. For propagations in imaginary time, where the same problem was already studied in detail,[111] the QITE algorithm from section 2.4.3 was developed, which can also be used for the non-Hermitian CAP operators in real-time evolutions.
Apart from the errors of the time decomposition and the Lie-Trotter-Suzuki decomposition, the Hamilton evolution is exact in the underlying basis and therefore on the same level as a TD-FCI calculation. Accordingly, reading and storing the quantum computer wave function on a traditional computer is not useful and in most cases impossible, since this wave function, like the FCI wave function, is also composed of exponentially many configurations. However, as shown in the examples in the previous chapter, it is not necessary either. Instead, properties like exciton descriptors or the time-dependent dipole moment can be read out. For this purpose, the Hadamard test algorithm introduced in section 2.4.3 was used to determine the dipole moment as the expectation value of the dipole operator from Eq. (2.45) after each time step. However, the dipole operator is not unitary as it is necessary for the Hadamard test. Therefore, the operator

$$\hat{U} = e^{-i\hat{\mu}\Delta x} \tag{3.10}$$

was used instead in the Hadamard test. From the expectation value of $\hat{U}$ the dipole moment can be obtained. Since the dipole moment is real, it is sufficient to determine the real part or the imaginary part of the eigenvalue to $\hat{U}$. The translation of $\hat{U}$ into quantum gates is similar to the translation of the propagator for a time step, where Δx is a multiplicative factor chosen to minimize the error of the Trotter decomposition.
All these partial algorithms can now be combined into a complete algorithm. Starting from state $|\bar{0}\rangle$ the initial state is prepared and propagated to the time step for the measurement of the dipole moment and then the Hadamard test is performed. To get the expectation value of the dipole moment, the whole algorithm has to be repeated several times. For the propagation, all non-Hermitian terms are replaced by Hermitian terms using the QITE algorithm. In order to obtain the time-dependent dipole moment for different time points, the entire algorithm has to be repeated for different propagation durations as well. Although the Hadamard test and QITE algorithms require many measurements, they can scale polynomially and thus offer advantages on a true error-free quantum computer over exponentially scaling FCI algorithms for traditional computers.
Modules for the preparation of a CI state, the Jordan-Wigner transformation of time-independent and time-dependent operators, as well as propagation with and without Hermitian operators combined with the Hadamard test have been implemented in a *Jellyfish* plugin along with tools for the extraction and evaluation of data such as states. For the simulation of quantum algorithms, a quantum computer simulator directly embedded in the plugin can be used.
The functionality of the algorithm was demonstrated for several examples against a TD-FCI reference. In the first examples, similar to the previous section, laser-driven state-to-state transition and the creation of an electronic wave packet in molecules were performed. For this purpose, hydrogen and lithium hydride were chosen.
For the generation of a wave packet with a short π-pulse in lithium hydride, the upper panel of Fig. 3.6 shows the populations of the states with the highest populations using the quantum algorithm (dashed) and TD-FCI (solid). In the lower panel of the same figure, the laser pulse used and the time-dependent dipole moment determined with the Hadamard test (purple) and TD-FCI (red) are shown.
It should be noted that the populations were read directly from the quantum computer simulator without modifying the state, which is impossible for real quantum computers. The populations show that the dynamics can be reproduced almost exactly by the quantum algorithm with a proper choice of parameters. The dipole moment could also be satisfactorily reproduced. For the decomposition in time steps, a fixed time step size of 0.2 a.u. was used and for the determination of the dipole moment, the Hadamard test was

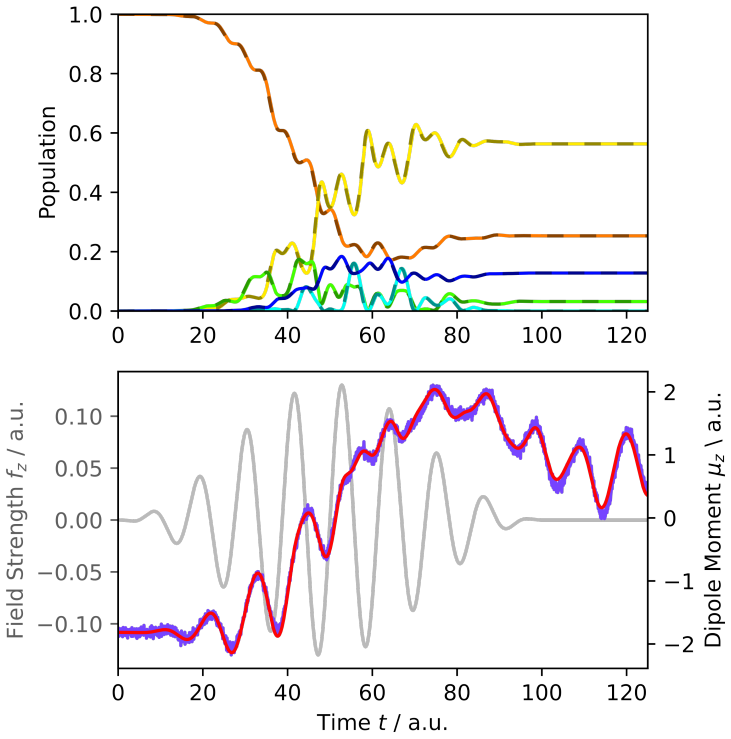

Figure 3.6: Comparison of simulations of the laser excitation of LiH by a short π pulse between the TF-FCI method and the quantum algorithm presented. In the upper panel the populations $P_i(t)$ of the most relevant states are shown (TD-CI populations with solid lines and quantum algorithm populations in dashed lines). In the lower panel, both the laser pulse (gray) and the determined time-dependent dipole moment (red for TD-CI and blue for the quantum algorithm) are shown. Figure adapted from **[5]**

repeated 20000 times at each time step. For Δx in Eq. (3.10) a value of 0.2 was chosen. In addition to examples with Hermitian operators, the algorithm was also demonstrated for laser-driven ionization dynamics in a hydrogen molecule that includes a CAP operator. Again, the dynamics of TD-FCI could be reproduced almost exactly, as shown by equal time-dependent populations and the time-dependent norm.

3.4 Overall conclusion

Although some of the projects presented were fundamentally different in the methods used, systems considered, and goals, each project contributed to expanding the capabilities of electron dynamics methods. Electron dynamics is increasingly attracting the interest of experimentalists and theorists, as new technologies provide more and more insights into

these processes and the processes themselves become more and more relevant for current and future technologies such as nanotechnology or quantum computing.
With the publications **[1, 2]** of this thesis, new details about the ICD process in quantum dots were presented which can help, for example, to design better quantum dot qubits. On the other hand, a GPU implementation of the existing MCTDH code was developed, allowing more complex computations with more electrons and a higher dimensionality than before.
In papers **[3, 4]**, the TD-CI program *Jellyfish*, newly developed in this work, was presented. *Jellyfish* allows the simulation of many-electron dynamics processes, such as laser excitations in molecules, and is more comprehensive, user-friendly, and, most importantly, easier to extend than previous programs in this field. Here, not only a platform for the actual propagation but also novel analysis tools for time-dependent excited states were created that even allow to visualize the processes.
In the last publication of this thesis **[5]**, it was shown how quantum computers can be used in the future for such electron dynamics simulations using a new quantum algorithm which was also implemented in *Jellyfish*. With the advancing development in quantum computing and the newly developed algorithm, electron dynamics simulations with molecular sizes and accuracies beyond the reach of traditional computers may be possible in the future.

4 Bibliography

[1] F. Langkabel, A. Bande, *The Journal of Chemical Physics* **2021**, *154*, 054111.

[2] J.-L. Schäfer, F. Langkabel, A. Bande, *Molecules* **2022**, *27*, 8713.

[3] F. Langkabel, P. Krause, A. Bande, *submitted*.

[4] F. Langkabel, P. A. Albrecht, A. Bande, P. Krause, *Chemical Physics* **2022**, *557*, 111502.

[5] F. Langkabel, A. Bande, *Journal of Chemical Theory and Computation* **2022**, *18*, 7082–7092.

[6] G. Palermo, M. D. Vivo in *Encyclopedia of Nanotechnology*, Drug Design, Springer Netherlands, **2015**, pp. 1–15.

[7] G. Sliwoski, S. Kothiwale, J. Meiler, E. W. Lowe, *Pharmacological Reviews* **2013**, *66*, 334–395.

[8] D. Gao, Y. Zhang, Z. Zhou, F. Cai, X. Zhao, W. Huang, Y. Li, J. Zhu, P. Liu, F. Yang, G. Wang, X. Bao, *Journal of the American Chemical Society* **2017**, *139*, 5652–5655.

[9] J. Ko, B.-K. Kim, J. W. Han, *The Journal of Physical Chemistry C* **2016**, *120*, 3438–3447.

[10] X. Diao, Y. Diao, Y. Tang, G. Zhao, Q. Gu, Y. Xie, Y. Shi, P. Zhu, L. Zhang, *Scientific Reports* **2022**, *12*, 12633.

[11] J. Shi, S. Yun in *Counter Electrodes for Dye-sensitized and Perovskite Solar Cells*, Wiley-VCH Verlag GmbH & Co. KGaA, **2018**, pp. 487–509.

[12] D. Muñoz, F. Illas, I. de P. R. Moreira, *Physical Review Letters* **2000**, *84*, 1579–1582.

[13] Z.-H. Cui, H. Zhai, X. Zhang, G. K.-L. Chan, *Science* **2022**, *377*, 1192–1198.

[14] R. Mirzoyan, R. G. Hadt, *Physical Chemistry Chemical Physics* **2020**, *22*, 11249–11265.

[15] A. D. Paolo, T. E. Baker, A. Foley, D. Sénéchal, A. Blais, *npj Quantum Information* **2021**, *7*, 11.

[16] D. Buterakos, S. D. Sarma, *PRX Quantum* **2021**, *2*, 040358.

[17] R. Borrego-Varillas, M. Lucchini, M. Nisoli, *Reports on Progress in Physics* **2022**, *85*, 066401.

[18] P. Krause, J. C. Tremblay, A. Bande, *The Journal of Physical Chemistry A* **2021**, *125*, 4793–4804.

[19] F. Bedurke, T. Klamroth, P. Krause, P. Saalfrank, *The Journal of Chemical Physics* **2019**, *150*, 234114.

[20] E. Luppi, E. Coccia, *Physical Chemistry Chemical Physics* **2021**, *23*, 3729–3738.

[21] S. Klinkusch, P. Saalfrank, T. Klamroth, *The Journal of Chemical Physics* **2009**, *131*, 114304.

[22] A. F. White, C. J. Heide, P. Saalfrank, M. Head-Gordon, E. Luppi, *Molecular Physics* **2015**, *114*, 947–956.

[23] F. Weber, J. C. Tremblay, A. Bande, *The Journal of Physical Chemistry C* **2020**, *124*, 26688–26698.

[24] P. Auger, *Journal de Physique et le Radium* **1925**, *6*, 205–208.

[25] L. S. Cederbaum, J. Zobeley, F. Tarantelli, *Physical Review Letters* **1997**, *79*, 4778–4781.

[26] S. Marburger, O. Kugeler, U. Hergenhahn, T. Möller, *Physical Review Letters* **2003**, *90*, 203401.

[27] T. Jahnke, A. Czasch, M. S. Schöffler, S. Schössler, A. Knapp, M. Käsz, J. Titze, C. Wimmer, K. Kreidi, R. E. Grisenti, A. Staudte, O. Jagutzki, U. Hergenhahn, H. Schmidt-Böcking, R. Dörner, *Physical Review Letters* **2004**, *93*, 163401.

[28] E. F. Aziz, N. Ottosson, M. Faubel, I. V. Hertel, B. Winter, *Nature* **2008**, *455*, 89–91.

[29] T. Jahnke, H. Sann, T. Havermeier, K. Kreidi, C. Stuck, M. Meckel, M. Schöffler, N. Neumann, R. Wallauer, S. Voss, A. Czasch, O. Jagutzki, A. Malakzadeh, F. Afaneh, T. Weber, H. Schmidt-Böcking, R. Dörner, *Nature Physics* **2010**, *6*, 139–142.

[30] J. Zobeley, R. Santra, L. S. Cederbaum, *The Journal of Chemical Physics* **2001**, *115*, 5076–5088.

[31] M. Hoener, D. Rolles, A. Aguilar, R. C. Bilodeau, D. Esteves, P. O. Velasco, Z. D. Pešić, E. Red, N. Berrah, *Physical Review A* **2010**, *81*, 021201.

[32] J. Titze, M. S. Schöffler, H.-K. Kim, F. Trinter, M. Waitz, J. Voigtsberger, N. Neumann, B. Ulrich, K. Kreidi, R. Wallauer, M. Odenweller, T. Havermeier, S. Schössler, M. Meckel, L. Foucar, T. Jahnke, A. Czasch, L. P. H. Schmidt, O. Jagutzki, R. E. Grisenti, H. Schmidt-Böcking, H. J. Lüdde, R. Dörner, *Physical Review Letters* **2011**, *106*, 033201.

[33] H.-K. Kim, H. Gassert, M. S. Schöffler, J. N. Titze, M. Waitz, J. Voigtsberger, F. Trinter, J. Becht, A. Kalinin, N. Neumann, C. Zhou, L. P. H. Schmidt, O. Jagutzki, A. Czasch, H. Merabet, H. Schmidt-Böcking, T. Jahnke, A. Cassimi, R. Dörner, *Physical Review A* **2013**, *88*, 042707.

[34] S. Yan, P. Zhang, X. Ma, S. Xu, B. Li, X. L. Zhu, W. T. Feng, S. F. Zhang, D. M. Zhao, R. T. Zhang, D. L. Guo, H. P. Liu, *Physical Review A* **2013**, *88*, 042712.

[35] K. Gokhberg, L. S. Cederbaum, *Physical Review A* **2010**, *82*, 052707.

[36] F. M. Pont, A. Molle, E. R. Berikaa, S. Bubeck, A. Bande, *Journal of Physics: Condensed Matter* **2019**, *32*, 065302.

[37] P. H. P. Harbach, M. Schneider, S. Faraji, A. Dreuw, *The Journal of Physical Chemistry Letters* **2013**, *4*, 943–949.

[38] J. Matthew, Y. Komninos, *Surface Science* **1975**, *53*, 716–725.

[39] T. D. Thomas, C. Miron, K. Wiesner, P. Morin, T. X. Carroll, L. J. Sæthre, *Physical Review Letters* **2002**, *89*, 223001.

[40] V. Averbukh, I. B. Müller, L. S. Cederbaum, *Physical Review Letters* **2004**, *93*, 263002.

[41] G. Öhrwall, M. Tchaplyguine, M. Lundwall, R. Feifel, H. Bergersen, T. Rander, A. Lindblad, J. Schulz, S. Peredkov, S. Barth, S. Marburger, U. Hergenhahn, S. Svensson, O. Björneholm, *Physical Review Letters* **2004**, *93*, 173401.

[42] T. Miteva, S. Kazandjian, P. Kolorenč, P. Votavová, N. Sisourat, *Physical Review Letters* **2017**, *119*, 083403.

[43] A. I. Ekimov, A. A. Onushchenko, *Soviet Journal of Experimental and Theoretical Physics Letters* **1981**, *34*, 345.

[44] D. Bera, L. Qian, T.-K. Tseng, P. H. Holloway, *Materials* **2010**, *3*, 2260–2345.

[45] P. Dolbundalchok, D. Peláez, E. F. Aziz, A. Bande, *Journal of Computational Chemistry* **2016**, *37*, 2249–2259.

[46] C. Kloeffel, D. Loss, *Annual Review of Condensed Matter Physics* **2013**, *4*, 51–81.

[47] G. Burkard, T. D. Ladd, A. Pan, J. M. Nichol, J. R. Petta, *Reviews of Modern Physics* **2023**, *95*, 025003.

[48] I. Cherkes, N. Moiseyev, *Physical Review B* **2011**, *83*, 113303.

[49] A. Bande, K. Gokhberg, L. S. Cederbaum, *The Journal of Chemical Physics* **2011**, *135*, 144112.

[50] A. Bande, *The Journal of Chemical Physics* **2013**, *138*, 214104.

[51] A. Haller, D. Peláez, A. Bande, *The Journal of Physical Chemistry C* **2019**, *123*, 14754–14765.

[52] F. Langkabel, M. Lützner, A. Bande, *The Journal of Physical Chemistry C* **2019**, *123*, 21757–21762.

[53] V. Guskov, F. Langkabel, M. Berg, A. Bande, *Quarks: Brazilian Electronic Journal of Physics Chemistry and Materials Science* **2020**, *3*, 17–30.

[54] N. Moiseyev, *Physics Reports* **1998**, *302*, 212–293.

[55] F. Neese, F. Wennmohs, U. Becker, C. Riplinger, *The Journal of Chemical Physics* **2020**, *152*, 224108.

[56] D. G. A. Smith, L. A. Burns, A. C. Simmonett, R. M. Parrish, M. C. Schieber, R. Galvelis, P. Kraus, H. Kruse, R. D. Remigio, A. Alenaizan, A. M. James, S. Lehtola, J. P. Misiewicz, M. Scheurer, R. A. Shaw, J. B. Schriber, Y. Xie, Z. L. Glick, D. A. Sirianni, J. S. O'Brien, J. M. Waldrop, A. Kumar, E. G. Hohenstein, B. P. Pritchard, B. R. Brooks, H. F. Schaefer, A. Y. Sokolov, K. Patkowski, A. E. DePrince, U. Bozkaya, R. A. King, F. A. Evangelista, J. M. Turney, T. D. Crawford, C. D. Sherrill, *The Journal of Chemical Physics* **2020**, *152*, 184108.

[57] Q. Sun, T. C. Berkelbach, N. S. Blunt, G. H. Booth, S. Guo, Z. Li, J. Liu, J. D. McClain, E. R. Sayfutyarova, S. Sharma, S. Wouters, G. K.-L. Chan, *WIREs Computational Molecular Science* **2017**, *8*, e1340.

[58] A. V. Luzanov, A. A. Sukhorukov, V. E. Umanskii, *Theoretical and Experimental Chemistry* **1976**, *10*, 354–361.

[59] F. Plasser, M. Wormit, A. Dreuw, *The Journal of Chemical Physics* **2014**, *141*, 024106.

[60] F. Plasser, *ChemPhotoChem* **2019**, *3*, 702–706.

[61] S. A. Mewes, F. Plasser, A. Krylov, A. Dreuw, *Journal of Chemical Theory and Computation* **2018**, *14*, 710–725.

[62] A. I. Krylov, *The Journal of Chemical Physics* **2020**, *153*, 080901.

[63] A. Szabo, N. S. Ostlund, *Modern quantum chemistry, introduction to advanced electronic structure theory*, Dover Publications, **1996**.

[64] S. R. White, *Physical Review Letters* **1992**, *69*, 2863–2866.

[65] R. P. Feynman, *International Journal of Theoretical Physics* **1982**, *21*, 467–488.

[66] F. Arute, K. Arya, R. Babbush, D. Bacon, J. C. Bardin, R. Barends, R. Biswas, S. Boixo, F. G. S. L. Brandao, D. A. Buell, B. Burkett, Y. Chen, Z. Chen, B. Chiaro, R. Collins, W. Courtney, A. Dunsworth, E. Farhi, B. Foxen, A. Fowler, C. Gidney, M. Giustina, R. Graff, K. Guerin, S. Habegger, M. P. Harrigan, M. J. Hartmann, A. Ho, M. Hoffmann, T. Huang, T. S. Humble, S. V. Isakov, E. Jeffrey, Z. Jiang, D. Kafri, K. Kechedzhi, J. Kelly, P. V. Klimov, S. Knysh, A. Korotkov, F. Kostritsa, D. Landhuis, M. Lindmark, E. Lucero, D. Lyakh, S. Mandrà, J. R. McClean, M. McEwen, A. Megrant, X. Mi, K. Michielsen, M. Mohseni, J. Mutus, O. Naaman, M. Neeley, C. Neill, M. Y. Niu, E. Ostby, A. Petukhov, J. C. Platt, C. Quintana, E. G. Rieffel, P. Roushan, N. C. Rubin, D. Sank, K. J. Satzinger, V. Smelyanskiy, K. J. Sung, M. D. Trevithick, A. Vainsencher, B. Villalonga, T. White, Z. J. Yao, P. Yeh, A. Zalcman, H. Neven, J. M. Martinis, *Nature* **2019**, *574*, 505–510.

[67] T. Albash, D. A. Lidar, *Reviews of Modern Physics* **2018**, *90*, 015002.

[68] B. T. Gard, K. R. Motes, J. P. Olson, P. P. Rohde, J. P. Dowling, **2014**, arxiv:1406.6767 [quant–ph].

[69] I. L. C. Michael A. Nielsen, *Quantum Computation and Quantum Information*, Cambridge University Pr., **2010**.

[70] C. J. Ballance, T. P. Harty, N. M. Linke, M. A. Sepiol, D. M. Lucas, *Phys. Rev. Lett.* **2016**, *117*.

[71] S. Bravyi, O. Dial, J. M. Gambetta, D. Gil, Z. Nazario, *Journal of Applied Physics* **2022**, *132*, 160902.

[72] H.-S. Zhong, Y. Li, W. Li, L.-C. Peng, Z.-E. Su, Y. Hu, Y.-M. He, X. Ding, W. Zhang, H. Li, L. Zhang, Z. Wang, L. You, X.-L. Wang, X. Jiang, L. Li, Y.-A. Chen, N.-L. Liu, C.-Y. Lu, J.-W. Pan, *Phys. Rev. Lett* **2018**, *121*.

[73] S. Slussarenko, G. J. Pryde, *Applied Physics Reviews* **2019**, *6*, 041303.

[74] B. M. Terhal, *Reviews of Modern Physics* **2015**, *87*, 307–346.

[75] Google Quantum AI, *Nature* **2023**, *614*, 676–681.

[76] P. Ball, *Nature* **2021**, *599*, 542–542.

[77] D. S. Abrams, S. Lloyd, *Physical Review Letters* **1999**, *83*, 5162–5165.

[78] Y. Cao, J. Romero, J. P. Olson, M. Degroote, P. D. Johnson, M. Kieferová, I. D. Kivlichan, T. Menke, B. Peropadre, N. P. D. Sawaya, S. Sim, L. Veis, A. Aspuru-Guzik, *Chemical Reviews* **2019**, *119*, 10856–10915.

[79] S. McArdle, S. Endo, A. Aspuru-Guzik, S. C. Benjamin, X. Yuan, *Reviews of Modern Physics* **2020**, *92*, 015003.

[80] P. W. Shor, *SIAM Journal on Computing* **1997**, *26*, 1484–1509.

[81] L. K. Grover, *Physical Review Letters* **1997**, *79*, 4709–4712.

[82] D. Solenov, J. Brieler, J. F. Scherrer, *Missouri medicine* **2018**, *115*, 463–467.

[83] Y. Cao, J. Romero, A. Aspuru-Guzik, *IBM Journal of Research and Development* **2018**, *62*, 6:1–6:20.

[84] H. Ma, M. Govoni, G. Galli, *npj Computational Materials* **2020**, *6*, 85.

[85] M. Ying, *Artificial Intelligence* **2010**, *174*, 162–176.

[86] M. Cerezo, A. Arrasmith, R. Babbush, S. C. Benjamin, S. Endo, K. Fujii, J. R. McClean, K. Mitarai, X. Yuan, L. Cincio, P. J. Coles, *Nature Reviews Physics* **2021**, *3*, 625–644.

[87] J. R. McClean, J. Romero, R. Babbush, A. Aspuru-Guzik, *New Journal of Physics* **2016**, *18*, 023023.

[88] J. Lee, D. W. Berry, C. Gidney, W. J. Huggins, J. R. McClean, N. Wiebe, R. Babbush, *PRX Quantum* **2021**, *2*, 030305.

[89] P. Jordan, E. Wigner, *Zeitschrift fuer Physik* **1928**, *47*, 631–651.

[90] H. F. Trotter, *Proceedings of the American Mathematical Society* **1959**, *10*, 545–551.

[91] M. Suzuki, *Communications in Mathematical Physics* **1976**, *51*, 183–190.

[92] D. J. Tannor, *Introduction to Quantum Mechanics, A Time-Dependent Perspective*, University Science Books, **2006**, p. 662.

[93] C. D. Sherrill, H. F. Schaefer in *Advances in Quantum Chemistry*, Elsevier, **1999**, pp. 143–269.

[94] T. D. Crawford, H. F. Schaefer in *Reviews in Computational Chemistry*, John Wiley & Sons, Inc., **2007**, pp. 33–136.

[95] C. C. J. Roothaan, *Reviews of Modern Physics* **1951**, *23*, 69–89.

[96] H.-D. Meyer, F. Gatti, G. A. Worth, *Multidimensional Quantum Dynamics*, Wiley, **2009**.

[97] P. Krause, T. Klamroth, P. Saalfrank, *The Journal of Chemical Physics* **2005**, *123*, 074105.

[98] L. Greenman, P. J. Ho, S. Pabst, E. Kamarchik, D. A. Mazziotti, R. Santra, *Physical Review A* **2010**, *82*, 023406.

[99] A. Castro, M. A. L. Marques, A. Rubio, *The Journal of Chemical Physics* **2004**, *121*, 3425–3433.

[100] J. Muga, J. Palao, B. Navarro, I. Egusquiza, *Physics Reports* **2004**, *395*, 357–426.

[101] P. Krause, J. A. Sonk, H. B. Schlegel, *The Journal of Chemical Physics* **2014**, *140*, 174113.

[102] E. Coccia, R. Assaraf, E. Luppi, J. Toulouse, *The Journal of Chemical Physics* **2017**, *147*, 014106.

[103] S. B. Bravyi, A. Y. Kitaev, *Annals of Physics* **2002**, *298*, 210–226.

[104] A. M. Childs, N. Wiebe, **2012**, arxiv:1202.5822 [quant–ph].

[105] G. H. Low, V. Kliuchnikov, N. Wiebe, **2019**.

[106] D. W. Berry, A. M. Childs, **2009**, arxiv:0910.4157 [quant–ph].

[107] D. W. Berry, A. M. Childs, R. Kothari, **2015**, arxiv:1501.01715 [quant–ph].

[108] G. H. Low, I. L. Chuang, *Quantum* **2019**, *3*, 163.

[109] G. H. Low, T. J. Yoder, I. L. Chuang, *Physical Review X* **2016**, *6*, 041067.

[110] D. Aharonov, V. Jones, Z. Landau, *Algorithmica* **2008**, *55*, 395–421.

[111] M. Motta, C. Sun, A. T. K. Tan, M. J. O'Rourke, E. Ye, A. J. Minnich, F. G. S. L. Brandão, G. K.-L. Chan, *Nature Physics* **2019**, *16*, 205–210.

[112] N. Gomes, F. Zhang, N. F. Berthusen, C.-Z. Wang, K.-M. Ho, P. P. Orth, Y. Yao, *Journal of Chemical Theory and Computation* **2020**, *16*, 6256–6266.

[113] M. Beck, *Physics Reports* **2000**, *324*, 1–105.

[114] V. Averbukh, P. Kolorenč, *Physical Review Letters* **2009**, *103*, 183001.

[115] G. A. Jones, D. S. Bradshaw, *Frontiers in Physics* **2019**, *7*, 100.

[116] B. P. Pritchard, D. Altarawy, B. Didier, T. D. Gibson, T. L. Windus, *Journal of Chemical Information and Modeling* **2019**, *59*, 4814–4820.

5 Publications

In this chapter, all scientific papers that are part of this dissertation are listed, sorted by topic. For each paper, the individual contributions of each author are given.

5.1 Three-electron dynamics of the interparticle Coulombic decay with two-dimensional continuum confinement

Fabian Langkabel and Annika Bande
J. Chem. Phys. 154, 054111 (2021)
DOI: doi.org/10.1063/5.0037806
URL: `https://doi.org/10.1063/5.0037806`

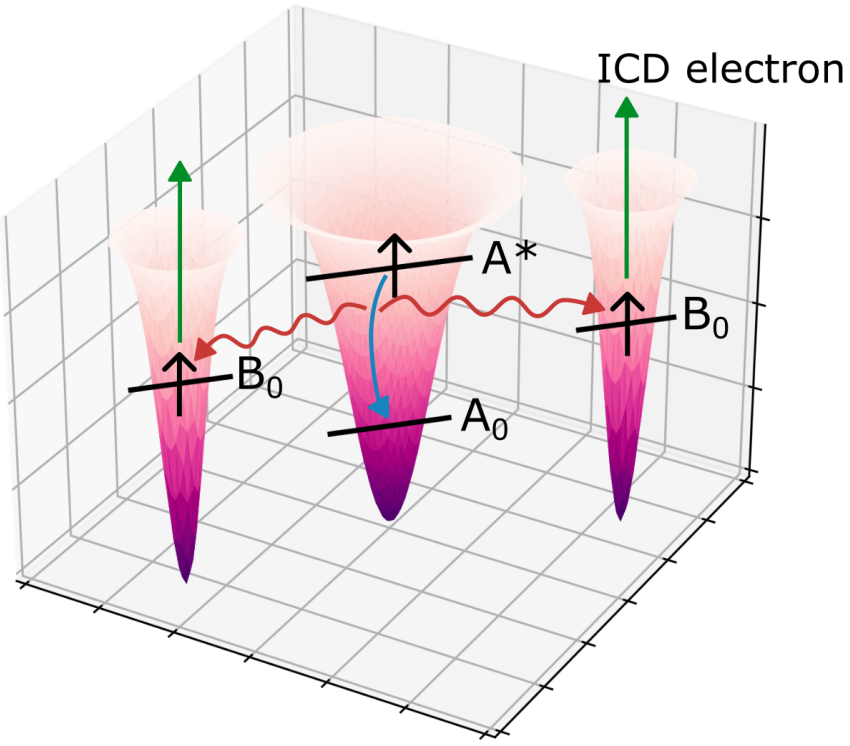

Figure 5.1: Graphical abstract created exclusively for this thesis

Author contributions: The conception of the project was done by AB and FL. FL has developed all MCTDH code modifications and performed all calculations. The structure of the manuscript was composed by both authors. The first draft on parts of the manuscript dealing with GPU implementations as well as equations were written by FL, the others by AB. The manuscript was finalized by both authors.

The Journal of Chemical Physics ARTICLE scitation.org/journal/jcp

Three-electron dynamics of the interparticle Coulombic decay with two-dimensional continuum confinement

Cite as: J. Chem. Phys. 154, 054111 (2021); doi: 10.1063/5.0037806
Submitted: 16 November 2020 • Accepted: 17 January 2021 •
Published Online: 4 February 2021

Fabian Langkabel[a] and Annika Bande[b]

AFFILIATIONS

Helmholtz-Zentrum Berlin für Materialien und Energie GmbH, Hahn-Meitner-Platz 1, 14109 Berlin, Germany

Note: This paper is part of the JCP Special Collection in Honor of Women in Chemical Physics and Physical Chemistry.

[a]Also at: The Institute of Chemistry and Biochemistry, Freie Universität Berlin, Arnimallee 22, 14195 Berlin, Germany and formerly at: The Department of Chemistry, Humboldt-Universität zu Berlin, Brook-Taylor-Str. 2, 12489 Berlin, Germany.
[b]Author to whom correspondence should be addressed: annika.bande@helmholtz-berlin.de. URL: https://hz-b.de/theochem

ABSTRACT

In a pair of self-assembled or gated laterally arranged quantum dots, an electronically excited state can undergo interparticle Coulombic decay. Then, an electron from a neighbor quantum dot is emitted into the electronic continuum along the two available dimensions. This study proves that the process is not only operative among two but also among three quantum dots, where a second electron-emitting dot causes a rate increase by a factor of two according to the predictions from the analytical Wigner–Weisskopf rate equation. The predictions hold over the complete range of conformation angles among the quantum dots and over a large range of distances. Electron dynamics was calculated by multiconfiguration time-dependent Hartree and is, irrespective of the large number of discrete variable representation grid points, feasible after having developed an OpenACC graphic card compilation of the program.

I. INTRODUCTION

For more than two decades, the interparticle Coulombic decay (ICD) process created a stir.[1–7] Theoreticians and experimentalists from disciplines ranging from atomic cluster physics[8–17] over biomedicine[18,19] to nanophysics[20–22] traced ICD and found it being effective in various systems. This general presence originates probably from the astonishing simplicity of the process. Nothing more happens than that an inner-valence excited or ionized electronic structure relaxes into its ground state efficiently because a neighboring structure has a valence electron that can take up the excess energy via Coulomb interaction only and is ionized in response. Many studies in the experimental disciplines were governed by energetic and structural considerations, i.e., one would know which Coulomb explosion products are collected in ion and electron detectors and what energy they have and reconstruct from this the progression of ICD[8,9,17] or one would record photoelectron spectra.[23–25] A recent alternative is the pump–probe technique.[16,26] The vast majority of theories considers initial resonances, final ionized states, and Coulomb interaction integrals, which are challenging, as highly excited and continuum states are to be calculated accurately.[2,4] Eventually, nuclear dynamics calculations aid to simulate the Coulomb explosion and deliver kinetic energy releases.[10,27–31] They were recently combined with electron dynamics.[32]

Indeed, as ICD is an ultrafast electronic decay process, it is of high interest to investigate it in the short-time domain of electron dynamics. This holds two interconnected challenges. One is the number of electrons, which, for reasons of computational feasibility, can only be in the order of ten, at least if highly correlated wavefunction-based methods are used. The other is electron correlation itself, which is essential to an accurate computation of the Coulomb interaction that is mediating ICD. Thus, in using the multiconfiguration time-dependent Hartree (MCTDH) method[33,34]

with antisymmetrization, a body of research works on the transient nature of ICD was formed to benchmark the fundamentals of ICD. Gaussian binding potentials were used, which represent the essentials of the electronic structure of atoms or molecules, in that they reflect a quasi-atomic structure. Moreover, they are established models for quantum dots (QDs).

The gains drawn from elucidating the electron dynamics during ICD so far are the following. First, the decays of two-site triplet[35] or singlet[36] ICD resonance states were shown in an effectively one-dimensional model, where the ICD electron can only leave along the coordinate connecting the two binding potentials, as was found likewise in the case of quantum wells.[37,38] The frequently considered analytical and approximate rate equation for well-separated subsystems[39,40] was confirmed in a separation-dependence study, showing that the Coulomb interaction of two neighbors alone determines the rate. However, it also revealed that a one-dimensional continuum is a special case in which rates are subject to oscillations around the monotonic behavior predicted from the asymptotic formulae. Second, the relative energy of electronic levels, modified in QDs through geometries, was shown to affect the ICD rate partially in a systematic way,[41] but partially also in a non-trivial way.[42] Third, it was shown that both electron capture[43,44] and electromagnetic oscillating fields[45,46] can initiate ICD. Fourth, the decay is altered by the level atom or potential vibrations.[47] Fifth, the role of an additional potential was elucidated from three viewing angles. When being at a long distance and only shallow or even repulsive, which means the extra potential can be interpreted as an impurity in the QD framework, a non-trivial alternation of the ICD rates is discovered.[48] When being a somewhat deeper binding potential in a short distance from the two partners undergoing ICD, the extra site, a QD of other geometry or material composition, supports superexchange ICD.[49] In addition, when a full-depth binding potential is added, i.e., another QD of the same material as the others, it acts as a participator in a three-electron ICD process.[50] This means among others that it supports the prefactor for the number of neighbors N predicted from the aforementioned analytical rate equation.[39,40]

Just recently, the ICD rate equation was also confirmed in electron dynamics calculations in two-electron systems with a two-dimensional electronic continuum.[48,51] The respective potentials correspond to laterally arranged self-assembled[52–54] or electrostatically confined QDs.[55] Therefore, the dynamics rates showed much less pronounced oscillations with parameter variations in comparison to the analytical monotonic rate as a function of the respective parameter, where the parameter considered so far was the inter-QD distance. In the past years, it was found that the related electron-transfer mediated decay process of three atoms depends on their exact constellation.[56] We assume the same for ICD. Therefore, we consider in this study systems of three binding sites with a two-dimensional continuum and a two-dimensional conformation space for their arrangement.

For the realm of electron dynamics calculations in QD models, this attempt is a novelty because it bridges the knowledge on three electrons in three sites[50] and the knowledge on a two-dimensional continuum.[48,51] We anticipate a reduction of rate fluctuations and an increase in the rate by a factor of two compared to the ICD rate with one neighbor only. The unknown regarding the physics is the role of the spatial arrangement of the three potentials in a straight or angled row. Moreover, previous calculations with three electrons and more with two continuum dimensions showed an increase in computation time within the Heidelberg MCTDH program[57,58] due to the required increase in basis size in a discrete variable representation (DVR).[57,59,60] Therefore, an essential technical development accompanies this work, which is namely a compilation and parallelization of MCTDH on graphics processing units (GPUs).

After introducing the method, model (Sec. II), and parameterization (Sec. III A), we hence introduce the GPU setup of MCTDH (Sec. III B). In the results, we discuss the latter at first (Sec. IV A), before we reveal the electronic structure (Sec. IV B) and dynamics in the linear (Sec. IV C 1) or angled (Sec. IV C 2) arrangement of the three sites and lead all to a concise conclusion (Sec. V).

II. THEORY

The method utilized to investigate ICD of an electronically excited state of one QD in the neighborhood of two other QDs allowing for ionization is the multiconfiguration time-dependent Hartree method (MCTDH)[33,34] in the Heidelberg implementation.[57,58] By imposing appropriate antisymmetry constraints to the wavefunction, MCTDH allows us to solve the electronic time-dependent Schrödinger equation for the three-electron-in-three-QD problem. The method has proven successful for the investigation of three QDs in a nanowire.[50] Here, it is going to be extended for laterally arranged QDs with a two-dimensional continuum, for which a model has been developed in another work considering two electrons.[48,51]

The electronic Hamiltonian contains the typical operators of the kinetic energy, the QD binding potential, the Coulomb interaction, and the complex absorbing potential (from left to right) and reads

$$\hat{H} = \sum_i \left(\hat{T}_i + \hat{V}_i^{QD} + \sum_{j<i} \hat{r}_{ij}^{-1} + \mathrm{i}\hat{W}_i \right). \tag{1}$$

Here, the indices i, j = 1, 2, 3 run over the two or three electrons of the two comparative sets of calculations. The potential $\hat{V}_i^{QD}$ reflects the two or three QDs from which electrons can be emitted into a two-dimensional unconfined (continuum) region. Two-dimensional Gaussians,

$$\hat{V}_i^{QD}(x_i, z_i) = \sum_q -D_q \cdot \exp\left\{-b_q\left[(\hat{z}_i - z_q)^2 + (\hat{x}_i - x_q)^2\right]\right\}, \tag{2}$$

as functions of x_i and z_i serve their description. q refers to the light-absorbing (A) and the two identical electron-emitting (E, E′) QDs. The central QD is the light-absorbing one and accommodates the energy levels A_1 and A_0, where the higher is twofold degenerate with respect to the two dimensions x and z if only the isolated AQD is considered. The isolated outer, electron-emitting QDs accommodate each only one level, E_0 and E_0'. Note that in the two-QD case, no E′QD and third electron is considered. The remaining variables of Eq. (2) are the QD positions x_q and z_q on the respective coordinates as well as the potentials' depths D_q and their widths' parameters $b_q = 4\ln(2)/r_q^2$, connecting to the half widths at half maximum r_q. They are tuned such that $E_{A1} > E_{E0} > E_{A0}$ and that the excitation

energy in the AQD, $\omega_A = E_{A1} - E_{A0}$, exceeds the ionization energy $IP = -E_{E0}$ to assure that ICD is energetically allowed.[35]

The Coulomb interaction among every two electrons, i.e., the essential mediator to ICD, is given in the approximate two-dimensional representation[51]

$$\hat{r}_{ij}^{-1} \Rightarrow [\hat{r}_{ij}^2 + \alpha^2 \cdot e^{-\beta \hat{r}_{ij}}]^{-1/2}. \tag{3}$$

$r_{ij} = |\mathbf{r}_i - \mathbf{r}_j| \rightarrow \sqrt{(x_i - x_j)^2 + (z_i - z_j)^2}$ is the distance between electrons i and j. Furthermore, a regularization through α and β reduces the Coulomb interaction to a finite value at the coincidence point of both electrons. This is necessary for the numerical stability within the MCTDH framework, in which a pseudo-spectral basis in the form of a finite discrete variable representation (DVR)[57,59,60] is used. Another important aspect is the required sum-of-products form of the four-dimensional interaction [Eq. (3)]. The multi-grid potfit (MGPF)[61] routine was proven to do this transformation in conjunction with a computationally inexpensive and sufficiently accurate truncation of the number of single-particle potential terms.[51]

$\hat{W}_i$ are the complex absorption potentials (CAPs)[62–65] that apply to each electron. They also apply to each of the six spatial coordinates $c_i = x_i, z_i$ in the positive and negative direction $\pm$. Therefore, they are defined by

$$\mathrm{i}\hat{W}_i = \mathrm{i}\sum_{c_i}\sum_{\pm} \hat{W}_{c_i}^{\pm} = \mathrm{i}\eta\,|c_i - c_i^{\pm}|^n\,\Theta(c_i - c_i^{n,p}). \tag{4}$$

The mathematical form of a CAP is a half-sided (Heaviside function Θ) nth order polynomial with onset $c_i^{\pm}$. Through its strength η, it is tuned such that it optimally absorbs the continuum parts of the MCTDH wavefunction.

The core method is to solve the MCTDH equations of motion[33,34] that arise when introducing the MCTDH wavefunction into the Dirac–Frenkel variational principle. This solves the time-dependent electronic Schrödinger equation. The wavefunction is, in the whole series of papers on QD-ICD, here for the first time six-dimensional with coordinates $c_1, \ldots, c_6 = x_1, x_2, x_3, z_1, z_2, z_3$ and reads

$$\Psi(c_1, \ldots, c_6, t) = \sum_{j_1} \cdots \sum_{j_6} A_{j_1,\ldots,j_6}(t) \prod_{\kappa=1}^{6} \varphi_{j_\kappa}^{(\kappa)}(c_\kappa, t). \tag{5}$$

$\varphi_{j_\kappa}^{(\kappa)}(c_\kappa, t)$ are a total of j_κ single-particle functions (SPFs) for each degree of freedom κ. $A_{\ldots j_a j_b,\ldots}(t) = -A_{\ldots j_b j_a,\ldots}(t)$ and $A_{\ldots j_a j_a,\ldots}(t) = 0$ antisymmetrize the wavefunction.

ICD is the decay of a resonance state Φ^{res}, which has its three electrons in the E_0, E_0', and A_1 levels of the three respective QDs. Due to the rotational symmetry of the isolated AQD, the excited state of the central potential is twofold degenerate. Therefore, the three-QD array has two resonances as well. Block improved relaxations using the Hamiltonian of Eq. (1) without the CAP operator are used to generate the two initial states as eigenstates to that reduced Hamiltonian. Applying then the real-time equations of motion under utilization of the full Hamiltonian reveals the decay of the initial wavepacket. It is quantified through the squared autocorrelation function

$$|a(t)|^2 = |\langle \Phi^{res} | \Psi(t) \rangle|^2 = e^{-\Gamma t/\hbar}, \tag{6}$$

i.e., the projection of the time-dependent wavefunction $\Psi(t)$ on the resonance function Φ^{res}. Its exponential slope can be fitted to deliver the ICD rate Γ. All what was described is identical for two QDs occupied by two electrons when removing the E′QD and the respective third electron coordinates.

This comparison of the two- and the three-electron case leads to the relative rates for the respective processes. Although rates can be obtained numerically via electron dynamics calculations, a rationale from analytic consideration will significantly support the understanding of the underlying processes and their interrelation. Such an analysis is available for two-site ICD systems in a Wigner–Weisskopf framework[39,40] based on the general golden rule ansatz. This leads [under the conditions of separability of the wavefunction into a product of single-electron state functions ϕ, no overlap of ϕ, negligible exchange, exclusion of antisymmetrization, and deliberate assignment of certain electrons (lower index to ϕ) to certain QD levels (upper index)] to a two-electron rate,[35,39]

$$\Gamma^{2e} = |\langle \phi_1^{A0} \phi_2^{C} | \hat{r}_{ij}^{-1} | \phi_1^{A1} \phi_2^{E0} \rangle|^2. \tag{7}$$

Equation (7) signifies that the single-electron states that underlie the resonance state [ket of Eq. (7)] and the multitude of final states (bra), including one electron in the continuum C, are Coulomb coupled in the form of two independent dipole transitions of the same energy in the AQD and the EQD subsystem.

The same type of derivation in the same framework of conditions has been formulated for a three-site system with three electrons.[50] For the single-ionization ICD energy condition $2 \cdot IP > \omega_A > 1 \cdot IP$, which is subject to the present study, i.e., for the case in which one of the two EQDs is ionized during ICD, the three-electron rate becomes

$$\begin{aligned}\Gamma^{3e} = |&2^{-1/2} \langle \phi_2^{A0} \phi_3^{C} | V_C^{23} | \phi_2^{A1} \phi_3^{E'0} \rangle \langle \phi_1^{E0} | \phi_1^{E0} \rangle \\ &+ 2^{-1/2} \langle \phi_1^{C} \phi_2^{A0} | V_C^{12} | \phi_1^{E0} \phi_2^{A1} \rangle \langle \phi_3^{E'0} | \phi_3^{E'0} \rangle|^2.\end{aligned} \tag{8}$$

Comparing Eqs. (7) and (8), hence, reveals $\Gamma^{3e} = 2 \cdot \Gamma^{2e}$ in agreement with the general equation

$$\Gamma^{(N+1)e} = N \cdot \Gamma^{2e} \tag{9}$$

for $(N + 1)$ electrons in $(N + 1)$ subsystems, indicating a linear dependence of the rate on N, the number of neighboring sites.[39,40]

III. COMPUTATIONAL DETAILS

A. Parameterization

The potentials defined in Eq. (2) were parameterized in a way to fulfill the energy condition for the two-electron and the single-ionization three-electron ICD process, to meet an experimentally

TABLE I. Parameterization of the binding potentials of Eq. (2). *min* and *max* indicate the ranges for parameter variations.

Units	Atomic	SI
D_A	2.0 a.u.	20.6 meV
b_A	0.25 a.u.	...
$2r_A$	3.33 a.u.	36.07 nm
D_E	2.0 a.u.	20.6 meV
b_E	1.0 a.u.	...
$2r_E$	1.67 a.u.	18.03 nm
R^{min}	10 a.u.	108.30 nm
R^{max}	25 a.u.	270.75 nm
α^{min}	30°	...
α^{max}	180°	...

meaningful material fabrication, and to allow for a reasonable scan over a number of inter-QD distances and angles. The computations in MCTDH are based on a parameterization in atomic units and such is the output. This allows comparison with the studies of others on ICD in QDs.[49,66] In order to make the numbers readable to QD experts as well, they are converted into material-specific numbers for GaAs in SI units[45] by considering the dielectric constant and effective mass of an electron in that material.[67] Table I summarizes all the parameters that define the binding potentials. For the angle and distance scans, the minimal and maximal values (*min*, *max*) are listed. Note that the parameterization with respect to the x and the z coordinate is identical. The potential for R = 108.3 nm and $\alpha = 90°$ is shown in Fig. 1.

The MCTDH program requires further parameterization of the other operators, the DVR basis, and other technical factors. A sine DVR with 140 points was employed in a range [−541.8 a.u.; 541.8 a.u.] ([−50 a.u.; 50 a.u.]). The multi-grid potfit[61] representation of the regularized Coulomb potential with α = 0.1 a.u. and β = 100 a.u. is defined as in the first study on two-dimensional potentials.[51] This means that the fine grid of 140 points per coordinate is supplemented by a coarse grid of only 35 points. The CAPs located on every end of the grid starting at $c_i^{\pm} = \pm 325.0$ nm (±30 a.u.) have the order $n = 4$ and the strength $\eta = 8.6997 \cdot 10^{-6}$.

MCTDH block improved relaxation calculations[68,69] with j_κ = 144 (52) SPFs [cf. Eq. (5)] in each coordinate were used to find the resonance states of two (three) electrons in two (three) QDs among the first 156 (240) states within 1.2 a.u. in time (or 0.08 ps in SI units of GaAs). The initial function for the relaxation was the antisymmetrized product of single-electron eigenfunctions representing a quartet configuration. The single-electron functions themselves were one of the ground state A_0 and one (two) of the lowest state on the full grid, which offer an optimal starting condition to both bound and continuum parts of the target state functions. The resonances were state nos. 143 and 144 (99 and 100), respectively. They were identified by their density pattern of an s-atomic orbital-like density on the two EQDs and a p-atomic orbital-like density on the AQD (cf. Figs. 3 and 4). Thus, the gained resonance wavefunctions were used as initial states for the MCTDH propagations. Here, only j_κ = 8 SPFs served as functional basis. Propagations were done for 10 000 a.u. in time (638.93 ps).

B. Graphic card programming

In order to shorten the runtimes of the computations within the MCTDH Heidelberg package[57,58] in its version MCTDH84.16, the usage of a graphics processing unit (GPU) compilation was

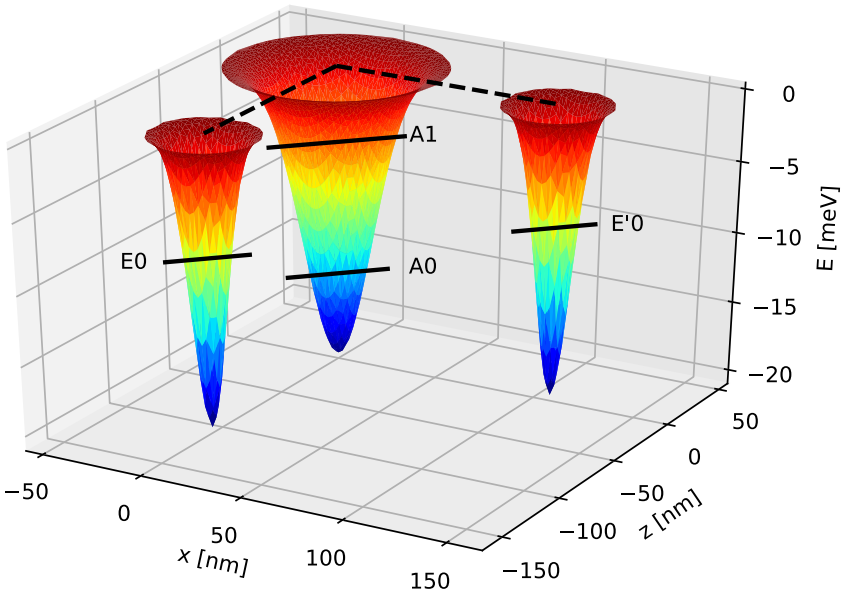

FIG. 1. Three-dimensional representation of the three two-dimensional Gaussians for R = 108.3 nm and $\alpha = 90°$. The horizontal black lines reflect the geometric position of the majority of electron densities concerned with the indicated energetic positions of the single-electron levels E_0 and E' in each outer QD, as well as A_0 and the two (near-)degenerate A_1 in the central QD.

considered. Therefore, test computations (lower dimensional propagations and relaxations) were performed using the GNU compiler collection (GCC) profiling tool gprof. They were analyzed based on flat profiles, i.e., summary tables listing the total time the program needs to execute each function, as well as call graphs, showing which function calls which other function how often. Based on this profiling, routines for matrix multiplications and routines for the multiplication of matrices with three-dimensional tensors were found to be particularly time-consuming. In total, these routines required up to 90% of the computing time. However, they are highly parallelizable and, in particular, each section is simple enough to allow for parallelization with GPUs. To this end, the respective routines were translated from Fortran77 to Fortran90 and compiler instructions for using GPUs were implemented in OpenACC. The program was compiled with the GCC9 compiler, which supports the OpenACC standard in version 2.5. MCTDH itself parallelizes superordinate routines that distribute the individual subroutines (matrix multiplications and others) onto the central processing unit (CPU) cores. Then, one specific GPU is assigned to each of them such that as many GPUs as CPU cores can be used.

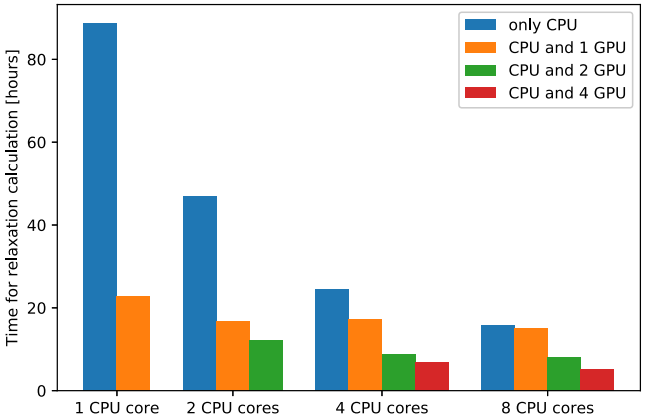

FIG. 2. Bar diagram on the compute time of a representative block-improved relaxation calculation as a function of the number of CPUs (abscissa) and GPUs (color-coded bars in groups).

IV. RESULTS

A. Technical improvements: GPUs

The modified MCTDH version is first applied to exemplary relaxation and propagation computations on three-QD three-electron ICD systems with different numbers of CPU cores and GPUs. Propagations showed a significant increase in computing time by a factor of up to 100 when using GPUs, irrespective of their exact number. The reason is that the multiplied matrices and tensors have so few entries (based on only eight SPFs for each degree of freedom) that the additional time needed to transfer the data from the main memory to the GPUs' memory and back clearly outweighs the gain in computation time on the GPU. Per contra, relaxation calculations use significantly more SPFs (52), which leads to much larger matrices and tensors, so that the gain in computation time on the GPUs trumps the time needed to transfer the data and a speedup is possible. Figure 2 shows the speedup in a bar chart for different combinations of GPU and CPU cores for a block improved relaxation calculation, however, with a factor four shorter relaxation duration than what it needed in the typical calculations of this study. The increasing number of CPUs applies to different groups of bars plotted from left to right, whereas the color code marks the number of GPUs that increases within each group of bars also from left to right. The test calculations were performed on computers with two Intel Xeon Gold 6136 CPUs and up to four P100 GPUs.

While doubling the number of CPU cores from 1 to 2 and from 2 to 4 without using GPUs (blue bars) almost halves the computing time, doubling from 4 to 8 CPUs only reduces the computing time by a factor of 1.4. Any further increase of the cores (not shown in Fig. 2) does not lead to significant reductions of the computing time, meaning that the internal parallelization via CPU cores is exhausted with eight CPU cores. However, the additional use of GPUs for the previously mentioned routines reduces the computing time. If only comparably few compute units are GPUs (compare the blue and orange bars for four and eight CPU cores), then the gain in compute time is marginal because the relative load of the GPU is high. However, if two or four GPUs are used together with as many as or more CPU cores (last two group of bars), a speedup factor of up to a 3.2 can be gained, as in the example of eight CPU cores with four GPUs compared to eight CPU cores without GPUs. This setting allows us to perform the relaxation calculations needed for this study (factor four longer compared to Fig. 2) in reasonable time, i.e., within 20 h compared to otherwise 63 h in pure CPU parallelization and 355 h without parallelization.

B. Electronic structure

In the description of the ICD resonances (Sec. II) and the parameterization of the potentials (Sec. III), it was said that the central QD, the AQD, supports a ground state electronic level at energy $E_{A0} = -11.62$ meV (-1.128 a.u.). There are further two degenerate single-electron states with energy $E_{A1} = -4.25$ meV (-0.413 a.u.), which resemble atomic p-type orbitals perpendicular to each other. The resonant excitation energies in either direction are thus $\omega_A = 7.37$ meV (0.715 a.u.).

The two EQDs are equal in shape and support one nodal-free bound state only at energy $E_{E0} = -5.43$ meV (-0.527 a.u.), which is the inverse to the ionization potential $IP = 5.43$ meV. With this energetics, the excitation energy in the central QD exceeds once the ionization energy, allowing thus for single-ionization ICD, i.e., in which only one of the EQDs is ionized.[50] This choice was made because calculations on systems that support $\omega_A > 2IP$ showed also only single-, but no double-ionization, ICD and were at the same time significantly less stable.[50]

The three-electron states are composed of the above described one-electron orbitals. Their true wavefunctions are of course influenced by the Coulomb interaction among electrons, but this does not change the fundamental level occupation underlying each of the states. The ground state has one electron in each QD in the lowest level. Therefore, it is denoted by $E_0A_0E_0'$.

The resonances are actually the states most relevant for this work as they have a finite lifetime and decay via ICD. They have two ground state electrons in the EQDs and an excited electron in the AQD. The latter can be in one of the two degenerate levels of the isolated AQD, which compare to p-type atomic orbitals. They are perpendicular to each other, but only in the linear array ($\alpha = 180^\circ$), they align with the z and x axis. In general, the array's symmetry enforces the orbitals to be either parallel to the axis connecting the two EQDs or perpendicular to it, as can be rationalized by inspecting the densities in Figs. 4(a) and 4(b). Thus, the states are termed $E_0A_1^{\parallel}E_0'$ and $E_0A_1^{\perp}E_0'$, respectively.

Their energies depend on the exact geometric arrangement of the three QDs, as is visualized in Fig. 5 for fixed $R = 108.3$ nm and varying angles α. It is most straightforward to analyze at first the overall trends of both curves, as both energies increase with a decrease in angle by about 1.5 meV. This trend originates in the increasing overlap of the electrons located on the EQDs. If they are distant by $2R = 216.6$ nm (20 a.u.) in the $\alpha = 180^\circ$ case, they contribute $1/R = 0.52$ meV (0.05 a.u.) to the total energy through their Coulomb interaction. At the high-energy side of $\alpha = 30^\circ$, the two EQDs are as near as 56.06 nm (5.176 a.u.). This leads to a Coulomb energy contribution of $1/R = 1.99$ meV (0.193 a.u.) and ultimately explains the overall increase in Fig. 5. The interesting aspect is, however, the relative energy of the parallel (red) and the perpendicular (yellow) case. In the linear array, the resonance state $E_0A_1^{\parallel}E_0'$ has a density in which the electron on the AQD directs as much as possible toward the EQDs [Fig. 3(a)]. This must lead to the highest possible orbital overlap of the electrons on the AQD and the EQDs, which is the origin of the higher resonance energy displayed in Fig. 5 (red line) at $\alpha = 180^\circ$. In contrast, the density of the perpendicular state $E_0A_1^{\perp}E_0'$ [cf. Fig. 3(b)] reveals the lowest orbital overlap in a linear arrangement and thus the lower energy (yellow line). When α is small, the energy contribution of the interaction of electrons in the EQD and the AQD for the parallel resonance $E_0A_1^{\parallel}E_0'$ (red line) drops compared to that as in the linear arrangement, which may be rationalized from the density representation in Fig. 4(a). In contrast, the same energy contribution in the perpendicular resonance $E_0A_1^{\perp}E_0'$ increases with decreasing α [orange in Fig. 5; state density in Fig. 4(b)]. This is the origin of the crossing of the total energy curves at $\alpha \approx 90^\circ$.

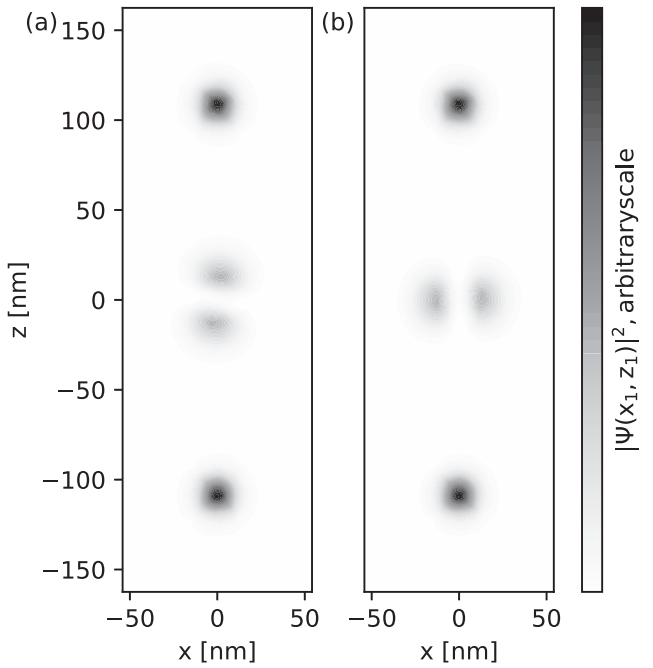

FIG. 3. Surface-projection plots of three-electron ICD resonance state densities for the linear array with $\alpha = 180^\circ$ and $R = 108.3$ nm as a function of the coordinate axes x and z: (a) z-polarized resonance with $A_1^{\parallel}$ and (b) x-polarized resonance with $A_1^{\perp}$.

C. Electron dynamics

1. Linear array

First, we investigate the distance dependence of ICD in a linearly arranged array of QDs. This is done in comparison for two and three QDs/electrons to confirm the validity of the rate prediction $\Gamma^{3e} = 2\Gamma^{2e}$ from the analytic Wigner–Weisskopf derivation[39,40] for a system with two continuum directions. This will complement our confirmation of the rate equation for QDs in a nanowire supporting a one-dimensional continuum for the ICD electron[50] and studies of others on atoms,[39,40] where ICD electrons leave the system in all three spatial dimensions.

As we have shown in previous studies on nanowires[35,50] and self-assembled QDs,[51] oscillations of the truly realized rates around the asymptote $\propto R^{-6}$ are to be expected. Hence, a sample of several R is needed to evaluate the rate ratio from the averages $\Gamma^{3e}/\Gamma^{2e} = \overline{\Gamma^{3e} \cdot R^6}/\overline{\Gamma^{2e} \cdot R^6}$.[50]

Different to what was investigated in a quasi-one-dimensional case,[50] two resonances are available for ICD. Let us start with the z-polarized parallel resonance ($E_0A_1^{\parallel}E_0'$) whose density is visualized in Fig. 3(a) for three electrons. In Fig. 6, the rates for its decay multiplied by R^6 are shown as functions of R. The blue solid line corresponds to $\Gamma^{3e} \cdot R^6$, and the orange solid line corresponds to $\Gamma^{2e} \cdot R^6$. As anticipated, both the rates oscillate around their averages shown as blue and orange dashed lines. Note that the rates for the

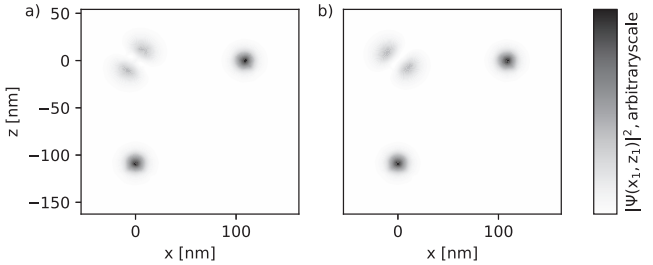

FIG. 4. Surface-projection plots of three-electron ICD resonance state densities for the angled array with $\alpha = 90^\circ$ and $R = 108.3$ nm as a function of the coordinate axes x and z: (a) resonance with $A_1^{\parallel}$ and (b) resonance with $A_1^{\perp}$.

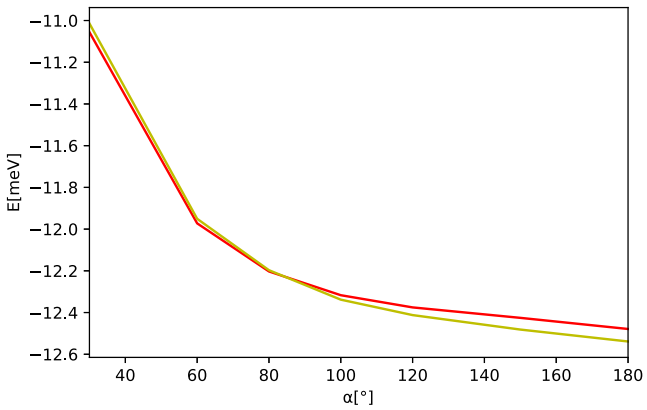

FIG. 5. Energies E of the three-electron resonance states $E_0A_1^{\parallel}E_0'$ (red line) and $E_0A_1^{\perp}E_0'$ (yellow line) as functions of the angle α for fixed R = 108.3 nm.

previously investigated Γ^{2e} case[51] were obtained only for a smaller span of R. This is because the technical parameters (cf. Sec. III) have been optimized for the new three-QD case but lead to technical instabilities for two QDs. The maximum (average) span of oscillations is 26.9% (9.1%) in the three- and 22.4% (10.9%) in the two-electron case. This amount of oscillation is in the order of magnitude of the formerly found deviations of 50% (24%) for a two-dimensional continuum and thus much smaller than the respective oscillations of 222% (85%) when only a one-dimensional continuum is available, where the ICD electron has no possibility (other than limited tunneling) to circumvent the Coulomb barrier imposed by the bound electron(s).[51] The ratio is Γ^{3e}/Γ^{2e} = 2.10 with a standard deviation of 0.33. This means that it supports the predicted factor 2 from the Wigner–Weisskopf theory.

The same type of analysis is made for the decay of the x-polarized resonance state ($E_0A_1^{\perp}E_0'$) with the density shown in Fig. 3(b). The data can be found in Fig. 7 with the same color and line-style coding as before. Again the three-electron ICD is faster by a factor of two. We obtain exactly Γ^{3e}/Γ^{2e} = 1.98(0.28), where the standard deviation is given in parentheses. This means that despite the fact that ICD rates are in general smaller for the x resonance than for the z resonance, which confirms earlier results,[51] the asymptotic equation keeps its generality.

2. Angled array

Another feature of SA QD arrays, in particular, and systems with a two-dimensional continuum, in general, is the option to arrange the individual QDs in a non-linear fashion. Here, we investigate the behavior of the R^6-normalized ICD rate as a function of the angle α that determines the QD constellation. Again, the two resonances ($E_0A_1^{\parallel}E_0'$ and $E_0A_1^{\perp}E_0'$) with their densities shown in Figs. 4(a) and 4(b) are available for the decay. Electron dynamics is only calculated exemplarily for three inter-QD distances R = 108.3 nm, 119.1 nm, and 130.0 nm (10, 11, 12 a.u.) for the sake of saving computer power. As Γ is known to oscillate as a function of R, we used the results at the three distances to average at each angle over $\Gamma_{\parallel}^{3e}\cdot R^6$ and $\Gamma_{\perp}^{3e}\cdot R^6$. Although an average over three data points is statistically not robust, one can at least deduce trends for the angle-dependence of the ICD rate.

Figure 8 shows that $\overline{\Gamma_{\parallel}^{3e}\cdot R^6}$ (red line) increases with increasing α, while $\overline{\Gamma_{\perp}^{3e}\cdot R^6}$ (yellow line) contrarily decreases. This behavior is obviously caused by the overlap of the lobes of electron density that can be seen in Figs. 3 and 4, which directly connect to the Coulomb interaction, as was discussed in Sec. IV B. The p-shaped density contribution on the central AQD of the parallel resonance ($E_0A_1^{\parallel}E_0'$) in the linear case [Fig. 3(a)] lies exactly along the array's z axis. This is the case of highest density overlap. When the array gets angled, the E_0 and E_0' density contributions from the two emitter QDs move away from the central QD's orbital axis. Hence, the Coulomb

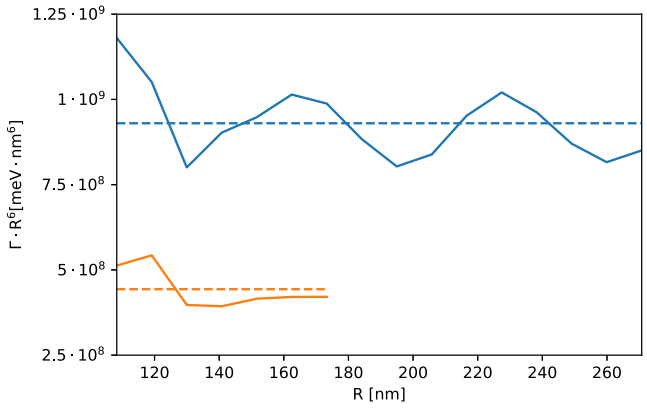

FIG. 6. R^6-normalized rates of the ICD of the $E_0A_1^{\parallel}E_0'$ resonance in a linear QD arrangement as a function of the inter-QD distance R. The blue lines correspond to the three-QD case, and the orange ones to the two-QD case. The actual values are drawn as solid lines, and their averages are drawn as dashed lines.

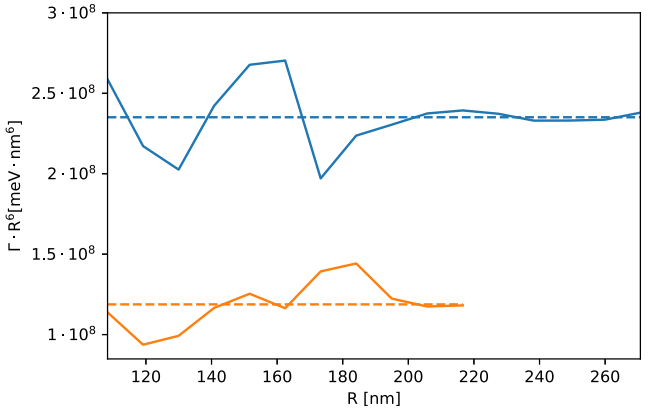

FIG. 7. R^6-normalized rates for the ICD of the $E_0A_1^{\perp}E_0'$ resonance ICD in a liner QD arrangement as a function of the inter-QD distance R. The blue lines correspond to the three-QD case, and the orange ones correspond to the two-QD case. The actual values are drawn as solid lines, and their averages are drawn as dashed lines.

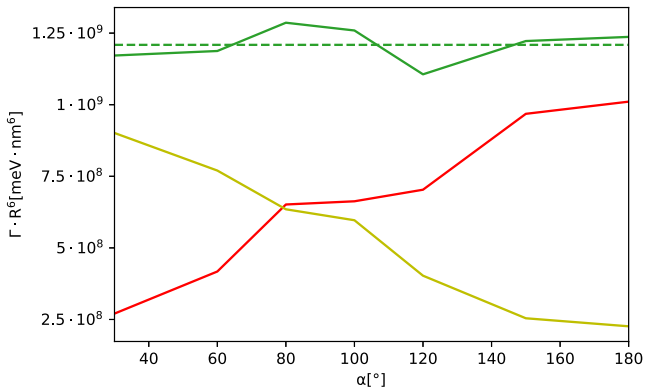

FIG. 8. R^6-normalized ICD rates as a function of α. $\overline{\Gamma_{\parallel}^{3e} \cdot R^6}$ (red), $\overline{\Gamma_{\perp}^{3e} \cdot R^6}$ (yellow), and their sum (green, top line) are displayed. The dashed line reflects the overall average rate.

interaction decreases and likewise the rate $\Gamma_{\parallel}^{3e}$ also decreases. The contrary is true for $\Gamma_{\perp}^{3e}$. The density of an electron in the perpendicular $A_1^{\perp}$ level points maximally away from the densities of electrons in the two E_0 levels when $\alpha = 180^{\circ}$. When the angle is small, the density contributions on the EQDs are near that lobe of the $A_1^{\perp}$ density, which is enclosed by the angle α. The crossing point of both curves lies near $\alpha = 90^{\circ}$. The sum of both rates and its average are shown as the green solid and dashed lines in Fig. 8. It reflects the overall ICD rate with three electrons, which turns out to be, besides statistical fluctuations, independent of the bending angle within the array. This is an important finding in conjunction with the analytical rate equation, which states that the rate increases with the number N of equidistant electron emitters irrespective of their relative arrangement.[40] Indeed, we find a rate ratio of $\Gamma^{3e}/\Gamma^{2e} = 2.15(0.28)$, where for Γ^{2e} we use the sum of average rates obtained from Figs. 6 and 7.

In studies on Ne clusters, it was found that the N-neighbor rates would increase stronger than linearly only when the number of neighbors gets large.[2,39] This was explained by the increasing overlap of electron density on the neighbors that come close together. Although in this study the two emitter QDs approach one another closely, no increase in the overall rate is observed at low angles. Either 30° is not enough to reveal an enhancement effect or the electron overlap among electrons on only two sites is not sufficient. Both these support the analytical prediction on rates increasing by factors of N for small numbers of neighbors even more.[40]

V. CONCLUSION

The three-site interparticle Coulombic decay was investigated by means of electron dynamics calculations in a multiconfiguration time-dependent Hartree framework for the special case that a two-dimensional emission continuum is available for the ICD electron. The technical aspects of this study center around the expensive computations of this two-dimensional continuum on a large discrete variable representation grid and for three electrons. They became feasible through the recently introduced multi-grid potfit representation of the Coulomb interaction potential and an OpenACC graphic card compilation of MCTDH developed in this study. In using finally 8 CPU cores with 4 GPUs, the computing time for relaxation calculations reduces to 31.7% compared to no-GPU usage and 5.8% of what would be needed on a single CPU core. This speedup strategy makes computations in even higher dimensions (more electrons or continuum dimensions) accessible. Further speedup may be achieved in coding GPU parallelization into the MCTDH code.

The physics results of this study close the knowledge gap in the three-site three-electron ICD process, which was previously only investigated for both an unconfined three-dimensional continuum and a strongly confined one-dimensional continuum for the cases of atom clusters and QDs in a nanowire, respectively. Here, self-assembled or gated laterally arranged QDs are exemplarily studied for enabling a general understanding on ICD with a two-dimensionally unconfined electron. The findings are compared to the analytical Wigner–Weisskopf rate equation prediction in showing, as studies in the other systems, that the ICD rate is a function of the number of electron emission sites adjacent to a single excited site in their center. The result is stable for changes in the arrangement of the emitters varied through distances and angles.

ACKNOWLEDGMENTS

We gratefully acknowledge financial support from the Volkswagen Foundation through the Freigeist Fellowship No. 89525. Particular thanks go to the HZDR for offering computer time for this work on their GPU Server with 4 T P100. Here, we also like to thank Henrik Schulz of HZDR for his support in using the cluster. We, furthermore, thank Daniel Peláez for preparing the extremely useful multi-grid potfit representation of the four-dimensional Coulomb potential in a former cooperation.

DATA AVAILABILITY

The data that support the findings of this study are available from the corresponding author upon reasonable request.

REFERENCES

[1] L. S. Cederbaum, J. Zobeley, and F. Tarantelli, Phys. Rev. Lett. **79**, 4778 (1997).
[2] R. Santra and L. S. Cederbaum, Phys. Rep. **368**, 1 (2002).
[3] U. Hergenhahn, J. Electron Spectrosc. Relat. Phenom. **184**, 78 (2011).
[4] V. Averbukh, P. V. Demekhin, P. Kolorenč, S. Scheit, S. D. Stoychev, A. I. Kuleff, Y.-C. Chiang, K. Gokhberg, S. Kopelke, N. Sisourat *et al.*, J. Electron Spectrosc. Relat. Phenom. **183**, 36 (2011).
[5] U. Hergenhahn, Int. J. Radiat. Biol. **88**, 871 (2012).
[6] T. Jahnke, J. Phys. B: At., Mol. Opt. Phys. **48**, 082001 (2015).
[7] T. Jahnke, U. Hergenhahn, B. Winter, R. Dörner, U. Frühling, P. V. Demekhin, K. Gokhberg, L. S. Cederbaum, A. Ehresmann, A. Knie *et al.*, Chem. Rev. **120**, 11295 (2020).
[8] X.-J. Liu, N. Saito, H. Fukuzawa, Y. Morishita, S. Stoychev, A. Kuleff, I. H. Suzuki, Y. Tamenori, R. Richter, G. Prümper *et al.*, J. Phys. B: At., Mol. Opt. Phys. **40**, F1 (2007).
[9] K. Kreidi, T. Jahnke, T. Weber, T. Havermeier, X. Liu, Y. Morishita, S. Schössler, L. Schmidt, M. Schöffler, M. Odenweller *et al.*, Phys. Rev. A **78**, 043422 (2008).

[10]N. Sisourat, N. V. Kryzhevoi, P. Kolorenč, S. Scheit, T. Jahnke, and L. S. Cederbaum, Nat. Phys. **6**, 508 (2010).
[11]N. Sisourat, H. Sann, N. V. Kryzhevoi, P. Kolorenč, T. Havermeier, F. Sturm, T. Jahnke, H.-K. Kim, R. Dörner, and L. S. Cederbaum, Phys. Rev. Lett. **105**, 173401 (2010).
[12]K. Sakai, S. Stoychev, T. Ouchi, I. Higuchi, M. Schöffler, T. Mazza, H. Fukuzawa, K. Nagaya, M. Yao, Y. Tamenori *et al.*, Phys. Rev. Lett. **106**, 033401 (2011).
[13]E. Fasshauer, M. Förstel, S. Pallmann, M. Pernpointner, and U. Hergenhahn, New J. Phys. **16**, 103026 (2014).
[14]K. Nagaya, D. Iablonskyi, N. V. Golubev, K. Matsunami, H. Fukuzawa, K. Motomura, T. Nishiyama, T. Sakai, T. Tachibana, S. Mondal *et al.*, Nat. Commun. **7**, 13477 (2016).
[15]S. Kazandjian, J. Rist, M. Weller, F. Wiegandt, D. Aslitürk, S. Grundmann, M. Kircher, G. Nalin, D. Pitters, I. Vela Pérez *et al.*, Phys. Rev. A **98**, 050701(R) (2018).
[16]G. Schmid, K. Schnorr, S. Augustin, S. Meister, H. Lindenblatt, F. Trost, Y. Liu, T. Miteva, M. Gisselbrecht, S. Düsterer *et al.*, J. Chem. Phys. **151**, 084314 (2019).
[17]A. Mhamdi, J. Rist, T. Havermeier, R. Dörner, T. Jahnke, and P. V. Demekhin, Phys. Rev. A **101**, 023404 (2020).
[18]X. Ren, E. Wang, A. D. Skitnevskaya, A. B. Trofimov, K. Gokhberg, and A. Dorn, Nat. Phys. **14**, 1062 (2018).
[19]S. Xu, D. Guo, X. Ma, X. Zhu, W. Feng, S. Yan, D. Zhao, Y. Gao, S. Zhang, X. Ren *et al.*, Angew. Chem., Int. Ed. **57**, 17023 (2018).
[20]V. Averbukh and L. S. Cederbaum, Phys. Rev. Lett. **96**, 053401 (2006).
[21]R. De, M. Magrakvelidze, M. E. Madjet, S. T. Manson, and H. S. Chakraborty, J. Phys. B: At., Mol. Opt. Phys. **49**, 11LT01 (2016).
[22]R. A. Wilhelm, E. Gruber, J. Schwestka, R. Kozubek, T. I. Madeira, J. P. Marques, J. Kobus, A. V. Krasheninnikov, M. Schleberger, and F. Aumayr, Phys. Rev. Lett. **119**, 103401 (2017).
[23]B. Winter, Nucl. Instrum. Methods Phys. Res. A **601**, 139 (2009).
[24]S. Thürmer, M. Ončák, N. Ottosson, R. Seidel, U. Hergenhahn, S. E. Bradforth, P. Slavíček, and B. Winter, Nat. Chem. **5**, 590 (2013).
[25]K. D. Mudryk, R. Seidel, B. Winter, and I. Wilkinson, Phys. Chem. Chem. Phys. **22**, 20311 (2020).
[26]U. Frühling, F. Trinter, F. Karimi, J. B. Williams, and T. Jahnke, J. Electron Spectrosc. Relat. Phenom. **204**, 237 (2015).
[27]R. Santra, J. Zobeley, L. S. Cederbaum, and N. Moiseyev, Phys. Rev. Lett. **85**, 4490 (2000).
[28]N. Moiseyev, R. Santra, J. Zobeley, and L. S. Cederbaum, J. Chem. Phys. **114**, 7351 (2001).
[29]S. Scheit, L. S. Cederbaum, and H.-D. Meyer, J. Chem. Phys. **118**, 2092 (2003).
[30]N. Sisourat, N. V. Kryzhevoi, P. Kolorenč, S. Scheit, and L. S. Cederbaum, Phys. Rev. A **82**, 053401 (2010).
[31]Y.-C. Chiang, F. Otto, H.-D. Meyer, and L. S. Cederbaum, Phys. Rev. Lett. **107**, 173001 (2011).
[32]R. Cabrera-Trujillo, O. Vendrell, and L. S. Cederbaum, Phys. Rev. A **102**, 032820 (2020).
[33]H.-D. Meyer, U. Manthe, and L. S. Cederbaum, Chem. Phys. Lett. **165**, 73 (1990).
[34]U. Manthe, H. D. Meyer, and L. S. Cederbaum, J. Chem. Phys. **97**, 3199 (1992).
[35]A. Bande, K. Gokhberg, and L. S. Cederbaum, J. Chem. Phys. **135**, 144112 (2011).
[36]A. Bande, F. M. Pont, P. Dolbundalchok, K. Gokhberg, and L. S. Cederbaum, EPJ Web Conf. **41**, 04031 (2013).
[37]T. Goldzak, L. Gantz, I. Gilary, G. Bahir, and N. Moiseyev, Phys. Rev. B **91**, 165312 (2015).
[38]T. Goldzak, L. Gantz, I. Gilary, G. Bahir, and N. Moiseyev, Phys. Rev. B **93**, 045310 (2016).
[39]R. Santra, J. Zobeley, and L. S. Cederbaum, Phys. Rev. B **64**, 245104 (2001).
[40]V. Averbukh, I. B. Müller, and L. S. Cederbaum, Phys. Rev. Lett. **93**, 263002 (2004).
[41]P. Dolbundalchok, D. Peláez, E. F. Aziz, and A. Bande, J. Comput. Chem. **37**, 2249 (2016).
[42]F. Weber, E. F. Aziz, and A. Bande, J. Comput. Chem. **38**, 2141 (2017).
[43]F. M. Pont, A. Bande, and L. S. Cederbaum, Phys. Rev. B **88**, 241304(R) (2013).
[44]A. Molle, E. R. Berikaa, F. M. Pont, and A. Bande, J. Chem. Phys. **150**, 224105 (2019).
[45]A. Bande, J. Chem. Phys. **138**, 214104 (2013).
[46]A. Haller, Y.-C. Chiang, M. Menger, E. F. Aziz, and A. Bande, Chem. Phys. **482**, 135 (2017).
[47]A. Bande, Mol. Phys. **117**, 2014 (2019).
[48]V. A. Guskov, F. Langkabel, M. Berg, and A. Bande, QUARKS: Braz. Electron. J. Phys. Chem. Mat. Sci. **3**, 17 (2020).
[49]H. Agueny, M. Pesche, B. Lutet-Toti, T. Miteva, A. Molle, J. Caillat, and N. Sisourat, Phys. Rev. B **101**, 195431 (2020).
[50]F. Langkabel, M. Lützner, and A. Bande, J. Phys. Chem. C **123**, 21757 (2019).
[51]A. Haller, D. Peláez, and A. Bande, J. Phys. Chem. C **123**, 14754 (2019).
[52]P. M. Petroff, A. Lorke, and A. Imamoglu, Phys. Today **54**(5), 46 (2001).
[53]L. Wang, A. Rastelli, S. Kiravittaya, M. Benyoucef, and O. G. Schmidt, Adv. Mater. **21**, 2601 (2009).
[54]E. Zallo, P. Atkinson, L. Wang, A. Rastelli, and O. G. Schmidt, Phys. Stat. Sol. B **249**, 702 (2012).
[55]W. G. van der Wiel, S. De Franceschi, J. M. Elzerman, T. Fujisawa, S. Tarucha, and L. P. Kouwenhoven, Rev. Mod. Phys. **75**, 1 (2002).
[56]E. Fasshauer, M. Förstel, M. Mucke, T. Arion, and U. Hergenhahn, Chem. Phys. **482**, 226 (2017).
[57]M. Beck, A. Jäckle, G. Worth, and H.-D. Meyer, Phys. Rep. **324**, 1 (2000).
[58]*Multidimensional Quantum Dynamics: MCTDH Theory and Applications*, edited by H.-D. Meyer, F. Gatti, and G. A. Worth (Wiley VCH, Weinheim, 2009).
[59]J. C. Light, *Time-Dependent Quantum Molecular Dynamics* (Plenum: New York, 1992), p. 185.
[60]J. C. Light and T. Carrington, Jr., Adv. Chem. Phys. **114**, 263 (2000).
[61]D. Peláez and H.-D. Meyer, J. Chem. Phys. **138**, 014108 (2013).
[62]D. Neuhauser and M. Baer, J. Chem. Phys. **90**, 4351 (1989).
[63]D. Neuhauser and M. Baer, Comput. Phys. Commun. **63**, 460 (1991).
[64]U. V. Riss and H.-D. Meyer, J. Phys. B: At., Mol. Opt. Phys. **26**, 4503 (1993).
[65]U. V. Riss and H. D. Meyer, J. Chem. Phys. **105**, 1409 (1996).
[66]I. Cherkes and N. Moiseyev, Phys. Rev. B **83**, 113303 (2011).
[67]See http://matprop.ru/GaAs_basic for the basic parameters (effective mass and dielectric constant) of gallium arsenide; accessed 21 November 2018.
[68]H.-D. Meyer and G. A. Worth, Theor. Chem. Acc. **109**, 251 (2003).
[69]H.-D. Meyer, F. L. Quéré, C. Léonard, and F. Gatti, Chem. Phys. **329**, 179 (2006).

5.2 Three-Electron Dynamics of the Interparticle Coulombic Decay in Doubly Excited Clusters with One-Dimensional Continuum Confinement

Joana-Lysiane Schäfer, Fabian Langkabel and Annika Bande
Molecules 27(24), 8713 (2022)
DOI: doi.org/10.3390/molecules27248713
URL: `https://doi.org/10.3390/molecules27248713`

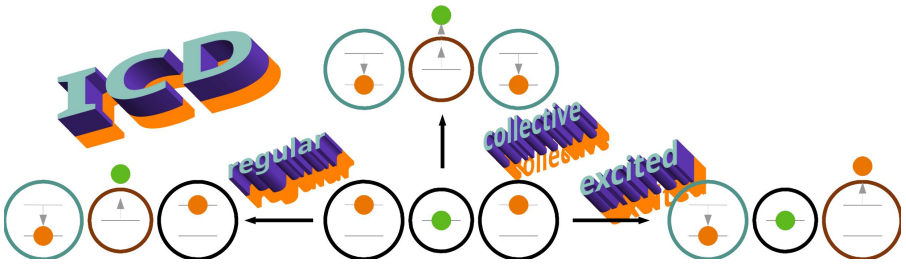

Figure 5.2: Graphical abstract. Reprint with permission from Schäfer et al. [2]

Author contributions: The conceptualization of the project was done by JS and AB. JS did all the calculations. FL supported with technical knowledge of the software and in setting up the calculation and analysis. The manuscript was written by JS and AB with FL providing assistance with the formulas for the asymptotic equations. All authors finalized the manuscript.

molecules

MDPI

Article

Three-Electron Dynamics of the Interparticle Coulombic Decay in Doubly Excited Clusters with One-Dimensional Continuum Confinement

Joana-Lysiane Schäfer [1,2], Fabian Langkabel [1,2] and Annika Bande [1,*]

[1] Helmholtz-Zentrum Berlin für Materialien und Energie GmbH, Hahn-Meitner-Platz 1, 14109 Berlin, Germany
[2] Institute of Chemistry and Biochemistry, Freie Universität Berlin, Arnimallee 22, 14195 Berlin, Germany
* Correspondence: annika.bande@helmholtz-berlin.de

Abstract: A detailed analysis of the electronic structure and decay dynamics in a symmetric system with three electrons in three linearly aligned binding sites representing quantum dots (QDs) is given. The two outer *A* QDs are two-level potentials and can act as (virtual) photon emitters, whereas the central *B* QD can be ionized from its one level into a continuum confined on the QD axis upon absorbing virtual photons in the inter-Coulombic decay (ICD) process. Two scenarios in such an *ABA* array are explored. One ICD process is from a singly excited resonance state, whose decay releasing one virtual photon we find superimposed with resonance energy transfer among both *A* QDs. Moreover, the decay-process manifold for a doubly excited (DE) resonance is explored, in which collective ICD among all three sites and excited ICD among the outer QDs engage. Rates for all processes are found to be extremely low, although ICD rates with two neighbors are predicted to double compared to ICD among two sites only. The slowing is caused by Coulomb barriers imposed from ground or excited state electrons in the *A* sites. Outliers occur on the one hand at short distances, where the charge transfer among QDs mixes the possible decay pathways. On the other hand, we discovered a shape resonance-enhanced DE-ICD pathway, in which an excited and localized B^* shape resonance state forms, which is able to decay quickly into the final ICD continuum.

Keywords: interatomic Coulombic decay; electron dynamics; quantum dots; continuum confinement; Coulomb barrier

Citation: Schäfer, J.-L.; Langkabel, F.; Bande, A. Three-Electron Dynamics of the Interparticle Coulombic Decay in Doubly Excited Clusters with One-Dimensional Continuum Confinement. *Molecules* **2022**, *27*, 8713. https://doi.org/10.3390/molecules27248713

Academic Editor: Sergey I. Bokarev

Received: 27 October 2022
Accepted: 5 December 2022
Published: 9 December 2022

1. Introduction

The inter-Coulombic decay process (ICD) transforms energy of an inner valence excited or ionized atom (*A*) into kinetic energy of an electron ionized from a nearby other atom (*B*) [1]. The initial state is a Feshbach resonance state [2], delocalized over both atoms, which decays by the two-electron rearrangement. In the past 25 years, ICD was observed and/or theoretically predicted for many different electronic systems, including noble gas clusters [3,4], molecular ensembles [1], biomolecules [5], fullerenes [6,7], and quantum dots (QDs) [8,9], where in the latter the hole level is not necessarily the inner-valence state.

Effectively, ICD is a radiationless energy-transfer (ET) process, which is mediated by the Coulomb interaction among the two involved partnering sites' electrons, from which the ICD rate is deduced. This resembles the Förster resonance energy transfer (FRET) among chromophores [10], but leads as a surplus not to a final bound but to a final continuum state. Both processes, nonetheless, can be recast into coupled dipole transitions on either site. In this sense, they nail down an asymptotic distance dependence of the rate via the inverse sixth power of the distance between photon donor and acceptor, as was formulated individually for the specific conditions of FRET [11] and of ICD [12,13].

Scientific intuition and simple rationalization suggest clearly that ICD must depend on several more characteristics of the full chemical systems rather than only particle distance, all the more so the less pointlike the acceptor and donor become, as has been compared

extensively for FRET [14]. For ICD, this effect was studied in the context of geometrical changes of QDs as ICD partners [15], but also in the context of polarization effects in adjacent molecules [16]. Moreover, the spatial confinement of the ionization continuum to two [17] or even one dimension [8] was found to cause significant deviations from the predicted ICD rate. Finally, neighboring sites may alter the rate already when they form only a barrier or a temporal electron binding site [18]. A strong rate increase can be observed when neighbors with virtual orbitals stabilize the wave function when being located at short distances from the ICD participants allowing for electronic coupling (superexchange ICD) [19–22]. However, even for well-separated and electronically decoupled neighbors, it was found that an increasing number (N) of neighbors of either A [23,24] or B [25,26] type makes ICD at least N times faster [13,27]. The effect depends on the specific geometric arrangement of the neighbors [26,28,29] as well as on the initially excited state. If, for example, two sites A are both excited, they may undergo excited ICD (exICD) between each other [23,30–34] or collective ICD (CICD) together with B, requiring multiple simultaneous energy-transfer processes to bring up the ionization energy for B [24].

Despite this first characterization of the listed ICD pathways, their occurrence and interplay is still rather unexplored. If, for example, asymptotic formulae were used for the prediction of the decay, each possible channel is treated individually [23,24], whereas the electron dynamics treatment includes the full multitude of decay channels [25,26]. However, electron dynamics calculations were not yet done for the ABA system, which was more intensely studied otherwise. Hence, in this paper we target a linearly aligned ABA systems with an electronic confinement along the alignment direction. Such an example is a model for quantum dots in a nanowire, as may be encountered in quantum networks. Moreover, we distinguish two initial resonances states, a singly excited (SE) and a doubly excited (DE) one and compare which processes occur at what inter-QD distance and how they contribute ICD.

In Section 2.1 the pathways are introduced via asymptotic equations, and in Sections 2.2 and 3 the model and the electron dynamics treatment is explained. In the result Sections 4.2.1 and 4.2.2, the rates are shown for the complete processes and for individual subprocesses in comparison in order to explain the unexpected lowering of rates compared to that of the regular two-site ICD process.

2. Theory

2.1. Pathways of the Inter-Coulombic Decay in a Linear ABA Array

The regular ICD process, an inherent two-electron effect, will occur in its extension by three electrons on three sites along different pathways simultaneously, depending on the underlying electronic structure of the model system. Here, we explicitly focus on a system composed of two two-level sites A and one one-level site B located exactly in their center as underlying all schematic representations in Figures 1 and 2. The outer sites A are separated by the distance R_{AA}, whereas the central site B in the coordinate origin is distant from each of the other sites A by $R_{AB} = R_{AA}/2$. Owing to this arrangement, every two-electron subprocess introduced below has an isoenergetic and symmetry-equivalent counterpart.

The two lowest-energy excited states localized in the array are A^*BA and ABA^*, in which one site A is in its excited state. By design of the energetic model it is a Feshbach resonance state [2], which is termed the SE resonance state throughout. With the ICD boundary condition for energies, $\Delta E_A > IP_B$, imposed, which says that the excitation energy ΔE_A of the A site has to be larger than the ionization potential IP_B of the B site, A^*BA can decay into AB^+A via regular ICD among only two of the neighbors participating, the third one remaining a spectator. This is sketched in the lower panel (b) of Figure 1 (on the left-hand side) with the relaxing site A being encircled in turquoise and the electron-emitting site B in brown, according to the persistent color code for this section ignoring for the moment the inactive black site. As said, the process can happen among the central B and either of the left- or right-hand side A.

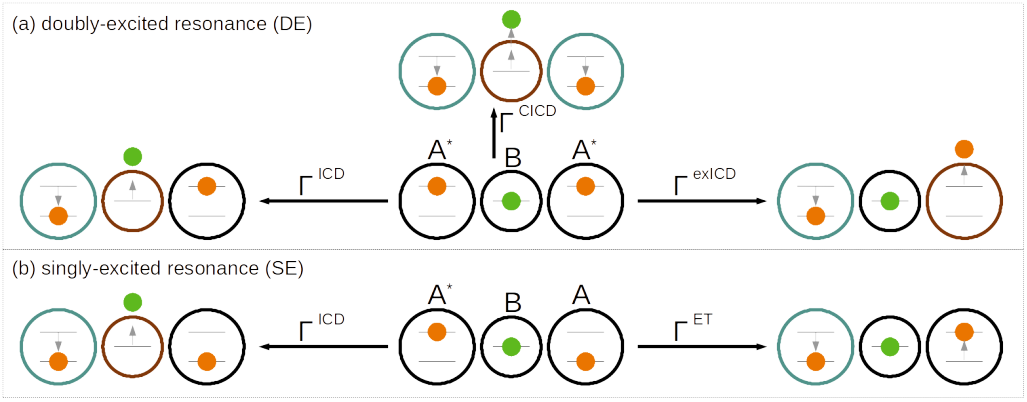

Figure 1. Overview of decay processes of up to three electrons on three Coulomb-coupled sites ABA in linear arrangement. The decaying (**a**) doubly excited (DE) and (**b**) singly excited resonances are shown in the center of each panel. To the left in (**a**) and (**b**) the standard inter-Coulombic decay (ICD) among two sites is shown with relaxation (turquoise) of the electron of site A (orange) and ionization (brown) of the electron from B (green). To the right, the coupled energy-transfer (ET) among the two sites A (orange electrons) is depicted, resulting in an excited-state ICD (exICD) for the DE resonance (**a**) and a Förster-like transfer for the SE resonance (**b**) not leading to ionization. In the DE case, a collective ICD (CICD) through two-photon transfer from relaxation of both A (turquoise) can lead to ionization of the central site B (brown) as shown along the upward direction.

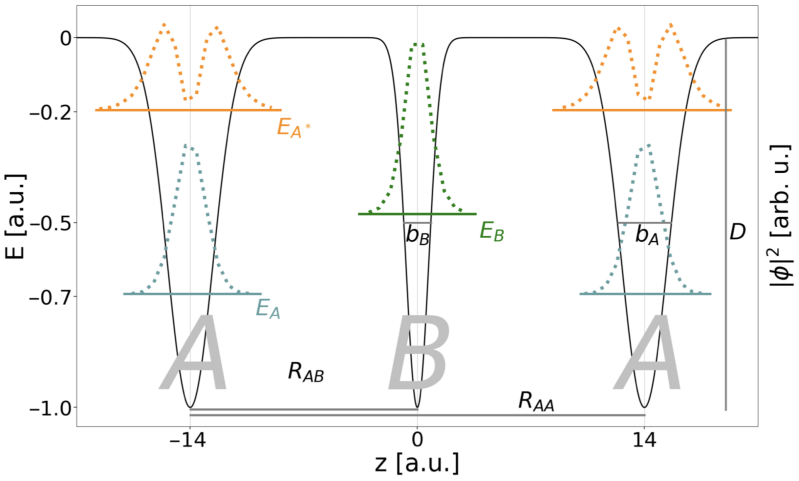

Figure 2. Representation of the three-QD array ABA for a distance $R_{AA} = 28$ a.u. parametrized according to Table 1. In the negative energy range the single-electron levels A (turquoise), B (green), and A^* (orange) are displayed together with the respective densities $|\phi|^2$. Furthermore, the geometric parameters of the binding potential (Equation (9)) are illustrated.

Table 1. Energies in a.u. of single- (E_{1e}) and three-electron states (E_{3e}), in the latter case for the minimum and maximum distance, $R_{AA}^{min} = 20$ a.u. and $R_{AA}^{max} = 70$ a.u., respectively.

E_{1e}		E_{3e}	R_{AA}^{min}	R_{AA}^{max}
E_{A^*}	−0.196	$E_{A^*BA^*}$	−0.613	−0.797
E_B	−0.477	E_{A^*BA}	−1.113	−1.295
E_A	−0.693	E_{ABA}	−1.613	−1.793

The rate Γ^{ICD} for a regular two-site ICD process $A^*B \rightarrow AB^+ + e^-$ in diverse chemical systems was in the past computed through various types of time-independent [35–40] as well as time-resolved [8] methods, which prove the validity of a simplified rate equation derived from the Wigner–Weisskopf theory [12,13]. Therein, one electron is assumed to

undergo spontaneous radiative decay $A^* \rightarrow A$ and the other photoionization $B \rightarrow B^+ + e^-$. The respective general golden rule ansatz is

$$\Gamma^{ICD} \propto 2\pi |\langle \phi_1^A \phi_2^{B+} | \hat{r}_{12}^{-1} | \phi_1^{A^*} \phi_2^B \rangle|^2. \tag{1}$$

In this spin-free ansatz, one assumes separability of the wave function into a product of nonoverlapping single-electron orbital functions ϕ and negligible exchange for the well-separated electrons enumerated 1 and 2, which we will also anticipate for all following derivations of this type. The respective decaying state is coupled by the Coulomb interaction operator $\hat{r}_{12}^{-1}$ to a multitude of final continuum states. One core result of Equation (1) for the distance dependence is $\Gamma^{ICD} \propto R_{AB}^{-6}$, which originates from the coupling of the two dipole transitions on the two subunits A and B. Another is that the rate increases linearly with the number N of neighbors [13,27], which will manifest itself in the following discussion.

For the SE decay process, the golden rule ansatz of Equation (1) is extended to three-orbital wave functions [25]. The final state is clearly $\phi_1^A \phi_2^{B+} \phi_3^A$. On the other hand, the decaying state must be an equal superposition of one excited outer site and one in its ground state, i.e., $2^{-1/2}(\phi_1^{A^*} \phi_2^B \phi_3^A + \phi_1^A \phi_2^B \phi_3^{A^*})$. Considering that the Coulomb interaction $\hat{r}_{ij}^{-1}$ always couples only two electrons, it allows the factorization of the rate equation into

$$\begin{aligned} \Gamma_{\mathrm{SE}}^{ICD} &\propto 2\pi |2^{-1/2} \langle \phi_1^A \phi_2^{B^+} | \hat{r}_{12}^{-1} | \phi_1^{A^*} \phi_2^B \rangle \langle \phi_3^A | \phi_3^A \rangle \\ &+ 2^{-1/2} \langle \phi_2^{B^+} \phi_3^A | \hat{r}_{23}^{-1} | \phi_2^B \phi_3^{A^*} \rangle \langle \phi_1^A | \phi_1^A \rangle|^2. \end{aligned} \tag{2}$$

Note that the only terms that are unity are those for which the overlap is kept among the ϕ_i orbitals factorized from the Coulomb integral (rightmost factor). In the absolute square of the Coulomb integrals (and the prefactors) we identify the two-electron ICD rate of Equation (1); hence

$$\Gamma_{\mathrm{SE}}^{ICD} = 2 \cdot \Gamma^{ICD}. \tag{3}$$

Beyond the interaction among the A and B site, a pathway that involves coupling of the two outer A sites shall be mentioned. As identical two-level systems, they are candidates for a Förster resonance energy transfer among the electrons depicted in orange in Figure 1b, whereas the green one is spectating [14]. This means that while the excitation on one site decays (turquoise circle), the other site is being excited but not ionized, i.e., $A^*A \rightarrow AA^*$. An ET-rate equation can be set up in the spirit of the ICD rate equation, resulting in

$$\begin{aligned} \Gamma_{\mathrm{SE}}^{ET} &\propto 2\pi |2^{-1/2} \langle \phi_1^{A^*} \phi_3^A | \hat{r}_{13}^{-1} | \phi_1^A \phi_3^{A^*} \rangle \langle \phi_2^B | \phi_2^B \rangle \\ &+ 2^{-1/2} \langle \phi_1^A \phi_3^{A^*} | \hat{r}_{13}^{-1} | \phi_1^{A^*} \phi_3^A \rangle \langle \phi_2^B | \phi_2^B \rangle|^2. \end{aligned} \tag{4}$$

According to Förster theory it likewise leads to a proportionality $\Gamma_{\mathrm{SE}}^{ET} \propto R_{AA}^{-6}$ [14]. ET is a reversible process in which at any time A^* levels are populated to a constant amount. Therefore, ICD is always likewise possible either with the A QD on the one side or the other. Moreover, ET does not lead to ionization, so that the rate of Equation (4) will not integrate into an overall decay rate for the three-electron SE system which thus remains $\Gamma_{SE} = \Gamma_{SE}^{ICD}$ following R_{AB}^{-6}.

In the upper panel (a) of Figure 1, all decay channels of a DE are collected. Given the single-electron levels available on the three sites, this resonance is A^*BA^*. The regular ICD process among two sites A and B is available for the SE resonance (to the left); here, keeping one spectating two-level site in its excited states A^* thus leads to the symmetry-equivalent final states A^*B^+A and AB^+A^*. The rate is given through the Wigner–Weisskopf derivation [13,25–27] as

$$\begin{aligned}\Gamma_{\mathrm{DE}}^{ICD} &\propto 2\pi|2^{-1/2}\langle\phi_2^{B^+}\phi_3^A|\hat{r}_{23}^{-1}|\phi_2^B\phi_3^{A^*}\rangle\langle\phi_1^A|\phi_1^A\rangle \\ &+ 2^{-1/2}\langle\phi_1^A\phi_2^{B^+}|\hat{r}_{12}^{-1}|\phi_1^{A^*}\phi_2^B\rangle\langle\phi_3^A|\phi_3^A\rangle|^2 \\ &= 2\cdot\Gamma^{ICD}. \end{aligned} \quad (5)$$

Next, there is also a process based on the Coulomb coupling of the electrons at both sites A (orange) as shown toward the right-hand side of Figure 1a. It resembles the resonance energy transfer that had been discussed for the SE decaying state and an ICD process at the same time. In addition, one excitation decays into its ground state $A^* \rightarrow A$ (turquoise circle). The transferred energy is sufficient to ionize the other site (brown circle) according to $A^* \rightarrow A^+$. The process, which we term here excited ICD to distinguish it from regular ICD, has been formulated before [23]. The rate equation is set up as

$$\begin{aligned}\Gamma_{\mathrm{DE}}^{exICD} &\propto 2\pi|2^{-1/2}\langle\phi_1^{A^+}\phi_3^A|\hat{r}_{13}^{-1}|\phi_1^{A^*}\phi_3^{A^*}\rangle\langle\phi_2^B|\phi_2^B\rangle \\ &+ 2^{-1/2}\langle\phi_1^A\phi_3^{A^+}|\hat{r}_{13}^{-1}|\phi_1^{A^*}\phi_3^{A^*}\rangle\langle\phi_2^B|\phi_2^B\rangle|^2 \end{aligned} \quad (6)$$

based on the fact that there may be two symmetry-equivalent pathways leading to the two final states ABA^+ and A^+BA. In terms of the decay behavior, this does not differ from any ICD process with lower exited states, i.e., it obeys the same distance behavior R_{AA}^{-6} as well as other relations which are deduced from the Wigner–Weisskopf rate equation. Note that in a collinear arrangement, the maximal distance among both sites A, $R_{AA} = 2R_{AB}$, may cause a significantly lower rate $\Gamma^{exICD} << \Gamma^{ICD}$ nonetheless, whereas some bent arrangements may cause a closer proximity among both A than among A and B, leading thus to a very fast exICD.

Note that the creation of a DE initial state is particular here, and can be achieved, e.g., by a very short [23] or intense pulse [30,31]. There had been a theoretical study on neon dimers undertaken with the Fano–Stieltjes approach, which considers exICD for neon distances shorter than the distance where the asymptotic formula might become valid [23]. It was followed by the derivation of analytical equations of motion for the electron dynamics combined with nuclear dynamics on the excited state potential energy surfaces [30] and ultimately confirmed experimentally in neon dimers [31] also for decay cascades including higher excited neon states in clusters [32]. The exICD was also shown for helium droplets, where it was found to scale with the number of neighbors [33,34].

Much more unexplored are the collective ICD processes [24], in which all electrons participate. In a two-photon energy transfer, the central site B is ionized (and excited, superscript $+*$) in that both sites A deexcite simultaneously, as depicted toward the top in Figure 1a. Note, if B was DE into a bound state, the process would be a special form of resonance energy transfer called energy pooling [14].

The Wigner–Weisskopf formulation for the CICD three-electron process based on two-electron interactions uses second-order perturbation theory [24], giving as rate ansatz for our A^*BA^* example system

$$\Gamma_{\mathrm{DE}}^{CICD} \propto 2\pi\sum_t \left|\frac{\langle\phi_1^A\phi_2^{B^{+*}}\phi_3^A|\hat{r}_{ij}^{-1}|\Phi_t\rangle\langle\Phi_t|\hat{r}_{ij}^{-1}|\phi_1^{A^*}\phi_2^B\phi_1^{A^*}\rangle}{E_{A^*BA^*}-E_t}\right|^2. \quad (7)$$

Here, the transitions of the three electrons are split into virtual two-photon processes with different intermediate configurations t. Those can be either the state resulting from two A relaxations, $2A^* \rightarrow 2A$, the state after the B ionization with two photons, $B \rightarrow B^{+*} + e^-$, or the states after a regular or excited ICD process, i.e., one state out of ABA, $A^*B^{+*}A^*$, $2^{-1/2}(AB^+A^* + A^*B^+A)$ or $2^{-1/2}(AB + BA)$. No matter which one is chosen, both Coulomb integrals in our QD formulation give a dependency R^{-3} for the dipole–dipole transition in the short-range resonance-energy transfer regime [14] appli-

cable to the distance and transferred energies encountered in the ABA system. As the two integrals in Equation (7) multiply and are being squared, the rate for CICD follows R_{AA}^{-12}. However, with R_{AA}^{-12} the rate Γ^{CICD} decreases much more quickly than that of regular ICD, making CICD generally noncompetitive at long distances. Hence, CICD could only be seen under rigorous energy constraints excluding regular and excited ICD. This can be rationalized by being an unlikely three-particle process [23]. Only at short distances might it dominate other decay channels, but for such cases, Fano–ADC calculations on Kr_2Ar clusters resulted in lower rates than were predicted by the asymptotic formula [24]. Note that in the first work on CICD on Kr_2Ar clusters, the authors have assumed one of the interatomic distances to be as large as the wavelengths of the transferred photon (approximately 100 nm) and hence one integral obey R^{-2} [24].

Conclusively, with three contributions, the overall rate for DE-ICD, $\Gamma^{DE} = \Gamma_{DE}^{ICD} + \Gamma^{exICD} + \Gamma^{CICD}$, is richer than for SE, where we can, however, expect a lowering importance of contributions from left to right. For the dominating rate Γ_{DE}^{ICD}, a rate doubling is expected with an additional rate increase of the latter terms.

Moreover, any other decay processes can be largely excluded for the underlying model. The occupation of each few-level site with only a single electron as well as the energetics within the system exclude the occurrence of an Auger–Meitner process [41,42], to which ICD has to be compared in core-excited or ionized atoms and molecules. Then, we exclude any nuclear motion of the atoms forming one site. In cases of the sites being atoms or small molecules, instead, the nuclear motion was found to lead to fluctuating ICD rates [4,43–47]. For the sites being quantum dots, they would not move with respect to one another but rather, internally. However, such phonon-mediated dissipation was found to not compete with ICD unless their distances become very large [48]. Finally, the most straightforward radiative decay of the excited state A^* is known to be significantly slower than the discussed energy-transfer processes for any of the studied ICD materials [8].

2.2. Electron Dynamics in Model Potentials

The purpose of this study is to investigate the interplay of several simultaneously available ICD and related processes' channels in the context of fully correlated electron-dynamics computations. For computational feasibility and for some freedom in designing a few-level electronic structure, model potentials are used to reflect the three electron-binding sites ABA. Furthermore, this arrangement allows us to deliberately remove the spectator electron and its binding site for the discussed two-electron subprocesses, so that we target the role of the respective spectator electron site with those two, which are active participators in the process. In particular we can also reformulate the model into a single-electron picture for the ICD electron, setting up effective potentials imposed by neighboring sites and electrons, which is another means for interpretation of the full three-electron dynamics observed.

The specific potentials displayed in Figure 2 are models for quantum dots in a nanowire [8,25], in which the electronic motion occurs in one dimension along the z direction only, such that the two other Cartesian coordinates can be omitted [49]. The respective one-dimensional electronic Hamiltonian in atomic units for N electrons and M QDs reads

$$\hat{H} = \sum_{i=1}^{N} \left(-\frac{1}{2}\nabla_{z_i}^2 + \sum_{k=1}^{M} \hat{V}_k^{\mathrm{QD}}(z_i) + \hat{V}_{\mathrm{CAP}}(z_i) + \sum_{j<i}^{N} \hat{r}_{ij}^{-1} \right). \tag{8}$$

The summands define the kinetic energy, the QD confinement potential for each QD k, as well as the complex absorbing potential (CAP) for each electron i and the Coulomb interaction between the two electrons i and j.

The electronic structures of QD conduction bands open to a nanowire environment are represented by Gaussian potentials shown in Figure 2 and given by

$$\hat{V}_k^{\mathrm{QD}}(z_i) = -D_k \exp\left(-b_k(\hat{z}_i - z_k)^2\right). \tag{9}$$

Here, b_k relates to the widths of the Gaussian potential and is reproducing the QD extension along the nanowire, and z_k marks the position. Throughout this study, the electron-emitting QD B with one electronic level is placed in the origin of the z axis and is framed by one or two two-level QDs A at positions $-R_{AB}$ only or $\pm R_{AB}$. R_{AA} is the distance between the minima of the respective potentials of the A-type QDs. D_k is finally the depth of the binding potential, and the energetic zero point marks the onset of the continuum for unconfined electrons.

The last single-electron operator of Equation (8) is a CAP with

$$\hat{V}^{\mathrm{CAP}}(z_i) = -\mathrm{i}\left(\hat{W}_z^L + \hat{W}_z^R\right). \tag{10}$$

Already anticipating the concepts of electron dynamics introduced below, the CAP hinders a continuum ICD electron wave packet from backscattering onto the QD system at the edges of the finite grid by transferring it into the imaginary space. Actually, two CAP operators

$$\hat{W}_z^{L,R} = \eta\ |z - z_{L,R}|^n\ \Theta(\pm(z - z_{L,R})). \tag{11}$$

are placed to the left (L) and the right (R) side of the QD array along the negative and positive z direction, respectively. They are defined through the strength parameter η, the order n, the onset position $z_{L,R}$ and the Heaviside step function Θ, which ensures that the CAP vanishes for $|z < z_{L,R}|$.

The Coulomb-interaction operator essentially mediating ICD, is by virtue six-dimensional and nonseparable. Because the two interacting particles are in a one-dimensional model, here an effective Coulomb potential,

$$\hat{V}(z)_{ij} = \sqrt{\frac{\pi}{2}} \exp\left(\frac{z_{ij}^2}{2}\right) \mathrm{erfc}\left(\frac{z_{ij}}{\sqrt{2}}\right), \tag{12}$$

is used [49,50]. It is derived for the case of a wire potential with a strong harmonic oscillator confinement in x and y directions, the excited states of which are energetically inaccessible here, such that the wave function can be separated and x and y components integrated.

For analysis reasons, we define an effective potential for the ICD electron j in B [8]. To this end, the electrons i occupying single-particle bound states $\phi_n(z_i)$ with $n = A$ or A^* of the two A QDs and their Coulomb repulsion with the B electron are added to the general binding potential giving

$$\hat{V}^{\mathrm{eff}}(z_j) = \sum_{k=1}^{M} \hat{V}_k^{\mathrm{QD}}(z_i) + \sum_{i=1}^{(N-1)} \langle \phi_n(z_i) | r_{ij}^{-1} | \phi_n(z_i) \rangle. \tag{13}$$

In order to execute electron dynamics simulations, the N-electron wave packet is given in the antisymmetrized multiconfiguration time-dependent Hartree (MCTDH [51,52]) form

$$\Psi(z_1, \ldots, z_N, t) = \sum_{j_1}^{n_1} \ldots \sum_{j_N}^{n_N} A_{j_1,\ldots,j_N}(t) \prod_{\kappa=1}^{N} \varphi_{j_\kappa}^{(\kappa)}(z_\kappa, t). \tag{14}$$

The antisymmetry in electron exchange is introduced by a condition on the expansion coefficients,

$$A_{j_1,\ldots,j_l,\ldots,j_k,\ldots,j_N}(t) = -A_{j_1,\ldots,j_k,\ldots,j_l,\ldots,j_N}(t), \tag{15}$$

thus realizing a quartet state for three electrons. Furthermore, a number of n_κ single-particle functions (SPFs) $\varphi_{j_\kappa}^{(\kappa)}(z_\kappa, t)$ for each degree of freedom (DOF) κ (each electron here) is used and expressed in a time-independent basis set as

$$\varphi_{j_\kappa}^{(\kappa)}(z_\kappa, t) = \sum_{i_1=1}^{N_\kappa} c_{i_\kappa}^{\kappa, j_\kappa}(t) \chi_{i_\kappa}^{(\kappa)}(z_\kappa), \tag{16}$$

where $c_{i_\kappa}^{\kappa,j_\kappa}(t)$ are the time-dependent expansion coefficients and $\chi_{i_\kappa}^{(\kappa)}(\mathbf{r}_\kappa)$ is a primitive basis function. On the basis level, those are ultimately implemented within a discrete variable representation (DVR) [53–55].

MCTDH approximates the solution of the time-dependent Schrödinger equation by using the Dirac–Frenkel variational principle to derive equations of motion for the MCTDH expansion coefficients and SPFs, which are propagated in time.

All desired observables for the interpretation of the dynamical processes of the electrons in the QD systems are obtained from the propagated wave packet. The absolute square of the projection of the time-dependent wave function $\Psi(t)$ onto the initial wave function $\Psi(0)$, i.e., the squared autocorrelation function, gives information about the decay process via the decay rate Γ [8], which is obtained by fitting the exponential slope to

$$|a(t)|^2 = |\langle\Psi(0)|\Psi(t)\rangle|^2 = e^{-\Gamma t}. \tag{17}$$

To analyse the populations of the different single-electron states s, a projection

$$P_s(t) = N|\langle\phi_s|\mathbf{1}^N|\Psi(t)\rangle|^2 \tag{18}$$

of the time-dependent N-electron wave function on the respective one-electron wave function ϕ_s with $s = A, A^*, B$ is performed, including a projection on an N-electron identity matrix $\mathbf{1}^N$. For continuum states, we are reintroducing the continuum contribution into their population [56].

3. Computational Details

MCTDH calculations are executed with the Heidelberg program [53,57]. A sine DVR in the interval $[-100, 100]$ with 300 grid points represents the primitive basis. CAPs are placed at $z_{L,R} = \pm 50$ a.u. The CAP order is set to $n = 3$ and the strength to $\eta = 9.5 \cdot 10^{-7}$ a.u. Furthermore, the effective Coulomb operator (Equation (13)) is brought into a sum-of-products form by using the potfit subroutine [58].

For block improved relaxations [59,60] in the CAP-free system, which give the eigenstates with discretized continuum, typically $n_\kappa = 48$ SPFs are used for each mode. In rare cases of numerical instabilities during relaxation, the number of SPFs is increased to at most 80 SPFs. In the propagations $n_\kappa = 8$ SPFs are sufficient. In both types of MCTDH calculations, a constant mean fields integrator (CMF) is applied with an accuracy of 10^{-2} a.u. or 10^{-8} a.u. for the relaxation and propagation calculations, respectively. CMF step sizes are fixed to 0.1 a.u. in relaxations and variable in propagations. The SPFs are relaxed (propagated) by using the Runge–Kutta method of order 8 with an error tolerance 10^{-6} (10^{-8}) a.u. and an initial step size of 0.1 a.u. Improved relaxation furthermore requires a Davidson routine to diagonalize the vector of MCTDH-coefficients, using here a maximal order of 800 and an accuracy of 10^{-6} a.u. The one-dimensional initial functions are chosen as Gaussian functions. Their width is 2.0 a.u. To propagate the vector of MCTDH coefficients, the short iterative Lanczos algorithm is used with an order of 15 and a step size of 10^{-8} a.u. The total propagation time is chosen differently for the systems (10^4–10^5 a.u.) to ideally reveal the decay happening at different rates.

The binding potential of the respective QD system is defined in Equation (9), with either two or three QDs, $M = 2, 3$. The depth of the respective binding potential is always $D = 1$ a.u. and the sizes of the QDs are chosen to be $b_A = 0.25$ a.u. and $b_B = 1.0$ a.u. A scan over the distance between the outer QDs is performed in the interval $R_{AA} = [20, 70]$ a.u.

4. Results

4.1. Electronic Structure

The present work focuses on the dynamical processes undergone by three electrons in three linearly aligned QDs. Figure 2 depicts the Gaussian binding potential model for the QD array which is designed such that the central QD is of B type with one energy level and the outer two of A type. The corresponding one-electron energy level values are

listed in the two leftmost columns of Table 1. The model was designed such that the energy difference between the two levels on site A, ΔE_A, is always larger than the ionization energy of B, IP_B. This implies that already only one excited outer electron in a state A^* suffices to open the ICD pathway, whereas ET is possible anyway. Likewise, for two excited electrons in two states A^* all SE and DE pathways sketched in Figure 1 shall be accessible.

An overview of energies and electron densities $|\Psi(0)|^2$ of the three-electron eigenstates with respect to increasing distance R_{AA} between the outer QDs is given in Figure 3 and in Table 1 as obtained from MCTDH relaxation calculations. In panels (a) and (c), corresponding to distances $R_{AA} = 20$ and 70 a.u., both localized resonance states of interest can be identified by density inspection. The DE resonance A^*BA^* depicted as dark green top line has the highest energy listed ($E_{A^*BA^*} = -0.613$ a.u. for $R_{AA} = 20$ a.u.). Its density clearly indicates the even distribution of electrons onto the QD. One electron is in QD B occupying its only state and hence showing a Gaussian-type density, while excited states A^* of the other two QDs are occupied such that the local density there has a node centered on the QD. Upon increase of the distance R_{AA}, the state energy clearly drops due to the significantly decreasing Coulomb interaction of electrons on each pair of sites A or B.

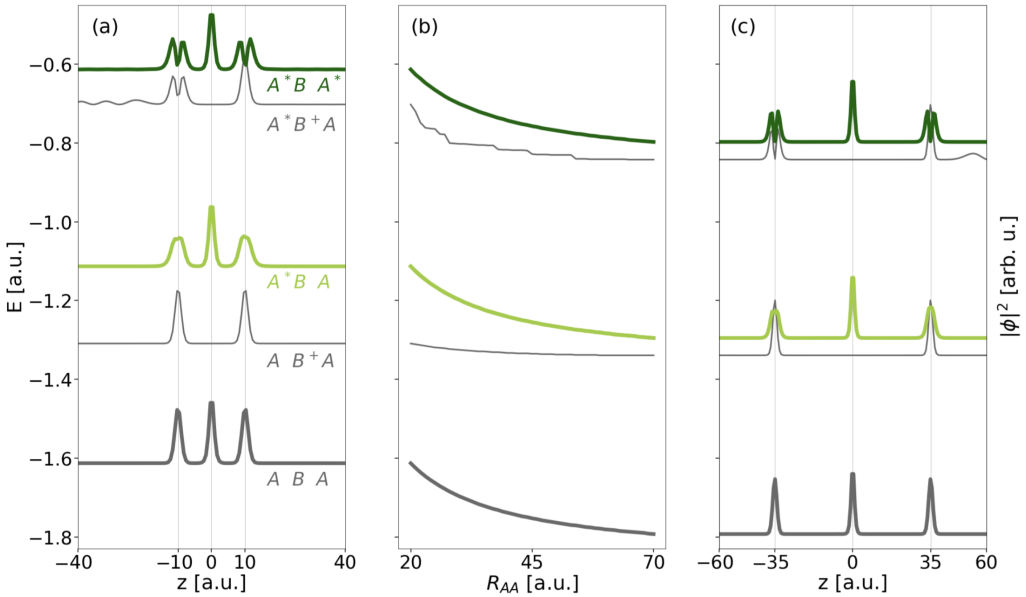

Figure 3. The energies of the key localized states of the three-electron three-QD system are displayed as a function of distance R_{AA} (panel (**b**)). From bottom to top ground state (ABA), first continuum state of type AB^+A, lower of SE resonances A^*BA, first continuum state of type A^*B^+A, and DE resonance A^*BA^* are displayed. The normalized three-electron densities $|\Psi(0)|^2$ in the left- and rightmost panel are leveled by the respective state energies at the given distance $R_{AA} = 20$ a.u. in (**a**) and 70 a.u. in (**c**).

The SE resonance (light green, third from top), which is twofold, degenerates into ABA^* and A^*BA serving both as initial states for the two processes presented in Figure 1b at $R_{AA} = 20$ a.u. It has with $E_{A^*BA} = -1.113$ a.u. a lower energy than the DE resonance by the approximately 0.5 a.u. corresponding to the energy difference among A and A^*, which likewise applies to all shorter distances as well. The local electron density on the outer QDs has a broad and flat peak due to the superposition of the A^* and A density contributions, whereas the local density contribution on B remains unchanged compared to A^*BA^*. The other, degenerate state (not shown) has generally the same density profile. The $E - R_{AA}$ profile (b) follows the same trend as of the DE resonance and likewise does the ground state. It has three localized electrons ABA and $E_{ABA} = -1.613$ a.u. at $R_{AA} = 20$ a.u. Both electrons on the A side occupy the lower state of the two-level system and have a narrow Gaussian-type density like the electron occupying B (thick black bottom line in Figure 3).

Energetically in between the ground state and each of the resonances, there are the onsets of the two series of ICD continua into which the respective DE and SE resonances can decay. For the SE resonance this continuum sets on at $E_{AB^+A} = -1.309$ a.u. ($R_{AA} = 20$ a.u.). It consists of states of type AB^+A, meaning that there are two electrons localized in the A levels of the outer QDs, whereas no electron resides in the central QD. The third electron establishes density outside the area of the QDs, which is not visible from the representation in Figure 3, because it particularly spreads beyond $z = \pm 70$ a.u. Compared to the localized states the energy slope (b) is less steep here, because the electron from B has moved toward the edge of the grid and is basically not contributing to the Coulomb interaction, which is then mainly composed of interaction of two electrons in both A sites of amount R_{AA}^{-1} only.

The other series of continuum states resulting from the ICD of the DE resonance sets has densities revealing the displayed A^*B^+A-type (and nearly isoenergetic inverted AB^+A^*-type states, not shown). Again, the B side is not populated, whereas one outer QD is populated in the excited and one in the ground state. As can be seen on the right-hand side of the density in panel (c) and on the left-hand side in panel (a), the emitted electron assembles outside the QD region and also beyond the area shown ($[-40, 40]$ a.u.). Note that the contribution of the emitted electron in (a) has nodes for $z \leq -15$ a.u. and sets on energetically at $E_{A^*B^+A} = -0.702$ a.u. ($R_{AA} = 20$ a.u.). As the first continuum states typically has no nodes, here we have certainly not fully converged the continuum in the improved block-relaxation computation. This does not affect the intuitive understanding of the state manifold, but the shape of the $E - R_{AA}$ curve (b), which is not as flat as seen for the other continuum. The propagation is later executed in another functional basis and will therefore not suffer from an inaccurate state representation here.

Although the energy difference between the two initial states for ICD is nearly constant with increasing R_{AA}, the energy difference among them and the onset of their ionization continuum decreases. The kinetic energy of the ICD electron decreases likewise. Moreover, for the one-dimensional continuum we have observed effects that depend on the continuum electron's energy in conjunction with effective repulsive Coulomb barriers established by the remaining bound electrons in their final states f [8,17,25,61,62]. The effective potentials (Equation (13)) established for the DE- and the SE-ICD final state are shown in Figure 4 as dark and light green lines relative to the pure binding potential (Equation (9)) in black.

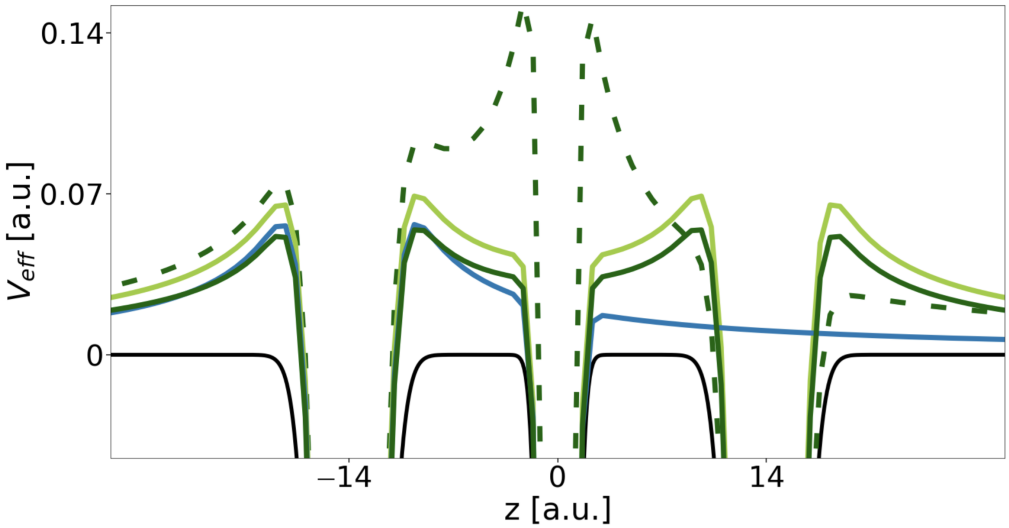

Figure 4. Illustration of the three-QD array ABA potential (black) displayed for $R_{AA} = 28$ a.u. within $[-0.045, 0.152]$ a.u. Furthermore, the effective Coulomb barriers resulting from electron configurations with the electron from B in the continuum, i.e., A^*B^+A (dark green), AB^+A (light green) and AB^+ (blue), respectively, as well as effective Coulomb barriers resulting from excited ICD electron configurations, i.e., ABA^+ (dashed dark green), are represented.

The DE final state (dark green) is a superposition state of A^*B^+A and AB^+A^* and shows a maximal barrier height of $E_B^f = 0.054$ a.u. Only when the electron ionized from B has sufficient kinetic energy to overcome this barrier can the decay process be expected to occur unhindered, which is the case for all $R_{AB} < 17$ a.u. (cf. Table 2). Otherwise situations may occur in which the electron is reflected from the Coulomb barriers and thus might be trapped in between both QDs or where the rate oscillates as a function of R_{AB}. For the SE resonance, the barrier height in the final state AB^+A is $E_B^f = 0.070$ a.u. It is higher, because an electron in the A ground level has a larger contribution to the effective potential compared to an electron in the A^* excited level. The ICD electron overcomes the barrier for distances below $R_{AB} = 25$ a.u. This distance is larger despite the higher barrier, because the SE resonance is higher above its continuum than the DE resonance (cf. Figure 3). For comparison the two-electron two-QD setup would establish one effective barrier maximum at $V_{\text{eff}} = 0.056$ a.u. hindering all electrons with $R_{AB} \geq 15.5$ a.u. Finally, one effective potential is shown for the final state of the exICD of the DE resonance, i.e., ABA^+ (dark green, dashed). Here, the two remaining electrons establish a huge barrier around the B QD of $E_B^f = 0.152$ a.u., however due to the large kinetic energy of the exICD electron not leading to its hindrance within the analyzed range of distances (only for $R_{AB} > 35.0$ a.u.).

Ultimately, all single-electron state energies increase within the effective potential, whereby a state in the AB^+A potential is higher than in the A^*B^+A potential, e.g. the energy of the A level in the DE potential is $E_A(R_{AA} = 28) = -0.599$ a.u. and in the AB^+A potential $E_A(R_{AA} = 28) = -0.528$ a.u.

Table 2. Barrier energies E_{CB}^f and minimal distances R_{AB}^f from which the kinetic energy of electron B (for exICD A) drops below E_{CB}^f are given for the effective Coulomb barriers resulting from final f electron configuration of the DE, SE, regular ICD, and exICD process.

	DE	**SE**	**ICD**	**exICD**
E_{CB}^f (a.u.)	0.054	0.070	0.056	0.152
R_{AB}^f (a.u.)	17.0	25.0	15.5	> 35.0

4.2. Electron Dynamics

In the following, the electron dynamics of the decays of the DE and SE resonances is presented in terms of rates Γ computed from the absolute square of the autocorrelation function (Equation (17)), the norm as function of time, and the transient population of single-electron states (Equation (18)). In addition to the overall three-electron dynamics, a comparison with related two-electron dynamics of subprocesses in all three or only two QD potentials is offered for the DE electron configuration.

Figure 5 collects all decay rates as function of the distance R_{AA} (top abscissa) and R_{AB} (bottom abscissa) in a double-logarithmic representation. As all processes are considered extensions to regular ICD among two electrons on two sites (cf. Figure 1, left), the top $\Gamma - R_{AB}$ curve (blue crosses) applies to this regular ICD among only two electrons, and its sketch is displayed right next to the graph. Furthermore, a solid blue line is the fit of the R_{AB}^{-6} Wigner–Weisskopf asymptote to the data. The rates follow the general asymptotic trend, but oscillate, which was observed likewise for slightly modified QD pairs earlier and can be explained by the Coulomb barrier hindering the free motion of the ICD electron within the one-dimensional continuum; however, they sometimes allowing for tunneling (at highest Γ), leading to an effect beyond three orders of magnitude [8,25,61,62]. Here for paired QDs, the blockade sets on from $R_{AB} > 15.5$ a.u. (cf. Table 2). Similar to these former results is the order of magnitude of the average rates, e.g., 10^{-3} a.u. at $R_{AB} \approx 12$ a.u. and 10^{-5} a.u. at around twice that distance [8,25,61,62]. Note that the other curves of Figure 5 are going to be discussed whenever the respective processes are discussed in the following sections.

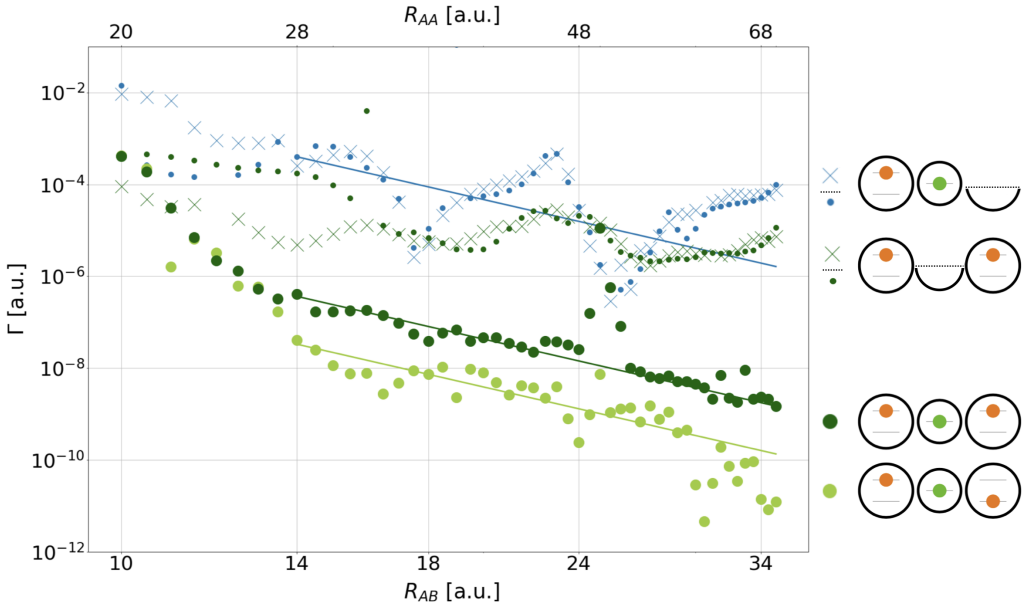

Figure 5. Double-logarithmic representation of the decay rates Γ as function of interdot distance R_{AB} (top abscissa R_{AA}) for the decay processes arising from the SE and DE initial electron configuration (light and dark green large dots). The configurations are shown on the right side (bottom) also for related two-electron processes (above) in the order of their decay rates. On top, the two-QD processes (blue, dark green crosses) are shown, followed by the two-electron, three-QD processes (blue, dark green small dots); the empty/removed QD is depicted as a half circle on the right. The asymptotic regime for regular, SE-, and DE-ICD is indicated by the rates' least-squares fit to R_{AB}^{-6} shown as solid lines in the corresponding color.

4.2.1. Dynamics of the Doubly Excited Resonance

The decay of the three-electron three-QD DE resonance A^*BA^* into the two symmetry-equivalent states A^*B^+A and AB^+A^* is the topic of this chapter. The most straightforward means to verify this expected decay is to inspect the level populations $P_s(t)$ in conjunction with the norm $N(t)$ as a function of time. The ones of $R_{AB} = 10$ a.u. (Figure 6) exemplify the behaviour for nearly all distances, for which the only distinguishing feature is the increasing duration of the process with distance (very few outliers will be discussed later). After an equilibration time of 300 a.u. for the initial noneigenstate, the decrease of the norm (solid dark-purple line) during propagation is exponential. It follows the decay of the squared autocorrelation function used to deduce the decay rate Γ_{DE}^{ICD} (Equation (17)). The decay comprises the emission of the B-type electron (dotted light-purple lines) and its absorption by the CAP along with the relaxation of the A^* electron (decreasing dashed line) into the A state (increasing dashed-dotted line). The behavior is the same as was observed for any regular two-electron ICD [8,61].

The rate of the DE resonance decay for all studied distances R_{AB} is displayed as dark green bold dots in Figure 5. The graph sets on at $4.63 \cdot 10^{-4}$ a.u., two orders below that of regular ICD, and firstly decreases quickly for 10 a.u. $\leq R_{AB} \leq$ 14 a.u. by nearly three orders of magnitude and then establishes its R_{AB}^{-6} trend within 14 a.u. $\leq R_{AB} \leq$ 35 a.u., leading in this larger range again to a decrease by more than two orders of magnitude. Two major differences in comparison to the two-electron ICD rate (blue crosses) jump to the eye: on the one hand, the A^*BA^* decays neatly, but less systematically, and follows the asymptote with only few obvious outliers around 25 a.u. and 32 a.u.

On the other hand, counterintuitively, the rates in the R_{AB}^{-6} regime are all in the range of $\Gamma_{DE} \approx 10^{-7}$–$10^{-9}$ a.u. and thus orders of magnitude smaller than the regular two-electron ICD rates of $\Gamma_{DE}^{ICD} \approx 10^{-3.5}$–$10^{-5.5}$ a.u. This disproves the original hypothesis $\Gamma_{DE} = \Gamma_{DE}^{ICD} + \Gamma^{exICD} + \Gamma^{CICD}$ of Section 2.1 for the one-dimensional continuum model system (cf. Figure 1), which postulated already a speeding according to $\Gamma_{DE}^{ICD} = 2\Gamma^{ICD}$ plus

contributions from the expectedly less relevant exICD and CICD processes. Given the trend of rates only, we cannot distinguish exICD with its R_{AA}^{-6} trend from ICD following the same asymptote. The only process we can exclude is CICD, as no trend R_{AA}^{-12}, e.g., along a steeper asymptotic slope, is seen in the asymptotic regime in the data points.

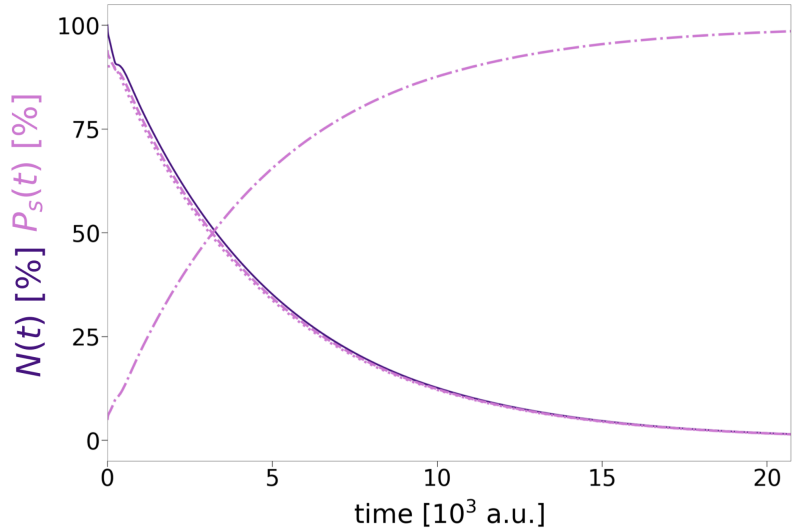

Figure 6. Time propagation of the norm $N(t)$ (dark purple, solid) as well as the single-state populations $P_s(t)$ (light purple) of A^* (dashed), A (dashed-dotted), and B (dotted) in % shown for $R_{AB} = 10$ a.u.

For the very low rates, inhibition of the ICD electron by the remaining bound electrons is of greatest importance. Two main profiles arise depending on the number of electrons surrounding the ICD electron. In two-electron systems as the one of regular ICD or the exICD system, the ICD electron populates an outermost QD. The related effective potentials, blue AB^+ and dashed dark green ABA^+ in Figure 4, respectively, have side-dependent barrier heights. By contrast, if the ICD electron is emitted from B in three linearly aligned QDs, a symmetric barrier is established along both emission directions (dark and light solid green lines), confining the electron from B. Here, the motion of the B electron is twice as restricted as in the two-electron systems and asymmetric exICD system. The rates are three orders lower. The amount of this lowering derives from the oscillations for regular ICD. The rate maxima (minima) correspond to a decay resulting in the continuum electron on one side (both sides) [8]. In the latter case, hindered electron tunneling through the effective barrier causes ICD slowing by two to three orders of magnitude. The emission of B within the three-electron dynamics involves tunneling through the effective barriers on both sides to which the B electron is evenly emitted. With the quantified barrier hindrance effect, the average rates for the DE decay (R_{AB}^{-6} asymptote in Figure 5) are indeed three orders lower than that of the averaged regular-ICD rates. Oscillations are flattened out due to the symmetry of the system. Based on electron dynamics in two-dimensional binding potentials with two-dimensional continua, in such systems a reduction of rates due to effective barriers can be expected to be less significant [17], such that in a continuum fully open in all directions, the asymptotic predictions with even a rate enhancement are supposedly fulfilled.

Having understood the overall rate trend, open questions remain on the short-distance behavior, the two additional processes CICD and exICD, and the rate outlier at $R_{AB} \approx 25.0$ a.u. To address the first, all three potential subprocesses are investigated individually, starting with the regular two-electron ICD process now in a three-QD setting with one empty QD A placed on the positive z axis. The rate is given as small blue points in Figure 5, compared to the blue-crossed rate of ICD in two QDs. Over large ranges of $R_{AB} \geq 15.5$ a.u., where the single-electron wave functions obey the asymptotic nonoverlapping condition, the rates are almost identical. They display the same oscillations known from the two-electron two-

QD case as caused by the Coulomb barrier of the electron remaining in A and massively determining the electron emission direction [8]. However, at smaller distances the rates turn out much lower in the presence of one empty A-type QD. The evolution of the electron density distribution in Figure 7 can explain this observation. It shows that the electron density in the initially empty QD A at $z = +14$ a.u., which should only be a spectator, increases over time as in this nonasymptotic regime charge transfer (CT) is not excluded. Density accumulates in its lower A level, and is therefore no more available to ICD. This means that solely the presence of one nearby potential already slows the decay process. At the shortest R_{AB}, this CT effect determines the overall rate Γ_{DE} in Figure 5 as here the small blue points are matching the large dark green ones for the DE decay.

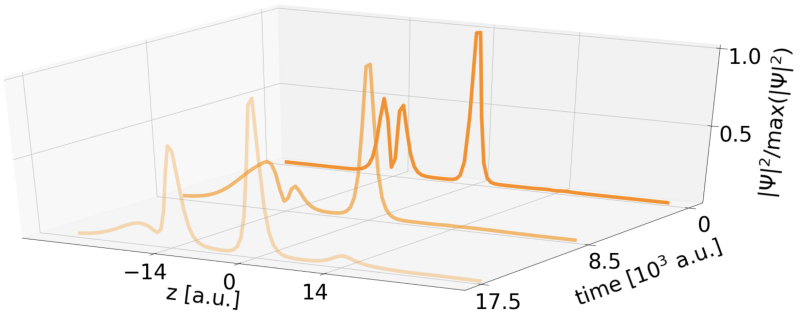

Figure 7. Illustration of the electron density distribution weighted to its maximal value for three propagation timesteps. The initial wavefunction has electron density corresponding to two electrons in one A^* state and in B separated by $R_{AB} = 14$ a.u., but no density in the other A site.

CICD was already excluded by rationalization, hence, of the other subprocess, exICD, remains for close investigation. The excited ICD process among the two outer QDs can be modeled for two electrons both in two and in three QDs. The respective graph symbols in Figure 5 are dark green crosses and small points. In general, the rates are decreasing and cover values of about $10^{-3.5}$–10^{-6} a.u. that are nearly identical for large $R_{AB} \geq 16$ a.u. where CT among QDs is excluded. There, rates oscillate with a similar period as those of regular ICD of A^*B, but with a significantly lower amplitude. This goes back to the fact that the exICD electron stems from a higher energy state, has therefore a higher kinetic energy, and is conclusively much less affected by the Coulomb barrier of the remaining electron (cf. Figure 4, dark green, solid line). The $\Gamma - R_{AB}$ trend does over long ranges not follow the asymptotic R_{AA}^{-6} trend, as was likewise observed for atomic clusters [23,32,34], but projections $P_S(t)$ on the state occupations (not shown) confirm exICD.

Another proof is the density inspection relating to the two-electron AA^* decay in Figure 8. Panel (a) reveals that the density strictly shows occupation of the A^* levels of the two only QDs A. It actually decreases over time, which is not seen due to renormalization. The sole observation is a widening of the local densities above both QDs due to the constant leak out of the continuum electron from both A^* levels.

As for short distances $R_{AB} < 16$ a.u. one finds again a discrepancy among the decay rates for two and three QDs with the difference to regular ICD that here the additional QD does not slow down the decay process as before, but actually speeds it up (small dark green dots above crosses in Figure 5). A hint for this behaviour can be gained from the electron density evolution with an additional empty B QD (Figure 8b). This empty well allows electron density to transfer into the B state and thus gives rise to regular ICD of A^*B. As ICD is obviously the faster decay pathway compared to exICD, the rate in the three-QD system is higher. Conversely, we can state that exICD is accelerated solely by the presence of one additional empty potential with a virtual B level in the vicinity. The process itself is not unknown. It was characterized in the context of atoms as superexchange ICD [19–22]. Here, we observe a similar rate increase for the two-electron exICD at shortening distances. As, moreover, the overall rate for three-electron DE decay at shortest distance increases,

this presumably has the same origin, because the B level constantly gets unoccupied by regular ICD and allows for superexchange ICD.

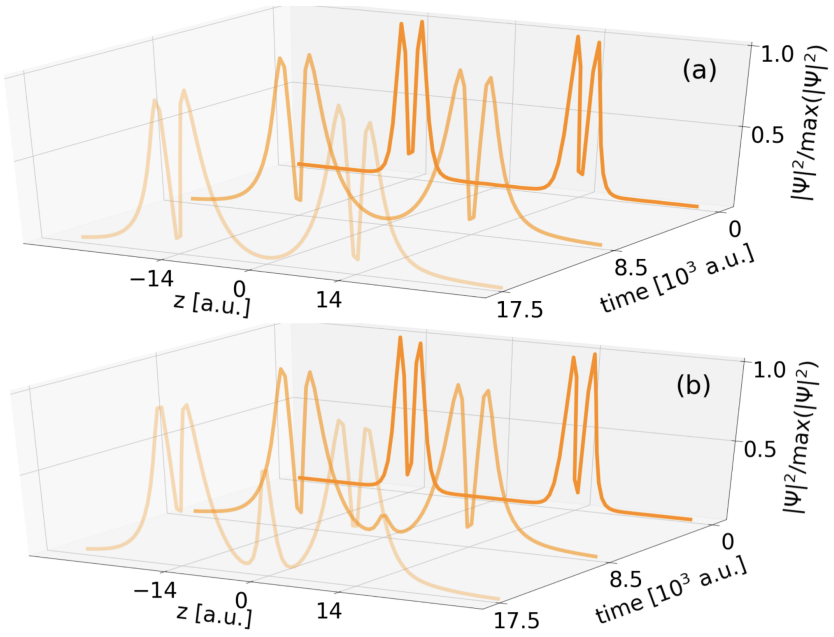

Figure 8. Comparison of the normalized electron density distribution of exICD of a two-electron A^*A^* state in two (**a**) and three QDs (**b**) for three propagation time-steps and $R_{AA} = 28$ a.u.

For the larger separations 17 a.u. $\leq R_{AB} \leq$ 35 a.u. the R_{AB}^{-6} Wigner–Weisskopf prediction and the Coulomb barriers dictate the rates. In the remainder of this section, we shall explicitly analyse the dynamic properties of the processes at distances where rate outliers occur. Around 31.5 a.u. $< R_{AB} <$ 34 a.u. a few rates deviate from the asymptote. The detailed analysis of the respective densities, populations, and energies does not, however, reveal any exceptional behaviour here, so we must assume that at these small rates, the limit of numerical accuracy is reached.

The most prominent outliers toward extremely large Γ_{DE} are in the range 24.5 a.u. $< R_{AB} <$ 27 a.u. The rates at $R_{AB} = 25$ and 25.5 a.u. lie almost exactly on the rate curve for regular two-electron ICD.

In Figure 9a, the level occupations $P_s(t)$ (light-purple lines, dashed for A^*, dashed-dotted for A, dotted for B), autocorrelation $|a(t)|^2$ with the initial resonance (dark purple), and the norm (light purple, solid line) are collected for $R_{AB} = 25$ a.u. As uniform to all decays studied, the norm decays exponentially on the full time scale of the process. In almost all other cases (e.g., Figure 6) level populations and squared autocorrelation have followed this monotonic trend, but in the time close-up of $50 \cdot 10^3$ a.u. in Figure 9a, they appear to oscillate strongly and periodically, the autocorrelation and the B population (dotted) in particular by about 50% reduction and rebuild. The population evolution of the two excited levels in the outer QDs (both dashed with different spacing) largely follow the autocorrelation in altering by half of the amount (25%), whereas the populations of the two ground states of the outer two-level QDs (dashed-dotted with different spacing) oppose. This suggests that a partial inversion of the population occurs in the respective two-level A sites, during which the energy is transferred to the B electron and exciting it. The specialty at this exclusive distance is that the B electron then can deexcite again. However, the three-QD system had been designed to have a single level in the B QD only and any excitation of the B electron should be into the continuum leading to disappearance of it into the CAP. Thus the question arises as to which type of state B^* is excited by.

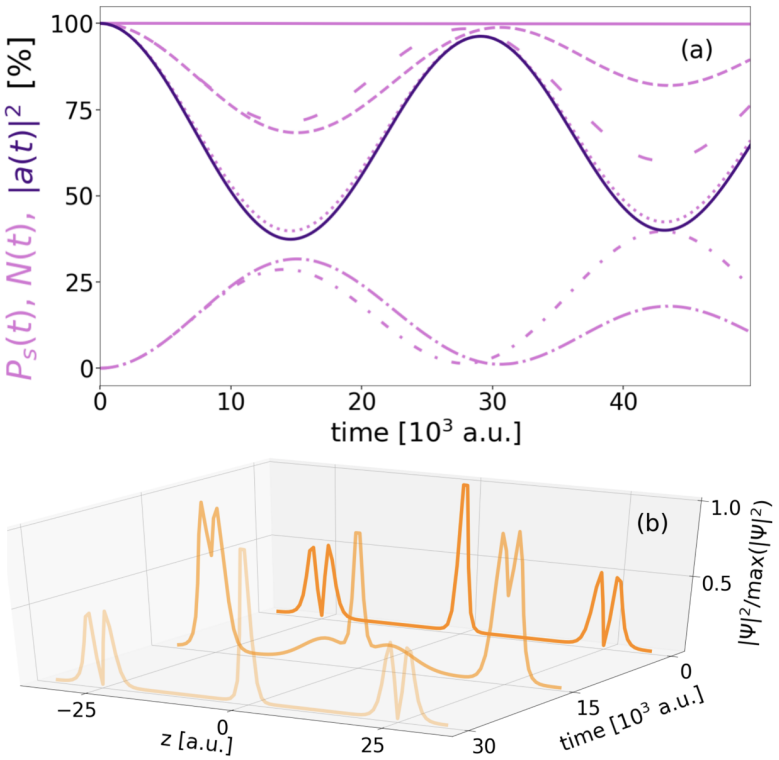

Figure 9. The DE decay's single-state populations $P_s(t)$ (light purple, interrupted), as well as the norm $N(t)$ (light purple solid) and the squared autocorrelation $|a(t)|^2$ (dark purple solid) as function of time for $R_{AB} = 25$ a.u. in (**a**). The three individual states s examined are A^* (dashed), A (dashed-dotted), distinguishable by tight or loose markers for right or left QD, and B (dotted). In (**b**) the normalized electron density distribution $|\Psi|^2 / \max(|\Psi|^2)$ is presented for three characteristic time steps of the propagation.

The electron density distributions in panel (b) for three critical time steps of the evolution shall give clarification. The initial electron density distribution shows a clear A^*BA^* state. At the turning point of minimal A^* and B of panel (a), i.e., after $15 \cdot 10^3$ a.u., the density on the outer QDs is a mixture of A and A^* density. Further density appears in between the A-sites centered around the B-level density peak, but filling almost all the area to the outer QDs. This indicates the excited B electron being trapped between the electrons in the A QDs. This way, the B electron remains in the QD region and is available to energy back-transfer to the A sites. And indeed, after another half period of oscillation, the initial distribution of electron density is almost regained. In the following the oscillations continue as typical for plain resonance-energy transfer [14].

A look at the effective potential for the final DE configuration at $R_{AB} = 25$ a.u. and is associated single-electron B^* state energy and density shall contribute to the understanding of why the process becomes so fast in this given setting (Figure 10b). The effective potential (green line) has two maxima at each side surrounding both A QDs. They are narrow near their peaks but widen quickly. Above the B side, this causes the formation of a very wide and flat potential well covering a range of approximately $z \in [-20; 20]$ a.u. Above the B ground state, which energetically locates in the narrow B potential with energy -0.459 a.u., an excited state B^* localizes in this wide, upper well at energy 0.030 a.u. such that the excitation energy is matching the one available through $A^* \rightarrow A$ relaxation. This B^* state's electron density piles up left and right of the B site limited to the other side by the effective potential barriers. Its shape resembles the density contribution discovered in Figure 9b, which made the wave function available for the oscillatory energy transfer seen in Figure 9a. In addition B^* energetically locates where the tunneling barriers are very narrow. This setting suggests that we found a shape resonance in the effective potential.

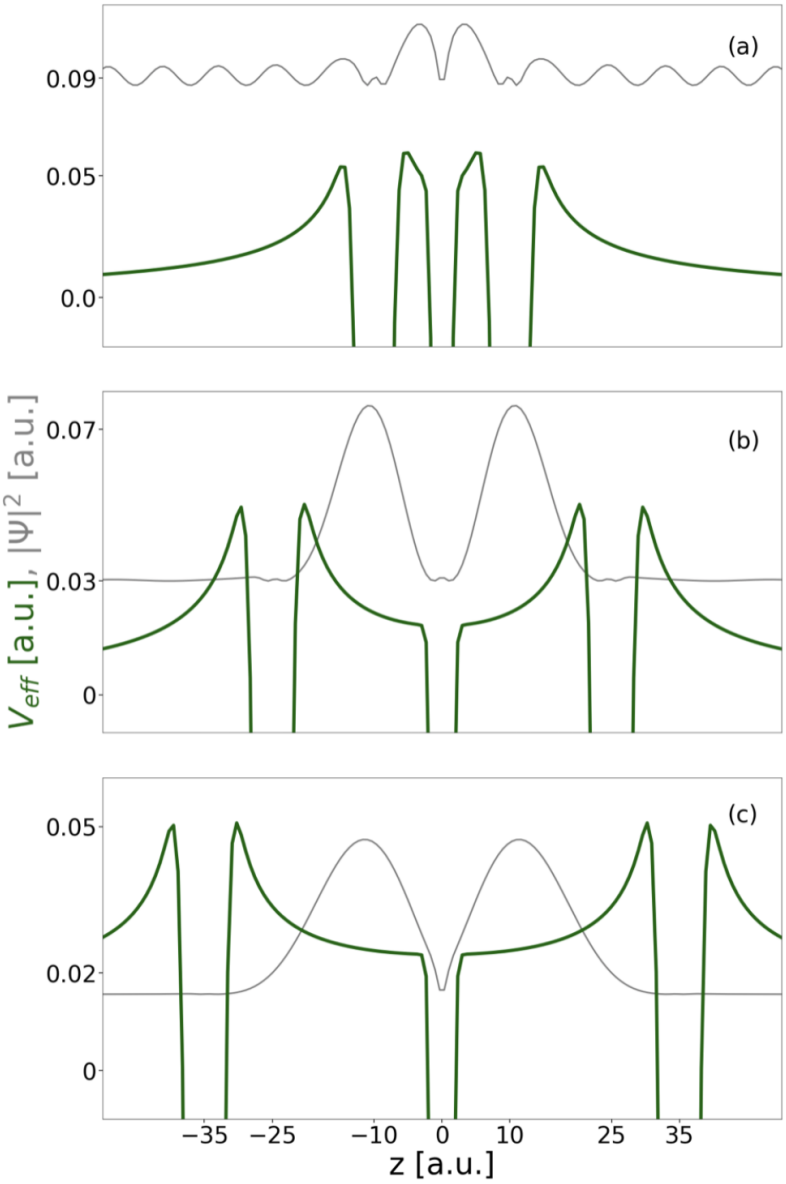

Figure 10. Illustration of the density $|\Psi|^2$ of the B^* single-electron state (thin, grey line) in the effective potential of the final DE electron configuration (thick, dark green line) for (**a**) $R_{AB} = 10$ a.u., (**b**) $R_{AB} = 25$ a.u., and (**c**) $R_{AB} = 35$ a.u.

The localized B^* state exists within a small range of distances only (where rates are high, Figure 5). If R_{AB} increases, the effective potential widens and the state's energy drops (Figure 10c). The B^* is there facing wider and relatively high barriers, makes tunneling less likely and a shape-resonance decay thus significantly slower. On the other hand, if the distances R_{AB} decrease, the energy of B^* increases above the effective Coulomb barrier, which occurs at energies $R_{AB} = 15.5$ a.u. The associated B^* density (Figure 10a) becomes delocalized and effectively that of a true continuum state.

The existence of a resonance state alone cannot lead to a high DE-ICD rate. Energetically, the shape resonance of the effective potential must occur at the energy of the three-electron final state, i.e., at the kinetic energy of the outgoing B electron, and likewise of the initial state, which are themselves determined by the geometry of the three-QD system. In Figure 11a the density of the AB^*A^* three-electron resonance is shown for which panel (b) presents the energy (grey) in comparison to the DE decaying state's energy (black). Obviously, the crossing is near $R_{AB} = 25$ a.u., which matches the region of

the largest DE-ICD rates. In all other regions in which there is no energy matching, the distance-dependent rates Γ^{DE} align to the R_{AB}^{-6} asymptote (cf. Figure 5).

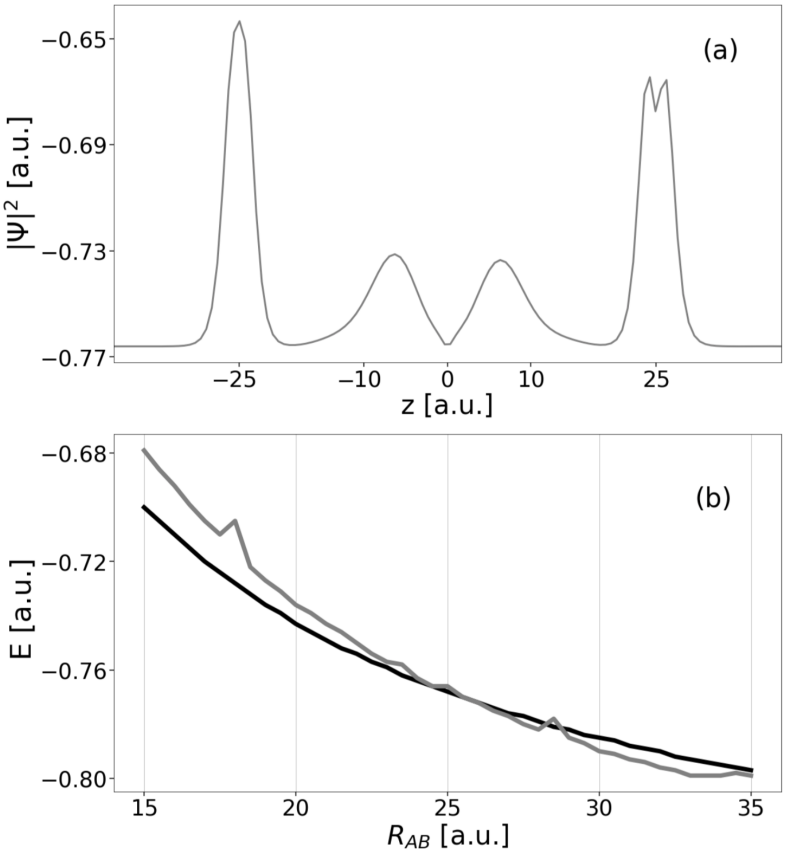

Figure 11. (**a**) Density $|\Psi|^2$ of the three-electron shape-resonance AB^*A^* (grey) at $R_{AB} = 25$ a.u. and (**b**) its state energy E (grey) compared to the energy of the initial electron DE state A^*BA^* (black) as function of R_{AB}.

Therefore, we found here a shape resonance-enhanced pathway to the decay of the A^*BA^* state, which is in all other cases a Feshbach resonance decay only. The pathway can only exist in systems with a continuum confinement and is available for very few energy settings. During the shape resonance-enhanced decay, the electronic configuration belonging to the shape resonance is reached quickly (within $15 \cdot 10^3$ a.u., Figure 9). It then decays efficiently into the final states A^*B^+A and AB^+A^*, as shape resonances always decay faster than two-electron Feshbach resonances (e.g. the ICD initial state) [8] .

4.2.2. Dynamics of the Singly Excited Resonance

In the following, we will focus on the dynamical processes of the SE resonance A^*BA, which include regular ICD among QDs A and B, as well as the Förster-like resonance energy transfer among the two outer QDs A (cf. Figure 1, bottom), where the latter, however, should not lead to a decay in competition with ICD. The expectation formulated for the decay is straightforwardly $\Gamma_{SE} = \Gamma_{SE}^{ICD}$. To recall, the SE resonance is a superposition of the two symmetry-equivalent eigenstates with a single excitation of either of the outer QDs, the left (A^*BA) or right (ABA^*). Therefore, every quantitative analysis (e.g., rates) is made according to this superposition.

Figure 5 shows Γ_{SE} as light green bold dots, revealing it to be the lowest overall rate at most inter-QD separations. The Γ_{SE}-R_{AB} graph divides into two ranges with different decay behavior. The rates at the short-distance range $R_{AB} \leq 14.0$ a.u., where the asymptotic equations are not valid, decrease steeply and are nearly equal to the DE rates. For larger distances $R_{AB} \geq 14$ a.u. the SE rates drop below the DE rates and then follow

the R_{AB}^{-6} asymptote. Overall outliers toward lower rates in both zones are the process at $R_{AB} = 11$ a.u. and those from $R_{AB} > 30$ a.u. The latter very low rates drop significantly below the asymptote and are artifact of the numerical limits of the calculations.

To understand the decay behavior, we can benefit from our investigations of DE processes. In SE processes, neither accelerating nor decelerating short-range CT effects can be observed. An acceleration effect would require an enhancement of the population of an A^*B state. In the DE case, this was obtained through CT of the A^* electron from the other site to B. Here, the corresponding tunneling would have to be from the lower A level with narrow density, which is energetically and in terms of overlap not favorable. Compared to the DE resonance, the SE resonance energy is almost twice as low (Figure 3), hence there are fewer ionization channels below. In the long-distance region of the Γ_{SE}-R_{AB} graph, SE dynamics does, like DE dynamics, follow the asymptote R_{AB}^{-6} without drastic rate oscillations as known from the regular ICD. The reason for this flatness is the symmetry of the effective barrier forming the B electron confinement. The rates are even one order slower as it has a significantly higher effective barrier to tunnel (cf. Figure 4).

As there are neither marked outliers in the behavior of Γ, nor does CT at short distances apply, the last analysis is directed to the observation of ET among the outer QDs as a potential side process to ICD. The norm and level populations of the three-electron SE dynamics are therefore compared for four representative distances (Figure 12). The initial wave functions for the analyses are obtained from the improved block relaxation and mostly represent neither a complete superposition nor a pure eigenstate of A^*B^+A and AB^+A^*, but actually their linear combinations. An even superposition, where the right QD is occupied in the A (dashed-dotted) and the A^* (dashed) level each by 50% arises for the case $R_{AB} = 10$ a.u. (Figure 12a, light purple lines). An identical occupation holds for the left QD (not shown). Over time, the population of the A^* levels reduces toward 0%, i.e., the A levels' occupation inverts. At the same time the B population (dotted) and the overall norm (solid line) both decrease exponentially from 100% according to Γ^{SE} as depicted in Figure 5. This is in principle the behavior as expected for a regular two-electron two-QD ICD process [56], but first traces of ET among both A QDs are evident from the numerical data.

This gets more pronounced and even visible from the propagation, when going to the larger distances, $R_{AB} = 13$ a.u. (Figure 12a, dark purple), $R_{AB} = 21$ a.u. and $R_{AB} = 34$ a.u. (light and dark purple in panel (b) with a longer observation time), where the dominance of ICD decreases. The decay becomes inherently slower, such that the B population and the norm remain majorly at their initial 100% in the displayed time window. In these scenarios, the level populations of the outer QDs display dominantly Förster-like ET dynamics by periodically inverting between A^* and A of the coupled dipoles over time, and overall $A^*A \rightleftharpoons AA^*$. For $R_{AB} = 13$ a.u. the full inversion is beyond the displayed data in (a), while the inversion or transfer time is $56 \cdot 10^3$ a.u. for $R_{AB} = 21$ a.u. and $257 \cdot 10^3$ for $R_{AB} = 34$ a.u. By using similar data for further distances we observe the transfer rate, the inverse of the transfer time, decrease with increasing R_{AB}. This is not surprising, as energy transfer processes also depend on Coulomb interaction (Equation (4)). Here, ET rates follow an R_{AB}^{-3} trend. This indicates that not all assumptions of a dipole–dipole transition are valid in the present system, because the short-range ET in atomic and molecular systems of typical electron excitation energies is supposed to be the coupling of dipole transitions leading to the well-known R_{AB}^{-6} dependence (Section 2.1). However, in other studies it was shown that the R dependence is not trivially predictable in significantly altered geometries and systems [14]. There is intermediate-range transfer with an R_{AB}^{-4} dependence and long-range energy transfer with a R_{AB}^{-2} rate dependence depending on the relation of size of the ET partners and the wave length of the transferred virtual photon. Besides the plain theory, distance dependencies of R_{AB}^{-3} and R_{AB}^{-5} have also been reported [63].

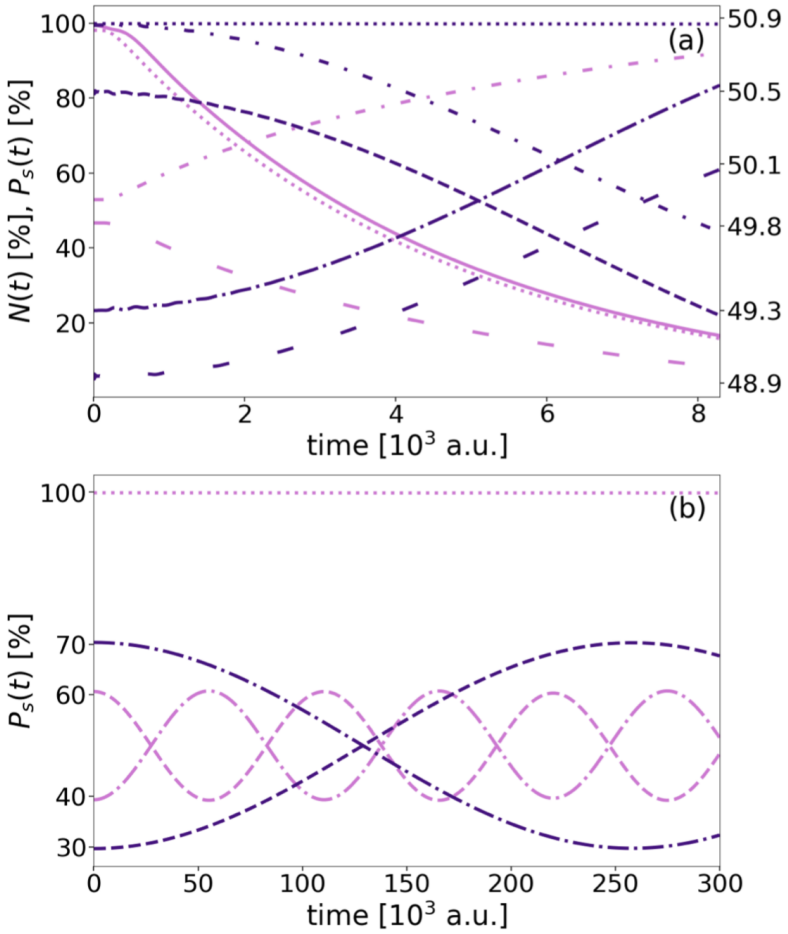

Figure 12. Single-state populations $P_S(t)$ (interrupted lines) and norm $N(t)$ (solid) in % as function of the propagation time for the SE decay. In (**a**) the left ordinate and light purple lines belong to $R_{AB} = 10$ a.u., whereas dark purple lines and the right ordinate correspond to $R_{AB} = 13$ a.u. In (**b**) projections corresponding to $R_{AB} = 21$ a.u. (34. a.u.) are indicated in light (dark) purple. The five individual states examined are A^* (dashed), A (dashed-dotted), each tight or loosely for right or left QD in (**a**), and B (dotted).

The absolute rates for this ET are all in the range of 10^{-5} a.u. for the wide range of distances given. Explicitly, they are $4.78 \cdot 10^{-5}$ a.u. $> \Gamma_{SE}^{\mathrm{ET}} > 0.39 \cdot 10^{-5}$ a.u. within 15.0 a.u. $< R_{AB} <$ 34.0 a.u. If comparing the rates with $\Gamma_{SE} = \Gamma_{SE}^{\mathrm{ICD}}$ in Figure 5, their crossing occurs near R_{AB} = 11.0–13.0 a.u., which matches the distance from which on CT of populations is overlaying ICD (Figure 12).

5. Conclusions

This paper comprises the study of the interparticle Coulombic decay process in an array of three linearly aligned binding sites with two virtual-photon donors A at the edges and an electron emitter B in the center. This ABA system design was chosen to provide a delineation of information to previously studied three-site ICD processes. To complement this, we investigate two possible excitation scenarios. In the SE scenario, only one photon donor is initially excited, whereas in the DE process, both A sites are. This work's investigations explore the electronic structure of the model system and, moreover, give a detailed description of the dynamics of three electrons in three linearly aligned QDs.

In a rationalization of possible subprocesses along with the formulation of their Wigner–Weisskopf rates, we analytically confirm predictions of at least a rate doubling with doubling of the number of photon emitters in agreement with previous findings. However, because this rate doubling is not confirmed by highly correlated electron dynamics, but

rather a strong rate decrease is found, all subprocesses are disentangled and studied individually. These are namely two-electron regular ICD for both initial states, for the DE case additionally excited ICD among only to excited photon emitters and collective ICD of three electrons, and for the SE case resonance energy transfer among the outer sites.

The breakdown into the individual subprocesses in conjunction with geometrical and energetic analyses revealed that a third, empty, site can affect the rates due to its ability to bind the electronic wave packet of a nearby neighboring site, which can in cases enhance (by superexchange ICD), and in others decrease the overall rates, depending on whether the electrons Coulomb interact more or less as a result of such charge transfer. Furthermore, linking information on the evolution of state energies and effective Coulomb barriers with inter-QD distance to dynamic quantities such as decay rates and population analyses provides insight into rate evolutions and relative speed of subprocesses.

For longer distances, a significant slowdown of the three-electron dynamics occurs compared to that of two electrons. We attribute this effect to the effective barriers hindering the ICD electron in the one-dimensional continuum to travel to any direction. In the SE case, those barriers are higher; hence, a generally more significant rate slowing is observed. This means that in the asymptotic regime, the decay of the SE or DE resonance would be overlaid by phonon-mediated dissipation [48] or radiative decay [8], which both have rates of about 10^{-6} a.u.

In the DE case, at a certain distance between sites, a synergistic effect of continuum confinement, energy levels, and Coulomb interaction emerges a shape-resonance pathway with an extraordinarily large rate. Here the *B* electron is initially excited into a localized, but nonetheless extended wave packet above the *B* site, from where it can decay quickly into the continuum.

Author Contributions: Conceptualization, J.-L.S. and A.B.; methodology, J.-L.S., F.L. and A.B.; software, F.L.; validation, F.L.; formal analysis, J.-L.S.; investigation, J.-L.S.; resources, A.B.; data curation, J.-L.S.; writing—original draft preparation, J.-L.S. and A.B.; writing—review and editing, J.-L.S., F.L. and A.B.; visualization, J.-L.S.; supervision, A.B.; project administration, A.B.; funding acquisition, A.B. All authors have read and agreed to the published version of the manuscript.

Funding: This research was funded by Volkswagen Foundation through the Freigeist Fellowship No. 89525.

Institutional Review Board Statement: Not applicable.

Informed Consent Statement: Not applicable.

Data Availability Statement: Data is available upon request from the authors.

Conflicts of Interest: The authors declare no conflict of interest.

References

1. Cederbaum, L.S.; Zobeley, J.; Tarantelli, F. Giant Intermolecular Decay and Fragmentation of Clusters. *Phys. Rev. Lett.* **1997**, *79*, 4778–4781. [CrossRef]
2. Feshbach, H. Unified theory of nuclear reactions. *Ann. Phys.* **1958**, *5*, 357. [CrossRef]
3. Morishita, Y.; Liu, X.J.; Saito, N.; Lischke, T.; Kato, M.; Prümper, G.; Oura, M.; Yamaoka, H.; Tamenori, Y.; Suzuki, I.H.; et al. Experimental Evidence of Interatomic Coulombic Decay from the Auger Final States in Argon Dimers. *Phys. Rev. Lett.* **2006**, *96*, 243402. [CrossRef] [PubMed]
4. Sisourat, N.; Kryzhevoi, N.V.; Kolorenc, P.; Scheit, S.; Jahnke, T.; Cederbaum, L.S. Ultralong-range energy transfer by interatomic Coulombic decay in an extreme quantum system. *Nature Phys.* **2010**, *6*, 508–511. [CrossRef]
5. Unger, I.; Hollas, D.; Seidel, R.; Thürmer, S.; Aziz, E.F.; Slavíček, P.; Winter, B. Control of X-ray Induced Electron and Nuclear Dynamics in Ammonia and Glycine Aqueous Solution via Hydrogen Bonding. *J. Phys. Chem. B* **2015**, *119*, 10750. [CrossRef] [PubMed]
6. Averbukh, V.; Cederbaum, L.S. Interatomic Electronic Decay in Endohedral Fullerenes. *Phys. Rev. Lett.* **2006**, *96*, 053401. [CrossRef]
7. De, R.; Magrakvelidze, M.; Madjet, M.E.; Manson, S.T.; Chakraborty, H.S. First prediction of inter-Coulombic decay of C60 inner vacancies through the continuum of confined atoms. *J. Phys. B* **2016**, *49*, 11LT01. [CrossRef]

8. Bande, A.; Gokhberg, K.; Cederbaum, L.S. Dynamics of interatomic Coulombic decay in quantum dots. *J. Chem. Phys.* **2011**, *135*, 144112. [CrossRef]
9. Cherkes, I.; Moiseyev, N. Electron relaxation in quantum dots by the interatomic Coulombic decay mechanism. *Phys. Rev. B* **2011**, *83*, 113303. [CrossRef]
10. Förster, T. Energiewanderung und fluoreszenz. Naturwissenschaften. *Naturwiss* **1946**, *33*, 166. [CrossRef]
11. Stryer, L.; Haugland, R.P. Energy transfer: A spectroscopic ruler. *Proc. Natl. Acad. Sci. USA* **1967**, *58*, 719–726. [CrossRef] [PubMed]
12. Santra, R.; Cederbaum, L.S. Non-Hermitian electronic theory and applications to clusters. *Phys. Rep.* **2002**, *368*, 1. [CrossRef]
13. Averbukh, V.; Müller, I.B.; Cederbaum, L.S. Mechanism of Interatomic Coulombic Decay in Clusters. *Phys. Rev. Lett.* **2004**, *93*, 263002. [CrossRef] [PubMed]
14. Jones, G.A.; Bradshaw, D.S. Resonance Energy Transfer: From Fundamental Theory to Recent Applications. *Front. Phys.* **2019**, *7*, 100. [CrossRef]
15. Weber, F.; Aziz, E.F.; Bande, A. Interdependence of ICD rates in paired quantum dots on geometry. *J. Comput. Chem.* **2017**, *38*, 2141. [CrossRef]
16. Stumpf, V.; Brunken, C.; Gokhberg, K. Impact of metal ion's charge on the interatomic Coulombic decay widths in microsolvated clusters. *J. Chem. Phys.* **2016**, *145*, 104306. [CrossRef]
17. Haller, A.; Peláez, D.; Bande, A. Inter-Coulombic Decay in Laterally Arranged Quantum Dots Controlled by Polarized Lasers. *J. Phys. Chem. C* **2019**, *123*, 14754–14765. [CrossRef]
18. Guskov, V.A.; Langkabel, F.; Berg, M.; Bande, A. An Impurity Effect for the Rates of the Interparticle Coulombic Decay. *QUARKS Braz. Electron. J. Phys. Chem. Mat. Sci.* **2020**, *3*, 31928. [CrossRef]
19. Miteva, T.; Kazandjian, S.; Kolorenč, P.; Votavová, P.; Sisourat, N. Interatomic Coulombic Decay Mediated by Ultrafast Superexchange Energy Transfer. *Phys. Rev. Lett.* **2017**, *119*, 083403. [CrossRef]
20. Votavová, P.; Miteva, T.; Engin, S.; Kazandjian, S.; Kolorenč, P.; Sisourat, N. Mechanism of superexchange interatomic Coulombic decay in rare-gas clusters. *Phys. Rev. A* **2019**, *100*, 022706. [CrossRef]
21. Bennett, R.; Votavová, P.; Kolorenč, P.; Miteva, T.; Sisourat, N.; Buhmann, S.Y. Virtual Photon Approximation for Three-Body Interatomic Coulombic Decay. *Phys. Rev. Lett.* **2019**, *122*, 153401. [CrossRef] [PubMed]
22. Agueny, H.; Pesche, M.; Lutet-Toti, B.; Miteva, T.; Molle, A.; Caillat, J.; Sisourat, N. Interparticle coulombic decay in coupled quantum dots: Enhanced energy transfer via bridge assisted mechanisms. *Phys. Rev. B* **2020**, *101*, 195431. [CrossRef]
23. Kuleff, A.I.; Gokhberg, K.; Kopelke, S.; Cederbaum, L.S. Ultrafast Interatomic Electronic Decay in Multiply Excited Clusters. *Phys. Rev. Lett.* **2010**, *105*, 043004. [CrossRef] [PubMed]
24. Averbukh, V.; Kolorenč, P. Collective Interatomic Decay of Multiple Vacancies in Clusters. *Phys. Rev. Lett.* **2009**, *103*, 183001. [CrossRef] [PubMed]
25. Langkabel, F.; Lützner, M.; Bande, A. Interparticle Coulombic Decay Dynamics along Single- and Double-Ionization Pathways. *J. Phys. Chem. C* **2019**, *123*, 21757. [CrossRef]
26. Langkabel, F.; Bande, A. Three-electron dynamics of the interparticle Coulombic decay with two-dimensional continuum confinement. *J. Chem. Phys.* **2021**, *154*, 054111. [CrossRef] [PubMed]
27. Santra, R.; Zobeley, J.; Cederbaum, L.S. Electronic decay of valence holes in clusters and condensed matter. *Phys. Rev. B* **2001**, *64*, 245104. [CrossRef]
28. Fasshauer, E.; Förstel, M.; Pallmann, S.; Pernpointner, M.; Hergenhahn, U. Using ICD for structural analysis of clusters: A case study on NeAr clusters. *New J. Phys.* **2014**, *16*, 103026. [CrossRef]
29. Förstel, M.; Mucke, M.; Arion, T.; Lischke, T.; Pernpointner, M.; Hergenhahn, U.; Fasshauer, E. Long-Range Interatomic Coulombic Decay in ArXe Clusters: Experiment and Theory. *J. Phys. Chem. C* **2016**, *120*, 22957. [CrossRef]
30. Demekhin, P.V.; Gokhberg, K.; Jabbari, G.; Kopelke, S.; Kuleff, A.I.; Cederbaum, L.S. Overcoming blockade in producing doubly excited dimers by a single intense pulse and their decay. *J. Phys. B At. Mol. Opt. Phys.* **2013**, *46*, 021001. [CrossRef]
31. Takanashi, T.; Golubev, N.V.; Callegari, C.; Fukuzawa, H.; Motomura, K.; Iablonskyi, D.; Kumagai, Y.; Mondal, S.; Tachibana, T.; Nagaya, K.; et al. Time-Resolved Measurement of Interatomic Coulombic Decay Induced by Two-Photon Double Excitation of Ne2. *Phys. Rev. Lett.* **2017**, *118*, 033202. [CrossRef]
32. Nagaya, K.; Iablonskyi, D.; Golubev, N.V.; Matsunami, K.; Fukuzawa, H.; Motomura, K.; Nishiyama, T.; Sakai, T.; Tachibana, T.; Mondal, S.; et al. Interatomic Coulombic decay cascades in multiply excited neon clusters. *Nat. Commun.* **2016**, *7*, 13477. [CrossRef] [PubMed]
33. LaForge, A.C.; Drabbels, M.; Brauer, N.B.; Coreno, M.; Devetta, M.; Di Fraia, M.; Finetti, P.; Grazioli, C.; Katzy, R.; Lyamayev, V.; et al. Collective Autoionization in Multiply-Excited Systems: A novel ionization process observed in Helium Nanodroplets. *Sci. Rep.* **2014**, *4*, 3621. [CrossRef]
34. Ovcharenko, Y.; Lyamayev, V.; Katzy, R.; Devetta, M.; LaForge, A.; O'Keeffe, P.; Plekan, O.; Finetti, P.; Di Fraia, M.; Mudrich, M.; et al. Novel collective autoionization process observed in electron spectra of He clusters. *Phys. Rev. Lett.* **2014**, *112*, 073401. [CrossRef]
35. Averbukh, V.; Cederbaum, L.S. Ab initio calculation of interatomic decay rates by a combination of the Fano ansatz, Green's-function methods, and the Stieltjes imaging technique. *J. Chem. Phys.* **2005**, *123*, 204107. [CrossRef] [PubMed]

36. Gokhberg, K.; Averbukh, V.; Cederbaum, L.S. Decay rates of inner-valence excitations in noble gas atoms. *J. Chem. Phys.* **2007**, *126*, 154107. [CrossRef]
37. Kolorenč, P.; Averbukh, V.; Gokhberg, K.; Cederbaum, L.S. Ab initio calculation of interatomic decay rates of excited doubly ionized states in clusters. *J. Chem. Phys.* **2008**, *129*, 244102. [CrossRef]
38. Averbukh, V.; Kolorenč, P.; Gokhberg, K.; Cederbaum, L.S. Quantum Chemical Approach to Interatomic Decay Rates in Clusters. In *Advances in the Theory of Atomic and Molecular Systems*; Springer: Dordreht, The Netherlands, 2009; Volume 20, p. 155.
39. Kreidi, K.; Demekhin, P.V.; Jahnke, T.; Weber, T.; Havermeier, T.; Liu, X.; Morishita, Y.; Schössler, S.; Schmidt, L.; Schöffler, M.; et al. Photo- and Auger-Electron Recoil Induced Dynamics of Interatomic Coulombic Decay. *Phys. Rev. Lett.* **2009**, *103*, 033001. [CrossRef] [PubMed]
40. Miteva, T.; Kazandjian, S.; Sisourat, N. On the computations of decay widths of Fano resonances. [CrossRef]
41. Åberg, T.; Howat, G. Corpuscles and Radiation in Matter I. In *Handbuch der Physick*; Springer: Berlin/Heidelberg, Germany, 1982; Volume 31, p. 419.
42. Matsakis, D.; Coster, A.; Laster, B.; Sime, R. A renaming proposal: "The Auger–Meitner effect". *Phys. Today* **2019**, *72*, 10–11. [CrossRef]
43. Santra, R.; Zobeley, J.; Cederbaum, L.S.; Moiseyev, N. Interatomic Coulombic Decay in van der Waals Clusters and Impact of Nuclear Motion. *Phys. Rev. Lett.* **2000**, *85*, 4490. [CrossRef] [PubMed]
44. Moiseyev, N.; Santra, R.; Zobeley, J.; Cederbaum, L.S. Fingerprints of the nodal structure of autoionizing vibrational wave functions in clusters: Interatomic Coulombic decay in Ne dimer. *J. Chem. Phys.* **2001**, *114*, 7351. [CrossRef]
45. Scheit, S.; Cederbaum, L.S.; Meyer, H.D. Time-dependent interplay between electron emission and fragmentation in the interatomic Coulombic decay. *J. Chem. Phys.* **2003**, *118*, 2092. [CrossRef]
46. Sisourat, N.; Kryzhevoi, N.V.; Kolorenč, P.; Scheit, S.; Cederbaum, L.S. Impact of nuclear dynamics on interatomic Coulombic decay in a He dimer. *Phys. Rev. A* **2010**, *82*, 053401. [CrossRef]
47. Chiang, Y.C.; Otto, F.; Meyer, H.D.; Cederbaum, L.S. Interrelation between the distributions of kinetic energy release and emitted electron energy following the decay of electronic states. *Phys. Rev. Lett.* **2011**, *107*, 173001. . [CrossRef] [PubMed]
48. Bande, A. Acoustic phonon impact on the inter-Coulombic decay process in charged quantum dot pairs. *Mol. Phys.* **2019**, *117*, 2014–2028. [CrossRef]
49. Pont, F.M.; Bande, A.; Cederbaum, L.S. Controlled energy-selected electron capture and release in double quantum dots. *Phys. Rev. B* **2013**, *88*, 241304. [CrossRef]
50. Bednarek, S.; Szafran, B.; Chwiej, T.; Adamowski, J. Effective interaction for charge carriers confined in quasi-one-dimensional nanostructures. *Phys. Rev. B* **2003**, *68*, 045328. [CrossRef]
51. Meyer, H.D.; Manthe, U.; Cederbaum, L. The multi-configurational time-dependent Hartree approach. *Chem. Phys. Lett.* **1990**, *165*, 73–78. [CrossRef]
52. Manthe, U.; Meyer, H.; Cederbaum, L.S. Wave-packet dynamics within the multiconfiguration Hartree framework: General aspects and application to NOCl. *J. Chem. Phys.* **1992**, *97*, 3199–3213. [CrossRef]
53. Beck, M.; Jäckle, A.; Worth, G.; Meyer, H.D. The multiconfiguration time-dependent Hartree (MCTDH) method: a highly efficient algorithm for propagating wavepackets. *Phys. Rep.* **2000**, *324*, 1–105. [CrossRef]
54. Light, J.C. *Time-Dependent Quantum Molecular Dynamics*; Plenum: New York, NY, USA, 1992; p. 185.
55. Light, J.C.; Carrington Jr, T. Discrete-Variable Representations and their Utilization. *Adv. Chem. Phys.* **2000**, *114*, 263. [CrossRef]
56. Bande, A. Electron dynamics of interatomic Coulombic decay in quantum dots induced by a laser field. *J. Chem. Phys.* **2013**, *138*, 214104. [CrossRef] [PubMed]
57. Meyer, H.D.; Gatti, F.; Worth, G.A. (Eds.) *Multidimensional Quantum Dynamics: MCTDH Theory and Applications*; Wiley-VCH: Weinheim, Germany, 2009.
58. Jäckle, A.; Meyer, H.D. Product representation of potential energy surfaces. *J. Chem. Phys.* **1996**, *104*, 7974. [CrossRef]
59. Meyer, H.D.; Worth, G.A. Quantum molecular dynamics: Propagating wavepackets and density operators using the Multi-configuration time-dependent Hartree (MCTDH) method. *Theor. Chem. Acc.* **2003**, *109*, 251. [CrossRef]
60. Meyer, H.D.; Le Quere, F.; Leonard, C.; Gatti, F. Calculation and selective population of the vibrational levels with the Multiconfiguration Time-Dependent Hartree (MCTDH) algorithm. *Chem. Phys.* **2006**, *329*, 179. [CrossRef]
61. Bande, A.; Pont, F.M.; Dolbundalchok, P.; Gokhberg, K.; Cederbaum, L.S. Dynamics of Interatomic Coulombic Decay in Quantum Dots: Singlet Initial State. *EPJ Web Conf.* **2013**, *41*, 04031. [CrossRef]
62. Berg, M.; Uranga-Piña, L.; Martínez-Mesa, A.; Bande, A. Wavepacket golden rule treatment of interparticle Coulombic decay in paired quantum dots. *J. Chem. Phys.* **2019**, *151*, 244111. [CrossRef]
63. Juzeliūnas, G.; Andrews, D.L. Quantum electrodynamics of resonant energy transfer in condensed matter. *Phys. Rev. B* **1994**, *49*, 8751. [CrossRef]

5.3 JELLYFISH: a modular code for wave function-based electron dynamics simulations and visualizations on traditional and quantum compute architectures

Fabian Langkabel, Pascal Krause and Annika Bande

Preprint version published and submitted to a peer-reviewed journal
DOI: doi.org/10.26434/chemrxiv-2023-p8384
URL: `https://doi.org/10.26434/chemrxiv-2023-p8384`

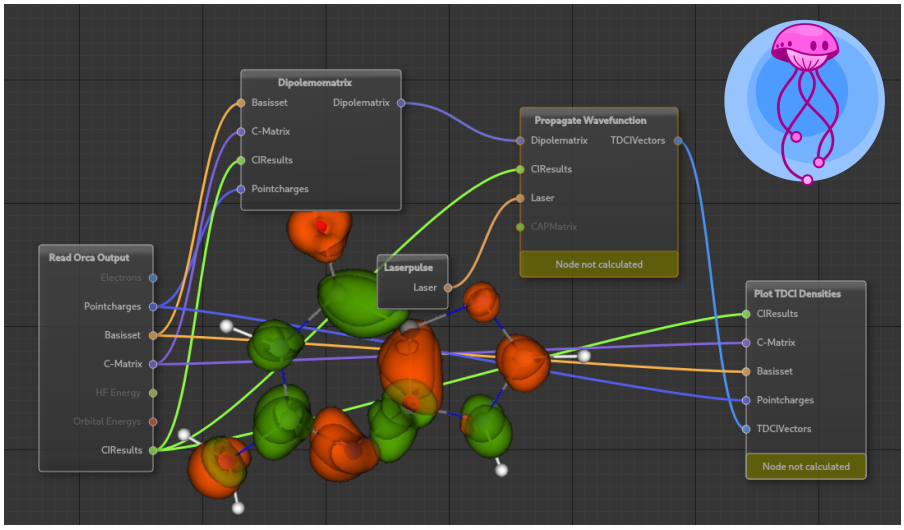

Figure 5.3: Graphical abstract created exclusively for this thesis

Author contributions: The need to develop a new dynamics program evolved from the initial implementation of the quantum algorithm in **[5]**. The goals for Jellyfish were defined by AB, PK, and FL. The code development was mainly done by FL and the program was extensively tested by PK. FL wrote the manuscript draft and all authors participated in the finalization.

JELLYFISH: a modular code for wave function-based electron dynamics simulations and visualizations on traditional and quantum compute architectures

Fabian Langkabel,[1, a)] Pascal Krause,[1] and Annika Bande[1, b)]

Helmholtz-Zentrum Berlin für Materialien und Energie GmbH, Hahn-Meitner-Platz 1, 14109 Berlin, Germany

(Dated: 6 July 2023)

Ultrafast electron dynamics has made rapid progress in the last few years. With Jellyfish we now introduce a program suite that enable to perform the entire workflow of an electron-dynamics simulation. The modular program architecture offers the flexible combination of different propagators, Hamiltonians, basis sets and more. Jellyfish can be operated by a graphical user interface, which makes it easy to get started for non-specialist users and gives experienced users a clear overview of entire functionality. The temporal evolution of a wave function can currently be executed in the time-dependent configuration interaction method (TDCI) formalism, however, a plugin system facilitates the expansion to other methods and tools without requiring in-depth knowledge of the program. Currently developed plugins allow to include results from conventional electronic structure calculations as well as the usage and extension of quantum-compute algorithms for electron dynamics. We present the capabilities of Jellyfish on two examples to showcase the simulation and analysis of light-driven correlated electron dynamics. The implemented visualization of various densities enables an efficient and detailed analysis for the long-standing quest of the electron-hole pair formation.

[a)] Also at the Institute of Chemistry and Biochemistry, Freie Universität Berlin, Arnimallee 22, 14195 Berlin, Germany

[b)] Electronic mail: annika.bande@helmholtz-berlin.de; https://hz-b.de/theochem

I. INTRODUCTION

Over the last years, there have been significant experimental advances in the field of spectroscopy that allow further insights into ultrafast processes. For example, thanks to attosecond electron/ion pump–probe spectroscopy, insights into the attosecond timescale are possible.[1] Such experiments help to understand the light-matter interaction in great detail for a variety of materials ranging from small molecules to nanostructures. Ultrafast electron dynamics plays a central role in the intricate ionization processes with strong fields of diatomic molecules, i.e. high-harmonics generation,[2,3] charge migration processes in organic molecules,[4,5] charge transfer in heterogeneous photocatalytic processes,[6] or energy transfer in semiconductor nanostructures.[7,8] In many studies of photo-induced processes in biological systems, few electronic states are considered with the focus on nuclear dynamics computations and the involvement of conical intersections, which play a significant role in the UV damage- and protection-mechanisms of DNA,[9] for example. The photochemical properties, however, are inherently the result of a state manifold, detailed understanding of radiation-induced electronic mechanisms, and the determination of excitation time scales and lifetimes of the states are of central interest.

Also in inorganic materials, the investigation of electronic processes in the time domain experiences a raising interest. One famous example are semiconductor quantum dots (QDs) that are increasingly gaining in importance for the usage as qubits in quantum computers,[10,11] for example. For the understanding of the capabilities of QDs as qubits, dynamical manipulation processes are investigated.[12] Moreover, undesired side effects are studied in order to estimate and suppress their influence.[13,14] These can be, among others, the Auger decay within a quantum dot[15,16] or the inter-Coulombic decay process between two or more QDs.[7,17] Both processes lead to the ionization of a QD and may decohere desired qubit states.

Even if many dynamical properties of a system like ionization rates or absorption spectra can be predicted from time-independent properties like transition dipole moments or excitation energies, the faster the considered processes happen and the more electronically excited states are involved, the more it is necessary to simulate the processes explicitly and to solve the time-dependent Schrödinger equation for the considered time period.

The methods used for this purpose are often extensions of the corresponding time-independent theories. There are single-reference methods, like time-dependent Hartree-Fock (TDHF)[18,19] or time-dependent configuration interaction (TDCI)[20–22] to propagate a wave function in time

explicitly. Also, time-dependent methodologies that propagate a reduced density matrix ρ in time to include effects of dissipation exist.[23,24] Multi-reference time-dependent methods like multiconfiguration time-dependent Hartree-Fock (MCTDHF)[25,26] are needed for situations with high static correlation like a photo-induced dissociation, for example. Even for the static density-matrix renormalization group (DMRG) methodology[27,28] there is a possibility for real-time evolutions by combining it with time-evolving block decimation (TEBD).[29]

For electronic structure calculations various programs like ORCA,[30] Psi4,[31] Q-Chem,[32] PySCF[33] and many more are available for academic users and commercially, which were developed over decades by large user and developer communities. They cover all steps from reading in and optimizing molecular structure to determining properties like nuclear magnetic resonance shielding parameters, dipole moments, vibrational and optical spectra at highest efficiency. This is not the case for most codes in the field of electron dynamics methods due to the younger age of the research field and the relatively smaller research community. Hence, available code is currently limited to executing the essential dynamic steps. This means that at the current state to perform and illustrate such dynamics calculations, several programs are needed and intermediate results have to be handled through various input and output files. A possible procedure for TDCI calculations as done for example by Weber *et al.*[34] consists of four steps. After geometry optimization, the molecule and basis set is read into ORCA to calculate the ground and all excited states using CI. The ORCA output file is then used in ORBKIT[35–37] to determine the full dipole matrix. Based on the ORCA output file and the dipole matrix, a ρ-TDCI calculation is performed using the GLOCT program.[24] Finally, the time-dependent wave function is analyzed and properties of interest are extracted. As can be seen from the example, many programs or tools are often designed for a single purpose – a single propagation method or a certain use case – and little attention was given to the possibility of successively extending them.

In this work, we introduce a platform with the program Jellyfish, which carries out electron dynamics simulations starting from the electronic structure calculation and ending with the visualisation of densities in motion in a single program. The main objective of the Jellyfish package is to provide a single program suite that is most easily expandable without becoming complicated for developers and users. These targets are obtained by a module and a plugin system. Individual partial calculations such as the calculation of dipole moments, the reading-in of a molecular geometry, for example, are developed as separate modules. These modules use the results of other modules and additional parameters for the successive calculations and then provide

output for the following modules. In this way, flexible computational workflows can be assembled by modules for a large variety of application purposes. Uncomplicated creation and modification of a workflow is possible through the graphical interface (GUI) that employs a NodeEditor to logically assemble and connect the modules. The incorporation of such a NodeEditor was inspired from other fields like 3D design, where the use of such a system has become a common interface. In combination with the use of a GUI instead of solely text-based input and output files allows an intuitive way of using the program. This makes it especially easy for new users to get started with the dynamics simulations.

Furthermore, a plugin system is underlying the code that allows to develop and compile modules independent from the main Jellyfish code. Several modules are bundled to a plugin and dynamically loaded into Jellyfish through an interface. New or modified methods and modules can thus be easily exchanged and published as plugins. To simplify the exchange of modules and the further development of Jellyfish, the code at its present state as well as the existing plugins is published under open source license. The plugins developed so far, have focused on the TDCI method, the visualization of time-independent and time-dependent wave functions, densities and orbitals, as well as fundamental quantum computing algorithms. With the functions available so far, Jellyfish can thus be used immediately for a number of dynamics problems without further development.

The paper is divided into four sections. In the section II. Design and Implementation, the exact requirements for Jellyfish are formulated and it is explained in how far these requirements are met by the design of the program. Here, the already mentioned module and plugin systems as well as the graphical user interface and the used file format are discussed. The next section III. Capabilities discusses which functions in the form of modules and plugins are already available with the release of the program. The section IV. Example Applications deals with two examples, which have been computed and evaluated with Jellyfish and demonstrate the functionality and flexibility of the program as well as key functions of the already implemented methods. In the last section V. Conclusion the main aspects and possibilities of the presented program are summarized.

II. DESIGN AND IMPLEMENTATION

The main objective of Jellyfish is to provide a platform that performs all steps necessary for a TDCI calculation and its visualization in a single program suite. To do so, a chain of calculations

and their post-processing can be set up in a consistent manner so that the users do not have to handle several programs and formats. That way, the margin for errors is reduced and, for example, conflicts due to updates for the data transfer from one program to the next can be avoided. In addition, the following demands were made for the development of Jellyfish:

1. Flexible: Jellyfish aims to provide a general interface in which various Hamiltonian, basis sets, wave function analysis tools, and other partial calculations can be arbitrarily combined as desired. For example, it should be possible to perform dynamics not only in molecules but also in a general electron-binding model potential. Also, a variety of propagators and time-dependent methods exist besides TDCI simulations. The time-dependent Hamiltonian also varies from application to application and may include, for example, interaction with external laser fields to compute laser-driven dynamics or complex absorption potentials to simulate ionization processes.

2. Extensible: The open-source Jellyfish code shall enable users to develop their own modules or routines. If possible, the development of extensions should not require in-depth knowledge of the program architecture and no or as little as possible modification of the existing program code.

3. User- and developer-friendly: Jellyfish should be user-friendly and self-explanatory. The goal is to keep the barrier to use the program and development of new code as low as possible.

4. Interactive: Often simulations require the evaluation of prior calculations and therefore cannot be automated. For example, for light-driven simulations the knowledge of target state properties are needed to determine the parameters of an external field. Jellyfish should enable such an analysis with subsequent adjustment and evaluation of the calculation on the fly, without the need to close the program and save and read in data in the form of various input and output files.

5. Efficient: Like almost all programs in the field of quantum theory, Jellyfish should run as efficiently as possible to allow for fast processing and the largest possible systems. Not only should it be written as an efficient code, but it should also enable to run calculations on headless servers and in combination with common parallelization options like MP, MPI or CUDA.

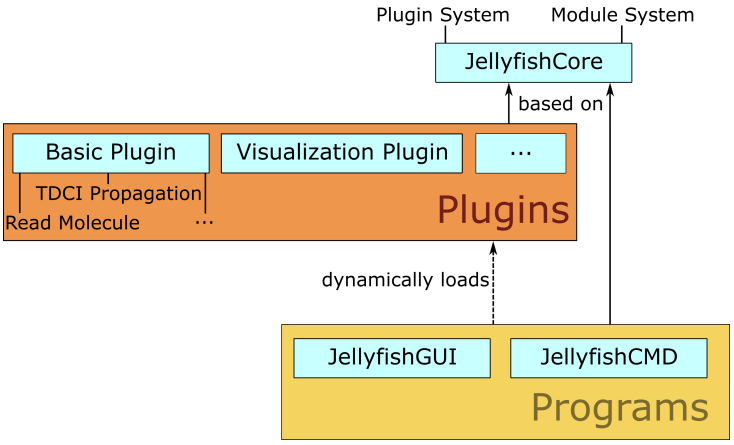

FIG. 1. Program architecture of Jellyfish. JellyfishCore contains the basic definitions of the plugin and module system and is linked to both plugins and programs to enable the necessary communication. The plugins contain the individual modules for Jellyfish and are dynamically loaded into the programs as a shared library.

The C++ programming language is chosen for these purposes as it is inherently object oriented and a widely used. C++ allows the compilation of very efficient code, for which a large number of libraries are available. Especially the application framework Qt which was used for the development of the here presented user interface was crucial.

A. NodeEditor / Visual Dataflow Programming

In order to meet the above requirements in an optimal way, Jellyfish orients on *dataflow programming*. In dataflow programming, a program is modeled as a directed graph in which data runs through various operations and is modified by them. This approach is realized in this work by a graphical user interface with a NodeEditor. Such approaches were already successfully used in programs from other fields, for example in 3D and game design. Each partial calculation or execution – may it be the reading in of a molecular geometry or carrying out an electronic structure calculation – is not only developed as a module but also represented graphically in a network in the NodeEditor by an individual node in form of a box with input and output slots, as displayed in Fig. 2. The implementation of such a partial calculation and everything associated with it is called a module, and instances of a module are called nodes. In a project, there can be several nodes instantiated from a module. For example, two nodes for generating basis sets. The nodes have

different identifiers to distinguish them. The network that is built from nodes is also referred to as a project in the following.

The input slots on the left side of a node box represent data types, for example, a matrix, and the output slots on the right of a node can be connected arbitrarily with the input slots of other nodes, as long as they have the same data type. The data is then propagated from one node to another and shared between the connected nodes. The node that creates the data (output node) always holds the data, while the nodes that use the data as input receive a reference (pointer) to that data. Such an approach allows the flexible construction of individual calculations for the most flexible purposes and can be extended or connected arbitrarily to other or new modules without having to modify existing code. Furthermore, the graphical approach avoids complicated input formats so that Jellyfish can be handled in a much more self-explanatory way than is possible by pure command line interfaces. Example networks for various simulations are published along with the code. Since a network of nodes can be extended and modified arbitrarily, even if other nodes are already calculated, calculations can be performed and modified interactively step by step. Furthermore, a new node may be added to the network from any type of source code in form of a plugin, see next subsection.

The underlying definitions of modules, nodes, connection and project files as well as the related functionalities have been developed as JellyfishCore. JellyfishCore is compiled as a static library and forms the fundament for the Jellyfish architecture.

B. Plugins

To separate the code of the modules from the user interface and to simplify the development of new modules, several modules are combined into one plugin. For example, different analysis modules were combined into the analysis plugin. The compilation of the plugins is independent of the user interface. The plugins are based on the JellyfishCore and contain the NodeRegistry, which creates, destroys, and stores instances of previously defined modules. Additionally, they have an interface which allows communication with the main program. Plugins are compiled as shared libraries, then placed in a plugin folder of the Jellyfish installation, dynamically loaded and included. As a blueprint, the C++ library micoplugins is used and heavily modified in house for our specific application purposes. This plugin structure allows modules or entire plugins to be easily added without having to modify or recompile the other program parts. Plugins can thus be

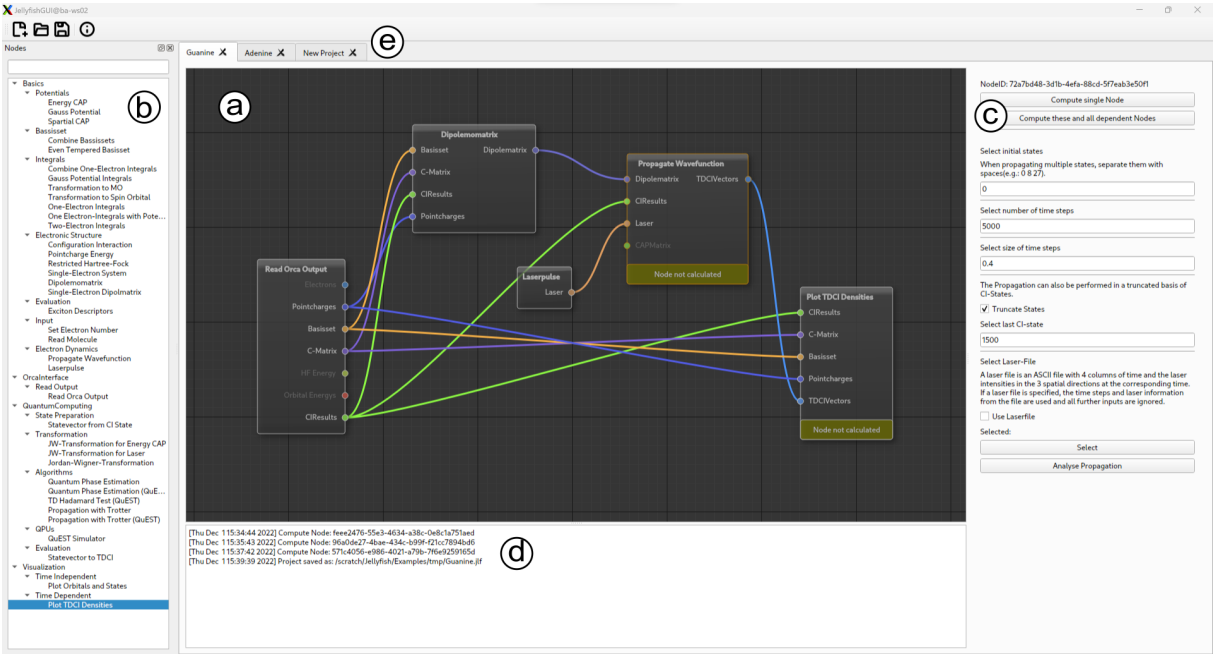

FIG. 2. Screenshot of the main window of the JellyfishGUI. Shown is the network to read in the electronic structure calculation from an ORCA log file to carry out a laser-driven electron dynamics simulation: (a) NodeEditor, central window in which modules can be selected, connected, disconnected and executed; (b) List of available plugins and their modules; (c) Detailed settings for the modules chosen; (d) Project log file; (e) Tabs for open of projects, to switch between projects.

developed separately and easily exchanged.

C. JellyfishGUI

JellyfishGUI is the primary input program with its graphical interface and a screenshot of the main window is shown in Fig. 2. On the left side it offers a list including a search function, which displays all available modules and offers the possibility to add them as a node to the network via drag and drop to the central part, the NodeEditor. In this space, see Fig. 2, the connecting and disconnecting of NodePorts is done. To include a NodeEditor in the Qt based user interface the library QtNodes[38] is adapted to the JellyfishCore and included in the code.

By selecting a node in the NodeEditor, node-dependent details and setting options are displayed on the right-hand side. In the example shown in Fig. 2, the propagation module was selected, which is why propagation parameters such as the number of time steps and their size can be set

accordingly. Also further functions or whole windows for individual nodes can be integrated. In the case of the propagation module, for example, a whole window is available behind the "Analyse Propagation" button in the figure, which is described in more detail in section IV A. Other examples for such additional function are the export of a laser pulse as ASCII file or the integration of the subprogram for the analysis of time-dependent electron densities as it was done in the *Visualization plugin*. Furthermore, the main window, shown in Fig. 2, offers the view of a project log, as well as the possibility to work on several projects at the same time by tabs and, of course, the loading and saving of project files.

D. JellyfishCMD

For the usage on headless servers in an HPC environment, JellyfishCMD was developed. It is a command-line interface allowing the calculation on individual nodes or entire node networks and, therefore, can be managed through scripts. A typical procedure for expensive computations in Jellyfish is the creation of a project in JellyfishGUI, the execution of the calculation on an HPC with JellyfishCMD, and subsequent evaluation with JellyfishGUI.

E. File Format

All data of a project are stored in a single Jellyfish file (file name extension .jlf). It is a ZIP archive created and read by employing the zlib and libzip libraries. Besides the computed data objects, e.g. excited state energies, or time-dependent populations and alike, this archive also contains module files that store information about the nodes and their connections in a JSON (JavaScript Object Notation, using the JSON for Modern C++ library[39]) format. In JSON file, the type of node and its unique GUID (Globally Unique Identifier, generated by the library stduuid) as well as its status – computed, not computed – are stored. To avoid multiple storage in memory, the data always belongs to the node in which it was calculated, while all connected nodes are assigned pointers to this data. Computed results are stored in files composed of the node GUID and a name of the result,“DensityMatrix" for example. All this data is also written directly into the JLF archive and read from it. The form in which the data is stored can be selected individually in each plugin. Saving the data as a binary file to save storage and to enable faster saving and loading is conceivable, the focus, however, was placed on being able to read the data as easily

as possible with external programs. Thus it is stored accordingly in plain text. The choice of a ZIP archive as format for the JLF files has on the one hand the advantage that it accounts for less storage space due to the compression that ZIP archives provide. On the other hand, objects are stored in separate, unique files in the archive, which simplifies the external access through scripts and programs. For example, the module file can be accessed and modified by a Python or shell script for further post-processing.

III. CAPABILITIES

A. Basic Plugin

The goal of the Basic Plugin is to provide all functionalities needed to prepare time-dependent configuration interaction simulations. For such simulations various modules have been implemented, starting from reading geometries of molecules or general binding potentials, through a Hartree-Fock section with its evaluation of one- and two-electron integrals and the time-independent configuration interaction calculation, to subsequent propagation of the wave function.

The first module allows the reading of molecular geometries in Cartesian coordinates (XYZ file format), the selection of a basis set and the assignment of a charge. Spherical as well as Cartesian Gaussian basis sets can be selected. The most common Pople and Dunning standard basis sets are readily implemented and more can be downloaded from Basis Set Exchange[40] in the same format as for Gaussian or Psi4. However, the addition of further basis functions with flexible, custom-made parameters is also possible. For example, it is possible to add any arbitrary set of basis functions, e.g., an even-tempered basis set as used for the example in section IV B.

For the calculation of various one- and two-electron integrals the library libcint[41] was included in the plugin. Further integrals between basis functions and arbitrary potentials, which are not analytically available, can be computed numerically on a grid and added to the total Hamiltonian. For this purpose, the library muparser was embedded, which allows the parsing of input functions.

To calculate the electronic structure, a restricted Hartree-Fock (RHF) and a configuration interaction module is available. The CI module is based on Slater determinants and can perform calculations at any CI truncation level. Also available are modules for the necessary orbital transformations from atomic orbitals to molecular and spin orbitals, respectively. The implemented electronic structure code is kept as simple as possible and is currently still inefficient,

which makes it suitable only for small calculations. As an alternative, however, an interface to the ORCA program package is provided. In a single module, it reads geometry, basis set, Hartree-Fock results and CI- or TDDFT-states from an ORCA log file and can be used for further processing, e.g., for the visualization of orbitals and stationary states or for time-evolution, as demonstrated in Sec. IV A. The development of a plugin which integrates other external electronic structure programs directly is planned. The open-source program package Psi4, for example, over the supplied application programming interface (API) for C++ would be suitable as an ideal interface.

As outlined before, subsequent to an electronic structure calculation, correlated electron dynamics simulations by TDCI can be carried out and visualized by corresponding modules. For the time evolution, a module is currently available that propagates the system on the basis of the CI states in time steps using the split operator technique.

For the set-up of a propagation several options are available. The propagation module offers the choice for the initial state, i.e., the ground state and simultaneously any excited state as well as the possibility to limit the number of CI states used during propagation. In addition to the time-independent Hamiltonian from the previous steady-state CI calculation, other time-independent operators can be added to the operator, both Hermitian or also non-Hermitian ones, where an example for the latter is a complex absorbing potential (CAP). In the case of the CAP, two options are available. A spatial, spherical CAP, which is defined by a radius around the center of the system,[42] or an energetic CAP, which is defined by the energy of virtual molecular orbitals.

Finally, time-dependent simulations are possible through the inclusion of the propagation module and a laser module. The network of a TDCI propagation when starting from a ORCA calculation is displayed in Fig. 2. The interaction with a laser field in TDCI is treated in the semi-classical dipole approximation $V^{\mathrm{ext}}(t) = \mu \cdot \vec{\mathrm{F}}(t)$. The laser module allows to set-up of an external electric field $\vec{\mathrm{F}}(t)$ and an input-connection for the dipole matrix of the CI states, $\mu = \langle f | \hat{\mu} | i \rangle$. For the calculation and display of the dipole matrix another module is implemented which also uses the libcint library for integration.

The modulation of a laser pulse is also available as a own module. The pulses have the form

$$\vec{\mathrm{F}}(t) = \vec{f_0} \cdot r(t, \omega) \cdot s(t) \tag{1}$$

where $s(t)$ defines the envelope function and $r(t, \omega)$ the driving field function of the pulse. Variations for these functions are readily available. In addition to the amplitude f_0 and frequency ω of the pulse, the pulse duration can be specified in atomic time units or in terms of number

of laser cycles. As polarization either a linear polarization with an arbitrary direction vector or a left or right rotating polarization can be used. The defined laser pulse can be visualized directly in the GUI before it is used in the propagation. More complicated pulses that cannot be modulated with these options can be imported from an externally generated ASCII file. After a propagation, properties like the populations, the norm of the wave function or the time-dependent dipole moment can be displayed and saved in the propagation module.

In many functions matrices or tensors are used in the program. For these and most operations from linear algebra, like matrix multiplications, eigenvalue determination and so on, the library Eigen[43] was used. Eigen has very efficient implementations of the functions, most of them also including parallelization via OpenMP.

B. Read External Plugin

The aim of Jellyfish is not to provide “another" HF/post-HF program suite for electronic structure calculations but rather to enable their post-processing with visualizations and/or time-dependent simulations. Even if the Basic Plugins provides these routines for electronic structure calculations, they are, as already mentioned, not yet optimized and thus comparatively slow.

The ORCA program allows such calculation in a more efficient form and a Read External Plugin that reads the log file is included in the Jellyfish release. That way also methods that are not included in the Basic Plugin can be used for Jellyfish processing. For example, it is possible to carry out light-driven dynamics simulations with Jellyfish by importing configuration interaction singles (doubles) (CIS(D)) or linear-response time-dependent density functional theory in Tamm-Dancoff approximation (LR-TDDFT) calculations, as presented in the example in section IV. Both methodologies improve on the system energetics while retaining the simple form of the CIS wave functions. In CIS(D), the double excitations are included as perturbative corrections[44] to the ground and excited state energies via an energy correction, while the wave functions are still the CIS wave functions. The CIS(D) method has the advantage of working with a CI matrix of the same size as CIS, while at the same time accounting for an improved treatment of electron correlation. In LR-TDDFT correlation is incorporated through the use of the exchange potential and excited states are obtained by orbital transitions with the ground state configuration as a single-reference. This makes it possible to construct a CIS-like pseudo wave function which then can be used in the TDCI methodology. The Read External Plugin has therefore a module, which makes

Property	Formula	stationary	time-dependent
Basis function/Atomic orbital	$\chi(\vec{r})$	✔	
Molecular orbital	$\phi(\vec{r})$	✔	
Molecular orbital density	$\|\phi(\vec{r})\|^2$	✔	
Local densities	$\rho_i(\vec{r})$	✔	✔
Difference densities	$\Delta_0 = \rho_i(\vec{r}) - \rho_j(\vec{r})$	✔	✔
Gradient densities	$\Delta_t = \rho(t,\vec{r}) - \rho(t-\Delta t,\vec{r})$		✔
Natural transition orbitals	$\phi^{NTO}(\vec{r})$	✔	
Natural transition orbital densities	$\rho^{NTO}(\vec{r})$	✔	✔

TABLE I. List of available visualization options for orbitals and electronic state properties

the import of basis set, molecule geometry, Hartree-Fock or Kohn-Sham orbitals as well as CI vectors and energies from an ORCA log file possible.

C. Visualization plugin

A special focus in the program development was given to the visualization plugin. The goal was to develop modules that enable visualization of wave functions and electron densities with a focus on laser-driven electron dynamics. Visualizations are implemented in two modules, one for stationary and one for time-dependent orbitals and densities and properties as listed in Tab. I. As a basis for the visualization, the VTK library has been directly linked into the plugin and a window to display orbitals and densities in terms of 3-dimensional isosurfaces has been developed, which can be called directly from the JellyfishGUI.

These plot modules offer the choice to also display the molecular structure (stick and ball) as well as a coordinate system. Besides the display of static atomic orbitals $\chi(\vec{r})$, molecular orbitals $\phi(\vec{r})$, and local state densities $\rho(\vec{r})$, several possibilities to analyse excited states are offered through difference densities (between states Δ_0 or between time steps Δ_t) as well as natural transition orbitals (NTOs $\phi^{NTO}(\vec{r})$) and their state NTO densities $\rho^{NTO}(\vec{r})$[45,46] for both static and time-dependent situations, as summarized in Tab. I.

The modules for the visualizations of static and time-dependent properties have a similarly structured window. A screenshot of the developed visualization front end, *Plot Orbitals and*

States, is shown in Fig. 3. Here, the time-dependent difference density for the nucleobase guanine is shown as an example. The visualization windows shows four areas. In the central panel (a) wave function objects, like orbitals or densities are displayed and can be viewed in free rotation controlled by the mouse of keyboard. On the left side of the window (b), the object to be plotted/rendered can be selected (cf. Tab. I, depending on the selection further options may become available). Along with a choice of the object type, certain time step or a time interval can be specified. The control of the graphics settings is on the right side of the window (c). Here, the object colors can be chosen along with graphics settings that control the quality, resolution and speed, as well as options to display additional objects like the molecular structure, a *xyz* axis, and the display of a time stamp. To enable to view a video "on-the-fly" in the main display window even for larger polyatomic molecules, a radius to truncate basis functions was introduced. This section also has options to export the in (a) displayed Objects/arrangement as a frame or as a movie. A log file (d) showing updates on the rendering and export progress is given below the main plotting window.

The spacial extend of orbitals and densities is represented by a isosurface composed of the sum of the basis function contributions. Their positive and negative values are displayed in two different colors. To additionally highlight their compactness or diffuseness, an option to also show multiple isosurfaces is available.

D. Quantum Computing Plugin

Additionally to the above outlined traditional way of simulating TDCI dynamics, Jellyfish also was used to develop algorithms for quantum computing.[47] Quantum computing promises for great advancement in electronic structure theory[48–50] as well as quantum dynamics.[51] Likewise, the field of electron dynamics would benefit from quantum computers and would make exact calculations in much larger molecules finally feasible. The quantum computing plugin for Jellyfish introduces all necessary modules to perform electron dynamics calculations on a quantum computer simulator. For gate-based quantum algorithms, the library QuEST,[52] which provides highly parallelized code, is embedded. Even noisy quantum computers can be simulated with QuEST. Modules available in the quantum computing plugin include the Jordan-Wigner[53] transformation of time-independent operator and laser fields to translate the integrals of molecular orbitals into weighted Pauli strings for the quantum computer. For propagation, a module for Hamiltonian simulation based on

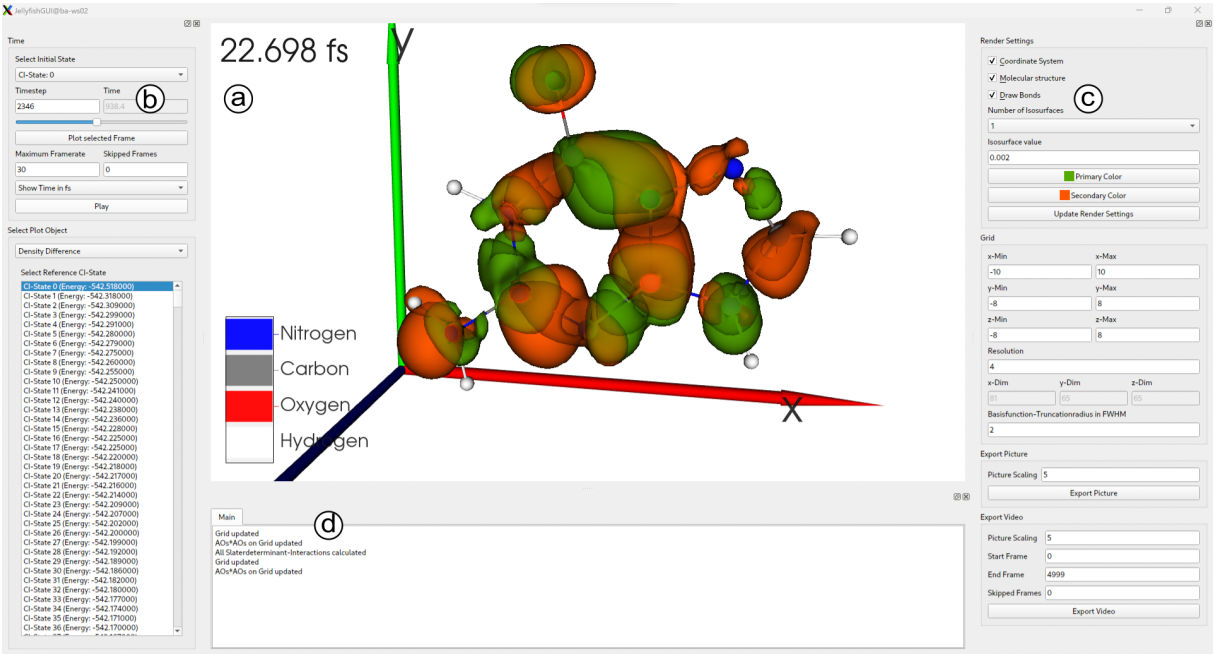

FIG. 3. Screenshot of the visualization module, Plot TDCI Densities, for time-dependent electron densities. (a) In the central window the wave function objects are rendered. In this case the difference density, Δ_0, between the ground state and the time-dependent density is shown; (b) The left panel allows the selection of density and the time frame. This selection menu changes depending on the chosen type of density; (c) Control options for the visualization, like the color and number of isosurfaces, as well as graphics settings controlling the picture quality and export functions; (d) The lower frame displays the log file of executed actions and error messages.

Trotter decomposition[54,55] is available, as well as an extension with the quantum imaginary time evolution (QITE)[56] algorithm to simulate ionization as well. Time-dependent expectation values can be determined with the help of a module for the Hadamard test.[57] More information about the complete algorithm developed with it can be found in Langkabel *et al.*.[47]

IV. EXAMPLE APPLICATIONS

A. Electronic transition in guanine

As a first example to illustrate the capabilities of the Jellyfish package in a many-electron simulation, a photoexcitation of the nucleobase guanine is presented. Guanine (2-amino-6-

oxopurine) is an aromatic heterocyclce consisting of a 6-membered and a 5-membered ring and has a total of 76 electrons. As a building block of DNA, it has been part of numerous photochemical studies. Highly accurate and computationally demanding multiconfigurational and and multireference electronic structure calculations were employed to compute the (minimum energy) reaction paths e.g., to study the efficiency of radiation-free decay mechanisms.[58] A comprehensive study on guanine tautomers, for example, discusses spectra and geometries employing CIS and CASSCF.[59] There, also electron density difference plots have been employed to illustrate the effect of structural changes. High-level computations of a reaction path are restricted to a few photochemically relevant excited states that are involved in the main electronic transitions. The here presented simulations can complement the picture by focusing on the initial excitation step the vertical photo-absorption employing a state manifold.

The network for such a computation is displayed in Fig. 2. Here, the Read External plugin is employed to read in the results of an ORCA calculation in order to carry out a state-selective excitation and to visualize the resulting many-electron dynamics. The dynamics is treated by the hybrid time-dependent density functional theory/configuration interaction (TDDFT/CI) formalism:[35,60] In a first step, the structure of guanine is optimized at CAM-B3LYP/cc-pVTZ level of theory using the ORCA package. From this geometry a total of 10109 singlet excited states are obtained using LR-TDDFT in the Tamm-Dancoff approximation. The output, namely the molecular geometry, basis set definition, orbitals, pseudo-CIS eigenvectors, and the corresponding state energies, is then read in and stored by the Read External module.

Once the wave function is available, the calculation of dipole matrices, $\mu_{i,j;q} = \langle \Psi_i^{\mathrm{CIS}} | \hat{\mu}_q | \Psi_j^{\mathrm{CIS}} \rangle$, is done using the Dipole Matrix module. It provides useful information on the state properties. The transition dipoles on the off-diagonal lay out which states can be addressed by optical excitation. The permanent dipoles on its diagonal allow a first estimation about the character of an induced transition. The picture is often supplemented by a visual inspection of the involved orbitals, in Jellyfish done by the *Plot Orbtials and States* module. Details on how fast a how fast a state-specific transition can be obtained within a large excited states manifold and what pulse intensities or shapes are necessary, can only be answered by explicit time-dependent numerical simulations. In Jellyfish they are available through the propagation module. In the following an exemplary excitation to a specific state is outlined.

The first excited state of our LR-TDDFT calculation was selected as the target for a state-to-state transition. It is a bright state with reasonably large transition dipole moments: $\mu_{0,1} =$

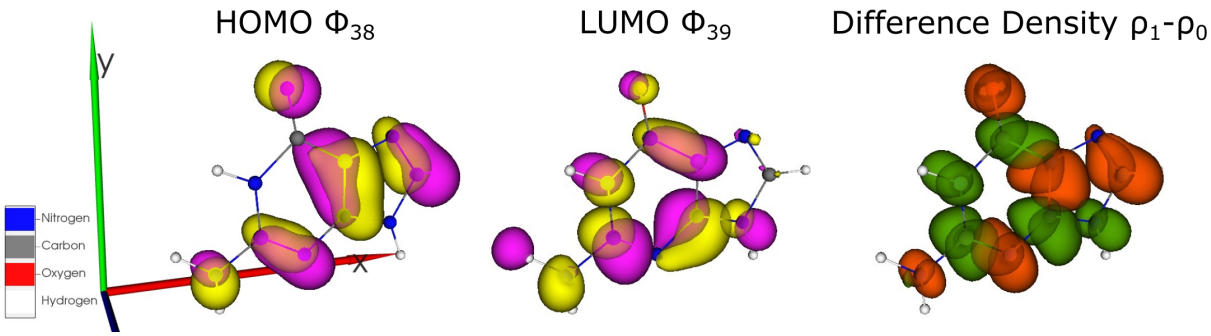

FIG. 4. Selected static properties of the first excited state of the guanine molecule: (a) LUMO, (b) HOMO, and (c) difference density between ground and first excited state, Δ_{10}

.

$(-0.788, -0.936, 0.010)$ $\mathrm{ea_0}$ thus making it easy to be addressed by linearly polarised laser field.

The target state is located 0.200 E_h (5.442 eV) above the ground state and consists primarily of a HOMO-LUMO transition (82%). These two frontier orbitals are depicted Fig. 4 (a) and (b). Excitation to this state involves a reorganization of the electronic π system with respect to the ground state as depicted by the difference density, Fig. 4 (c). It reveals the overall rearrangement of π orbitals on almost all atomic centers upon excitation. The red isosurfaces show the withdrawal of electronic density while the green ones show the gain and, thus the excitation can clearly be characterised as $^1(\pi\pi^*)$ state.

To obtain this rearrangement of stationary densities, a full population inversion between ground and target state has to be induced by a laser pulse. This may be achieved by more or less complex shaped pulses, in the following, however, a resonant excitation by a so-called π pulse with optimized parameters to obtain the targeted transition, is presented.

In the following the photoexcitation by a cosine squared laser pulse with the duration of $2\sigma = 2000\,\hbar/E_\mathrm{h}(48$ fs) is presented. Regarding the conditions for a π pulse, $f_0 = \pi\hbar/\sigma|\mu_{i,f}|$, this duration is resulting in a moderate maximum field amplitude of 0.002 $E_\mathrm{h}/\mathrm{ea_0}$. The propagation was performed in 5000 time steps with a step size of $0.4\,\hbar/E_\mathrm{h}$ in the basis of the 1500 energetically lowest pseudo-CIS states.

The time-dependent state populations, $P_i(t) = |\langle\Psi_i|\Psi(t)\rangle|$, and the time-dependent dipole moment as a result of the π pulse excitation are shown in Fig. 5. Note in passing that for this figure, both the state populations as well as the time-dependent dipole moment have been exported from Jellyfish and plotted by an external program. As seen, the populations smoothly interchange

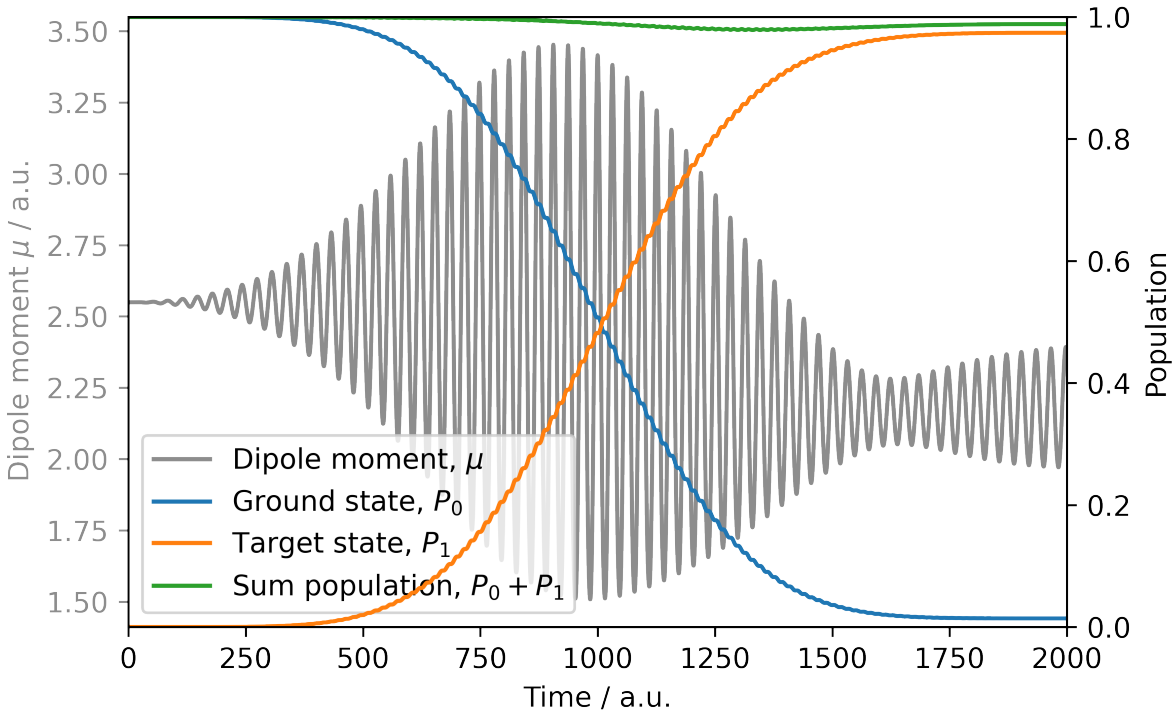

FIG. 5. Time-dependent dipole moment (gray) and the population of the ground (blue) and target (orange) states of guanine during a state-to-state transition by a π pulse.

with minute oscillations originating from the half-cycles of the oscillation laser field. At the end of the pulse, however, the target state population (orange curve) nearly reaches the maximum value of 1 and the ground state population (blue curve) nearly completely drops to 0. That means, the state-to-state transition is incomplete, which can be due to several effects. For one, the coupling of the permanent dipole moments to an intense external field can modify the transition energy so that it becomes time-dependent (dynamic Stark effect). Furthermore, a short laser pulse has a relatively broad spectral width, so that also neighboring states can be reached by the pulse. The incompleteness in this particular case, however, is mostly due to multi-photon transitions to higher excited states, as seen in the sum population of ground and target state (green curve). Inspection of the entire state population revealed that a multitude of states at integer multiples of the incident laser frequency have gained very small occupations ($< 1\%$) during the pulse excitation.

The time-dependent dipole moment, plotted in gray, starts at the total permanent dipole moment of the ground state ($|\mu_0| = 2.549\ \mathrm{ea_0}$) and shows distinct oscillations during the excitation. These

oscillations coincide with frequency and the evolving intensity of the laser pulse. At the end of the pulse (2000 a.u.) the time-dependent dipole moment has almost reached the value of the permanent dipole moment of the target excited state of $|\mu_1| = 2.178\ \mathrm{ea_0}$. Since the excitation is not complete, by the end of the propagation an electronic wave packet has been created, so that the dipole moment is noticeably oscillating (and would continue to oscillate even after the pulse is off).

Aside from these quantifiable observables, the depiction of densities gives detailed information of the electronic redistribution in terms of their spacial extend and their localization at atomic centers. Especially the view of the evolution in time can be insightful. For the purposes of the program presentation, a short Jellyfish animation is provided. Please visit Ref. [7] for a more comprehensive description and Jellyfish analysis of an excitation to a charge transfer state.

A video of four different density representations over the period of the central laser cycle from 900 $\hbar/E_\mathrm{h}$ to 1100 $\hbar/E_\mathrm{h}$ can be found in the supporting information. This animation is also summarized in a sequence of snapshots in Fig. 6 at significant point of the laser cycle. For a carrier frequency of $\hbar\omega = 0.2\ E_\mathrm{h}$ the zero crossings of the center optical cycle are roughly at $t = 984\ \hbar/E_\mathrm{h}$, $t = 1000\ \hbar/E_\mathrm{h}$, and $t = 1016\ \hbar/E_\mathrm{h}$, so that the minimum and maximum field strengths are reached around $t = 992\ \hbar/E_\mathrm{h}$ and $t = 1008\ \hbar/E_\mathrm{h}$, respectively.

In the first column of the figure the time-dependent difference density is shown where the red isosurface corresponds to a loss and the green isosurface to a gain of local density. The second column displays the gradient density with blue isosurfaces indicating a gain and pink a loss of electron density. In the last two columns the NTO densities for hole (gray) and particle (blue) are rendered.

Before looking at the progressions on certain atomic centers, the four displayed densities seem to be divided in two groups. Apparent at first sight is that both NTO densities on the right, $\rho_{e/h}^{NTO}$, evolve much less dynamically but rather show a smooth and steady increase in volume, while the two kinds of difference densities on the left, Δ_0 and Δ_t, show more complex structures along rapid oscillations. Note, the stationary electron-hole NTO density and the difference density are in the CIS formalism mathematically equivalent. This is not the case during an laser excitation. The time-dependent NTOs show the formation of hole and particle in terms of the rising population in the excited states, cf. Fig. 6 Thus, the NTOs are essentially excited state quantities/properties, since they are calculated with the ground state contributions are being removed to ensure orthogonality during time propagations (cf. Ref.[47])

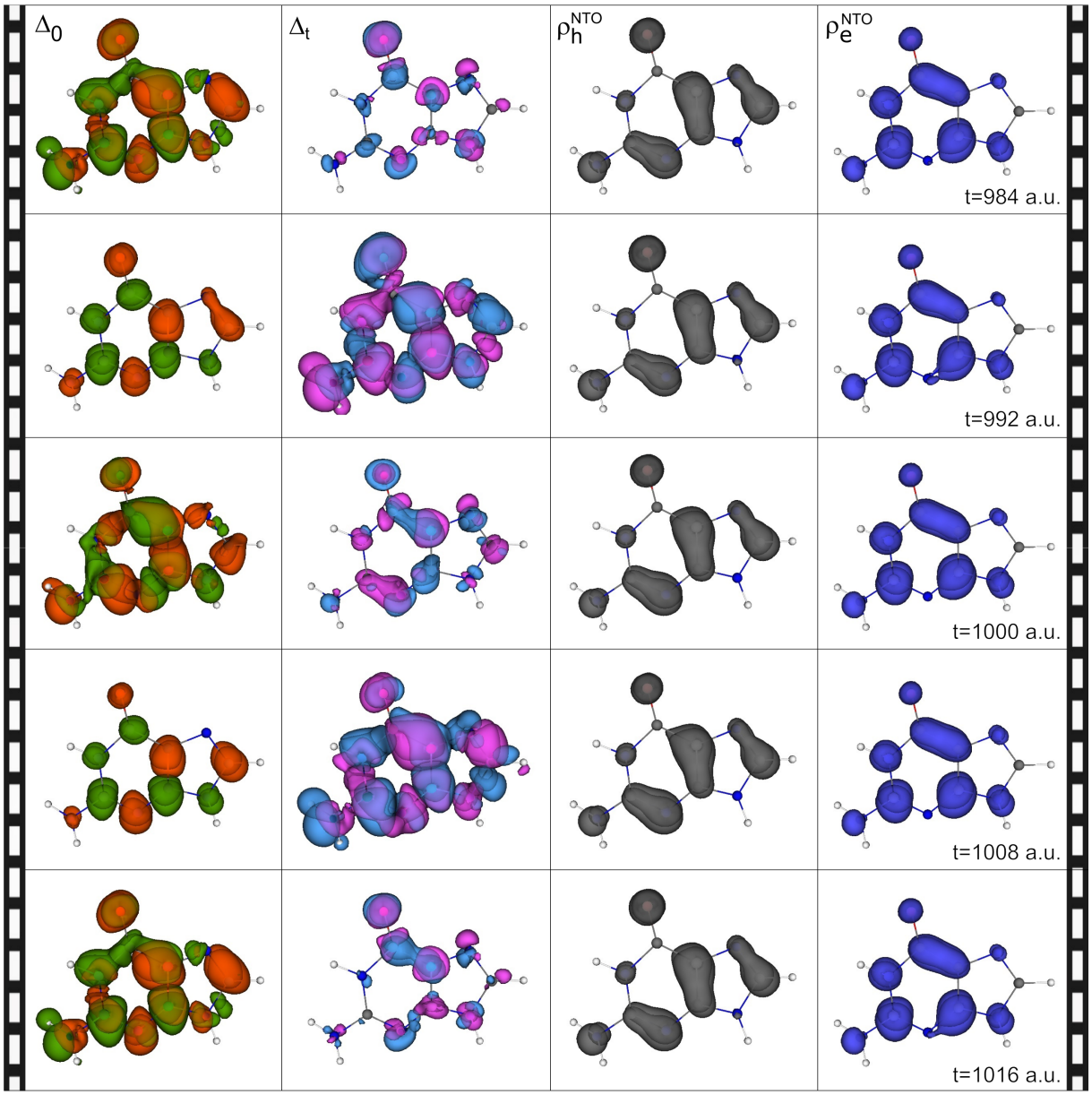

FIG. 6. Sequence of density snapshots shows the excitation process of guanine by a resonant π pulse during the most intense central laser cycle. The first column shows the difference density with respect to the ground state, the second the difference with respect to the previous time step's density, the third the NTO hole density, and the fourth the NTO particle density.

However, the two types of difference densities are calculated directly from the field-dependent densities and therefore show pronounced oscillations that coincide with the slopes of the external field. The oscillations of Δ_0 mirror the oscillations of the dipole moments, compare Fig. 6, while the induced flow of current at this time is visualized by the gradient density Δ_t.

For the difference densities the picture of p orbitals on atomic centers being perpendicular to the ring plane is true for certain times only. That is, when the slope of the optical cycles is zero, e.i., when an laser cycle reached its maximum or minimum. In between these significant points in time, the isosurfaces reflecting loss and gain have complex shapes similar to heavily distorted d orbitals with contributions of loss and gain at opposite sides of a single atomic center.

The participation of certain atomic centers in the density rearrangement is not equally distributed. For example, among the hetero atoms the oxygen atom of the carbonyl group is showing more loss than gain in average, while the adjacent carbon atom gets involved only after first third of the propagation (not shown) showing mostly the deposition of electronic density once the laser strength has become more intense. Same applies for the nitrogen atom N_7 in the 5-membered ring, it seems rather inert during the first third of the pulse.

Furthermore, while the three hydrogen atoms of the 5- and 6-membered rings do not participate much, the two hydrogen atoms of the methylidene group show an active involvement in the rearrangement of electronic density. This activity during the pulse excitation is not apparent from the analysis of stationary densities (only slightly suggested from the HOMO and LUMO figures).

B. Laser Ionization in Quantum Dots

Dynamics simulations by means of propagating an electronic wave function can be done in an explicitly atomistic descriptions but also by model potentials. To illustrate the capabilities of the Jellyfish package we present a model potential description of a quantum dot and its light-induced ionization process. QDs are semi-conductor nanomaterials. Their optical and electronic properties can be controlled through their size and shape or by gating through external electrodes and can be captured by effective mass model potentials, e.g., Gauss functions[46,61,62] of the form

$$\hat{V}^{\mathrm{QD}} = -D \cdot e^{-br^2}\,, \tag{2}$$

where D is the depth and b a measure of the width of the quantum dot in atomic units. Here the parameters for b and D are $0.2\,a_0^{-2}$, $2\ E_{\mathrm{h}}$, respectively, which is supposed to resemble a gallium-arsenide QD from experimental data.[61] Standard basis sets have been optimized for bound states of atoms of the periodic table but not for Gauss potentials. However constructing custom-made basis sets following the systemics known for atoms can be done in the form of an even-tempered basis set, generated with the corresponding module in Jellyfish. Even-tempered basis functions

centered at the coordinate origin are defined according to

$$\phi = x^{a_x} y^{a_y} z^{a_z} e^{\alpha\beta^{i-1} r^2}, \quad i = 1, 2, ..., N, \tag{3}$$

where a_j is the angular momentum in the corresponding spatial direction. They cover the Hilbert space evenly, which allows them to represent both bound and continuum states. Due to their squared exponential form, they can be computed efficiently with the same integrators as for standard basis sets. For our example, two sets of even-tempered basis functions with total angular momentum $a = a_x + a_y + a_z = 0$, $\alpha = 0.07$, $\beta^0 = 1.5$, and $N = 11$, as well as with angular momentum $a = 1$, $\alpha = 10^{-4}$, $\beta^0 = 1.8$, and $N = 21$ were chosen. Smaller values for β^0, i.e., more diffuse Gaussians, can lead to linear dependencies. Here, the model potential is considered for two electrons occupying both the single bound state available. From a full-CI calculation a ground state energy of $-1.149\ E_\mathrm{h}$ was obtained and an ionization energy of $\varepsilon^\mathrm{HOMO} = 0.277\ E_\mathrm{h}$ was determined using Koopmans' theorem. To simulate ionization in this system a $\cos^2$ laser pulse (Eq. (1)) as shown in the bottom panel of Fig. 7 (c) was used with a frequency of $\hbar\omega = 0.057$ E_h, corresponding to a typical 800 nm Ti-sapphire laser, with a maximum amplitude of $f_0 = 0.2$ $E_\mathrm{h}/\mathrm{ea}_0$ and a pulse duration of 700 $\hbar/E_\mathrm{h}$ (17 fs). The laser intensity was chosen to promote an electron above the ionization barrier. Free propagation of an unbound electron, however, is restricted due to the use of atom-centered basis sets. To compensate for such numerical issues a spherical complex absorbing potential in real space, cf. section III A was introduced to the total Hamiltonian. The CAP has a quadratic rise sitting on a distance from the origin of 15 a_0. It has a quadratic fall-off until the maximum value of 10 E_h is reached.[63] The necessary integrals between the CAP and the basis functions were obtained by numerical integration on an even spaced grid between $[-25a_0; 25a_0]$ with 200 grid points. Propagation was performed for 1600 time steps with a step size of $\Delta t = 0.5\ \hbar/E_\mathrm{h}$ using all 5041 CI states as basis. All steps for the calculations the evaluation was also performed directly in the JellyfishGUI. Here, the time-dependent populations were calculated and displayed as shown in the screenshot in Fig. 7 (a).

States that have an overlap of at least 1 % at any point in time to the total time-dependent wave function are displayed in the corresponding window. The highest of these states (state 76) has an excitation energy of $0.770\ E_\mathrm{h}$. All states except the ground state are continuum states and the ionization progression is reflected in the time-dependent norm, as displayed in the screenshot in Fig. 3 (b). From the populations it can be seen that already at a slow increase of the laser amplitude starting at about 100 $\hbar/E_\mathrm{h}$ first transitions into energetically low continuum states (58, light green

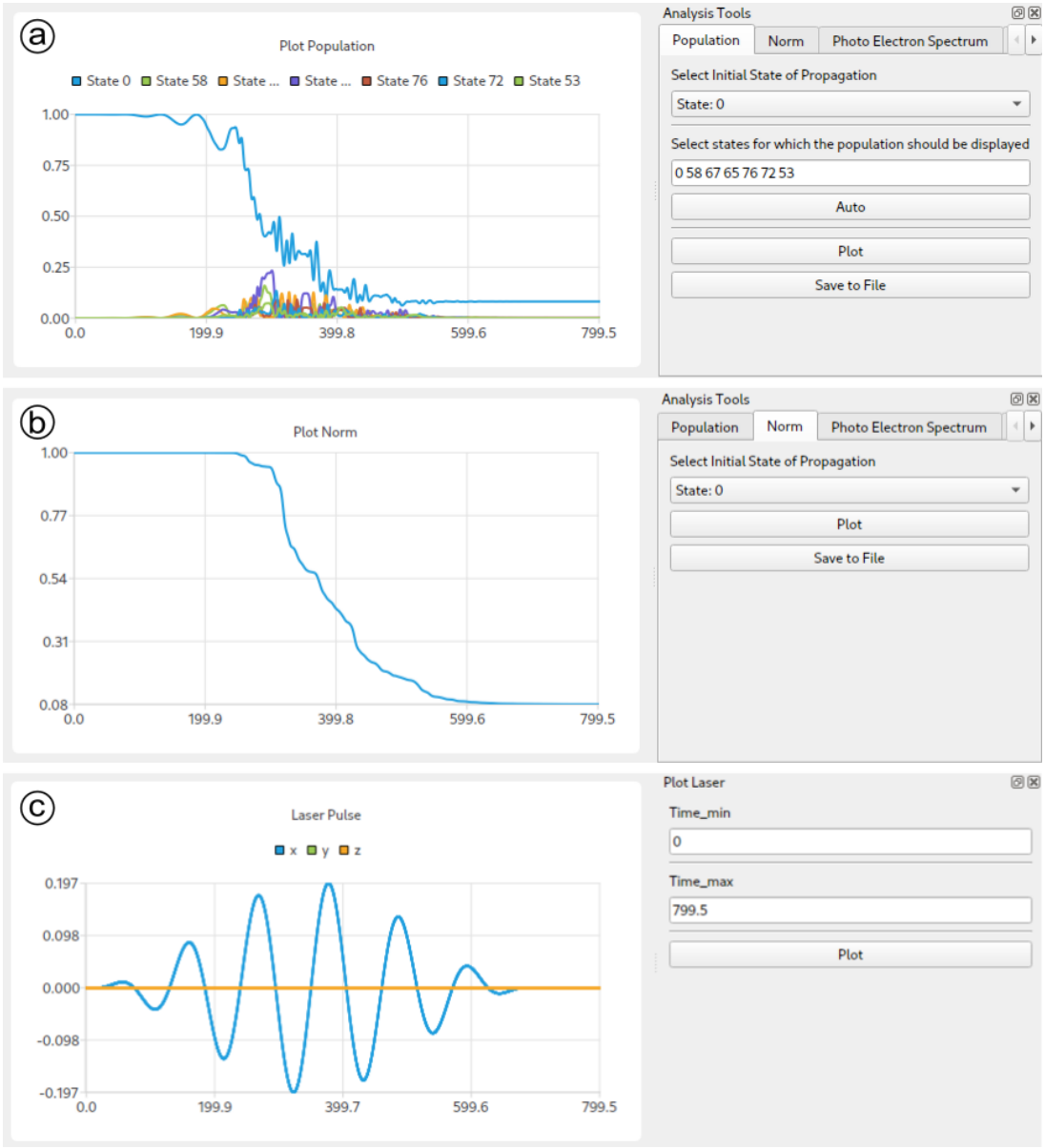

FIG. 7. JellyfishGUI screenshots from subwindows for the evaluating of driving laser field and time-dependent properties. (a) Population of all states with an overlap of at least 1 % with the wave function, (b) norm, (c) lase pulse.

and 67, yellow) takes place. However, the ground state and these continuum states have very little overlap with the CAP, so that the norm barely changes. With higher amplitudes, starting at 200 $\hbar/E_\mathrm{h}$ the electron is excited into energetically higher continuum states, which have a larger overlap with the CAP, i.e. the continuum electron has a higher kinetic energy and the electron density of the corresponding states is thus removed from the system more quickly. With decreasing

laser amplitude excitation into continuum states stops. At the same time the electron density of previously populated continuum states is completely removed so that after the termination of the pulse only population in the ground state remains.

V. CONCLUSION

Electron dynamics is a very active research field where experimental techniques and theoretical developments are rapidly evolving. Unlike in the related field of electronic structure methods, the existing dynamics programs are mostly limited to a few specific methods and systems. With Jellyfish, we have developed a program that provides a flexible, user- and developer-friendly environment. This is possible on the one hand by the graphical user interface which allows the flexible set-up of a simulation through a nodal network, as well as the control of input parameters. On the other hand, the Jellyfish code is build strictly modular, thus, it is easily extendable by self-written modules.

The methods implemented so far focus on the TDCI methodology with the corresponding plugins for light-driven dynamics simulations, both on traditional and on quantum computers. TDCI plugins also exist in form of a visualization front end to produce snapshots and animations of various densities and wave function properties.

This report demonstrated the application possibilities and flexibility of Jellyfish on two systems. The first example describes and illustrates the state-selective excitation in the guanine molecule. Extended excited-state analysis revealed not only the character of the induced rearrangement of electronic density but also the region and timing of the most significant of these changes. In the second example the ionization dynamics in model potential simulations by an intense laser pulse and the ionization yields by the introduction of a CAP operator was presented.

ACKNOWLEDGMENTS

The authors are grateful for financial support from the Volkswagen Foundation through the Freigeist Fellowship no 89525. They also thank Paul Anton Albrecht and Manuel Güterbock who contributed to the development of Jellyfish and Alejandro Saenz for discussing the usage of even-tempered basis sets in model potentials. Finally, we acknowledge the computational resources of the Helmholtz-Zentrum Berlin and thank in particular Robert Grzimek for his support

in establishing the development environment.

DATA AVAILABILITY STATEMENT

The code is made available under the GPL-3.0 licence on github: `https://github.com/FabianLangkabel/Jellyfish`

REFERENCES

[1]R. Borrego-Varillas, M. Lucchini, and M. Nisoli, Reports on Progress in Physics **85**, 066401 (2022).

[2]P. Saalfrank, F. Bedurke, C. Heide, T. Klamroth, S. Klinkusch, P. Krause, M. Nest, and J. C. Tremblay, in *Chemical Physics and Quantum Chemistry* (2020), pp. 15–50.

[3]B. S. Ofstad, E. Aurbakken, Ø. S. Schøyen, H. E. Kristiansen, S. Kvaal, and T. B. Pedersen, WIREs Computational Molecular Science (2023).

[4]A. I. Kuleff and A. Dreuw, The Journal of Chemical Physics **130**, 034102 (2009).

[5]I. Barth, J. Manz, Y. Shigeta, and K. Yagi, Journal of the American Chemical Society **128**, 7043 (2006).

[6]F. Buchner, T. Kirschbaum, A. Venerosy, H. Girard, J.-C. Arnault, B. Kiendl, A. Krueger, K. Larsson, A. Bande, T. Petit, et al., Nanoscale **14**, 17188 (2022).

[7]F. Langkabel and A. Bande, The Journal of Chemical Physics **154**, 054111 (2021).

[8]P. Krause, J. C. Tremblay, and A. Bande, The Journal of Physical Chemistry A **125**, 4793 (2021).

[9]S. Matsika and P. Krause, Annual Review of Physical Chemistry **62**, 621 (2011).

[10]B. Trauzettel, D. V. Bulaev, D. Loss, and G. Burkard, Nature Physics **3**, 192 (2007).

[11]D. Li and N. Akopian (2021), arXiv:2107.05960 [quant-ph].

[12]P. Parafiniuk and R. Taranko, Physica E: Low-dimensional Systems and Nanostructures **40**, 3078 (2008).

[13]A. Bechtold, D. Rauch, F. Li, T. Simmet, P.-L. Ardelt, A. Regler, K. Müller, N. A. Sinitsyn, and J. J. Finley, Nature Physics **11**, 1005 (2015).

[14]D. Buterakos and S. D. Sarma, PRX Quantum **2**, 040358 (2021).

[15]V. I. Klimov, A. A. Mikhailovsky, D. W. McBranch, C. A. Leatherdale, and M. G. Bawendi, Science **287**, 1011 (2000).

[16]L.-W. Wang, M. Califano, A. Zunger, and A. Franceschetti, Physical Review Letters **91**, 056404 (2003).

[17]A. Haller, D. Peláez, and A. Bande, The Journal of Physical Chemistry C **123**, 14754 (2019).

[18]C. Bardos, F. Golse, A. D. Gottlieb, and N. J. Mauser, Journal de Mathématiques Pures et Appliquées **82**, 665 (2003).

[19]B. Zhang, J. Yuan, and Z. Zhao, Computer Physics Communications **194**, 84 (2015).

[20]P. Krause, T. Klamroth, and P. Saalfrank, The Journal of Chemical Physics **123**, 074105 (2005).

[21]L. Greenman, P. J. Ho, S. Pabst, E. Kamarchik, D. A. Mazziotti, and R. Santra, Physical Review A **82**, 023406 (2010).

[22]J. A. Sonk, M. Caricato, and H. B. Schlegel, The Journal of Physical Chemistry A **115**, 4678 (2011).

[23]J. C. Tremblay, T. Klamroth, and P. Saalfrank, The Journal of Chemical Physics **129**, 084302 (2008).

[24]J. C. Tremblay, S. Klinkusch, T. Klamroth, and P. Saalfrank, The Journal of Chemical Physics **134**, 044311 (2011).

[25]D. J. Haxton, K. V. Lawler, and C. W. McCurdy, Physical Review A **83**, 063416 (2011).

[26]T. Sato, Y. Orimo, T. Teramura, O. Tugs, and K. L. Ishikawa, in *Springer Series in Chemical Physics* (2018), pp. 143–171.

[27]S. R. White, Physical Review Letters **69**, 2863 (1992).

[28]S. R. White, Physical Review B **48**, 10345 (1993).

[29]A. J. Daley, C. Kollath, U. Schollwöck, and G. Vidal, Journal of Statistical Mechanics: Theory and Experiment **2004**, P04005 (2004).

[30]F. Neese, F. Wennmohs, U. Becker, and C. Riplinger, The Journal of Chemical Physics **152**, 224108 (2020).

[31]D. G. A. Smith, L. A. Burns, A. C. Simmonett, R. M. Parrish, M. C. Schieber, R. Galvelis, P. Kraus, H. Kruse, R. D. Remigio, A. Alenaizan, et al., The Journal of Chemical Physics **152**, 184108 (2020).

[32]Y. Shao, Z. Gan, E. Epifanovsky, A. T. Gilbert, M. Wormit, J. Kussmann, A. W. Lange, A. Behn, J. Deng, X. Feng, et al., Molecular Physics **113**, 184 (2014).

[33]Q. Sun, T. C. Berkelbach, N. S. Blunt, G. H. Booth, S. Guo, Z. Li, J. Liu, J. D. McClain, E. R. Sayfutyarova, S. Sharma, et al., WIREs Computational Molecular Science **8** (2017).

[34]F. Weber, J. C. Tremblay, and A. Bande, The Journal of Physical Chemistry C **124**, 26688 (2020).

[35]G. Hermann, V. Pohl, J. C. Tremblay, B. Paulus, H.-C. Hege, and A. Schild, Journal of Computational Chemistry **37**, 1511 (2016).

[36]V. Pohl, G. Hermann, and J. C. Tremblay, Journal of Computational Chemistry **38**, 1515 (2017).

[37]G. Hermann, V. Pohl, and J. C. Tremblay, Journal of Computational Chemistry **38**, 2378 (2017).

[38]D. Pinaev, *Qtnodes. node editor*, `https://github.com/paceholder/nodeeditor` (2017).

[39]L. Niels, *Json for modern c++*, `https://github.com/nlohmann` (2022).

[40]B. P. Pritchard, D. Altarawy, B. Didier, T. D. Gibson, and T. L. Windus, Journal of Chemical Information and Modeling **59**, 4814 (2019).

[41]Q. Sun, Journal of Computational Chemistry **36**, 1664 (2015).

[42]J. Muga, J. Palao, B. Navarro, and I. Egusquiza, Physics Reports **395**, 357 (2004).

[43]G. Guennebaud, B. Jacob, et al., *Eigen v3*, http://eigen.tuxfamily.org (2010).

[44]M. Head-Gordon, R. J. Rico, M. Oumi, and T. J. Lee, Chemical Physics Letters **219**, 21 (1994).

[45]F. Langkabel, P. A. Albrecht, A. Bande, and P. Krause, Chemical Physics **557**, 111502 (2022).

[46]A. Bande, in *Chemical Modelling* (Royal Society of Chemistry, 2022), pp. 91–152.

[47]F. Langkabel and A. Bande, Journal of Chemical Theory and Computation **18**, 7082 (2022).

[48]Y. Cao, J. Romero, J. P. Olson, M. Degroote, P. D. Johnson, M. Kieferová, I. D. Kivlichan, T. Menke, B. Peropadre, N. P. D. Sawaya, et al., Chemical Reviews **119**, 10856 (2019).

[49]S. McArdle, S. Endo, A. Aspuru-Guzik, S. C. Benjamin, and X. Yuan, Reviews of Modern Physics **92**, 015003 (2020).

[50]J. Lee, D. W. Berry, C. Gidney, W. J. Huggins, J. R. McClean, N. Wiebe, and R. Babbush, PRX Quantum **2**, 030305 (2021).

[51]P. J. Ollitrault, A. Miessen, and I. Tavernelli, Accounts of Chemical Research **54**, 4229 (2021).

[52]T. Jones, A. Brown, I. Bush, and S. C. Benjamin, Scientific Reports **9** (2019).

[53]P. Jordan and E. Wigner, Zeitschrift fuer Physik **47**, 631 (1928).

[54]H. F. Trotter, Proceedings of the American Mathematical Society **10**, 545 (1959).

[55]M. Suzuki, Communications in Mathematical Physics **51**, 183 (1976).

[56]M. Motta, C. Sun, A. T. K. Tan, M. J. O'Rourke, E. Ye, A. J. Minnich, F. G. S. L. Brandão, and G. K.-L. Chan, Nature Physics **16**, 205 (2019).

[57]D. Aharonov, V. Jones, and Z. Landau, Algorithmica **55**, 395 (2008).

[58]A. Giussani, J. Segarra-Martí, D. Roca-Sanjuán, and M. Merchán, in *Topics in Current Chemistry* (2013), pp. 57–97.

[59]I. Pugliesi and K. Müller-Dethlefs, The Journal of Physical Chemistry A **110**, 13045 (2006).

[60]P. Hoerner, M. K. Lee, and H. B. Schlegel, The Journal of Chemical Physics **151**, 054102 (2019).

[61]A. Bande, K. Gokhberg, and L. S. Cederbaum, The Journal of Chemical Physics **135**, 144112 (2011).

[62]I. Cherkes and N. Moiseyev, Physical Review B **83**, 113303 (2011).

[63]P. Krause, J. A. Sonk, and H. B. Schlegel, The Journal of Chemical Physics **140**, 174113 (2014).

5.4 Making optical excitations visible – An exciton wavefunction extension to the time-dependent configuration interaction method

Fabian Langkabel, Paul Anton Albrecht, Annika Bande and Pascal Krause
Chem. Phys. 557, 111502 (2022)
DOI: doi.org/10.1016/j.chemphys.2022.111502
URL: `https://doi.org/10.1016/j.chemphys.2022.111502`

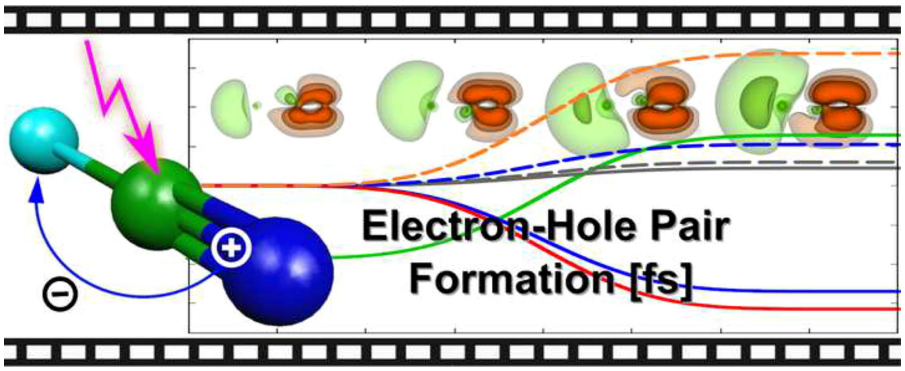

Figure 5.4: Graphical abstract. Reprint with permission from Langkabel et al. [4] (Copyright Elsevier (2022))

Author contributions: The project was conceived by AB, PK, and FL. Code developments were performed by PA and FL. PK and FL performed calculations with the developed code in the examples shown and created all figures and videos. The manuscript draft was written by PK and FL. All authors contributed to bringing the manuscript into the final form.

Chemical Physics 557 (2022) 111502

Contents lists available at ScienceDirect

Chemical Physics

journal homepage: www.elsevier.com/locate/chemphys

Making optical excitations visible – An exciton wavefunction extension to the time-dependent configuration interaction method

Fabian Langkabel [a,b], Paul Anton Albrecht [a,b], Annika Bande [a,*], Pascal Krause [a]

[a] Theory of Electron Dynamics and Spectroscopy, Helmholtz-Zentrum Berlin für Materialien und Energie GmbH, Hahn-Meitner Platz 1, 14109 Berlin, Germany
[b] Physical and Theoretical Chemistry, Institute of Chemistry and Biochemistry Freie Universität Berlin, Arnimallee 22, 14195 Berlin, Germany

ARTICLE INFO

Keywords:
Correlated electron dynamics
Time-dependent Schrödinger equation
Density visualization
Time-dependent natural transition orbitals
Optical excitation

ABSTRACT

We report the animation and analysis of laser-driven many-electron dynamics by means of time-dependent local densities and quantities derived from the one-particle transition density matrix, such as time-dependent natural transition orbital densities, particle and hole positions and exciton size. The time-dependent configuration interaction method was used to revisit studies on hydrogen molecule and lithium cyanide by Saalfrank and coworkers and our study shines new light on the optical transitions in these small molecules to benchmark the implemented time-dependent exciton properties. One focus of our simulations is the comparison of the local densities to the quantities of the two-body exciton wavefunction for resonant excitations leading either to state-to-state transitions or to the creation of a wave packet.

1. Introduction

Electrons interacting with photons give rise to an astonishing wealth of fascinating phenomena. Modern experimental techniques further reveal details of the intricate processes of the electronic motion for various material classes ranging from atoms over small molecules to large clusters and extended structures. Since for the design of modern electronic devices the knowledge of the time scales of electronic processes is of utmost importance, advances in time and spatial resolution have been made also in the theoretical description that enable a deepening insight into the effects of light-matter interaction. The increasing number of publications in the field of correlated *ab initio* simulations emphasizes the interest of understanding optical excitations in the time domain [1–7], just to name a few very recent ones.

The theoretical frameworks that enables to capture the electron dynamics while maintaining the single-electron picture in an explicitly time-dependent fashion can be multi-reference descriptions as the time-dependent multiconfiguration self-consistent field method (TD-MCSCF), also known as multiconfiguration time-dependent Hartree–Fock (MCTDHF) [8–14], and single-reference descriptions like time-dependent coupled cluster (TD-CC) [2,6,15,16], hybrid time-dependent density functional theory/configuration interaction (hybrid TDDFT/CI) [17,18], also known as time-dependent Tamm-Dankov approximation (TD-TDA) [19], and last but not least, time-dependent configuration interaction (TD-CI) [20–27].

The TD-CI method has proven to capture the fundamental electronic response properties within the bound-state manifold since the Coulomb interaction of the created electron-hole pair is naturally included. The description of electronic correlation can be systematically improved towards the full-CI solution. The laser-induced excitation was successfully modeled within the bound-state manifold [21,28], e.g., addressing charge transfer states [5,29–32]. Systematic extensions have been implemented also to the Hamiltonian, e.g., to include the coupling with the continuum via an absorbing potential in real or energy space. Such methods have shown to be very successful for the simulation of ionization processes [7,33–35], including high-harmonics generation [36–39].

Steady progress is being made in formulations that further provide intuitive understandings of the underlying processes through visualization and analysis of electron-hole pairs for the description of electronically excited states. Simple visualization of molecular orbitals (MOs) or excited state densities does not sufficiently explain properties and dynamics, especially for larger system or for very short excitation times when electron correlation becomes more relevant. The local density does not provide enough information on the excited state dynamics because it remains relatively unaltered throughout the process. Capturing the characteristics of excited states, however, can be achieved through concepts like dipole-induced transition orbitals [40], which employ an approximate set of electron-hole orbitals, or by Dyson

* Corresponding author.
E-mail address: annika.bande@helmholtz-berlin.de (A. Bande).

https://doi.org/10.1016/j.chemphys.2022.111502
Received 1 November 2021; Received in revised form 18 January 2022; Accepted 26 February 2022
Available online 2 March 2022

orbitals [41,42] when ionization is considered. Moreover, conditional electron densities have been used to visualise excited state correlation by electron and hole quasi-particles [43].

Already in the 1970s, the idea to obtain an observable measure for the analysis of excited states was formulated in terms of transition densities [44,45]. In particular, the one-particle transition-density matrix (1TDM), which can be regarded as an exciton wavefunction, can be a key parameter in the understanding of electronic excited states [43,46–49] and is easy to evaluate even for larger systems. Furthermore, a singular value decomposition of the 1TDM gives access to natural transition orbitals (NTOs). Their graphical representation renders a visual understanding of the excitation. The consideration of the 1TDM and the associated hole and particle NTO densities provide a compact representation and can be compared to the local densities, for example. Such an exciton-based evaluation is independent of the underlying orbitals and allows an easy differentiation of excited states via properties like the separation of hole and particle. Furthermore, the evaluation can be applied to different excited-state approaches, allowing comparison of exciton properties across methods.

For a visual tracking of electron dynamics, it would be desirable to transfer the above concepts of NTOs, or more generally of 1TDMs, to the time domain. In the frameworks of algebraic diagrammatic construction (ADC), Dutoi et al. have derived the related one-particle difference density [50] and visualized the natural orbitals of electrons and holes for an alkane scaffold [51], a conjugated π system and a chain of three Ne atoms [52].

In this work, we like to follow the exciton wavefunction analysis and present a derivation and implementation of an explicitly time-dependent version of these properties. Besides the direct depiction of NTOs and local densities for the illustration of the change of hole and electron position driven by light, also exciton descriptors are introduced to quantify and accompany the visualization of some local densities. For the first application of such a time-dependent exciton analysis, this work is revisiting laser-driven simulations on H_2 [53] and LiCN [29]. These two studies describe the laser conditions under which on the one hand a state-to-state transition can be induced in a controlled fashion or on the other hand a wave packet is formed.

All dynamics computations and analyses of this study are performed with the *Jellyfish* TD-CI program package that is developed in our group. Due to its modular structure it allows the flexible execution of TD-CI including the underlying electronic structure calculations such as Hartree–Fock or CI at any truncation level. *Jellyfish* comes with a graphical user interface (GUI) that enables flexible compilation of calculations or the implementation of interfaces to other quantum chemistry programs like *ORCA* [54]. Additionally it contains graphics modules using the open-source library *VTK* for on-the-fly rendering of stationary and time-dependent wavefunctions or orbitals, respectively. These modules are implemented so that the user can control various parameters like isosurface values, plot range, resolution, or color scheme, for example. They enable the export of video animations and snapshots of the time-dependent wavefunctions as presented in this work. Further details of the *Jellyfish* package will be given soon in a separate publication. For this study, however, we developed several modules that enable post-processing of dynamical simulations. Here, we present the implementation of the aforementioned excited state analysis by means of the 1TDM, as well as the visualization of various wavefunction densities.

As the title suggests, one driving force of this study is the possibility to visualize the quantum mechanical process of the light-induced excitation of the electronic system. The results of the computations are summarized and interpreted in figures and text for a printable copy, however, we would like to encourage the reader to view as well the videos provided along this publication.

This paper is organized as follows: in Section 2 the theoretical background for the analysis of laser-induced electron dynamics is introduced with a special focus on time-dependent local densities and 1TDM descriptors. Section 3 presents and discusses the electron dynamics on H_2 and LiCN in terms of time-dependent exciton properties and local densities. Section 4 concludes the most significant results and gives an outlook. Atomic units ($e = \hbar = m_e = 4\pi\varepsilon_0 = 1$) are used if not stated otherwise.

2. Theory

2.1. Time-dependent CI in a nutshell

The many-electron dynamics driven by an external light source can be computed numerically from the time-dependent Schrödinger equation (TDSE)

$$i\partial_t|\Psi_{el}(t)\rangle = \left[\hat{\mathbf{H}}_{el} + \widehat{\vec{\mu}}\cdot\vec{\mathrm{F}}(t)\right]\Big|\Psi_{el}(t)\rangle, \tag{1}$$

provided that the electronic wavefunction, $|\Psi_{el}(t)\rangle$, at a given initial time, t_0, is known. Here, the electronic Hamiltonian is $\hat{\mathbf{H}}_{el} = \hat{\mathbf{T}}_{el} + \hat{\mathbf{V}}_{el,el} + \hat{\mathbf{V}}_{el,nuc}$. The oscillating external field $\vec{\mathrm{F}}(t)$, e.g., a laser pulse is treated in the semi-classical dipole approximation, since the molecular systems under study are relatively small in size compared to the electromagnetic wavelength. Specifically, we use linearly polarized $\cos^2$-shaped laser pulses of the form: $\vec{\mathrm{F}}(t) = \vec{f}_0 \cdot sin(\omega(t-t_p))\cdot\cos^2(\frac{\pi}{2\sigma}(t-t_p))$ with the carrier frequency, ω, and the pulse width, σ centered at t_p. The molecular dipole operator for a system composed of N electrons and N_A nuclei is given by $\widehat{\vec{\mu}} = -\sum_i^N \vec{r}_i + \sum_A^{N_A} Z_A \vec{R}_A$.

The expansion of the electronic wavefunction in CI eigenfunctions, Φ_i,

$$|\Psi_{el}(t)\rangle = \sum_i B_i(t)|\Phi_i\rangle, \tag{2}$$

leads to the time-dependent CI methodology and reduces Eq. (1) to the propagation of the time-dependent expansion coefficients $B_i(t)$. This way, time-dependent populations, for instance, are expressed by $P_i(t) = |\langle\Phi_i|\Psi(t)\rangle|^2 = |B_i(t)|^2$. In the results, we present laser-driven dynamics simulations with wavefunctions obtained from the configuration interaction singles (CIS), the configuration interaction singles doubles (CISD), and the configuration interaction singles including perturbative doubles corrections (CIS(D)). In CISD, the ground state wavefunction includes electron correlation due to singly- and doubly-excited determinants, while the CIS ground state is equal to the Hartree–Fock ground state. In CIS(D), the wavefunctions remain at CIS level, however, their energies (ground state included) contain perturbative corrections. Further details to the TD-CI methodology are outlined elsewhere [29,36].

2.2. Time-dependent density and difference densities

The time-dependent local density can be computed from the CI expansion (Eq. (2)) as [18,55]

$$\rho^{CI}(r,t) = \sum_k |B_k(t)|^2 \langle\Phi_k|\hat{\rho}(r)|\Phi_k\rangle + 2\sum_k\sum_{l<k} Re(B_k^*(t)B_l(t))\langle\Phi_k|\hat{\rho}(r)|\Phi_l\rangle. \tag{3}$$

The matrix elements $\langle\Phi_k|\hat{\rho}(r)|\Phi_l\rangle$ are evaluated from the CI amplitudes, $B_k(t)$, and follow the Slater-Condon rules. With that, the difference of the local densities from the wavefunction at two different times can be calculated as

$$\rho(r,t) - \rho(r,t') = \sum_k\sum_l Re(B_k'^*(t')B_l'(t'))\langle\Phi_k|\hat{\rho}|\Phi_l\rangle - \sum_k\sum_l B_k'^*(t')B_l'(t')\langle\Phi_k|\hat{\rho}|\Phi_l\rangle. \tag{4}$$

Two kind of difference densities $\Delta\rho(\boldsymbol{r},t)$ are of particular relevance: for t'

being the initial time, the difference density $\rho(r,t) - \rho(r,t=0) \equiv \Delta_0(t)$ traces the evolution of the local density with respect to the initial state. For t' being the previous time step, the difference $\rho(r,t_n) - \rho(r,t_{n-1}) \equiv \Delta_t(t)$ captures a step-wise change of the density reflecting the time-progress as computed by Eq. (1) and will be called gradient density in the following. Both time-dependent difference quantities, $\Delta_0(t)$ and $\Delta_t(t)$, will be used to visualize the dynamical process.

2.3. One-particle transition density matrix

The local (difference) densities provide information on the multi-electron system as a whole. The one-particle transition density matrix enables to gain insight into the dynamics in the excited state alone. By adopting the analysis of static excited state properties derived from the 1TDM, also termed exciton wavefunction [47,49,56], we present a time-dependent variant of the same. It is the matrix between the ground state $\langle\Phi_0|$ and, in this case, the time-dependent wavefunction $|\Psi(t)\rangle$ given explicitly as

$$\chi_{exc}(r_h, r_e, t) = \int \dots \int \Phi_0(r_h, r_2, \dots, r_N) \cdot \Psi(r_e, r_2, \dots, r_N, t)\, dr_2, \dots, dr_N, \tag{5}$$

where N is the number of electrons, r_i the spatial-spin coordinates of ith electron, and r_h and r_e are the hole and particle (electron) coordinates, respectively. From a singular value decomposition (SVD) of this matrix natural transition orbitals (NTOs) for the electron-hole pairs are obtained in case stationary functions are used.

By formulating the time-dependent version of the exciton wavefunction, however, Φ_0 and $\Psi(t)$ cannot be assumed to be orthogonal at all times. At the start of propagation, when $\Psi(t=0) = \Phi_0$, such an "exciton wavefunction" would correspond to the density matrix of the ground state Φ_0 and the time-dependent dipole moment would directly relate to the time-dependent "particle-hole" distance defined below. However, the corresponding NTO densities derived from the 1TDM then can no longer be termed "particle" or "hole" densities. In order to maintain the single-particle orbital picture of electron and hole, only the component of $\Psi(t)$ that lies in the orthogonal complement space of Φ_0 is considered for our time-dependent analysis. This is achieved by the projection $(1 - |\Phi_0\rangle\langle\Phi_0|)\ |\Psi(t)\rangle$ that removes the ground state contribution from the time-dependent wavefunction in the following derivation and analysis of exciton properties.

The matrix representation of the one-particle transition density in the basis of the underlying spin orbitals is given as

$$\gamma^{t0}_{\mu\nu}(t) = \langle\Psi(t)\left|\hat{a}^\dagger_\mu \hat{a}_\nu\right|\Phi_0\rangle, \tag{6}$$

where $\hat{a}^\dagger_\mu$ and $\hat{a}_\nu$ are the creation and annihilation operators to the spin orbitals χ_μ and χ_ν, respectively.

For configuration interaction singles, $\gamma^{t0}_{\mu\nu}$ can be calculated from the expansion coefficients of the time-dependent wavefunction $B_j(t)$ and the wavefunction amplitudes of the underlying CI eigenstates C^a_{ij} as $\gamma^{t0}_{\mu\nu}(t) = \sum_j B_j(t)\delta_{\mu a}\delta_{\nu i}C^a_{ij}$. Here, C^a_{ij} is the excitation coefficient from occupied orbital i to virtual orbital a for the j-th eigenstate. [1]

By introducing time-dependent NTOs, an alternative and even more compact representation of the exciton wavefunction is obtained

$$\chi_{exc}(r_h, r_e, t) = \sum_K \sigma_K(t)\psi^h_K(r_h,t)\psi^e_K(r_e,t), \tag{7}$$

where each of the K NTO pairs corresponding to a singular value σ_K is composed of a hole state ψ^h_K and an electron state ψ^e_K. They can be obtained from a SVD of the transition density matrix

$$\boldsymbol{\gamma}^{0t}(t) = \mathbf{U}(t)\boldsymbol{\Sigma}\mathbf{V}^T(t), \tag{8}$$

such that the hole NTOs become

$$\psi^h_K(r,t) = \sum_q U_{qK}(t)\chi_q(r) \tag{9}$$

and the electron NTOs

$$\psi^e_K(r,t) = \sum_q V_{qK}(t)\chi_q(r). \tag{10}$$

With Eq. (9) the NTO hole density can be defined as

$$\rho^{NTO}_h(r_h,t) = \sum_K \sigma_K(t)^2 \psi^h_K(r_h,t)^2. \tag{11}$$

The NTO electron density is obtained analogously.

The norm of the 1TDM quantifies the single excitation component of the excitation from Φ_0 to $\Psi(t)$

$$\Omega(t) \equiv \langle\chi_{exc}(t)|\chi_{exc}(t)\rangle = \sum_{\mu\nu}\left(\gamma^{0t}_{\mu\nu}(t)\right)^2 = \int \chi_{exc}(r_h,r_e,t)^2 dr_h dr_e. \tag{12}$$

The normalization can also be expressed in matrix elements as

$$\Omega(t) = \mathbf{tr}\left(\boldsymbol{\gamma}^{t0}(t)\mathbf{S}\boldsymbol{\gamma}^{0t}(t)\mathbf{S}\right), \tag{13}$$

where $\mathbf{S}$ represents the overlap matrix in the basis of the Hartree–Fock orbitals.

The exciton wavefunction can be analyzed more deeply by expectation values to operators of interest

$$\langle\widehat{O}\rangle_{exc}(t) = \frac{1}{\Omega(t)}\langle\chi_{exc}(t)|\widehat{O}|\chi_{exc}(t)\rangle, \tag{14}$$

where the operators are composed of electron and hole multipole moments [47]. This expression can be used to compute exciton quantities that further characterize the electron-hole pair creation and it spatial evolution in the excited states. For example, the distance between the centroids of electron and hole is given as

$$d_{h\to e} = \left|\langle r_h - r_e\rangle_{exc}\right|, \tag{15}$$

and complementary to this is the exciton size, which is defined as the root-mean-square separation between electron and hole position

$$d_{exc} = \sqrt{\left\langle |r_h - r_e|^2 \right\rangle_{exc}}. \tag{16}$$

Similar to the exciton size, the hole size is calculated as

$$\sigma_h = \sqrt{\langle r_h^2\rangle_{exc} - \langle r_h\rangle^2_{exc}} \tag{17}$$

and analogously for the particle size.

Removing the ground state from the total wavefunction makes a renormalization necessary to recover the time-dependent contribution of the excited states for the time-dependent treatment. That means, the exciton quantities given above are multiplied by the norm of the exciton wavefunction. For example, the time-dependent particle-hole distance is calculated as $\Omega(t)\cdot d_{h\to e}$ for the evaluation of dynamics. Additionally, the time-independent values for the normalized exciton wavefunction as derived from the stationary state analysis [47] are noted in the respective figures for comparison.

2.4. Computational Details

The numerical propagations have been carried out using an operator splitting technique [57] with a time step of $\Delta t = 0.2\,\hbar/\mathrm{E_h}$. Visualization

[1] In a Hermitian formalism like CI, the exchange of bra and ket state corresponds to the Hermitian conjugate of the transition density matrix $\left(\boldsymbol{\gamma}^{0t}\right)^T = \boldsymbol{\gamma}^{t0}$.

of the different densities by three isosurfaces with gradually decreasing transparency is chosen to capture the gradient of the fall-off of density. Except for the time-independent CIS(D)[2] calculations, which were performed with *ORCA* program package[54], all calculations shown were performed with the newly developed program *Jellyfish*, i.e., electron structure and dynamics calculations as well as all shown evaluations. A working version can be obtained upon request from the authors and a polished version will be released under an open source license in 2022.

3. Results and Discussion

3.1. Dynamics in the hydrogen molecule

In this section, we are revisiting a study of Saalfrank and coworkers on the H_2 molecule [53]. The visualizations provide further insight on the excitation process as a result of two of pulse intensities. A comparison of underlying wavefunctions is given and the analysis through the time-dependent exciton wavefunction.

The stationary CI states of the hydrogen molecules are calculated for a fixed bond length of $R_0 = 1.401\,\mathrm{a_0}$ employing the aug-cc-pVDZ basis set [58,59]. CIS, CIS(D), and CISD singlet states are used for the time propagations. In all calculations, the first singlet excited state ($^1\Sigma_u$ symmetry) is dominated by a HOMO–LUMO transition and accessible by optical excitation from the ground state by a relatively large transition dipole moment parallel to the bond axis, $\mu_{0,1;z} = \langle\Psi_0|\hat{\mu}_z|\Psi_1\rangle$, of 1.012 $\mathrm{ea_0}$ (2.573 Debye) for CIS and 0.994 $\mathrm{ea_0}$ (2.525 Debye) for CISD.

In accordance to the dipole selection rules, a z-polarized pulse creates a nodal plane perpendicular to this axis, reflecting a $\sigma\rightarrow\sigma^*$ transition of one electron. Such a state-to-state transition can be achieved by so-called π pulses. For the used $\cos^2$ pulse envelope the relation between π pulse duration, σ, and its field amplitude, $\overrightarrow{f}_0$ is given by $\sigma\cdot\overrightarrow{f}_0 = \pi/\overrightarrow{\mu}_{0,1}$. In the following, the dynamics due to two z-polarized pulses are presented: a "short" and intense π pulse ($\sigma = 50\,\hbar/\mathrm{E_h}$ (1.2 fs), $f_{0;z} = 0.062\,\mathrm{E_h/ea_0}, 1.35{\cdot}10^{14}$ W/cm^2) and a "long" one with moderate intensity ($\sigma = 1000\,\hbar/\mathrm{E_h}$ (24.2 fs), $f_{0;z} = 0.003\,\mathrm{E_h/ea_0}, 3.15{\cdot}10^{11}$ W/cm^2), both with the same carrier frequency resonant to the first excited state of $\omega_{0,1}^{\mathrm{CIS}} = 0.466\,\mathrm{E_h}/\hbar$, $\omega_{0,1}^{\mathrm{CIS(D)}} = 0.466\,\mathrm{E_h}/\hbar$, and $\omega_{0,1}^{\mathrm{CISD}} = 0.465\,\mathrm{E_h}/\hbar$, respectively.

At first, before describing the full excitation process, a comparison of the dynamics as a consequence of three TD-CI methods is discussed. This comparison is presented in Fig. 1 and in the Animation in the Supplementary in terms of local densities, $\rho^{CI}(t)$ (yellow surfaces), difference densities, $\Delta_0(t)$ (green and red isosurfaces), and gradient density, $\Delta_t(t)$ (pink and blue) for the TD-CIS, TD-CIS(D), and TD-CISD. The green and red isosurfaces of the difference density show the increase and decrease of local electronic density when compared to the initial, ground state density. As an additional measure, only available in the time regime, the gradient density, $\Delta_t(t)$, is introduced. It evaluates the difference density to the previous time step, and therefore visualizes the dynamics as computed by the time-dependent Schrödinger equation, Eq. (1). Negative values of $\Delta_t(t)$ are represented by pink isosurfaces and illustrate the loss of local density with respect to the previous time step, while positive values illustrate the increase of electronic density by blue isosurfaces.

Shown in panel (A) of Fig. 1 are the local and the difference densities at the start and at the end of propagation for the three TD-CI methods in comparison. The local densities of the ground state display the well-known ellipsoid of the binding $^1\Sigma_g$ state. At the end of propagation the first excited state with σ^* character has a population of $P_1 = 0.999$ for all methods. The local densities at the end of the propagation reflect the expected transition of a single electron by a reduced ellipsoidal core and a more diffuse density aside of the nuclear position with a clear indentation in the center. This transition of a single electron from the core to the valence regions is much more clearly seen in the difference density, where electron density was removed from the center (red surfaces) and has moved to the outer sides of each H atom (green surfaces). These densities are essentially identical for all underlying CI methodologies. Noteworthy is that the final TD-CISD local density shows somewhat more compactness in the center, the overall differences, however, are rather small.

The density redistribution upon excitation establishes during the whole propagation and a close view on the dynamics around the midpoint of the propagation is also discussed. The Animation in the Supplementary shows the dynamics at every computed time step for the 15 central laser cycles. Fig. 1(B) summarizes this animation in a compact manner by displaying snapshots during the central optical cycle (around $t = 1000\,\hbar/\mathrm{E_h}$, also plotted in panel (B), middle), where the laser intensity reaches its maximum for TD-CIS on the left and TD-CISD on the right side, respectively.

Best seen in the animation is how the local density oscillates along the molecular axis due to the z-polarized field. During each laser cycle, the amount of density gain in the valence regions increases as the dynamics of the difference density confirms. The electronic density, however, is lagging behind the oscillations of the driving field as seen in the time-dependent dipole moment. Known from classical mechanics, this is the signature of an excitation at the transition frequency, where a phase shift of $\pi/2$ is observed. As a consequence, at the pulse maxima, the local densities show a symmetric distribution while at time steps where the field strength is zero, the local density is displaced towards the positive z direction. In this regard, $\Delta_0(t)$ visualizes the oscillations of the charges as monitored by the time-dependent dipole moment.

The gradient density shows the flow of the electron density in the moment of this time step. For the sake of readability, we term positive and negative gradient density in the following as "transient particle" (blue isosurfaces) and "transient hole" (pink isosurfaces). The oscillations of $\Delta_t(t)$ are in phase with the laser pulse cycles. The transient hole has its maximal extent when the optical cycle reaches a maximum and it is minimal when the field is crossing zero.[3] While the transient holes and particles have a symmetric distribution along the bond axis just after maximal field strength. They are interchanging their positions in a particular way: while both minimize their spatial extent, the transient hole shrinks and moves along the H-H bond. Meanwhile, the transient particle is never to be found between the atoms but instead surrounding the transient hole by forming a ring torus for a single time step (seen in the video at $t = 1000.4\,\hbar/\mathrm{E_h}$, for example).

Comparing the TD-CIS, TD-CIS(D), and TD-CISD methods across the video sequence, the density progressions are virtually indistinguishable. This is literally illustrating that even for the most sensitive local density evaluation, the gradient density, no differences have manifested and, in the case of a single-electron process, the dynamics can be regarded as independent of the underlying CI level. While Fig. 1 presents the dynamics by mere illustration, a more quantitative approach is provided in the following by TD-CIS(D) propagations.

The full excitation process to the first excited state can be viewed in the Animation in the Supplementary. Fig. 2 summarizes these TD-CIS(D) dynamics. In addition to the above presented local densities of the many-body wavefunction, $\rho^{CI}(t)$ and $\Delta_0(t)$, also time-dependent NTO densities, $\rho^{\mathrm{NTO}}(t)$ are introduced as defined in Eq. (11). Furthermore, the time-dependent exciton descriptors like the hole and particle positions, their size (Eq. (17)), the hole-particle distance (Eq. (15)), as well as the exction size (Eq. (16)) are used to evaluate and quantify the dynamics.

The difference density at the end of the propagation ($\Delta_0(t =$

[2] The MP2 double corrections to the CIS energies have been calculated employing the resolution of identity algorithm with an automated auxiliary basis set.

[3] Note, in the current *Jellyfish* implementation the laser is starting at the first time step, not at the zeroth and is therefore shifted by 0.2 $\hbar/\mathrm{E_h}$.

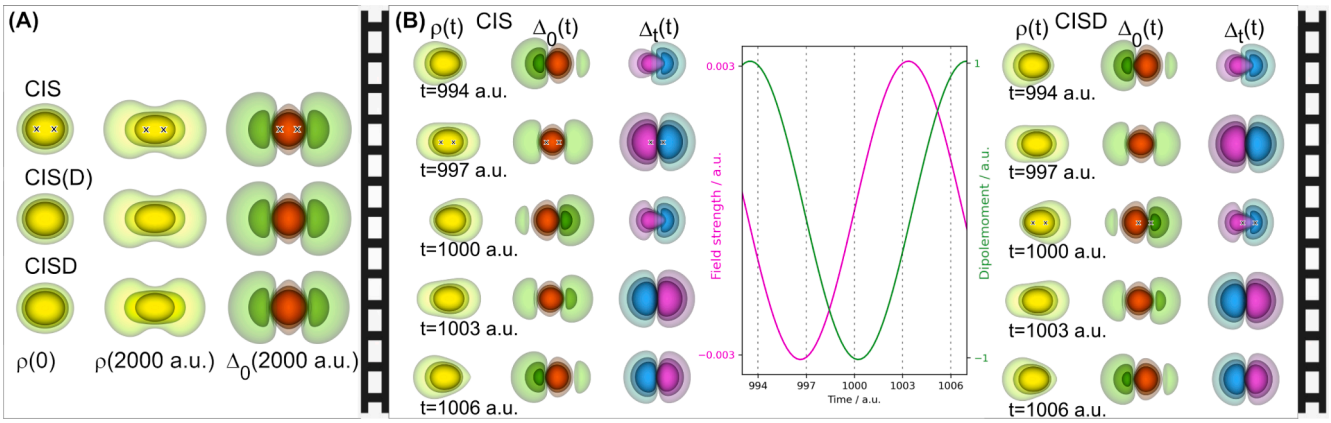

Fig. 1. Shown are various densities at different times from the propagation with the long π pulse of the width $\sigma = 1000\,\hbar/\mathrm{E_h}$. Panel (A) shows the local density $\rho^{CI}(t)$ (yellow isosurfaces) at the initial and the final time and the density difference $\Delta_0(t_{\mathrm{end}})$ (positive density in green and negative in red isosurfaces) at the final time. Panel (B) depicts several snapshots of the local density, difference density, $\Delta_0(t)$, and density gradient, $\Delta_t(t)$, as a result of the single cycle in the center of the π pulse (shown in the central plot). The CIS and CISD densities are on the left and right side. The atomic positions are marked as crosses on top of the isosurfaces. A video of this Figure content is available in the Supplementary.

$2000\,\hbar/\mathrm{E_h}$, red and green isosurfaces) compares very well to hole and electron NTO densities (gray and blue isosurface). In the time-dependent view, however, differences among the densities are clearly visible. While the electron NTO densitiy, $\rho_e^{\mathrm{NTO}}(t)$, majorly rises in spatial extent – due to increasing NTO orbital population –, the difference density $\Delta_0(t)$ shows an explicit time dependence. In the first third of the pulse duration, negative and positive difference densities are created at the atomic centers and interchanging their positions with the pulse cycles (the above mentioned phase shift of $\pi/2$ is hardly noticeable on this time scale). Then, around the halftime, when the pulse reaches its maximum, the negative difference density (red surfaces) becomes more localized around the atomic bond in the shape of an ellipsoid and remains slightly oscillating in this region during the end of the propagation. At the same time the positive difference density – the gain of local density (green surface) – oscillates at the outer regions of the atomic centers while increasing its spatial extent at each cycle until the oscillation dies out with decreasing pulse intensity. The oscillations of the difference density can be directly correlated to the time-dependent dipole moment (green curve of the center plot).

The NTO density for the electron (blue isosurfaces) and the hole

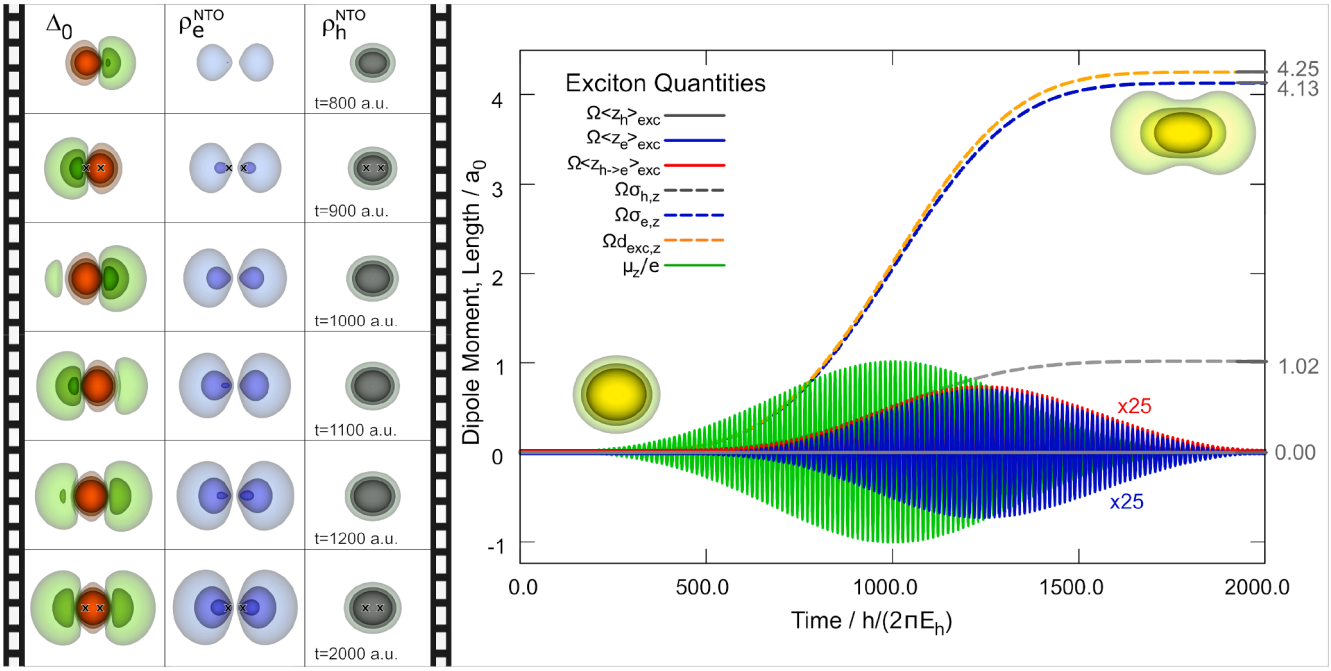

Fig. 2. Summary of the H_2 excitation dynamics using the "long" π pulse. Shown on the left are difference densities (red and green isosurfaces), and NTO densities for electron and hole (blue and gray isosurfaces) for selected times. Shown in the right is the z component of the time-dependent dipole moment (green) together with various time-dependent exciton properties: hole and particle position (gray, blue), hole-particle distance (red), hole and particle size (dashed gray, blue), and the exciton size (orange). Local densities (yellow isosurfaces) are given for the initial and the final time. The atomic positions are indicated by crosses on top of some isosurfaces. Values for the exciton wavefunction employing the stationary analysis according to [47] are noted in gray color on the left y axis. A video of this Figure content is available in the Supplementary.

(gray) do not show much of this oscillation. Both NTO densities mostly rise in their spatial extent with increasing occupation. This volume increase of both NTO densities is well reflected by the smooth rise of their corresponding exciton quantifiers, the sizes for hole, particle, and exciton (dashed blue, dashed gray and dashed orange lines). The small noticeable oscillations of the electron NTO density are captured by its position expectation value, $\Omega(t)\langle z_p\rangle$ (blue solid line, magnified by a factor of 25), while the hole position, monitored by $\Omega(t)\langle z_h\rangle$ (gray solid line), remains at its position around the hydrogen bond. Thus, the expectation value for the particle-hole distance, $\Omega(t)\langle z_{p\to h}\rangle$ (red solid line, also magnified by a factor of 25), is entirely composed of the position of the electron.

The same analysis is applied for the optical excitation with the short π pulse as seen in the Animation in the Supplementary and summarized in Fig. 3. For this intense pulse, a coherent superposition of excited states, an electronic wave packet, is created. Here, the laser pulse consists of eight optical cycles only and dynamics become noticeable early in the propagation. Compared to the smooth state-to-state transition of the previous case, here, the local density (yellow) shows not only a very dynamical behavior in its outer isosurface, but also in its core ellipsoid. $\Delta_0(t)$ illustrates this motion in terms of difference to the ground state. Theses oscillations are well captured by the time-dependent particle NTO density, ρ_e^{NTO}, that reproduces the progression of the positive difference density in terms of shape and spatial extent. But the hole NTO density cannot reproduce the dynamics as they are visible in the negative difference density (red isosurfaces). Since the ground state of the H_2 molecule is composed of one doubly occupied MO only, the hole density necessarily corresponds to the density of that MO and further dynamics in the hole is not to be expected. The particle wavefunction, on the other hand, results from multiple occupied virtual orbitals, thus depicting a dynamical shape.

As expected and seen in the animation, or on the right-hand side panel of Fig. 3, the hole density solely increases its spatial extent, quantified by $\Omega\sigma_{h,z}$ (dashed gray line), while its position, $\Omega\langle z_h\rangle_{\mathrm{exc}}$ (solid gray), remains constant at $0\,\hbar/\mathrm{E_h}$. All of the exciton quantities are hence determined by the particle properties. Like the exciton size (dashed orange line) rises jointly with the particle size (dashed blue), the hole-particle distance (solid red line) is ruled by the position expectation value of the electron (solid blue) and both oscillate equally around the molecular center even after the pulse is off. Their oscillation amplitudes differ from the time-dependent dipole moment (solid green line) since the exciton quantities are computed by excluding the ground state, they record the dynamics in the excited states alone. As a consequence, the oscillations of the hole-particle distance scales with increasing population of the excited states.

3.2. Charge transfer dynamics in LiCN

The collinear three-atomic LiCN molecule is a much favored test system for a light-induced charge transfer (CT) along the molecular axis [5,31]. In this section, again, an illustrative update to the dynamics simulations by Saalfrank and coworkers [29] is given. Here, their level of theory and their comparison of optical excitation by two different π pulses is reproduced. Specifically, the electron dynamics from excitation with a "short" π pulse of a width of $\sigma = 100\,\hbar/\mathrm{E_h}$ (2.4 fs) and a field strength of $f_{0;x} = 0.103\ \mathrm{E_h/ea_0}$ ($3.7{\cdot}10^{14}$ W/cm^2) is compared to a "long" π pulse of a width $\sigma = 2000\,\hbar/\mathrm{E_h}$ (48.4 fs) and a field strength of $f_{0;x} = 0.005\ \mathrm{E_h/ea_0}$ ($9.24{\cdot}10^{11}$ W/cm^2). The *ORCA* program package [54] is used to carry out the electronic structure calculation at CIS(D)/6-31G* [60] level of theory with LiCN being oriented parallel to the z axis at fixed internuclear distances of $R_{\mathrm{Li-C}} = 3.683\,\mathrm{a_0}$ and $R_{\mathrm{C-N}} = 2.168\,\mathrm{a_0}$. Freezing four core electrons leads to 204 singlet CIS(D) states, all of which are included in the subsequent TD-CIS(D) simulations.

LiCN in the ground state has an ionic character ($\mathrm{Li^+CN^-}$) leading to a permanent dipole moment of $\mu_{0;z} = -3.707\ \mathrm{ea_0}$ (-9.422 Debye), while the target CT state is twofold degenerate and has a permanent dipole of $\mu_{2/3;z} = +2.802\ \mathrm{ea_0}$ ($+7.122$ Debye). Optical excitation to the particular CT state, thus, is accompanied by a large change of the dipole moment which reflects the transfer of negative charge, i.e., electron density, from the HOMO localized on the CN group to the LUMO localized on the Li atom. The transition to either of the degenerate CT

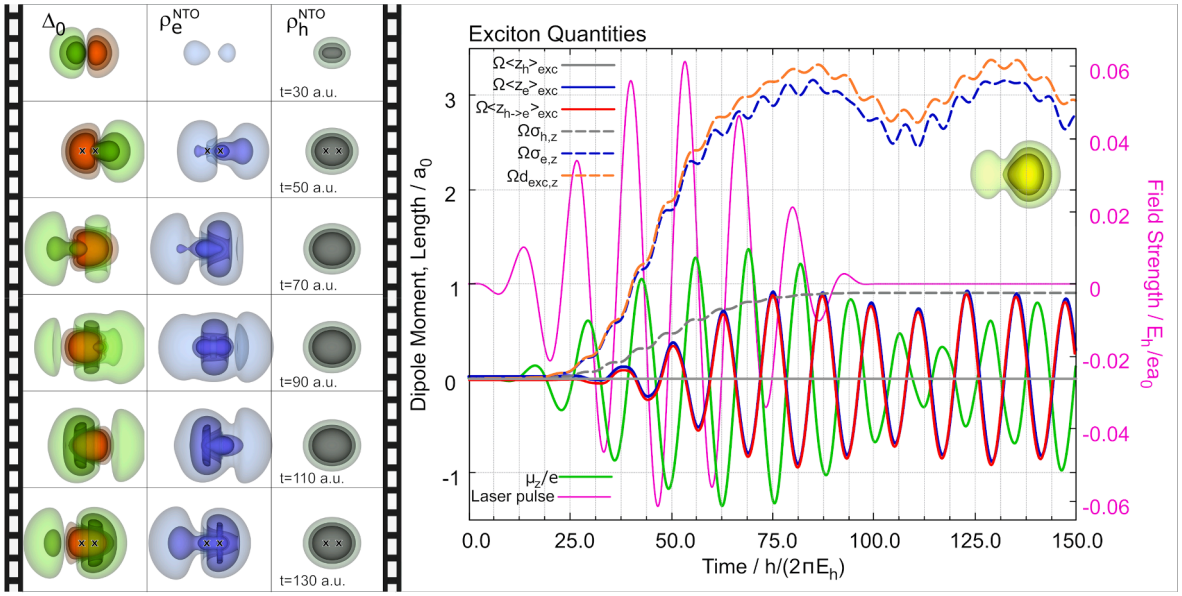

Fig. 3. Summary of the H_2 excitation dynamics using the "short" and intense π pulse. Shown on the left are difference densities (red and green isosurfaces), and NTO densities for electron and hole (blue and gray isosurfaces) for selected times. Shown in the right is the z component of the time-dependent dipole moment (green) together with the laser pulse (pink) and various time-dependent exciton properties: hole and particle position (gray, blue), hole-particle distance (red), hole and particle size (dashed gray, blue), and the exciton size (orange). Local densities (yellow isosurfaces) are given for the final time. The atomic positions are indicated by crosses on top of some isosurfaces. A video of this Figure content is available in the Supplementary.

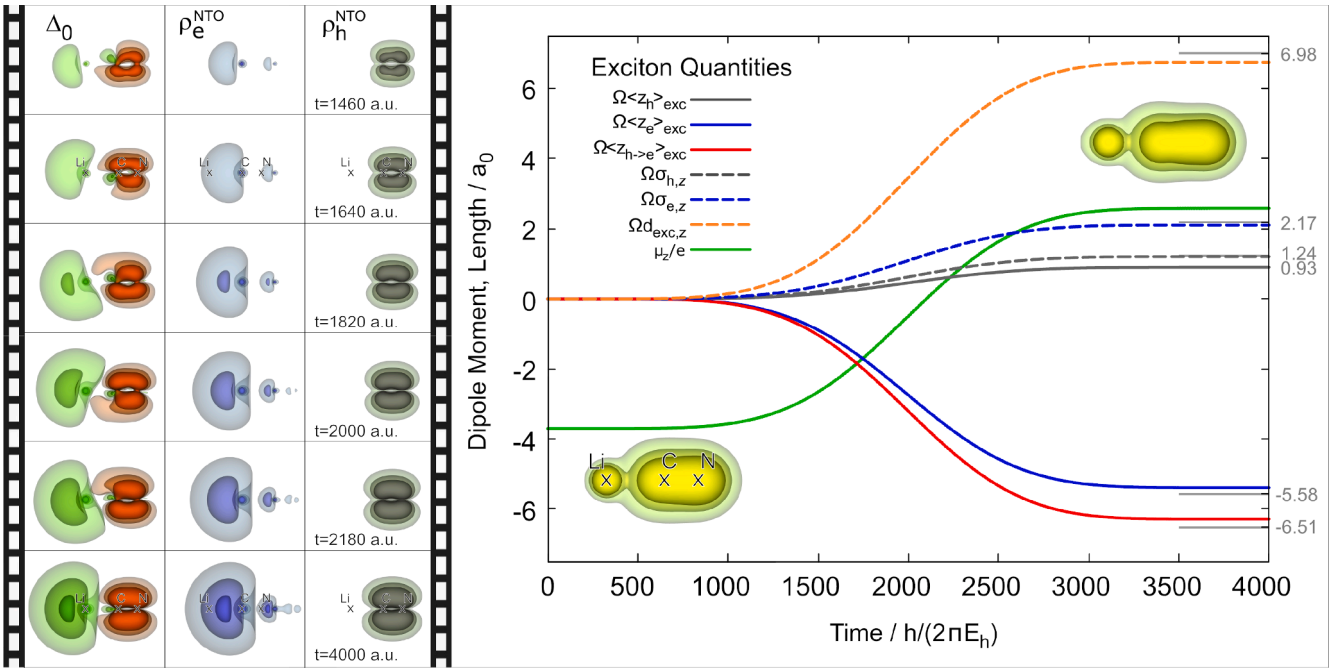

Fig. 4. Summary of the LiCN excitation dynamics using the "long" π pulse. Shown on the left are difference densities (red and green isosurfaces), and NTO densities for electron and hole (blue and gray isosurfaces) for selected times. Shown on the right is the z component of the time-dependent dipole moment (green) together with various time-dependent exciton properties: hole and particle position (gray, blue), hole-particle distance (red), hole and particle size (dashed gray, blue), and the exciton size (orange). Local densities (yellow isosurfaces) are given for the initial and the final time. The atomic positions are indicated by crosses on top of some isosurfaces. A video of this Figure content is available in the Supplementary.

states is possible due to a large transition dipole moment along the x or y direction. The corresponding transition dipole moments are $\mu_{0,2;x} = 0.306\ \mathrm{ea_0}$, $\mu_{0,2;y} = -0.003\ \mathrm{ea_0}$ and $\mu_{0,3;x} = -0.003\ \mathrm{ea_0}$, $\mu_{0,3;y} = -0.306\ \mathrm{ea_0}$. The excitation to the CT state is addressed by an x-polarized π pulse, where the small transition dipole moment along y is omitted for the sake of simplicity.

First, the laser-driven dynamics as a consequence of the long-pulse excitation is discussed. Animation in the Supplementary and Fig. 4 show the local (difference) and NTO densities, as well as the progression of the exciton descriptors along the molecular axis. The electron density for LiCN (yellow isosurfaces) depicts only small changes during laser excitation since only one electron out of 16 is promoted to a virtual orbital. The circular indentation between the Li atom and the CN group reflects the ionic character of this compound and is not affected by the CT.

The transfer of charge from the CN group to the Li atom can already be seen in the time-dependent dipole moment (green curve) along the z direction. It changes smoothly from the value of the ground state to almost the one of the excited state which reflects the target state population of 97% at the end of the propagation. A more detailed view is provided by the local difference density and the NTO densities. The respective exciton properties allow a quantification of the CT character. The hole position and size (solid and dashed gray) change by about $1.0\ \mathrm{a_0}$ and remain located on the CN group. The particle position (solid blue) changes by about $-5.6\ \mathrm{a_0}$ while its size (dashed blue) increases about $2.2\ \mathrm{a_0}$. In terms of charge separation, the recorded $-6.5\ \mathrm{a_0}$ for the hole-particle distance (solid red) and $7.0\ \mathrm{a_0}$ for the exciton size (dashed orange) even exceed the molecular size of $-5.9\ \mathrm{a_0}$, the distance between the Li and the N atom. The creation of the hole on the CN group and the creation of a particle at the Li atom, are captured by the visualization of the difference and the NTO densities. The NTO densities allow a general description of the hole and particle formation. The local difference density captures the oscillations along the laser polarization. In the beginning of the propagation rapid oscillations along the x direction on the CN group are visible. During the cause of increasing field strength, negative difference density, a hole, is manifesting on this side while on the other side, at the Li atom the positive difference density is accumulating in an oscillatory manner. At the end of the pulse, the difference densities and the respective hole and particle NTO densities have a very similar shape and spatial extent.

The dynamics due to the short pulse can be viewed in Animation in the Supplementary and its summary in Fig. 5. The excitation with an intense pulse, again, creates a coherent superposition of excited states. This electronic wave packet leads to rapid oscillations in all quantities persistent even after the pulse is off at $t = 200\,\hbar/\mathrm{E_h}$. A complete interpretation is limited since single- and multi-photon transitions from the ground state as well as between the excited states are induced by the intense laser field. Hence, the exciton wavefuntion is composed of excitations from and to multiple MOs in LiCN and dynamics in both hole and particle NTO densities are expressed more pronounced. While for the long pulse the hole density is dominated by a transition from a single π orbital on the CN group, the hole density for the short pulse originates from transitions from lower-lying σ orbitals. As a consequence, the hole density exhibits more dynamics extending also to the Li atom. Nonetheless, the hole remains localized as it originates from binding orbitals only. The corresponding particle ends up in valence orbitals so that the particle NTO density (blue isosurfaces) exhibits large changes in shape and the delocalization extends over the whole molecule for this short pulse excitation. The diffuse distribution also becomes evident in the particle size (dashed blue line), which oscillates around a larger value than in the case of the long pulse. The comparatively larger delocalization manifests also in large values of particle position (solid blue) and hole-particle distance (solid red) and exciton size (dashed orange). In the case of multiple orbital contributions, the dynamic shapes of the NTO densities much closer reflect the positive and negative difference densities over the time since the whole process is more dominated by the dynamics in the excited states.

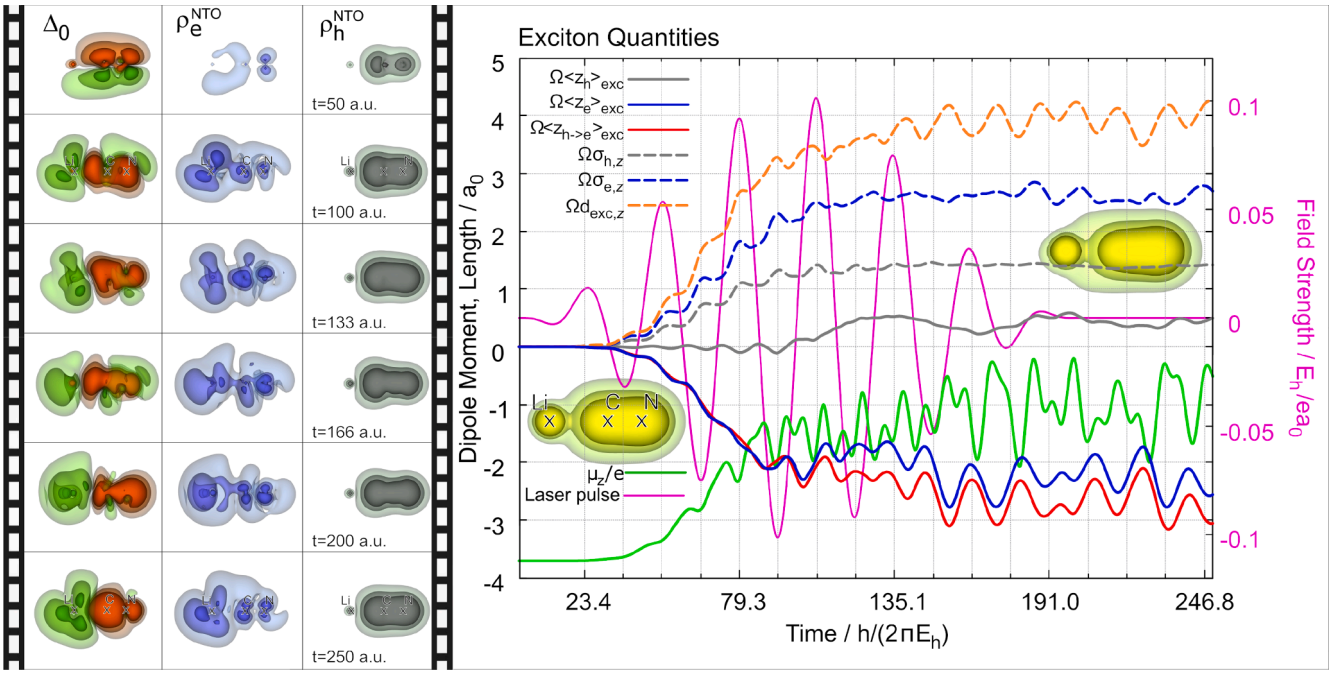

Fig. 5. Summary of the LiCN excitation dynamics using the "short" and intense π pulse. Shown on the left are difference densities (red and green isosurfaces), and NTO densities for electron and hole (blue and gray isosurfaces) for selected times. Shown on the right is the z component of the time-dependent dipole moment (green) together with the laser pulse (pink) and various time-dependent exciton properties: hole and particle position (gray, blue), hole-particle distance (red), hole and particle size (dashed gray, blue), and the exciton size (orange). Local densities (yellow isosurfaces) are given for the final time. The atomic positions are indicated by crosses on top of some isosurfaces. A video of this Figure content is available in the Supplementary.

4. Conclusions and Outlook

Making optical excitations visible and moreover quantifying the results of light-driven excited state dynamics is a long-standing quest in the electron dynamics community, both for the experimentalists and the theorists. In this TD-CI study we have derived time-dependent quantities for the excited states from the one-particle transition density matrix, such as natural transition orbital densities, position expectation values for hole and particle, or the estimation of sizes for hole, electron, and exciton. This exciton wavefunction extension to TD-CI was implemented into our group-owned program *Jellyfish*. The time-dependent 1TDM quantities were supplemented with the local density and two kinds of difference densities as complementary time-resolving analysis tool. The small molecular systems H_2 and LiCN served as test systems for resonant π pulse excitations that either induce a pure excited state population by a long pulse or create an electronic wave packet as a consequence of a short and intense pulse.

For H_2, the TD-CIS, TD-CIS(D), and TD-CISD method were compared but showed no obvious differences with respect to the considered densities in the state-to-state transitions. This confirms that both the ground and the respective excited state densities can be satisfactorily described with the underlying CIS wavefunction. For the propagation with the long laser pulse, the local (difference) densities oscillate in the laser field, while the NTO densities do not exhibit such dynamics but rather increase in space. Here, the hole NTO density remains localized at the molecular center, while the electron occupies the more diffuse valence regions outside the H-H bond. For the short pulse propagation, where a coherent superposition of excited states was created, the exciton descriptors show non-trivial progressions that provide further information about the dynamics in the multiply populated excited states.

LiCN served as a benchmark system for a charge transfer excitation. This transition was archived by a long π pulse. The charge transfer was visible in all densities except for the local density. Parallel to the changing dipole moment, the difference density reflected the flow of electron density from the CN group to the Li atom. Same was observed for the NTO densities as the particle has build up on Li while the hole emerges at the CN group, resulting in an increased hole-particle distance. The exciton descriptors have proven to be useful in describing such a charge transfer. For the creation of a wave packet by the short and intense pulse, the NTO densities well depicted the transitions from lower-lying MOs and thus expressing an explicit time dependence in the electron and the hole NTO densities.

The time-dependent exciton properties reflect what is visualized by the NTO densities and thus serve as a good measure to quantify their evolution in time. This is even more apparent for intense pulses leading to complicated wave packet dynamics. Its arising complexity is not easily describable by the use of spatial densities. Instead, the exciton properties facilitate interpretation through stable average values at the end of the pulse and can capture the electron dynamics in the excited states.

Beyond the time-dependent exciton properties we presented transient hole and particles through the gradient densities, shown here, to our knowledge, for the first time. They are a measure only available in the time regime and we plan further application and analysis of this property. To capture more of the complex excitation process, the time-dependent NTO densities may be extended by their phase information through coloration of the isosurface [52]. In terms of underlying methods, a comparison of the dynamics, as obtained, with other methods, e.g., from the hybrid TDDFT/CI methods, will be illustrative.

Besides these purely scientific considerations, the visualization itself is holding promising didactical opportunities for students of all chemical disciplines that seek an understanding of optical excitations. Specifically for theoretical chemistry, the program *Jellyfish* will proof to be a useful teaching instrument to foster an intuitive understanding for the quantum mechanical origin of dynamics. Due to its graphical interface and its modular structure, setting up dynamics calculations is simple and time-

dependent densities and properties are obtained straightforwardly for analysis.

Declaration of Competing Interest

The authors declare that they have no known competing financial interests or personal relationships that could have appeared to influence the work reported in this paper.

Acknowledgements

The authors are grateful to the Volkswagen Foundation for financial support through the Freigeist Fellowship no 89525. We acknowledge the compute cluster of the Helmholtz-Zentrum Berlin for computational time. The authors thank J. C. Tremblay for various scientific discussions. Pascal Krause thanks Peter for inducing a long-term interest in the shortest timescales chemistry has to offer.

References

[1] P. Saalfrank, F. Bedurke, C. Heide, T. Klamroth, S. Klinkusch, P. Krause, M. Nest, J. C. Tremblay, Chapter Two - Molecular attochemistry: Correlated electron dynamics driven by light, Advances in Quantum Chemistry 81 (2020) 15–50, https://doi.org/10.1016/bs.aiq.2020.03.001.
[2] H. Pathak, T. Sato, K.L. Ishikawa, Time-dependent optimized coupled-cluster method for multielectron dynamics. II. A coupled electron-pair approximation, J. Chem. Phys. 152 (12) (2020) 124115, https://doi.org/10.1063/1.5143747.
[3] M.K. Lee, P. Hoerner, W. Li, H.B. Schlegel, Effect of spin-orbit coupling on strong field ionization simulated with time-dependent configuration interaction, J. Chem. Phys. 153 (2020) 244109, https://doi.org/10.1063/5.0034807.
[4] X. Li, N. Govind, C. Isborn, A.E. DePrince, K. Lopata, Real-time time-dependent electronic structure theory, Chem. Rev. 120 (2020) 9951–9993, https://doi.org/10.1021/acs.chemrev.0c00223.
[5] P. Grobas Illobre, M. Marsili, S. Corni, M. Stener, D. Toffoli, E. Coccia, Time-resolved excited-state analysis of molecular electron dynamics by TDDFT and Bethe-Salpeter equation formalisms, J. Chem. Theor. Comp. 17 (2021) 6314–6329, https://doi.org/10.1021/acs.jctc.1c00211.
[6] B.C. Cooper, L.N. Koulias, D.R. Nascimento, X. Li, A.E. DePrince, Short Iterative Lanczos Integration in Time-Dependent Equation-of-Motion Coupled-Cluster Theory, J. Phys. Chem. A 125 (2021) 5438–5447, https://doi.org/10.1021/acs.jpca.1c01102.
[7] P. Hoerner, W. Li, H.B. Schlegel, Sequential double ionization of molecules by strong laser fields simulated with time-dependent configuration interaction, J. Chem. Phys. 155 (2021) 114103, https://doi.org/10.1063/5.0060365.
[8] M. Nest, T. Klamroth, P. Saalfrank, Ab initio Electron Dynamics with the Multi-Configuration Time-dependent Hartree-Fock Method, Zeitschr. Phys. Chem. 224 (2010) 569–581, https://doi.org/10.1524/zpch.2010.6124.
[9] T. Sato, K.L. Ishikawa, Time-dependent complete-active-space self-consistent-field method for multielectron dynamics in intense laser fields, Phys. Rev. A 88 (2013) 023402, https://doi.org/10.1103/PhysRevA.88.023402.
[10] H. Miyagi, L.B. Madsen, Time-dependent restricted-active-space self-consistent-field theory for laser-driven many-electron dynamics. II. Extended formulation and numerical analysis, Phys. Rev. A 89 (2014) 063416, https://doi.org/10.1103/PhysRevA.89.063416.
[11] A. Haller, A. Bande, Favoritism of quantum dot inter-Coulombic decay over direct and multi-photon ionization by laser strength and focus, J. Chem. Phys. 149 (2018) 134102, https://doi.org/10.1063/1.5042208.
[12] A. Haller, D. Peláez, A. Bande, Inter-Coulombic Decay in Laterally Arranged Quantum Dots Controlled by Polarized Lasers, J. Phys. Chem. C 123 (2019) 14754–14765, https://doi.org/10.1021/acs.jpcc.9b01250.
[13] H. Liu, A.J. Jenkins, A. Wildman, M.J. Frisch, F. Lipparini, B. Mennucci, X. Li, Time-Dependent Complete Active Space Embedded in a Polarizable Force Field, J. Chem. Theor. Comp. 15 (2019) 1633–1641, https://doi.org/10.1021/acs.jctc.8b01152.
[14] R. Binder, I. Burghardt, First-principles description of intra-chain exciton migration in an oligo(*para*-phenylene vinylene) chain. II. ML-MCTDH simulations of exciton dynamics at a torsional defect, J. Chem. Phys. 152 (2020) 204120, https://doi.org/10.1063/5.0004511.
[15] C. Huber, T. Klamroth, Explicitly time-dependent coupled cluster singles doubles calculations of laser-driven many-electron dynamics, J. Chem. Phys. 134 (2011) 054113, https://doi.org/10.1063/1.3530807.
[16] D.R. Nascimento, A.E. DePrince, Linear Absorption Spectra from Explicitly Time-Dependent Equation-of-Motion Coupled-Cluster Theory, J. Chem. Theor. Comput. 12 (2016) 5834–5840, https://doi.org/10.1021/acs.jctc.6b00796.
[17] S. Klinkusch, J.C. Tremblay, Resolution-of-identity stochastic time-dependent configuration interaction for dissipative electron dynamics in strong fields, J. Chem. Phys. 144 (2016) 184108, https://doi.org/10.1063/1.4948646.
[18] G. Hermann, V. Pohl, J.C. Tremblay, An open-source framework for analyzing N-electron dynamics. II. Hybrid density functional theory/configuration interaction methodology, J. Comput. Chem. 38 (2017) 2378-2387 doi:10.1002/jcc.24896. URL: https://doi.org/10.1002/jcc.24896.
[19] P. Hoerner, M.K. Lee, H.B. Schlegel, Angular dependence of strong field ionization of N2 by time-dependent configuration interaction using density functional theory and the Tamm-Dancoff approximation, J. Chem. Phys. 151 (5) (2019) 054102, https://doi.org/10.1063/1.5108846.
[20] H.B. Schlegel, S.M. Smith, X. Li, Electronic optical response of molecules in intense fields: Comparison of TD-HF, TD-CIS and TD-CIS(D) approaches, J. Chem. Phys. 126 (2007) 244110.
[21] J.A. Sonk, H.B. Schlegel, TD-CI Simulation of the Electronic Optical Response of Molecules in Intense Fields II: Comparison of DFT Functionals and EOM-CCSD, J. Phys. Chem. A 115 (2011) 11832–11840, https://doi.org/10.1021/jp206437s.
[22] J.C. Tremblay, T. Klamroth, P. Saalfrank, Time-dependent configuration interaction calculations of laser-driven dynamics in presence of dissipation, J. Chem. Phys. 129 (2008) 084302, https://doi.org/10.1063/1.2972126.
[23] L. Greenman, P.J. Ho, S. Pabst, E. Kamarchik, D.A. Mazziotti, R. Santra, Implementation of the time-dependent configuration-interaction singles method for atomic strong-field processes, Phys. Rev. A 82 (2010) 023406, https://doi.org/10.1103/PhysRevA.82.023406.
[24] G. Hermann, J.C. Tremblay, Laser-Driven Hole Trapping in a Ge/Si Core–Shell Nanocrystal: An Atomistic Configuration Interaction Perspective, J. Phys. Chem. C 119 (2015) 25606–25614, https://doi.org/10.1021/acs.jpcc.5b08606.
[25] E. Coccia, E. Luppi, Optimal-continuum and multicentered Gaussian basis sets for high-harmonic generation spectroscopy, Theor. Chem. Acc. 135 (2016) 43, https://doi.org/10.1007/s00214-015-1770-z.
[26] I.S. Ulusoy, Z. Stewart, A.K. Wilson, The role of the CI expansion length in time-dependent studies, J. Chem. Phys. 148 (2018) 014107, https://doi.org/10.1063/1.5004412.
[27] P.J. Lestrange, M.R. Hoffmann, X. Li, Chapter Seventeen - Time-Dependent Configuration Interaction Using the Graphical Unitary Group Approach: Nonlinear Electric Properties, Advances in Quantum Chemistry 76 (2018) 295–313, https://doi.org/10.1016/bs.aiq.2017.06.003.
[28] P. Krause, J.C. Tremblay, A. Bande, Atomistic Simulations of Laser-Controlled Exciton Transfer and Stabilization in Symmetric Double Quantum Dots, J. Phys. Chem. A 125 (2021) 4793–4804, https://doi.org/10.1021/acs.jpca.1c02501.
[29] P. Krause, T. Klamroth, P. Saalfrank, Time-dependent configuration-interaction calculations of laser-pulse-driven many-electron dynamics: Controlled dipole switching in lithium cyanide, J. Chem. Phys. 123 (2005) 074105, https://doi.org/10.1063/1.1999636.
[30] P. Krause, T. Klamroth, Dipole switching in large molecules described by explicitly time-dependent configuration interaction, J. Chem. Phys. 128 (2008) 234307, https://doi.org/10.1063/1.2939241.
[31] J.C. Tremblay, P. Krause, T. Klamroth, P. Saalfrank, Time-dependent response of dissipative electron systems, Phys. Rev. A 81 (2010) 0634205, https://doi.org/10.1103/PhysRevA.81.063420.
[32] F. Weber, J.C. Tremblay, A. Bande, Proton-Coupled Electron-Transfer Dynamics of Water Oxidation at N-Doped Graphene Oxides, J. Phys. Chem. C 124 (2020) 26688–26698, https://doi.org/10.1021/acs.jpcc.0c08937.
[33] S. Klinkusch, P. Saalfrank, T. Klamroth, Laser-induced electron dynamics including photoionization: A heuristic model within time-dependent configuration interaction theory, J. Chem. Phys. 131 (2009) 114304, https://doi.org/10.1063/1.3218847.
[34] A.F. White, C.J. Heide, P. Saalfrank, M. Head-Gordon, E. Luppi, Computation of high-harmonic generation spectra of the hydrogen molecule using time-dependent configuration-interaction, Mol. Phys. 114 (2016) 947–956, https://doi.org/10.1080/00268976.2015.1119900.
[35] P. Krause, H.B. Schlegel, Angle-Dependent Ionization of Small Molecules by Time-Dependent Configuration Interaction and an Absorbing Potential, J. Phys. Chem. Lett. 6 (2015) 2140–2146, https://doi.org/10.1021/acs.jpclett.5b00929.
[36] F. Bedurke, T. Klamroth, P. Krause, P. Saalfrank, Discriminating organic isomers by high harmonic generation: A time-dependent configuration interaction singles study, J. Chem. Phys. 150 (2019) 234114, https://doi.org/10.1063/1.5096473.
[37] E. Luppi, E. Coccia, Probing the molecular frame of uracil and thymine with high-harmonic generation spectroscopy, Phys. Chem. Chem. Phys. 23 (2021) 3729–3738, https://doi.org/10.1039/D0CP05559J.
[38] C.F. Pauletti, E. Coccia, E. Luppi, Role of exchange and correlation in high-harmonic generation spectra of H_2, N_2, and CO_2: Real-time time-dependent electronic-structure approaches, J. Chem. Phys. 154 (2021) 014101, https://doi.org/10.1063/5.0033072.
[39] F. Bedurke, T. Klamroth, P. Saalfrank, Many-electron dynamics in laser-driven molecules: wavefunction theory vs. density functional theory, Phys. Chem. Chem. Phys. 23 (2021) 13544–13560, https://doi.org/10.1039/D1CP01100F.
[40] G. Hermann, L.E. Marsoner Steinkasserer, B. Paulus, J.C. Tremblay, Dipole-Induced Transition Orbitals: A Novel Tool for Investigating Optical Transitions in Extended Systems, J. Phys. Chem. Lett. 9 (2018) 6624–6630, https://doi.org/10.1021/acs.jpclett.8b02253.
[41] C.M. Oana, A.I. Krylov, Dyson orbitals for ionization from the ground and electronically excited states within equation-of-motion coupled-cluster formalism: Theory, implementation, and examples, J. Chem. Phys. 127 (2007) 234106, https://doi.org/10.1063/1.2805393.
[42] T.-C. Jagau, A.I. Krylov, Characterizing metastable states beyond energies and lifetimes: Dyson orbitals and transition dipole moments, J. Chem. Phys. 144 (2016) 054113, https://doi.org/10.1063/1.4940797.
[43] F. Plasser, Visualisation of Electronic Excited-State Correlation in Real Space, ChemPhotoChem 3 (2019) 702–706, https://doi.org/10.1002/cptc.201900014.

[44] A.A.S.A.V. Luzanov, V.E. Umanskii, Application of transition density matrix for analysis of excited states, Theor. Exp. Chem. 10 (1976) 354–361, https://doi.org/10.1007/BF00526670.
[45] A.V. Luzanov, V.F. Pedash, Interpretation of excited states using charge-transfer number, Theor. Exp. Chem. 15 (1980) 338–341, https://doi.org/10.1007/BF00520694.
[46] F. Plasser, M. Wormit, A. Dreuw, New tools for the systematic analysis and visualization of electronic excitations. I. Formalism, J. Chem. Phys. 141 (2014) 024106, https://doi.org/10.1063/1.4885819.
[47] S.A. Mewes, F. Plasser, A. Krylov, A. Dreuw, Benchmarking Excited-State Calculations Using Exciton Properties, J. Chem. Theory Comput. 14 (2018) 710–725, https://doi.org/10.1021/acs.jctc.7b01145.
[48] F. Plasser, TheoDORE: A toolbox for a detailed and automated analysis of electronic excited state computations, J. Chem. Phys. 152 (2020) 084108, https://doi.org/10.1063/1.5143076.
[49] A.I. Krylov, From orbitals to observables and back, J of Chemical Physics 153 (2020) 080901, https://doi.org/10.1063/5.0018597.
[50] A.D. Dutoi, L.S. Cederbaum, M. Wormit, J.H. Starcke, A. Dreuw, Tracing molecular electronic excitation dynamics in real time and space, J. Chem. Phys. 132 (2010) 144302, https://doi.org/10.1063/1.3353161.
[51] A. Dutoi, L. Cederbaum, An Excited Electron Avoiding a Positive Charge, J. Phys. Chem. Lett. 2 (2011) 2300, https://doi.org/10.1021/jz200887k.
[52] A.D. Dutoi, Visualising many-body electron dynamics using one-body densities and orbitals, Mol. Phys. 112 (2014) 1–11, https://doi.org/10.1080/00268976.2013.845311.
[53] P. Krause, T. Klamroth, P. Saalfrank, Molecular response properties from explicitly time-dependent configuration interaction methods, J. Chem. Phys. 127 (2007) 034107, https://doi.org/10.1063/1.2749503.
[54] F. Neese, The ORCA program system, Comp. Mol. Sci. 2 (2012) 73–78, https://doi.org/10.1002/wcms.81.
[55] V. Pohl, G. Hermann, J.C. Tremblay, An open-source framework for analyzing *N*-electron dynamics. I. Multideterminantal wave functions, J. Comput. Chem. 38 (2017) 1515–1527, https://doi.org/10.1002/jcc.24792.
[56] S.A. Bäppler, F. Plasser, M. Wormit, A. Dreuw, Exciton analysis of many-body wave functions: Bridging the gap between the quasiparticle and molecular orbital pictures, Phys. Rev. A 90 (2014) 052521, https://doi.org/10.1103/PhysRevA.90.052521.
[57] A.D. Bandrauk, E. Aubanel, S. Chelkowski, Molecules in Intense Laser Fields: Applications, Femtosecond Chemistry 2 (1995) 731, https://doi.org/10.1002/9783527619436.ch25.
[58] T.H. Dunning, Gaussian basis sets for use in correlated molecular calculations. I. The atoms boron through neon and hydrogen, J. Chem. Phys. 90 (1989) 1007–1023, https://doi.org/10.1063/1.456153.
[59] A.K. Wilson, T. van Mourik, T.H. Dunning, Gaussian basis sets for use in correlated molecular calculations. VI. Sextuple zeta correlation consistent basis sets for boron through neon, J. Mol. Struct: Theochem. 388 (1996) 339–349, https://doi.org/10.1016/S0166-1280(96)80048-0.
[60] P.C. Hariharan, J.A. Pople, The influence of polarization functions on molecular orbital hydrogenation energies, Theoret. Chim. Acta 28 (1973) 213–222, https://doi.org/10.1007/BF00533485.

5.5 Quantum-Compute Algorithm for Exact Laser-Driven Electron Dynamics in Molecules

Fabian Langkabel and Annika Bande

J. Chem. Theory Comput. 18, 7082-7092 (2022)

DOI: doi.org/10.1021/acs.jctc.2c00878

URL: `https://doi.org/10.1021/acs.jctc.2c00878`

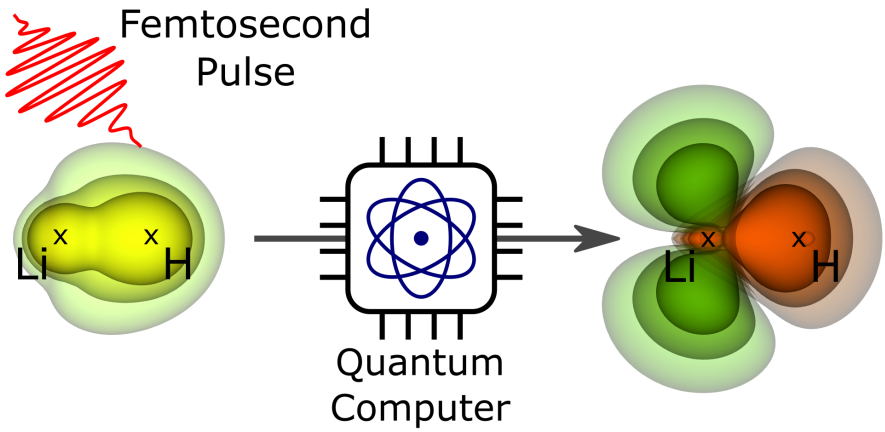

Figure 5.5: Graphical abstract. Reprint with permission from Langkabel et al. [5] (Copyright American Chemical Society (2022))

Author contributions: AB and FL designed the project. The quantum algorithm shown was developed, implemented, and applied by FL with input from AB. The manuscript was mostly written by FL under the supervision of AB. Both authors finalized the manuscript.